



T.C.
MANİSA CELAL BAYAR ÜNİVERSİTESİ
FEN BİLİMLERİ ENSTİTÜSÜ

MANİSA CELAL BAYAR UNIVERSITY
INSTITUTE OF NATURAL&APPLIED
SCIENCE

CİLT:18 SAYI :1 YIL:2022
VOLUME:18 ISSUE:1 YEAR:2022

ISSN: 1305-130X
e-ISSN: 1305-1385

**CELAL BAYAR ÜNİVERSİTESİ
FEN BİLİMLERİ DERGİSİ**

**CELAL BAYAR UNIVERSITY
JOURNAL OF SCIENCE**

**CELAL BAYAR
ÜNİVERSİTESİ**



Journal of Science

Volume: 18, Issue: 1, Year: 2022

Contact

Manisa Celal Bayar University
Institute of Natural and Applied Sciences
Campus of Şehit Prof Dr İlhan Varank 45140 Yunusmre – MANİSA, TURKEY
Tel: (00 90) 236 201 27 05
Fax: (00 90) 236 241 21 49
e-mail: cbujos@gmail.com
Web: <https://dergipark.org.tr/tr/pub/cbayarfbe>

“CBU Journal of Science is indexed by ULAKBIM-TUBITAK TR-DIZIN”



ISSN 1305-130X

E-ISSN 1305-1385

CBUJOS is published quarterly at Manisa Celal Bayar University Printing House

“CBU Journal of Science is a refereed scientific journal”



Celal Bayar University Journal of Science

Owner

Manisa Celal Bayar University,

Editors : Assoc. Prof. Dr. Kamil ŞİRİN

Assoc. Prof. Dr.. Emine KEMİKLİOĞLU

Assistant Editor: Assoc. Prof. Dr. Mustafa AKYOL

Layout Editor & Secretary

Dr. İlker Çetin KESKİN

International Scientific Advisory Board

Prof. Dr. Arianit REKA; State University of Tetova, Macedonia

Prof. Dr. Tomasz NIEMIEC; Warsaw University of Life Sciences, Poland

Prof. Dr. Alyani ISMAIL; Universiti Putra, Malaysia

Prof. Dr. Iuliana APRODU; Dunarea de Jos University, Romania

Assoc. Prof. Dr. Johanan Christian PRASANNA; Madras Christian College, South India

Assoc. Prof. Dr. Noureddine ISSAOUI; Université de Monastir, Tunisie.

Assoc. Dr. Edward Albert UECKERMANN; North-West University, South Africa

Assoc. Dr. Zhi-Qiang ZHANG; The University of Auckland, Holland

Assist. Prof. Dr. Young Ki KIM; Pohang University of Science and Technology, South Korea

Assist. Prof. Can BAYRAM; University of Illinois, USA

Assist. Prof. Dr. Mona MIRHEydARI; Rutgers University, USA

Assist. Prof. Dr. Donatella ALBANESE; Università Degli Studi Di Salerno, Italy

Assist. Prof. Dr. Jinghua JIANG; The University of Memphis, USA

Assist. Prof. Dr. Jens OLDELAND; University of Hamburg, Germany

Dr. Cheng CHENG; Apple Inc., USA

Dr. Sajedah AFGHAH; Microsoft Corporation, USA

Dr. Jinghua JIANG; The University of Memphis

National Scientific Advisory Board

Prof. Dr. Mustafa Ersöz; Selçuk University

Prof. Dr. Oğuz Gürsoy; Mehmet Akif University

Prof. Dr. Mehmet Çevik; İzmir Katip Çelebi University

Prof. Dr. Sezgin Çelik; Yıldız Teknik University

Prof. Dr. Osman Dayan; Çanakkale Onsekiz Mart University

Prof. Dr. Serdar İplikçi; Pamukkale University

Prof. Dr. Yasin Üst; Yıldız Teknik University

Prof. Dr. Mahmut Kuş; Konya Teknik University

Prof. Dr. Ertuğ Gundüz; Hacettepe University

Prof. Dr. Tülin Aydemir; Manisa Celal Bayar University

Prof. Dr. Sezai Taşkın; Manisa Celal Bayar University

Prof. Dr. Fatma Şaşmaz Ören; Manisa Celal Bayar University

Assoc. Prof. Dr. Fatih Doğan; Çanakkale Onsekiz Mart University

Assoc. Prof. Dr. Erol Akpınar; Abant İzzet Baysal University

Assoc. Prof. Dr. Yeliz Yıldırım; Ege University

Assoc. Prof. Dr. Serap Derman; Yıldız Teknik University

Assoc. Prof. Dr. Hayati Mamur; Manisa Celal Bayar University

Assoc. Prof. Dr. Fatih Selimefendigil; Manisa Celal Bayar University

Assoc. Prof. Dr. Özlem Çağındı; Manisa Celal Bayar University

Assoc. Prof. Dr. Osman Çulha; Manisa Celal Bayar University

Assoc. Prof. Dr. Ali Demir; Manisa Celal Bayar University

Assoc. Prof. Dr. Ali Konuralp; Manisa Celal Bayar University

Assist. Prof. Dr. Nil Mansuroğlu; Ahi Evran University

Assist. Prof. Dr. Zeynep Çipiloğlu Yıldız; Manisa Celal Bayar University



CBU Journal of Science

Celal Bayar University Journal of Science (CBUJOS) covers scientific studies in the fields of Engineering and Science and publishes accounts of original research articles concerned with all aspects of experimental and theoretical studies. CBU Journal of Science is a refereed scientific journal published four times annually (March, June, September and December) by Institute of Natural and Applied Sciences of Manisa Celal Bayar University. CBU Journal of Science considers the original research articles written in English for evaluation.

CBU Journal of Science is indexed by TUBİTAK ULAKBİM TR-DİZİN, and also is included in DOAJ, Cite Factor, Journal TOCS, Advanced Science Index and OAJI databases. Digital Object Identifier (DOI) number will be assigned for all the articles being published in CBU Journal of Science.

Instructions for Authors and Article Template can be found on the main page of MCBU Institute of Natural and Applied Sciences (<http://fbe.cbu.edu.tr>)





Vol: 18, Issue: 1, Year: 2022

Contents

Research Article

Pages

Prolonged Biomolecule Release from Titanium Surfaces via Titania Nanotube Arrays

DOI: 10.18466/cbayarfbe.972316

Cem Bayram

1-7

The Effect of Wood Species and Strip Width on Bending Strength and Modulus of Elasticity in End-Grain Core Blockboard

DOI: 10.18466/cbayarfbe.958377

Yasemin Öztürk, Kıvanç Yılmaz, Erol Burdurlu

9-16

The Production and Characterization of Aluminum Barrier Laminate Tubes and Comparison of Mechanical Properties with Reference Material

DOI: 10.18466/cbayarfbe.870469

Mahir Doğan, Keriman Şanlı, Gizem Güler, Yusuf Över

17-21

Comparison of the Host-Based Intrusion Detection Systems and Network-Based Intrusion Detection Systems

DOI: 10.18466/cbayarfbe.832533

Ahmet Efe, İrem Nur Abacı

23-32

Efficient Web-Based Application Development for Carbon Footprint Calculation: Example of Burdur Province

DOI: 10.18466/cbayarfbe.977279

Mustafa Batar

33-39

Self-tuning Fuzzy PID Controller Design and Energy Management in DC Microgrid: Standalone and Grid Connected Mode

DOI: 10.18466/cbayarfbe.832874

Ahmet Kaysal, Selim Köroğlu, Yüksel Oğuz

41-51

Performing DoS Attacks on Bluetooth Devices Paired with Google Home Mini

DOI: 10.18466/cbayarfbe.856119

Tuğrul Yüksel, Ömer Aydın, Gökhan Dalkılıç

53-58

Radar Absorber Fabric Design Based on Periodic Arrays of Circular Shaped Conductive Patches

DOI: 10.18466/cbayarfbe.915217

Muhammet Hilmi Nisancı, Baha Kanberoğlu, Yılmaz Çiğdem, Fatih Özkan Alkurt, Muharrem Karaaslan

59-65

A Review: The Physical, Nutritional, Bioactive Properties and Health Benefits of Jujube Fruit

DOI: 10.18466/cbayarfbe.913267

Fadime Begüm Tepe, Raci Ekinci, Çetin Kadakal, Nizam Mustafa Nizamlıoğlu


67-75



- Boron Removal from Colemanite Mine Wastewater by Coagulation using Zinc Hydroxide—A Factorial Optimization Study 77-83
DOI: 10.18466/cbayarfbe.951542
Mustafa Korkmaz, Cengiz Özmetin, Elif Özmetin, Elif Çalgan, Öznur Ziyanak
- The Effect of Coating Parameters of Active Layer on the Performance of Polymer Solar Cells 85-89
DOI: 10.18466/cbayarfbe.992952
Esma Yenel
- General Atom-Bond-Connectivity Index of Graphs 91-94
DOI: 10.18466/cbayarfbe.975636
Seda Kınacı
- Phytochemistry, Biological Activity and Toxicity of Botanical Dietary Supplement: KL21 95-105
DOI: 10.18466/cbayarfbe.957203
Çinel Kösal Karayıldırım, Adem Güner, Gürkan Yiğittürk, Altuğ Yavaşoğlu, N. Ülkü Karabay Yavaşoğlu
- Long-term Stability of Cationic Phytosphingosine Nanoemulsions as Delivery Systems for plasmid DNA 107-118
DOI: 10.18466/cbayarfbe.948114
Selen Isar, Yiğit Şahin, Hasan Akbaba, Ayşe Nalbantsoy, Gülşah Erel Akbaba, Yücel Başpınar



Prolonged Biomolecule Release from Titanium Surfaces via Titania Nanotube Arrays

Cem Bayram^{1*} 

¹Hacettepe University, Graduate School of Science and Engineering, Nanotechnology and Nanomedicine
Department, Beytepe, 06800, Ankara, Turkey

*cemb@hacettepe.edu.tr

* Orcid : 0000-0001-8717-4668

Received: 16 July 2021

Accepted: 20 January 2022

DOI: 10.18466/cbayarfb.972316

Abstract

Surface modifications against the failure of titanium implants used in hard tissue repair has become a trend in recent years. In the last decade, it has been investigated that nanoscale tubular spaces on the titanium surface can be used as a local drug release reservoir without the need for any chemical binder or polymeric coating. It is possible to obtain one-dimensional structures that can be grown by electrochemical anodic oxidation by controlling the diameters of less than 100 nanometers on titanium metal surfaces. The major disadvantage of biomolecules released from titania nanotube structures to the environment is the hard control of release kinetics and more than half of the loading amount releases in the first few hours of interaction with the biological fluid. Although the studies on controlling the kinetics have been tried to overcome by covering the nanotube arrays with barriers such as polymer structures, the risk of delamination of the polymers from the surface during implantation brings additional problems. In this manuscript, vancomycin and bovine serum albumin were loaded into titania nanotubes formed by anodic oxidation technique on titanium metal plates and the tube ends has been narrowed by gold sputtering technique. With this narrowing at the tube-ends, the length of the release time and the change in diameter according to the hydrodynamic diameter of the released biomolecule were investigated. It is seen that the increased gold sputtering time prolongs the release rate of biomolecules and offers a promising approach for sustained local drug releasing implants.

Keywords: titanium, sustained release, drug loading, implant, anodic oxidation, nanotube

1. Introduction

Millions of hard tissue cases require surgical operations worldwide, including hip and knee replacements, fracture fixations or missing tooth implants due to implant failure. The major reasons of implant failure are aseptic loosening and insufficient osseointegration during the post operation process and drug therapy approach is often recommended to inhibit infections or inflammations that may develop in the post-op period after implantation, or to eliminate the need for revision surgery that results in implant failure. [1-3]. The oral or intravenous administration of drugs have well known disadvantages like systemic toxicity and low efficiency at the target area after elimination throughout the body. Localized delivery of active agents and therapeutics is one of the most efficiently validated approaches, which helps to reduce systemic disadvantages of the administered drugs [4-6]. Additionally, it also maximizes the bioavailability of drugs preventing them

to be eliminated by systemic circulation or gastrointestinal tract. Although implants that release drugs or active substances through polymer or ceramic coatings have been used to eliminate the above-mentioned disadvantages, these conventional approaches are often subject to remove/delaminate from the surface as a result of interactions and frictions in the application area. [7].

Even though, titanium and its alloys are the materials of choice in the majority of hard tissue and dental implant applications, they are still open to many challenges arising from bacterial infections, inflammation or poor adhesion of osteoblast cells, leading to implant failure [8-10]. Although titanium has excellent bulk properties, implant success lies behind its surface morphology and chemistry. The success of a bone/dental implant is highly dependent on the properties of the surface of the implant.

Electrochemical anodic oxidation is a classical technique used on titanium, however the use of fluoride containing organic electrolytes in the last decade has provided the opportunity to control oxide layer produced on titanium surface in terms of both composition and morphology. Controlled oxide dissolution rate achieved by newer electrolyte systems allows to design the surface architecture precisely. In the anodic oxidation process, it is possible to achieve a high aspect ratio or to extend the nanotube size by creating a localized acidification at the bottom of the pore and maintaining the pH value in the pore wall and its surroundings by controlling the TiO_2 dissolution in a controlled manner [11].

In the past decade, research on the direct release of biologically active molecules and drugs from metal surfaces has been intensively studied. The usability of nanotubular structures with less than 100 nm in diameter and controllable length, which can be formed on titanium surfaces by anodic oxidation as local release reservoirs have been tested in these studies. It has been reported that these nanotube structures can release different drugs and biomolecules for several days to several weeks as a result of varying diameters and lengths.

It is known to use small molecules such as antibiotics and macromolecules like growth hormone and therapeutic protein in implants that release bioactive and biological agents. For this reason, an antibiotic and a protein were included in the study as a model compound to test the capability of nanotubes as active agent reservoirs. Vancomycin and BSA molecules were selected in the study. The molecular weight difference was considered as the first criterion in the selection of these two biomolecules. By loading the drugs into the nanotubular cavities produced by anodic oxidation, release profiles with various periods of several hours to a couple of weeks were reported [12-15]. The parameters affecting this diversity in release duration include differences in hydrodynamic diameter of molecule, nanotube length, nanotube diameter and loading procedures of the active agent. Popat et al used gentamicin antibiotics with a simple pipetting on the nanotubular layer and the colonization of *S. epidermidis* bacteria reduced by 40% compared to the control group [12]. In the loading procedures, drug release duration can reach several weeks by coating the nanotubular surfaces with polymeric or ceramic layers [13,16, 17]. As a result of loading operations performed without any additional coating on the surface, it was reported that the release from metal surface was completed within a few days [15,18]. Although the biocompatibility and in vitro stability of polymeric or ceramic coatings to prolong the release time are satisfactory, there is also the possibility of delamination and / or disintegration of these layers having micrometer thicknesses from the

surface of the material during implantation or in a dynamic environment.

The inability to control the release kinetics and the burst release of titanium dioxide nanotubes as a local release element is one of the most important problems. It is inevitable for biomolecules, which stand out as much smaller compared to their nanotube diameters, to exhibit sudden release within the first few hours. In this study, nanotube diameters obtained after anodic oxidation were narrowed by gold, which is known by biocompatible and inert material for implant applications, after the biomolecule loading. The effect of sputtering time to the releasing time behavior were investigated in terms of diameter and the hydrodynamic radius of the biomolecule.

2. Materials and Methods

2.1. Nanotube Formation on Titanium Plates

A two-step anodic oxidation process was performed on the surface of titanium metal plates with a purity of 99.7% (Strem Chemicals, USA). In the process, titanium plates were subjected to the first step of the anodic oxidation for 2 hours by applying 80 V potential voltage in ethylene glycol electrolyte containing 1% of ammonium fluoride (NH_4F) by weight. A platinum mesh electrode was used as counter electrode. After the first step of anodic oxidation, titanium plates were cleaned in an ultrasonic bath for 2 hours for the removal of titanium dioxide nanotubes with irregular orientation. In the second step, titanium dioxide nanotube structures with controllable aspect ratio were created. In the second anodic oxidation step, 30 V potential applied for 120 min.

2.2. Active Agent Loading into Nanotube Structures

Bovine serum albumin (BSA) and vancomycin.HCl were used as model molecules in protein (large molecule) and drug (small molecule) studies to be loaded onto titanium surfaces. BSA and vancomycin.HCl at a concentration of 5 mg/mL were pipetted onto 10 mm x 10 mm cut, nanotube array produced sample surfaces in a volume of 30 μL and subjected to low-speed radial movement on the orbital shaker to diffuse into the nanotubes at room temperature. The samples were dipped in deionized water to wash away the adsorbed protein/drug to the surface and dried at 37 °C overnight.

2.3. Tube-end Narrowing by Gold Sputter

Tube-ends of the protein/drug loaded nanotubes were subjected to gold sputtering in order to reduce the diameter. In a typical process, samples having different diameters were placed in sputtering chamber and gold was coated on the top of the nanotube layer with a rate

of 2.5 nm per minute. Sputtering time was differed as 2, 5 and 10 mins to evaluate the effect of the narrowing on active agent release. The narrowing ratio of diameters were investigated by microscopic methods. Nanotube morphology and diameter measurements were analysed by scanning electron microscopy (SEM) and atomic force microscopy (AFM).

2.4 Spectroscopic and Structural Characterizations

X-Ray Diffraction (XRD) pattern and Attenuated Total Reflection - Fourier Transform Infrared Spectroscopy (ATR-FTIR) data were obtained in order to characterize the crystal structure of surfaces and functional groups, respectively. 1x2 cm samples were analysed in XRD (Rigaku D Max-B, Japan) between 20 – 60 2 θ degrees and 2000 – 600 cm⁻¹ wavenumbers in ATR-FTIR (Thermo, Nicolet iS50, USA).

2.5. Drug Release Studies

Each sample placed separately in 1 mL PBS (pH = 7.2) containing closed vials and the total protein and drug amount released from titanium plates were analyzed with the Nanodrop UV spectrophotometer device (Thermo Scientific, USA) in A280 total protein amount and UV-Vis spectroscopy measurement mode, respectively. Release studies continued until the release curve reach to plateau. Tested samples were summarized in Table 1.

Table 1. Samples tested in release studies.

Sputtering time	Drug/protein	Sample code
Without gold sputter	Vancomycin.HCl	30V_vanco
	BSA	30V_BSA
2 min gold sputter	Vancomycin.HCl	30V_2min_vanco
	BSA	30V_2min_BSA
5 min gold sputter	Vancomycin.HCl	30V_5min_vanco
	BSA	30V_5min_BSA
10 min gold sputter	Vancomycin.HCl	30V_10min_vanco
	BSA	30V_10min_BSA

3. Results and Discussion

3.5. Morphologic Evaluations

The surfaces obtained by the first step of anodic oxidation of are shown in Figure 1a. After the first treatment, the surface character is composed of nanotubes having inner diameters of approximately 100 nm. As mentioned in general information, these tubes are mechanically unstable as a result of the random alignment on the metal surface by different orientations, which makes them easily affected by external forces. The surface shown in Figure 1a was cleaned from nanotubes in the ultrasonic bath for 2 hours by applying low frequency (37 Hz) and high power (100 W) agitation to obtain the surface of Figure 1b. These concave homogeneous regions served as guides for the

structures to be formed on the surface in the second step.

In the second step anodic oxidation process, 30 V potential was applied for 2 hours. Inner growth of new nanotubes was obtained, and the diameters of these nanotubes were found narrower than the template as the anodic oxidation voltage is in proportion with the tube diameter. By applying field-enhanced dissolution on the nanotube template-formed surfaces, the orientation of the nanotube formations on the entire surface was produced in the same direction. According to this, inward growing nanotubes through the template after anodic oxidation with a potential voltage of 30 V were achieved (Figures 1c).

After the gold sputtering step, it has been observed that the tube-endings start to get narrower. Although the narrowing of the tube diameters performed using 2 minutes of coating was not evident in the images, a significant restriction of the outer tube mouth diameters occurred, especially after 5 and 10 minutes of spraying. Especially after 10 minutes of sputtering, the decrease in outer diameter is evident (Figure 2b-d).

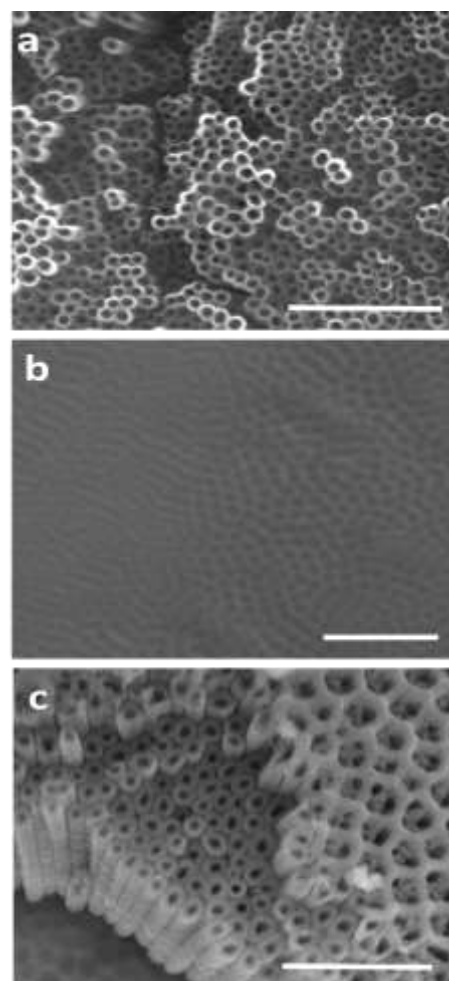


Figure 1. Titanium surfaces after first anodic oxidation process (a) after sonic treatment (b) and after second anodic oxidation (c). White bar indicates 1 μ m.

Figure 3 also indicates that the narrowing of the tube ends, especially after 5 and 10 minutes of sputtering. Images were obtained by an AFM system (Asensis, Turkey). Particularly after 10 minutes of spraying, the outer tube diameter of around 100 nm has been reduced

to approximately 50-70 nm and the internal diameter shrinkage can be observed from the images (Figure 3).

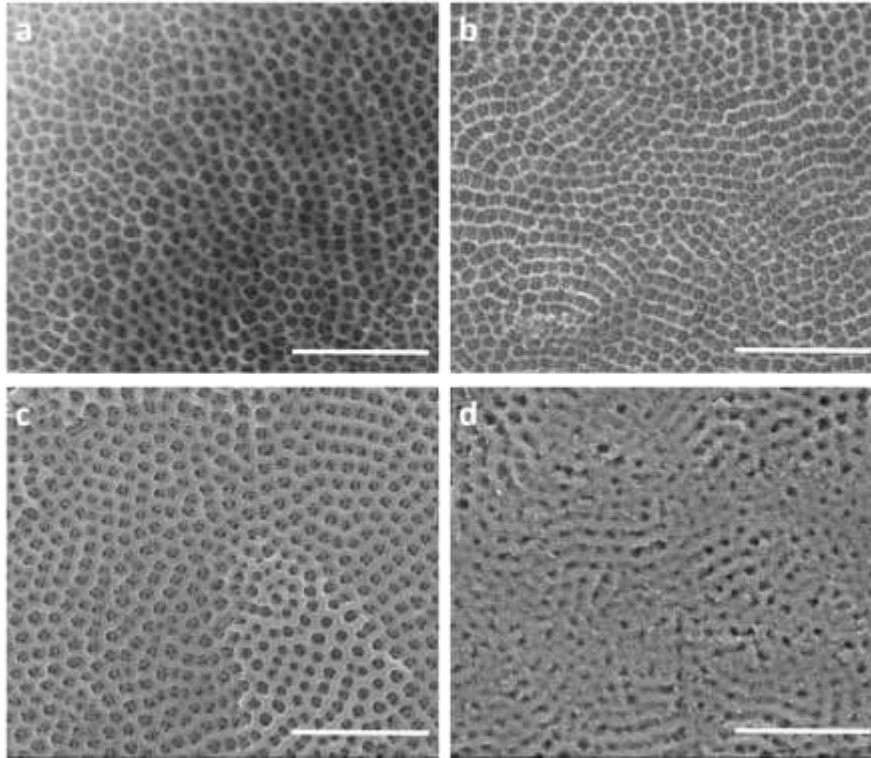


Figure 2. SEM images of titanium surfaces after 2nd anodization (a) and after subsequent 2 (b), 5 (c) and 10 mins (d) of Au sputtering.

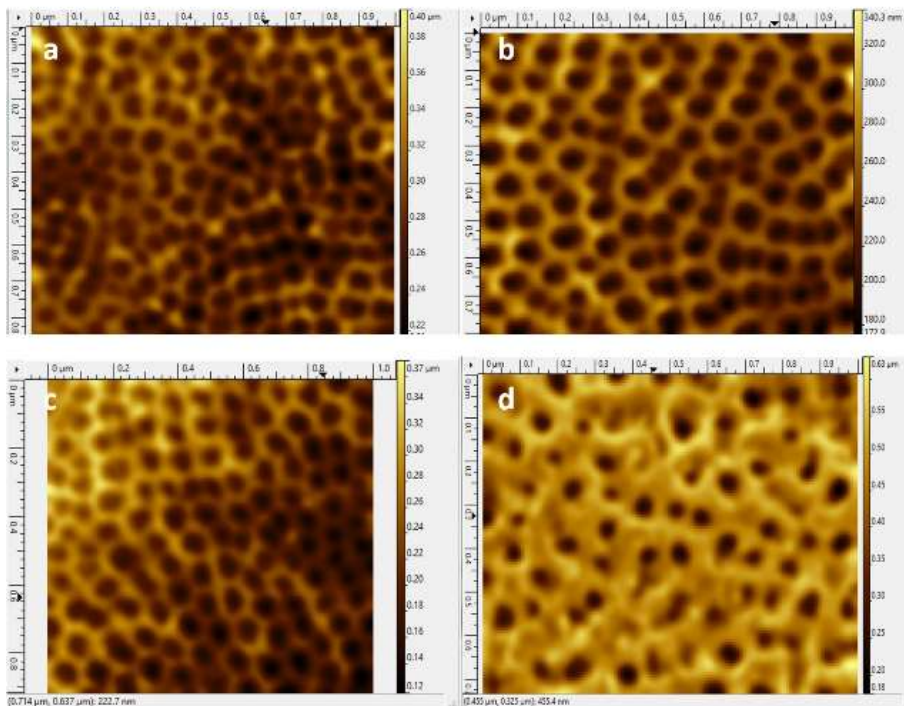


Figure 3. AFM images of titanium surfaces after 2nd anodization (a) and after subsequent 2 (b), 5 (c) and 10 mins (d) of Au sputtering.

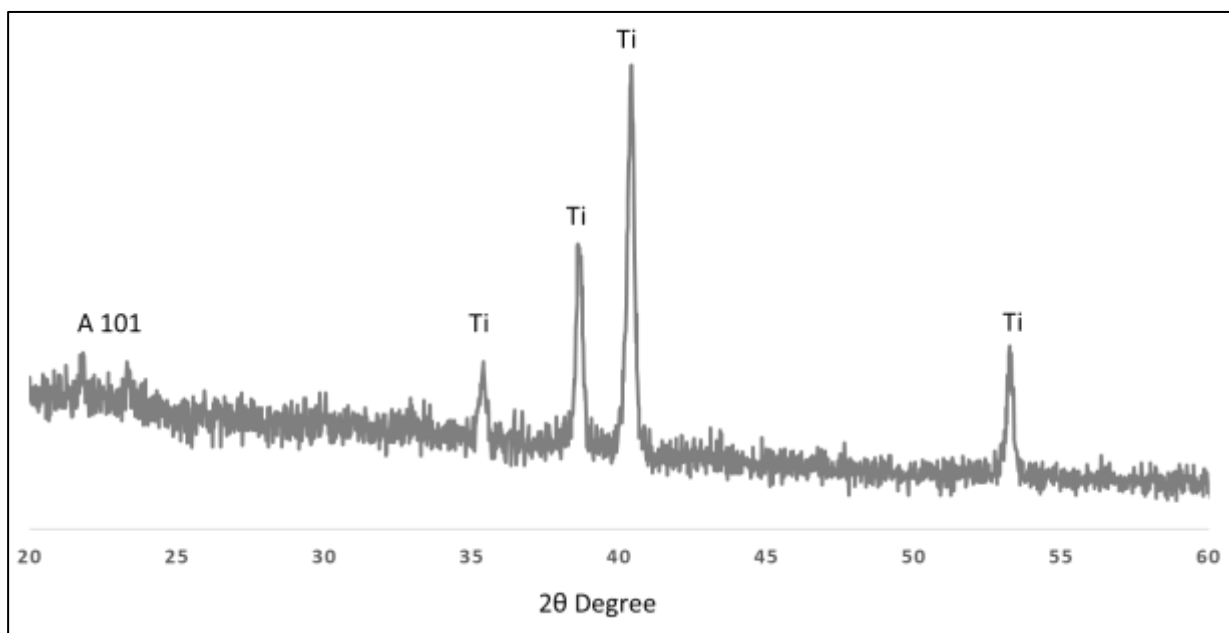


Figure 4. XRD diffraction pattern of anodized TiO₂ surfaces.

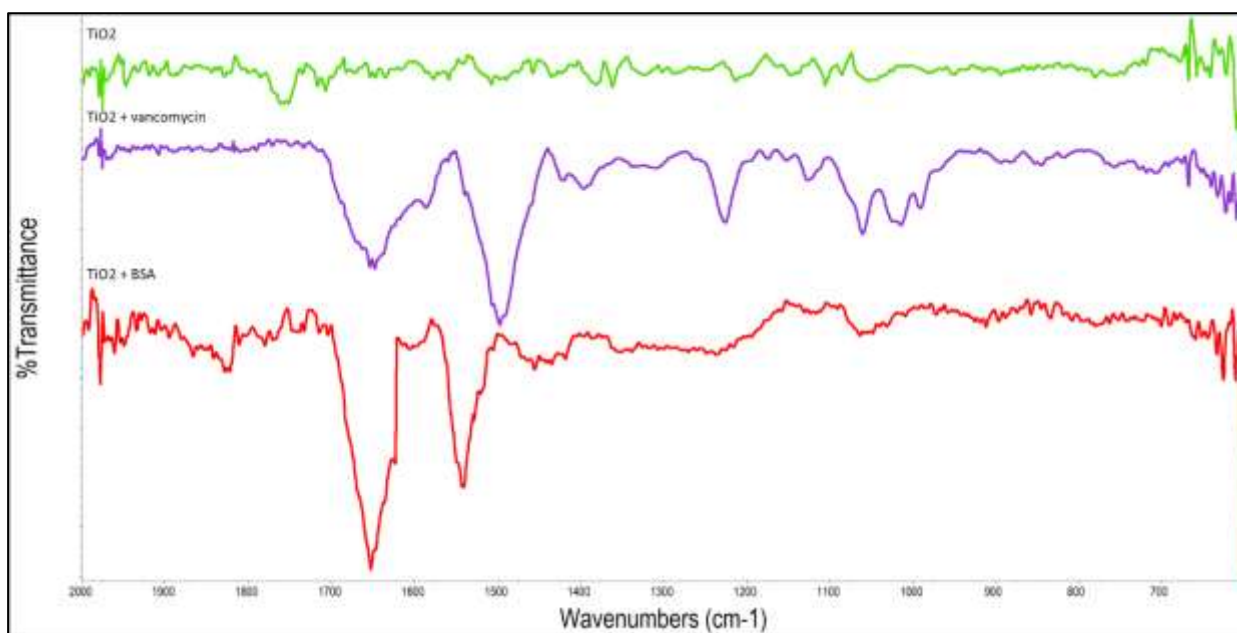


Figure 5. FTIR spectra of TiO₂, vancomycin loaded TiO₂ and BSA loaded TiO₂ surfaces.

3.6. Spectroscopic and Structural Characterizations

Figure 4 shows XRD patterns of prepared anodic TiO₂ nanotube array. The resulting surface exhibits clear Ti peaks as indicated on the graph along with the anatase (101) reflection peaks between 20-25 theta. Since the surface was not exposed to any heat treatment sharp crystal anatase structures were not observed.

The presence of vancomycin and BSA were analyzed with infrared spectroscopy. Vancomycin loaded sample exhibits a wide carbonyl stretching at 1650 cm⁻¹. The

other indicators can be observed at 1500 and 1230 cm⁻¹ for aromatic C=C and phenol ring, respectively. As for BSA loaded sample, The amide I and II bands are clear at 1650 and 1545 cm⁻¹, respectively (Figure 5).

3.7. Drug Release Studies

Two model compounds of bioactive substances with small and large hydrodynamic diameters were investigated in the release studies from titanium dioxide nanotube structures with different diameter openings. The release profiles of vancomycin.HCl (<1 nm) with

small hydrodynamic diameter and BSA (3.48 nm) molecules with large hydrodynamic diameter were investigated separately. The molecular weight difference was considered as the first criterion in the selection of these two biomolecules. It was desired to observe the trend of vancomycin with a weight of 1.4 kDa and BSA with a size of 65 kDa in the loading and release criteria. This molecular weight difference also affects the hydrodynamic diameters. Both components were selected as water soluble and the difference in hydrophilic-hydrophobic effect was eliminated in the release experiments.

Profiles for the release of small hydrodynamic diameter molecules vancomycin.HCl from titanium surfaces are given in Figure 6. The amount of drug released into the medium in all release trials reached the plateau at the end of the 4th day.

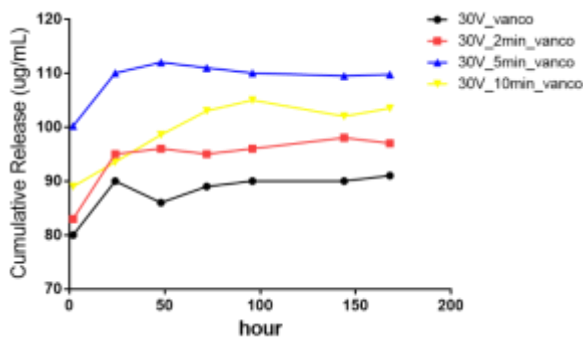


Figure 6. Release profile of vancomycin.HCl from titanium surfaces.

The drug released from the nanotubes reached the maximum level at the end of 24 hours on untreated surfaces, and the narrowing of the tube-ends obtained on the surface after 2 and 5 minutes of sputtering did not extend this period. The duration of release with narrowing in the tube diameters for a period of 5 minutes was one day longer than the first two sample groups; The release from the nanotube structures obtained after 10 minutes of sputtering continued for an additional period of 3 days. No further drug release from the tubes was observed in any sample group after day 4 (Figure 4).

BSA release from the surfaces was monitored up to one week. The release time was observed for 3 to 4 days on untreated and gold-sputtered surfaces for 2 min, respectively and extended to 6 days on 5-min and 10-min gold-sprayed surfaces (Figure 7). BSA release from titanium surfaces was longer in all sample groups compared to vancomycin.HCl release time, and the effect of gold sputtering was more effective than small hydrodynamic diameter molecular release.

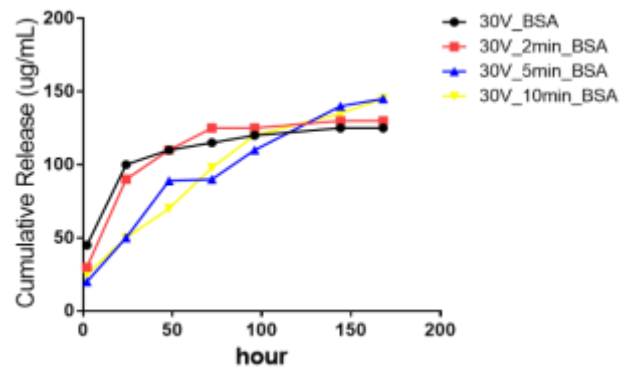


Figure 7. Release profile of BSA from titanium surfaces.

The prolongation of release time is much more evident in experiments with protein. There are two main reasons behind this. The first is that the hydrodynamic diameter of the protein is several times larger than the vancomycin.HCl molecule, as it is considered during the experimental design. Smaller molecules are known to diffuse more rapidly during diffusion. However, another factor slowing protein release can be considered as hydrophobic nature of the protein. Although BSA protein is a water soluble protein, the interaction of hydrophobic regions with titanium structure is much greater than vancomycin.HCl. This interaction is also thought to cause an additional delay in during release.

In the preliminary study conducted by Peng et al. [14] the length of the nanotubular structure was found as the most important parameter affecting the release time; whereas the diameter of the nanotube (when the length was held constant) was the most important parameter affecting the amount of drug loaded. In another study by Çalıřkan et al.[19], Parallel findings were observed and parameters affecting drug loading amount and release time were also reported as nanotube diameter and length, respectively. By revealing the importance of the effect of nanotube aspect-ratio in barrier-free studies, this feature became controllable and became a priority for localized drug release studies.

4. Conclusion

Direct release of active biomolecules from metallic implants is a challenge for implant applications. Although titania nanotube layers offer an opportunity for drug releasing reservoirs, sustained release remains as a problem. In order to eliminate the risk of infection that may arise from the operation in the critical period after the surgical process, there is a need for implants that can release the antibacterial active substance locally or metal surfaces that will contain larger macromolecules such as growth hormone to accelerate osseointegration. For this reason, burst and rapid release should be avoided. Sputter coating of tube ends with inert metals may be a promising approach to overcome this drawback. In this study, titania nanotube structures with adjustable mouth widths on titanium metal plates

were obtained as a result of a two-step anodization process. Vancomycin and BSA as biomolecules with small and large hydrodynamic diameters were also used as model releasing compounds within these nanostructures. In order to prolong the release duration, the tube-ends were narrowed by gold sputter method and the effect of these narrowings on the release profiles was investigated separately for both molecules. It is seen that the increasing sputtering time slows down the release rate of BSA, which is selected as a large molecule. Within the scope of this study, it was planned to obtain a narrowing on the surfaces of titania nanotubes, which are intended to be used as local release reservoirs, with gold, a bioinert material that will not be affected by mechanical abrasion and friction in the local region after implantation. The findings obtained were promising results and the feasibility of the approach will be tried to be demonstrated with the studies to be carried out with bacteria and osteoblasts in the next steps.

Acknowledgement

This project was financially supported by Hacettepe University, Scientific Research Projects Coordination Unit with the project number FHD-6700.

Author's Contributions

Cem Bayram: The hypothesis of the study, experimental design, performance, result analysis and writing of the study.




Ethics

There are no ethical issues after the publication of this manuscript.

References

- [1]. Dong, H, Liu, H, Zhou, N, Li, Q, Yang, G, Chen, L, Mou, Y. 2020. Surface Modified Techniques and Emerging Functional Coating of Dental Implants. *Coatings*, 10(11), 1012.
- [2]. Palka, K, Pokrowiecki, R. 2018. Porous Titanium Implants: A Review. *Advanced Engineering Materials*. 20,1700648.
- [3]. Nicholson, JW. 2020. Titanium Alloys for Dental Implants: A Review. *Prosthesis*, 2(2), 100-116.
- [4]. Draghi, L, Preda, V, Moscatelli, M, Santin, M, Chiesa, R. 2020. Gentamicin-Loaded TiO₂ Nanotubes as Improved Antimicrobial Surfaces for Orthopedic Implants. *Frontiers in Materials*, 7:233.
- [5]. Ion, R, Necula MG, Mazare A, Mitran V, Neacsu P, Schmuki P, Cimpean A. 2020. Drug Delivery Systems Based on Titania Nanotubes and Active Agents for Enhanced Osseointegration of Bone Implants. *Current Medicinal Chemistry*, 27(6), 854-902.
- [6]. Losic, D. 2021. Advancing of titanium medical implants by surface engineering: recent progress and challenges, *Expert Opinion on Drug Delivery*, 10.1080/17425247.2021.1928071.
- [7]. Zhao, L, Chu, PK, Zhang, Y, Wu, Z. 2009. Antibacterial coatings on titanium implants, *Journal of Biomedical Material Research B Applied Biomaterials*, 91, 470-480.
- [8]. Turanlı, AE, Sokullu, E, Nikolayev, A, Dagci, T, Öztarhan, A. 2016. Dental İmplant Materyallerin İyon İmplantasyon Yöntemiyle Modifikasyonlarının in vitro Hücre Tutunmasına Etkisi, *CBÜ Fen Bil. Dergi*, Cilt 12, Sayı 2, 243-251.
- [9]. Sarkar, N, Bose, S. 2020. Controlled Delivery of Curcumin and Vitamin K2 from Hydroxyapatite-Coated Titanium Implant for Enhanced in Vitro Chemoprevention, Osteogenesis, and in Vivo Osseointegration. *ACS Applied Materials and Interfaces*, 12(12),13644-13656.
- [10]. Zilberman, M, Elsner, JJ. 2008. Antibiotic-eluting medical devices for various applications. *Journal of Controlled Release*,130, 202-215.
- [11]. Macak, JM, Tsuchiya, H, Schmuki, P. 2005. High-Aspect Ratio TiO₂ Nanotubes by Anodization Titanium, *Angewandte Chemistry International Edition*, 44, 2100-2102.
- [12]. Popat, KC, Eltgroth, M, LaTempa, TJ, Grimes, CA, Desai, TA. 2007. Decreased Staphylococcus epidermis adhesion and increased osteoblast functionality on antibiotic-loaded titania nanotubes, *Biomaterials*, 28, 4880-4888.
- [13]. Yao, C, Webster, TJ. 2009. Prolonged Antibiotic Delivery from Anodized Nanotubular Titanium Using a Co-precipitation Drug Loading Method, *Journal of Biomedical Material Research B Applied Biomaterials* 91B: 587-595.
- [14]. Peng, L, Mendelsohn, AD, LaTempa, TJ, Yoriya, S, Grimes, CA, Desai, TA. 2009 Long-Term Small Molecule and Protein Elution from TiO₂ Nanotubes, *Nano Letters*, 9, 1932-1936.
- [15]. Ma, M, Kazemzadeh-Narbat, M, Hui, Y, Lu, S, Ding, C, Chen, DDY, Hancock, REW, Wang, R. 2012. Local delivery of antimicrobial peptides using self-organized TiO₂ nanotube arrays for peri-implant infections, *Journal of Biomedical Material Research* 100A: 278-285.
- [16]. Sinn Aw, M, Kurian, M, Losic, D. 2014. Non-eroding drug-releasing implants with ordered nanoporous and nanotubular structures: Concepts for controlling drug release, *Biomaterials Science*, 9, 9243-9257.
- [17]. Gulati, K, Kant, K, Findlay D, Losic, D. 2015. et al., Periodically tailored titania nanotubes for enhanced drug loading and releasing performances. *Journal of Material Chemistry B*, 2015. 3: p. 2553-2559.
- [18]. Gulati, K, Ramakrishnan, S, Aw, MS, Atkins, GJ, Findlay, DM, Losic, D. 2012. Biocompatible polymer coating of titania nanotube arrays for improved drug elution and osteoblast adhesion, *Acta Biomaterialia*, 8, 449-456.
- [19]. Caliskan, N, Bayram, C, Erdal, E, Karahaliloglu, Z, Denkbaz, EB. 2014. Titania nanotubes with adjustable dimensions for drug reservoir sites and enhanced cell adhesion. *Material Science and Engineering C*, 2014. 35: p. 100-105.
- [20]. Chopra, D, Gulati, K, Ivanovski, S. 2021. Understanding and optimizing the antibacterial functions of anodized nano-engineered titanium implants. *Acta Biomaterialia*, 2021. 127:80-101.

The Effect of Wood Species and Strip Width on Bending Strength and Modulus of Elasticity in End-Grain Core Blockboard

Yasemin Öztürk^{1*} , Kıvanç Yılmaz^{1,2} , Erol Burdurlu¹ 

¹Faculty of Technology, Gazi University, Dept. of Wood Products Industrial Engineering, Ankara, Turkey

²School of Vocational Technology, Hacettepe University, Dept. of Wood Products Industrial Engineering, Ankara, Turkey

* yozturk@gazi.edu.tr

* Orcid: 0000-0003-2292-2447

Received: 27 June 2021

Accepted: 8 March 2022

DOI: 10.18466/cbayarfbe.958377

Abstract

It is aimed to compare the bending strength and modulus of elasticity of end-grain (vertical strip) core blockboard, unlike the usual (lengthwise strip core) blockboard construction, with that of the traditional blockboard with the face-grain or edge-grain core construction. Oriental beech and black poplar woods are provided by taking care to avoid the grain irregularities and visible defects are used in the study. These timbers are used to obtain the core, top and bottom layers of the blockboard. PVAc mounting glue is used for bonding the layers together. According to the test data: The bending strength and modulus of elasticity of oriental beech blockboard are 39% and 26% higher respectively than that of end-grain core black poplar blockboards. If we evaluated by neglecting wood species, strip width was an effective factor in the bending strength and ineffective modulus of elasticity. In addition, the bending strength of the end-grain core oriental beech blockboard is 79 MPa and that of the end-grain core black poplar blockboard is 57 MPa, regardless of the width of the core strip. When these values are compared with the values of other engineered wood, the result is considered open to improvement and satisfactory.

Keywords: Blockboard, Core Structure, Wooden Board, Bending Strength, Modulus of Elasticity

1. Introduction

Blockboard is defined as "A core layer made of strip bonded side by side and face layers formed by glueing at least one sheet perpendicular to the fiber direction on both sides of this layer under pressure". The blockboards are divided into two types, three-ply and five-ply, according to the number of layers, and the sheets forming the outer layers must be of the same wood species[1].

Blockboard is one of the alternative materials with better bending strength performance than plywood. The main prominent feature of the blockboard material is that it is produced from a core-containing frame formed by end-to-end additions from different types of wood materials, compressed with cross bands or face coverings on both sides and surrounded by solid wood borders, as can be seen in Figure 1 [2,3]. Blockboards produced by bonding under high pressure and temperature are considered as different types of plywood[4]. Blockboards are widely used in products such as furniture, cabinet backs and centre panels for framed doors, kitchen cabinets, cores for recessed doors, light and decorative doors[5,6].

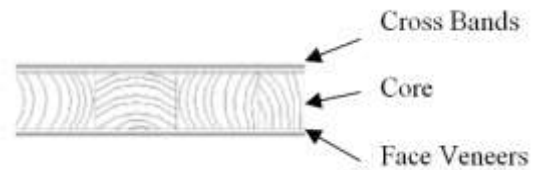


Figure 1. Cross-sectional view of a blockboard[7]

The wood species and quality of the layers, the type of glue used in bonding, fiber direction and angle affect the physical and mechanical properties of the wooden products[8–11].

Miter or notched joints are used instead of straight joints in the end-to-end joining of the bending strength of the blockboard [12]. The use of oiled wood dowel in the transverse direction and along the middle with the glue to bring the strips forming the mid-layer (core) side by side has positive effects on the bending strength, modulus of elasticity, and water resistance of the board [13]. In the cores of blockboards that can be used in different places such as flooring, formwork plate, floor

coverings of railway wagons and caravans, barrel bottom and cover; using solid wood pieces combined side by side with dowels at an angle of up to 20 degrees increase the bending and tensile strength up to 20% [14]. By using different materials in the core, relatively lighter, environmentally friendly and lower cost blockboards can be produced [15,16]. By placing materials such as glass fiber, gauze, cotton fabric and jute between the core and both top and bottom face layer, an increase in the breaking and elastic modulus of the blockboard can be achieved from 35% to 245% [17].

The impregnation of the solid wood material used in its core with boron compounds increases the resistance of the blockboard against fungi that cause rotting [18]. The veneers used in the blockboard were treated with either boric acid (BA), disodium octoborate tetrahydrate (DOT), alumina trihydrate (ATH), or a BA/DOT mixture. Treatments had a little negative effect on flexural strength; flexural stiffness was significantly lower for the highest treatment levels [19].

By comparing the flexural performance of unreinforced low-grade glulam and glulam which was reinforced with adhesively bonded recyclable Fibre-reinforced polymers (FRPs), Raftery and Harte[20] found that glass fibre reinforced polymer plates could be a good alternative to serve both as flexural reinforcement for low-grade glulam beams and a substitute for high-quality wood laminations.

The massive parts used in the production of the core in the usual blockboard production are horizontal and the fiber direction is parallel to the horizontal (face-grain structure)[21].

It has been observed that the direction of the forces applied on the glue line and the densities of the wood materials used are effective in the strength values in two different studies conducted to determine the flexural strength and elasticity modulus values of wood-based laminated materials obtained by using Eastern beech and Lombardy poplar. In both studies, the flexural strength and modulus of elasticity values of the test materials were observed to be high against the forces applied parallel to the glue line[22,23].

In the study, it was aimed to determine the bending strength and modulus of elasticity of the blockboard, which was constructed by directing vertically the fiber directions of the solid wood strips used as core with a different technique (end grain structure).

2. Materials and Methods

2.1. Materials

Oriental beech (*Fagus Orientalis L.*) and black poplar (*Populus Nigra L.*) woods provided from a supplier as timber in Ankara/Siteler region by taking care to avoid the grain irregularities and visible defects were used in the study as core and face materials.

APEL brand PVAc mounting glue was used for bonding the core strips and facings together. According to the values reported by the manufacturer, the minimum film-forming temperature of the glue is 7°C, and the curing time varies between 45 minutes and 2 hours.

2.2. Preparation of Test Samples

A sufficient number of core strips were cut from oriental beech and black poplar timbers in finished dimensions of 14 x 22 mm, 28 x 22 mm and 42 x 22 mm (width x thickness) and 500 mm length. In addition, oriental beech and black poplar sheets in 5 mm x 22 mm x 380 mm dimensions were manufactured to form the top and bottom layer of the blockboards. Panels with dimensions of 22 x 380 x 500 mm were manufactured by glueing 14 mm, 28 mm and 42 mm strips side by side with PVAc glue, separately in each size group. The glueing process was carried out by applying an equal amount of 250 grams per square meter, depending on the manufacturer's recommendation. Panels were machined to a finished thickness of 20 mm by passing through a calibrated sanding machine with 80-grade sandpaper at a speed of 10 m / sec. The pieces were cut so that the core thickness was 16 mm and the sheets were bonded with PVAc glue on top and bottom of these pieces. Subsequently, the pieces were machined to a finished size of 20x 26 x 360 mm. Completely solid wood control samples of 20x20x360 mm were prepared from oriental beech and black poplar (Figure 2).



Figure 2. The process of preparing test samples (a: 14, 28 ve 42 mm; b: 22 mm e: 20 mm; d: 16 mm; c: 14, 28 ve 42 mm; f: 5 mm)

2.3. Methods

In the tests of bending strength perpendicular to the surface, the principles specified in the [24] standard were followed. In the tests, the samples were loaded right in the middle and the loading speed of the test device was set as 2 mm/min. The bending strength was calculated by:

$$F_m = (3 \times F_{max} \times L) / (2 \times b \times h^2) \quad (2.1)$$

Where F_m is bending strength (MPa), F_{max} is the maximum load at break (N), L is support clearance (mm), b is sample width (mm) and h is sample thickness (mm).

In bending tests, the modulus of elasticity was also calculated. For this purpose, the principles specified in the [25] standard were followed and the calculations were made according to:

$$E = (\Delta F \times L^3) / (4 \times b \times h^3 \times \Delta f) \quad (2.2)$$

Where E is the modulus of elasticity (MPa), ΔF is the difference in applied forces (N), L is support clearance (mm), b is sample width (mm), h is sample thickness (mm) and Δf is displacement amount (mm).

2.4. Statistical Analysis

In order to determine the statistical analysis method, whether the data obtained from the tests show a normal distribution or not was tested with IBM SPSS Statics Version 22 package program and it was seen that the data showed normal distribution according to the distribution criteria of kurtosis and skewness [26]. After this analysis, multiple variance analysis was performed in the MSTAT-C Version 5.4 package program to determine whether the independent variables of wood type and middle layer strip width affect the dependent variable of elasticity modulus in bending. Duncan's multiple range test was used to level the effect sizes of variables in case of interaction between variables.

3. Results and Discussion

3.1. The Effect of Wood Type and Strip Width on Bending Strength

The bending resistance values obtained as a result of the tests are given in Table 1 and shown in Figure 3 according to the wood type and strip width.

Table 1. Bending strength values of end-grain core blockboard according to wood type and strip width

	Bending Strength Values (MPa)							
	Oriental Beech				Black Poplar			
	Control	14 mm	28 mm	42 mm	Control	14 mm	28 mm	42 mm
Minimum	84.67	65.62	54.35	65.52	91.16	37.01	31.90	32.04
Maximum	120.54	78.60	74.34	83.13	124.81	46.62	48.38	49.59
Average	108.27	71.78	66.13	73.50	105.73	42.07	39.59	41.53
Standard deviation	9.56	3.45	4.07	4.33	9.37	2.98	4.72	3.43
Coefficient of variation	8.83	4.81	6.15	5.89	8.86	7.09	11.93	8.26

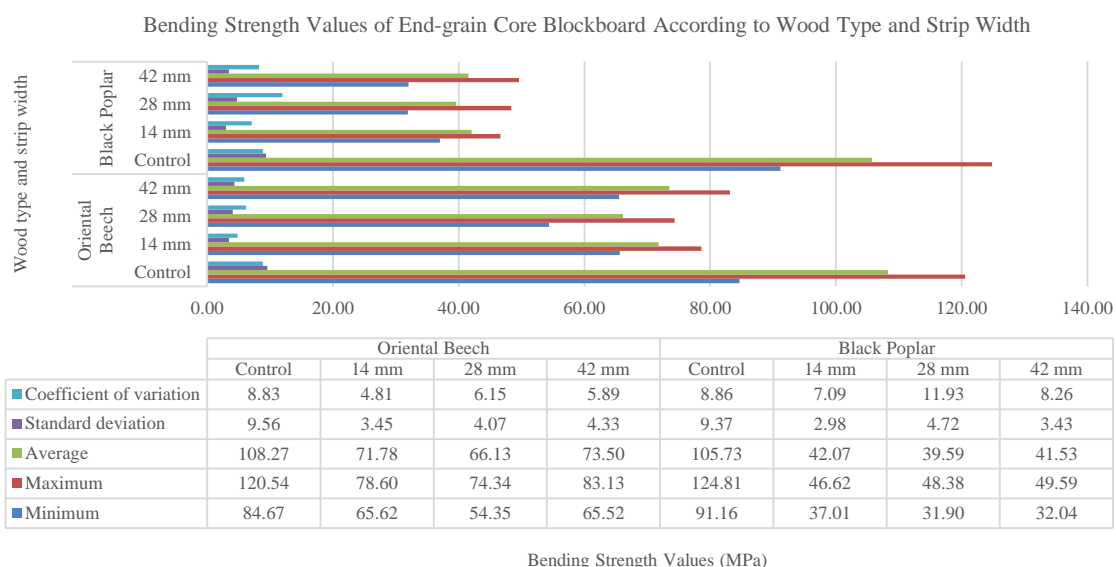


Figure 3. Bending strength values of end-grain core blockboard according to wood type and strip width

According to the bending strength values given in Table 1, the analysis of variance was given in Table 2 to determine whether the wood species and width of the strip used in the core affected the bending strength.

As seen from Table 2, the wood species of strip used in the core, strip width and the dual interaction of these two variables were effective on the bending strength ($p < 0.05$).

Table 2. Multiple variance analysis for the effect of wood type and strip width on bending strength

Variance Sources	Degree of Freedom	Sum of Squares	Average of Squares	F Value	Probability of Error ($p < 0.05$)
Strip width (A)	3	79,261.22	26,420.41	745.79	0.00*
Wood species (B)	1	20,595.87	20,595.87	581.38	0.00*
AB	3	5,563.37	1,854.46	52.35	0.00*
Error	152	5,384.73	35.43		
Total	159	110,805.19			

* $p < 0.05$

The levelling made depending on the importance of the differences between the bending strength values obtained depending on the width of each strip is given in Table 3.

Table 3. Levelling of bending strength values depending on strip widths

Strip Width	Bending Strength (MPa)	Homogeneity Group
Control Group	107.00	A
14 mm	56.93	B
28 mm	52.86	C
42 mm	57.52	B

Least Significant Difference (LSD) = 2.63

According to the strip widths, the highest bending strength was obtained with 107 MPa from the control samples, while the difference between them was insignificant, followed by the samples with 14 mm and 42 mm strip widths, and the lowest bending strength was obtained in the samples with 28 mm strip width.

The levelling made depending on the importance of the difference between the bending strength values depending on the wood species is given in Table 4.

Table 4. Levelling bending strength values depending on the wood species

Wood Species	Bending Strength (MPa)	Homogeneity Group
Oriental Beech	79.92	A
Black Poplar	57.23	B

Least Significant Difference (LSD) = 1.859

With the value of 79.92 MPa, the bending strength values of the blockboards with oriental beech core were higher than the blockboards with black poplar core (57.23 MPa).

The levelling made depending on the importance of the differences between the bending strength values due to the binary interaction of strip width and wood species is given in Table 5.

Table 5. Levelling bending strength values based on binary interaction of strip width and wood species

Interaction Type	Bending Strength (MPa)	Homogeneity Group
Control x Oriental Beech	108.30	A
Control x Black Poplar	105.70	A
42 mm x Oriental Beech	73.50	B
14mm x Oriental Beech	71.79	B
28 mm x Oriental Beech	66.13	C
14 mm x Black Poplar	42.07	D
42 mm x Black Poplar	41.53	D
28 mm x Black Poplar	39.59	D

Least Significant Difference (LSD) = 3.72

Depending on the dual interaction of strip width and wood species, the highest bending strength was achieved in the oriental beech end-grain core blockboards with 42 mm and 14 mm strip width, followed by oriental beech end-grain core blockboards with 28 mm strip width. Strip width was not found to be effective on bending strength in black poplar end-grain core blockboards.

3.2. The Effect of Wood Type and Strip Width on Elasticity Modulus in Bending

The test values of modulus of elasticity in bending obtained from the tests according to the wood species and strip width are given in Table 6 and shown in Figure 4.

Table 6. Modulus of Elasticity values of end-grain core blockboard according to wood species and strip width

	Modulus of Elasticity (MPa)							
	Oriental Beech				Black Poplar			
	Control	14 mm	28 mm	42 mm	Control	14 mm	28 mm	42 mm
Minimum	7,183.21	6,683.75	5,057.79	6,440.85	8,404.97	3,979.49	3,609.12	3,097.60
Maximum	10,320.84	8,449.78	7,760.02	8,653.74	12,046.47	5,728.67	5,701.49	5,320.68
Average	9,307.02	7,531.54	6,975.45	7,205.49	10,466.59	4,726.28	4,864.54	4,623.77
Standard deviation	783.29	422.21	524.40	543.92	920.06	494.88	552.18	524.47
Coefficient of variation	8.42	5.61	7.52	7.55	8.79	10.47	11.35	11.34

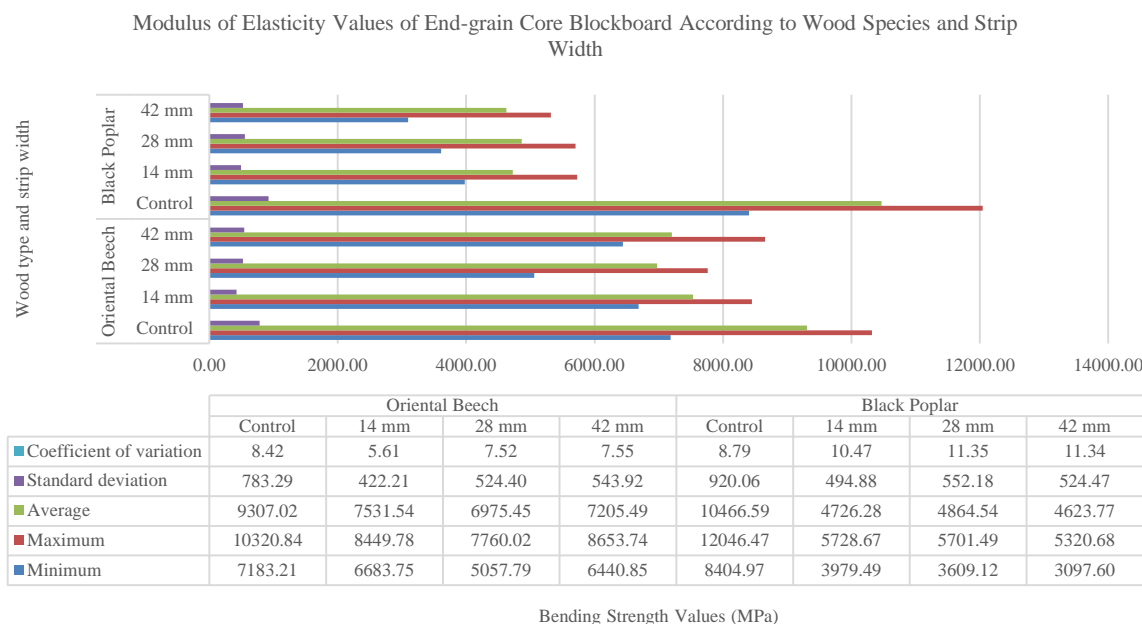


Figure 4. Modulus of Elasticity values of end-grain core blockboard according to wood species and strip width

According to the bending strength values given in Table 6, an analysis of variance is given in Table 7 to determine whether the wood species and width of strip used in the core affect the bending strength. As can be

seen from Table 7, strip width, wood species and mutual interaction of these two variables were effective on elastic modulus in bending.

Table 7. Multiple variance analysis of the effect of wood species and strip width on elastic modulus in bending

Variance Sources	Degree of Freedom	Sum of Squares	Average of Squares	F Value	Probability of Error (p < 0.05)
Strip width (A)	3	457,762,038.72	152,587,346.24	381.68	0.00*
Wood species (B)	1	100,592,063.80	100,592,063.80	251.62	0.00*
AB	3	102,681,051.93	34,227,017.31	85.61	0.00*
Error	152	60,766,458.67	399,779.33		
Total	159	721,801,613.12			

*p<0.05

The levelling made depending on the importance of the differences between the elasticity modulus values in bending obtained depending on the width of each strip is given in Table 8.

The elastic modulus (9,889 MPa) of the control group samples was higher than the elastic modulus values of the end-grain core blockboards. Since the difference between elastic modulus values was insignificant, strip width did not affect the elastic modulus in bending.

Table 8. Levelling of elastic modulus values in bending depending on strip widths

Strip Width	Modulus of Elasticity (MPa)	Homogeneity Group
Control Group	9,889	A
14 mm	6,129	B
28 mm	5,920	B
42 mm	5,915	B

Least Significant Difference (LSD) = 279.2

Table 9. Levelling the elastic modulus values in bending depending on the tree type

Wood Species	Modulus of Elasticity (MPa)	Homogeneity Group
Oriental Beech Core	7,756	A
Black Poplar Core	6,170	B

Least Significant Difference (LSD) = 197.40

The levelling made depending on the importance of the differences between the elasticity modulus values in bending according to the wood type is given in Table 9.

As seen from Table 9, the modulus of elasticity in bending (7,756 MPa) of the blockboard with oriental

beech core was higher than that of the blockboard with black poplar core (6,170 MPa).

The levelling made depending on the importance of the difference between the modulus of elasticity values due to the dual interaction of strip width and wood species is given in Table 10.

Table 10. Levelling of the modulus of elasticity values based on binary interaction of strip width and wood species

Interaction Type	Modulus of Elasticity (MPa)	Homogeneity Group
Control x Black Poplar	10,470	A
Control x Oriental Beech	9,312	B
14mm x Oriental Beech	7,532	C
42 mm x Oriental Beech	7,205	CD
28 mm x Oriental Beech	6,975	D
28 mm x Black Poplar	4,865	E
14 mm x Black Poplar	4,726	E
42 mm x Black Poplar	4,624	E

Least Significant Difference (LSD) = 394.90

As seen from Table 10, the highest modulus of elasticity was obtained in the blockboard from black poplar with the value of 10,470 MPa, followed by the blockboard from oriental beech with the value of 9,312 MPa. While the width of the strip was found effective on the modulus of elasticity in the oriental beech core blockboards, it was not found effective on the black poplar ones.

4. Conclusions

This study, it is aimed to determine the effect of strip width and wood species on the modulus of elasticity in bending and bending strength in end-grain core blockboards. In the usual blockboards, the direction of the strips forming the core is parallel to the horizontal and in the direction of the length. In this study, the strips forming the core were perpendicular to the horizontal and in the direction of the thickness of the blockboard to ensure more effective use of waste and non-standard wooden parts and this study is a pioneering work in this respect.

The bending strength and modulus of elasticity of oriental beech end-grain core blockboards were 39% and 26% higher, respectively, compared to black poplar ones. It is thought that the higher the density of the oriental beech and the lower the void ratio affected this result. In oriental beech end-grain core blockboards, higher bending strength and modulus of elasticity values were obtained in the blockboards with core from the strips 14 mm and 42 mm in width compared to 28 mm

strip width without any noticeable difference between them. And also, the strip width was not an effective factor in bending strength and modulus of elasticity in black poplar end-grain core blockboards. As another result, regardless of the wood type, strip width was an ineffective factor on the modulus of elasticity, but effective on bending strength.

Efe and Kasal[27], determined bending strengths as 129 MPa in oriental beech, 73 MPa in Scots pine, 65 MPa in Okume blockboard, 32 MPa in MDF (Medium-Density Fiberboard) and OSB (Oriented Strand Board) in their studies. In the same study, the modulus of elasticity was found as 12,250 MPa, 11,760 MPa, 7,730 MPa, 5,498 MPa, 6,530 MPa, respectively. Altınok and Kılıç found the bending strength of particleboard as 12 MPa and the bending strength of particleboard faced with laminate (CPL) as 24 MPa [28].

According to the data obtained from this research, the bending strength of the end-grain core oriental beech blockboard is 79 MPa and that of the end-grain core black poplar blockboard is 57 MPa, regardless of the width of the core strip. When these values are compared with the values of other engineered wood, the result is considered open to improvement and satisfactory.

By using the wood species, strip width and adhesive type variables, it is possible to manufacture different end-grain (vertical strip) core blockboard and strength values can be further improved.



Author's Contributions

Yasemin Öztürk: Made literature search, prepared the samples used in the experimental work, wrote the manuscript, and performed the experiment and result in analysis.

Kıvanç Yılmaz: Made literature search, prepared the samples used in the experimental work, wrote the manuscript, and performed the experiment and result in analysis.

Erol Burdurlu: Supervised the experiment's progress, result in interpretation and helped in manuscript preparation.

Ethics

There are no ethical issues after the publication of this manuscript.

References

- [1]. TSE, *TS 1047 - Blockboards for general purposes-with rotary cut veneer*. Turkey: Turkish Standardization Institute (TSE), 1982.
- [2]. Eterno Teixeira, D., & Penna Firme de Melo, M. 2017. Effect of battens edge bonding in the properties of blockboards produced with pinus sp. recycled from construction sites. *Asian Journal of Advances in Agricultural Research*; 4(2), 1-11. <https://doi.org/10.9734/AJAAR/2017/38389>.
- [3]. Nazerian, M., Moazami, V., Farokhpayam, S., Gargari, R. M. 2018. Production of blockboard from small athel slats end-glued by different type of joint. *Maderas, Cienc. tecnol*; 20(2): 277-286. ISSN 0718-221X. <http://dx.doi.org/10.4067/S0718-221X2018005021101>.
- [4]. Zanuttini, R., Cremonini, C. 2002. Optimization of the test method for determining the bonding quality of core plywood (Blockboard). *Mater Struct*; 35(246):126-132.
- [5]. Laufenberg, T., Ayrilmis, N. and White, R. 2006. Fire and bending properties of blockboard with fire retardant treated veneers. *Holz Roh Werkst*; 64: 137-143, <https://doi.org/10.1007/s00107-005-0041-4>.
- [6]. Kartal, S. N., Ayrilmis, N. 2005. Blockboard with boron-treated veneers: laboratory decay and termite resistance tests, *International Biodeterioration & Biodegradation*; 55(2): 93-98, ISSN 0964-8305, <https://doi.org/10.1016/j.ibiod.2004.08.001>.
- [7]. Kiran, M. C., Dhanapal, S., Uday, D., Vijay Kumar, P. 2020. Block Board from Melia dubia. *International Journal of Forestry and Wood Science*, 7(2): 096-100.
- [8]. Hearmon, R. F. S. 1948. Elasticity of Wood and Plywood. *Nature*; 162(4125): 826-826, doi: 10.1038/162826a0.
- [9]. Dzięgielewski, A., Wilczyński, St. 1990. Elasticity of furniture elements glued by layers. *Zesz. Probl. Postępów Nauk Rol.*; 379: 89-107.
- [10]. Prekrat, S. and Smardzewski, J. 2008. Effect of wood species and glue type on contact stresses in a mortise and tenon joint. *Proc. Inst. Mech. Eng. Part C J. Mech. Eng. Sci.*; 222(12); 2293-2299, doi: 10.1243/09544062JMES1084.
- [11]. Fakoor, M. and Rafiee, R. 2013. Transition angle, a novel concept for predicting the failure mode in orthotropic materials. *Proc. Inst. Mech. Eng. Part C J. Mech. Eng. Sci.*; 227(10); 2157-2164, doi: 10.1177/0954406212470905.
- [12]. Nazerian, M., Moazami, V., Farokhpayam, S. and Gargari, R. M. 2018. Production of blockboard from small athel slats end-glued by different type of joint. *Maderas Cienc. y Tecnol.*; 20(2): 277-286, doi: 10.4067/S0718-221X2018005021101.
- [13]. Segovia, C., Zhou, X. and Pizzi, A. 2013. Wood blockboards for construction fabricated by wood welding with pre-oiled dowels. *J. Adhes. Sci. Technol.*; 27(5-6): 577-585, doi: 10.1080/01694243.2012.690616.
- [14]. Belleville, B., Segovia, C., Pizzi, A., Stevanovic, T. and Cloutier, A. 2011. Wood Blockboards Fabricated by Rotational Dowel Welding. *J. Adhes. Sci. Technol.*; 25(20): 2745-2753, doi: 10.1163/016942410X537323.
- [15]. Haseli, M., Layeghi, M. and Hosseinabadi, H. Z. 2018. Characterization of blockboard and battenboard sandwich panels from date palm waste trunks. *Measurement*; 124: 329-337, doi: 10.1016/j.measurement.2018.04.040.
- [16]. El-Mously, H. Rediscovering Date Palm by-products: an Opportunity for Sustainable Development, Materials Research Forum LLC, Materials Research Proceedings 11, 2019, pp. 3-61, doi: 10.21741/9781644900178-1.
- [17]. Ispas, M., Cosereanu, C., Zeleniuc, O. and Porojan, M. 2019. Flexural properties of blockboard reinforced with glass fiber and various types of fabrics. *BioResources*; 14(4): 9882-9892, doi: 10.15376/biores.14.4.9882-9892.
- [18]. Kartal, S. N. and Ayrilmis, N. 2005. Blockboard with boron-treated veneers: laboratory decay and termite resistance tests. *Int. Biodeterior. Biodegradation*; 55(2): 93-98, doi: 10.1016/j.ibiod.2004.08.001.
- [19]. Laufenberg, T., Ayrilmis, N. & White, R. 2006. Fire and bending properties of blockboard with fire retardant treated veneers. *Holz Roh Werkst*; 64: 137-143, doi: <https://doi.org/10.1007/s00107-005-0041-4>
- [20]. Raftery, G. M. and Harte, A. M. 2011. Low-grade glued laminated timber reinforced with FRP plate. *Compos. Part B Eng.*; 42(4): 724-735, doi: 10.1016/j.compositesb.2011.01.029.
- [21]. Altenbach, H. 2011. Mechanics of advanced materials for lightweight structures. *Proc. Inst. Mech. Eng. Part C J. Mech. Eng. Sci.*; 225(11): 2481-2496, doi: 10.1177/0954406211417068.
- [22]. Kilic, M. 2011. The effects of the force loading direction on bending strength and modulus of elasticity in laminated veneer lumber (LVL). *BioResources*; 6(3): 2805-2817.
- [23]. Burdurlu, E., Kilic, M., Ilce, A. C. and Uzunkavak, O. 2007. The effects of ply organization and loading direction on bending strength and modulus of elasticity in laminated veneer lumber (LVL) obtained from beech (*Fagus orientalis* L.) and lombardy poplar (*Populus nigra* L.). *Construction and Building Materials*; 21(8): 1720-1725, ISSN: 0950-0618, <https://doi.org/10.1016/j.conbuildmat.2005.05.002>.
- [24]. TSE, *TS 2474 - Wood-determination of ultimate strength in static bending*. Turkey: Turkish Standardization Institute(TSE), 1976.
- [25]. TSE, *TS 2478 - Wood-Determination of Modulus of Elasticity In Static Bending*. Turkey: Turkish Standardization Institute(TSE), 1976.
- [26]. Wright, D. B. and Herrington, J. A. 2011. Problematic standard errors and confidence intervals for skewness and kurtosis. *Behav. Res. Methods*; 43(1): 8-17, doi: 10.3758/s13428-010-0044-x.



- [27]. Efe, H. and Kasal, A. 2007. Determination of Some Physical and Mechanical Properties of Various Wood and Wood Composite Materials. *J. Polytech*; 10(3): 303–311, Retrieved from: <https://dergipark.org.tr/tr/pub/politeknik/issue/33026/367180>.
- [28]. Altınok, M. and Kılıç, A. 2003. Determination of some mechanical performances of particle board covered with roll (continue press laminate) laminate. *Gazi Univ. J. Sci.*; 16(3): 559–566, Retrieved from: https://dergipark.org.tr/tr/pub/gujs/issue/7405/97150#article_cite.

The Production and Characterization of Aluminum Barrier Laminate Tubes and Comparison of Mechanical Properties with Reference Material

Mahir Doğan^{1*} , Keriman Şanlı¹ , Gizem Güler¹ , Yusuf Över¹ 

¹Pilenpak Packaging R&D Center, Manisa, Turkey

*mahirrdogan@gmail.com

* Orcid: 0000-0003-1412-1789

Received: 29 January 2021

Accepted: 25 February 2022

DOI: 10.18466/cbayarfbe.870469

“III. Presented at the National University-Industry Collaboration, R&D and Innovation Congress”

Abstract

This study investigates the characterization of aluminum barrier laminate tubes and how mechanical properties change by difference of polymeric raw materials. In this study, four different prototypes have been produced and compared with themselves plus two different references. References have been obtained from the market with taking into consideration of the most common ones. After the examination of cross section images, it has observed that the main difference of produced prototypes from reference sample is layer distribution. Main layers are thicker in prototypes than reference samples. Prototypes have been produced by different formula and in some cases, different raw materials. Characterization measurements were taken by dynamic scattering calorimetric thermograms. For comparison of mechanical properties, young modulus values were obtained by using tensile meter for measurements of 250µm thickness 25mm wide, 50mm length foil samples. Aim of this study is the discovering possible ways of reaching 600-700 N/mm² in young modulus value by different formula like reference samples.

Keywords: Aluminum barrier laminate tubes, flexible packaging, plastics, young modulus.

1. Introduction

Since the discovery of polyethylene (PE) and polypropylene (PP), plastics have easily found their way into every aspect of our lives. Although it is very difficult to build a world without plastics that contains synthetic or organic polymers these days, the emergence of the plastic industry dates back to the recent past ~1950s. The use of the plastic was in the military field at first. Then it started to be used in different sectors such as construction after the World War II. However, the plastic industry market has made its biggest leap in the packaging sector. Currently, the packaging sector without plastics is unthinkable [1,2].

The most basic task of a package is to protect the product to be included in it from environmental factors and help the product to protect its shelf life. In addition, it facilitates the transportation and storage of the product. It informs the consumer about product and has an attractive effect for the consumer with its design. Packaging is divided into three different categories:

Flexible, semi-flexible and rigid. Paper-plastic bags and pet food packages fall into the flexible category. Paperboard boxes are an example of the semi-flexible category. Rigid packaging involves materials with higher strength such as glass bottles and metal cans [3].

Recently, there has been a transition from rigid to flexible form in PE and PP based plastics. The most important factor in this is to obtain less thick structures

with the use of less plastic in flexible packaging. In addition, flexible packaging has many advantages such as versatility, high resistance, light weight, less waste and being suitable for different printing techniques [1]. Thanks to these advantages, it is very easy to come across flexible packaging solutions with different structures in different sector such as food, hygiene and cosmetics. One of these structures is *laminate tubes*, which are a type of packaging where aggressive chemicals such as toothpaste, hair dye and pharmaceutical cream [4,5]. Laminate tubes have a longitudinal back seam along their body as a

characteristic feature. They can be in different colors and with or without print. Closing the tubes filled with the product to be placed inside can be easily done by thermal processes. These tubes are designed using five layers: a heat sealable layer, a first tie layer, a barrier layer, a second tie layer and an outer layer. Polymeric materials such as low density polyethylene (LDPE) and high density polyethylene (HDPE) are generally used for heat sealable and outer layers, respectively. Ethylene acrylic acid (EAA) or ethylene methacrylic acid (EMAA) copolymers are often preferred for tie layers [6,7]. One of these layers provides a barrier feature to the packaging, in other words, to the laminate tube, helping it protect the products shelf life. According to the difference in the barrier layer, these tubes are separated into two groups: *Aluminum Barrier Laminate (ABL)* and *Plastic Barrier Laminate (PBL)*. Barrier property in PBL tubes is provided by ethylene vinyl alcohol (EVOH) layer [8]. In the study of Feng et al., it is clearly seen that the oxygen permeability decreases with the increases of the EVOH ratio in the EVOH/LDPE composition [9]. However, ABL tubes include aluminum foil providing barrier properties as shown in Figure 1. This layer protects the product, from environmental factors such as corrosion, diffusion and light, as well as preventing changes in the flavor and odor of the product due to the excellent barrier property provided by aluminum foil [8].

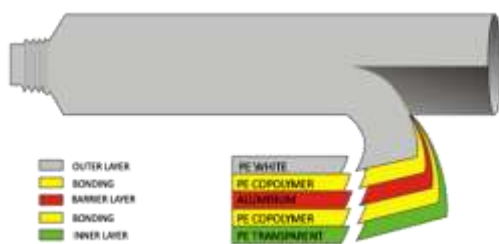


Figure 1. ABL tube layers [10].

Samples are produced as taking into consideration of most common ABL tubes in market and this refers as 12/250. The meaning of 12/250 comes from 12 μ m for aluminum thickness and 250 μ m for total thickness. Inner and outer layers are produced in blown PE film production lines as co-extruded films. Then, these films are laminated via melted polymers with aluminum foil in extrusion lamination lines. ABL tubes should be examined considering many mechanical properties such as coefficient of friction, tear resistance and stiffness value. Stiffness is a very important parameter especially when filling the tube with product. If the tube is not tough enough, problems such as loosening in the tube and flowing of the product occur during filling.

In this study, it is aimed to characterize ABL tubes produced with different formulas by comparing them with reference materials and to compare the stiffness of laminants. Thus, it will be learned how changes in formulas affect stiffness or young modulus values.

2. Materials and Methods

A, B, C and D samples were fabricated using different polymeric raw materials such as HDPE, LDPE, linear low density PE (LLDPE), metallocene low linear density PE (mLLDPE) and cyclic olefin copolymer (COC). Trials were done using different resins with melt flow index (MFI) and density values for the same type of raw materials. The density values of raw materials are 0,95, 0,923, 0,918, 0,918, 1,01 g/cm³ for HDPE, LDPE, LLDPE, mLLDPE and COC, respectively. The MFI values are 1,5, 0,75, 1, 1 and 2 g/10 min in the same order. Inner and outer PE layers were produced in Windmüller Hölischer (2010) branded blown film line. Then, the PE films were laminated in Erwepa-Davis Standart (2015) branded extrusion lamination machine. Dynamic Scattering Calorimetry (DSC) analysis was used for the characterization and verification of the samples. DSC thermograms were taken with Perkin Elmer-DSC 4000 device. Lloyd Instrument's tensilemeter device was used for young modulus values. Olympus-BX53F2 branded microscopy device was used for the thickness distribution of the ABL structures.

2.1 Samples Preparing

Compared to market leaders' products, the product subject to this work has a particular difference in layer distribution. In this project, production has been making with thicker inner and outer layers despite thinner tie layers. This adjustment is mostly relevant to production technologies and limitations. Examined reference sample has been produced in consecutive extrusion lamination lines which are specially designed for ABL productions. These production lines allow applying higher polymer melt weights which mean thicker tie layer in another saying.

In this project, ABL production has been making in a compact extrusion lamination line which is designed for thinner packaging. PE films of inner and outer layers has been produced in Pilenpak PE film production site by 5-layer Windmüller & Hölischer blown film lines. PE film formulation had been designed in the scope of this study. Hereby different versions of 120 μ m thickness white PE for outer layer and 70 μ m transparent PE film for inner layer had been produced. Beside that two reference samples had been chosen according the customer's referral and market share of ABL laminates. As the customer's feedbacks, these two references show ideal production efficiency and provide consumer satisfaction. Reference samples' microtome cross sections have been examined under microscope to determine thickness of each layer. Cross section of sample B is shared in Figure 2 as an example.

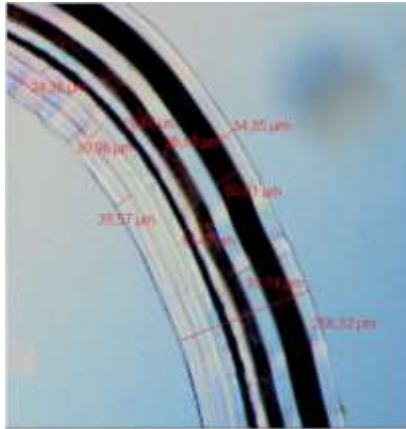


Figure 2. Cross-section of sample B.

Layer distributions of sample A, B, C, D and reference samples are given into Table 1. Since outer and inner layers constitute almost 70% of finished good by weight, actions to increase stiffness have been made by focusing to edit these layers. Four different samples have been produced by editing formulas of inner and outer layers.

Table 1. Layer distributions of ABL samples.

	A-B-C-D	Ref. 1	Ref. 2
PE White (outer)	120µm	113µm	80µm
Tie layer	21µm	35µm	68µm
Aluminum	12µm	12µm	12µm
Tie layer	27µm	30µm	40µm
PE Transparent (inner)	70µm	60µm	50µm
Total	250µm	250µm	250µm

Table 2. Material dispersions of inner and outer layers of sample A, B, C and D.

	A	B	C	D
LDPE	35-50%	25-40%	40-55%	20-35%
LLDPE	2-15%	2-15%	10-25%	
MDPE	15-30%	15-30%	15-30%	
mLLDPE	10-25%	10-25%	5-20%	25-40%
HDPE (0,3)				20-35%
HDPE (1,5)		5-20%		
COC			5-20%	

3. Results and Discussion

3.1 Characterization

DSC thermograms were taken into consideration to crosscheck which materials have been used. DSC analysis has been designed as 5 steps. First, samples have been heated 50°C to 150°C at 50°C/min. After have been held a minute in 150°C as step 2, samples have been cooled back to 0°C at 15°C/min. Then again, held a minute. And last, have been heated 0°C to 150°C at 10.00°C/min which is relatively slower. That's why more clear outcomes are expected from step 5.

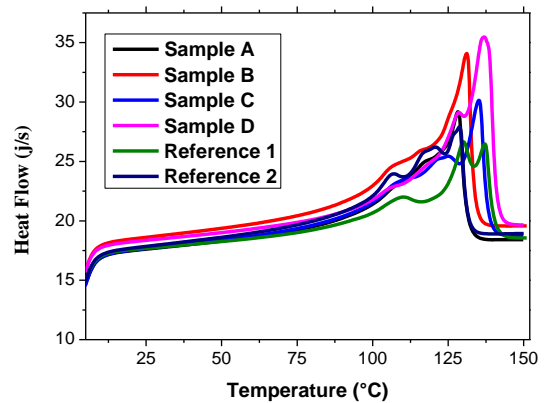


Figure 3. DSC thermograms of samples A,B,C, D, Reference 1 and Reference 2.

In Figure 3, DSC thermograms of sample A, B, C, D with reference 1 and 2 based on step 5 outcomes. Especially LDPE, LLDPE, HDPE and COC materials are able to specified on DSC depending their relatively different melting temperatures. On the flipside mLLDPE – LLDPE and MDPE – HDPE have quite close melting temperatures therefore these materials may be confused on DSC thermograms [11].

3.2 Mechanical Properties

Young modulus values have been considered to compare samples due to their stiffness. Young modulus or in another saying elastic modulus can be referred as ratio of strain to unit elongation in strength. Unit elongation is ratio of length difference to first length. In tensile tester devices, young modulus is calculated with curve of strain to unit elongation as shown in Figure 4 [12].

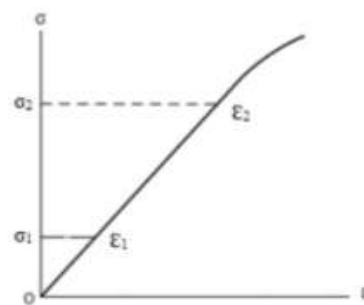


Figure 4. Strain-unit elongation curve [12].

Young modulus (E) is equals to ratio of strain differences ($\Delta\sigma$) to elongation differences ($\Delta\epsilon$).

$$E = \frac{\Delta\sigma}{\Delta\epsilon}$$

In this work, samples have been prepared as 25mm width, 10cm length and 250µm thickness and analyzed machine direction (MD) and transverse direction (TD) both. In other saying, MD is the direction which melt flows through and TD is the vertical direction to this.

Tensile tester has been drawn until samples elongate 1%. To elongate the samples 1%, ratio of required strength to surface area is based as young modulus which makes the unit N/mm^2 . Outcomes are shared in Table 3 and Figure 5.

Table 3. Young Modulus values.

Direction of section	A	B	C	D	Ref 1	Ref 2
MD	589	613	706	758	675	738
TD	457	623	743	685	654	758

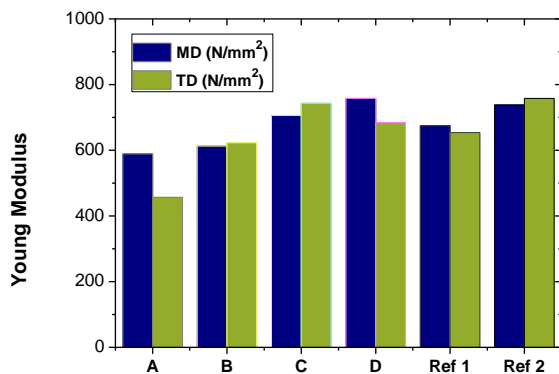


Figure 5. Young Modulus Comparison.

The result has shown that reference samples has at least $650 N/mm^2$ young modulus values for MD and TD both. Hereunder $650 N/mm^2$ young modulus value has been set as target in this project. Sample A which had been mostly made of LDPE, LLDPE and MDPE has been achieved lowest Young modulus values. Accordingly, LDPE, LLDPE and MDPE combination is insufficient can be deduced to reach target. Especially in TD, there is a huge gap between target. Sample C has quite promising outcomes. COC provides the ending good a significant stiffness and this may be considered as working solution. Yet according to reference termograms, there is no sign to COC is used. Sample B and D are HDPE added prototypes. They also show some promise by increasing young modulus values. As a comparison to each other, using HDPE with lower MFI effects more to increase young modulus. Low MFI HDPE use may be considered as key inference of this work.

4. Conclusion

In this study, ABL tubes have been fabricated by using different polymeric raw materials and formulas. Lower stiffness causes ovalization problem and this leads to loss while filling of ending good. In the examination of Pilenpak's products and reference samples, significant difference between young modulus values had been observed and this had linked to stiffness failure. Target value in young modulus were determined as $600-650 N/mm^2$ by reference materials from the market. To

increase Young modules, 4 different samples have been produced. Sample A had been produced mainly by LDPE and Sample B is the theoretically 5-20% HDPE included version of A. In sample C, Cyclic Olefin Copolymer (COC) had been used 5-20% and sample D had been designed with lower MFI HDPE (0.3 in $190^\circ C$ and 2.16 kg). DSC thermograms have showed that reference samples involve HDPE and according to cross section images, main layers are thinner compared to produced prototypes. Using thicker tie layer may provide higher young modulus. Because of the limits of Pilenpak production lines, tie layer can only be this much thicker. That's why different formulas and raw materials had been used to increase young modules.

When the results are examined, Sample A and B show lower young module values than the other samples. It was observed that using COC and HDPE with lower MFI work to increase young modules. Sample C and D looks comparable with references in terms of young modules. The difference of Sample B and C is the using different HDPE especially with different MFI. Results show that lower MFI HDPE provides better young modulus comparing to higher MFI and this supports Abbas-Abadi and friends [13]. Sample D also shows promising results. COC is known for providing stiffness and lower tear resistance on PE films [14]. Especially in MD, Sample D has exceeded target values and made better results. Sample C and D, 706 and $758 N/mm^2$ young modulus values in MD and 743 and $685 N/mm^2$ in TD which are significantly promising results compared to references..

Acknowledgement

This work is supported by 1501 program of the Scientific and Technological Research Council of Turkey (TUBITAK) with the project number 3180082. We would like to thank all our teammates working at Research and Development Center in Pilenpak Packaging and Mr. Murat Özhun and his family for providing opportunities in the project.

Author's Contributions

Mahir Doğan: Drafted and wrote the manuscript, performed the experiment and result analysis.

Keriman Şanlı: Performed the characterization studies and helped in manuscript preparation.

Gizem Güler: Drafted and wrote the manuscript.

Yusuf Över: Performed the evaluation of the results and helped in manuscript preparation.

Ethics

There are no ethical issues after the publication of this manuscript.



References

- [1]. Horodytska, O, Valdes, F, Fullana, A. 2018. Plastic Flexible films waste management- A state of review. *Waste Management*, 77: 413-425.
- [2]. Geyer, R, Jambeck, J, Law, K. 2017. Production, use and fate of all plastics ever made. *Science Advances*; 3: 1-5.
- [3]. A Brief History of Packaging; University of Florida Cooperative Extension Service, Institute of Food and Agricultural Sciences, EDIS, 2002; pp 1.
- [4]. Laminate Tubes. <http://www.laminated-tubes.com/laminate-tubes> (accessed at 26.01.2021).
- [5]. Maurice, T, Suter, J, Miskevich, R. (2013). Laminated Material Suitable for Forming Containers. US 8,377,532 B2. United States Patent.
- [6]. Bhattacharya, S, Banerjee, M. (2014). Aluminum Barrier Laminate. US 2014/0186561 A1. United States Patent.
- [7]. Zuscik, E. (1985). Laminate for Making Tubes. 4,539,259. United States Patent.
- [8]. Laminate Tubes. <http://www.imsors.com.mk/en/products/aluminum-and-pvc-packaging-for-pharmaceutical-industry/laminate-tubes.html> (accessed at 26.01.2021).
- [9]. Feng, J, Li, Z, Olah, A, Baer, E. 2018. High oxygen barrier multilayer EVOH/LDPEfilm/foam. *Journal of Applied Polymer Science*; 135: 46425.
- [10]. Tube Packaging: How to print on lami tube material. <http://www.blog.mps4u.com/tube-packaging-how-to-print-on-lami-tube-material> (accessed at 27.01.2021).
- [11]. Fonseca, C, Harrison, I. 1997. An investigation of co-crystallization in LDPE/HDPE blends using DSC and TREF. *Thermochimica Acta*; 313: 37-41.
- [12]. Aydemir, B, Elmas, B, Ayan, E. 4th International Mediterranean Science and Engineering Congress (IMSEC 2019), Alanya, Antalya, Turkey, 2019, pp 597-603.
- [13]. Abbas- Abadi, Mehrdad Seifali, Mehdi Nekoomanesh Haghghi, and Hamid Yeganeh. "Effect of the melt flow index and melt flow rate on the thermal degradation kinetics of commercial polyolefins." *Journal of applied polymer science* 126.5 (2012): 1739-1745.
- [14]. Durmus, Ali, Mine B. Alanalp, and Ismail Aydin. "Investigation of morphological, rheological, and mechanical properties of cyclic olefin copolymer/poly (ethylene-co-vinyl acetate) blend films." *Journal of Plastic Film & Sheeting* 34.2 (2018): 140-159.

Comparison of the Host-Based Intrusion Detection Systems and Network-Based Intrusion Detection Systems

Ahmet Efe^{1*} , İrem Nur Abacı² 

¹PhD, CISA, CRISC, PMP, International Federation of Red Cross and Red Crescent Societies, Internal Auditing Department, Ankara, Turkey

²Gazi University, Department of Computer Sciences, Ankara, Turkey

* icsiacag@gmail.com

*Orcid: 0000-0002-2691-7517

Received: 27 November 2020

Accepted: 24 January 2022

DOI: 10.18466/cbayarfbe.832533

Abstract

Advanced Persistent Threat (APT) has recently emerged as sophisticated and tailor-made attacks. APTs pose threats mainly targeting military, defense, security infrastructure, high profile companies, and government units. Intrusion detection mechanisms are crucial for adequate protection, especially as a countermeasure for APT attacks done by hackers, cyber warriors, and cyber terrorists over management information systems (MIS) of government institutions and e-government applications. In this study, intrusion detection and prevention systems have been studied in detail after being referred to the tasks and abilities of the intrusion detection systems that are at the core of the computer security technology presented today to meet the increasing need for information and network security. This paper aims to specify the differences between Host Based Intrusion Detection Systems (HIDS) and Network-Based Intrusion Detection Systems (NIDS) and compares the tools using HIDS and NIDS. It is asserted that to better assurance for APT attacks, there should be a Hybrid IDS approach covering both networks and hosts using both signature and behavioral detection mechanisms based on deep learning algorithms.

Keywords: Intrusion detection systems, Host-based intrusion detection systems (HIDS), Network-based Intrusion detection systems (NIDS), Hybrid IDS, MIS security

1. Introduction

One of the main issues of trust in E-government implementation is security. The information age makes information to be accessed all over the world without any constraints due to the usage of technological advancement that provides solutions for efficiency, confidentiality, and availability concerns. Citizens prefer to use traditional ways rather than an unsecured website [1]. So information services located on servers become widespread, and data stored on these services become vulnerable to exposure and cyber-attacks. Mainly cloud services provide omnipresent opportunities for information processing and fast access, and it also makes information more vulnerable a target for hackers, cyber warriors, and cyber terrorists. Cyber-attacks have existed, evolved, and become more sophisticated than ever in recent times as Advanced Persistent Threats (APTs) come into view.

Along with the widespread use of the internet, threats to information systems have also increased dramatically and widened in types of attacks. Along with the rapid increase in the number and types of security threats, security technologies are also undergoing rapid development. Security mechanisms such as authentication and access control were first developed to ensure the security of computers, prevent unauthorized access to systems, and capture or modify information. Such mechanisms constitute the first step of safety. Firewalls, vulnerability scanners, and intrusion detection systems form the second stage of security mechanisms. None of these security technologies alone is fully adequate because each one is focused on different security points. For a secure system, these structures must be used together to support each other. The purpose of intrusion detection is to classify all intrusion attempts correctly and notice activities that should not be tagged as an intrusion. In this context, an intrusion is a resource accessibility violation. Systems that detect these actions are named

Intrusion Detection Systems-IDS. IDS use system network or data to find attacks.

IDS provides three essential security functions: monitoring, detecting, and responding to unauthorized activities. IDS are generally classified as follows [2]:

1. Host-Based (HIDS): Host-based intrusion detection systems run on individual hosts/devices on the network.
2. Network-Based (NIDS): Network-based intrusion detection systems monitor traffic between all devices on the network.

In general, the effectiveness of the intrusion detection system depends on its "Configurability" (Ability to define and add new specifications attack), robustness (fault tolerance), and the small number of false positives (false alarms) and false negatives (undetected attacks) it generates [3]. The remainder of the paper is organized as follows: Introduction to intrusion detection systems; advantages and disadvantages of both network-based IDS and Host-based IDS; expectations from sound intrusion detection systems; intrusion detection tools; and conclusions are drawn before future work discussed.

2. The E-Government Security Risks to Be Mitigated by IDS Systems

According to a study, the development of e-government faces fatal security problems due to the complexity and vulnerability of networks [4]:

2.1 Information Intercepting

If interceptors cannot be detected in a system, information confidentiality will not be adequately managed.

2.2 Information Tampering

If information tampering cannot be detected in a system, information integrity and availability will not be appropriately managed.

2.3 Services Denying

It is the complete invalidation of the network system or the server's system in some period.

2.4 System Resources Stealing

In the network system environment, stealing the system resources is very common.

2.5 Information Faking

The primary forms include pretending users get illegal certifications, forging emails, etc. The risks mentioned above related to e-government applications and e-business systems can be mitigated by using IDS systems properly.

3. Intrusion Detection Systems-IDS

Intrusion means any set of actions that dare to risk a source's integrity, confidentiality, or availability. Such computer system violations can cause problems: data integrity, access denied for online resources, the leak of confidential data, and taking benefit of private resources. Denning implemented an intrusion detection system (IDS) in 1987. Since then, IDS has become a hot analysis topic essential for network security. IDS protects external users and inner attackers, wherein visitors do not pass beyond the firewall at all. Intrusion Detection Systems are divided into identification methods and attack detection.

Intrusion Detection Systems are based on their established environment; Network Intrusion Detection Systems and Host-based Intrusion Detection Systems. Intrusion Detection Systems are divided into signature-based Intrusion Detection Systems and anomaly-based Intrusion Detection Systems according to intrusion detection methods. Signature-based Intrusion Detection Systems use attack signatures in an attack signature database to detect attacks. Anomaly-based Intrusion Detection Systems perform intrusion detection based on the anomalies in the network traffic without using attack signatures. Signature Based Intrusion Detection Systems can only detect attacks on the attack database. They have no chance of seeing new episodes. Since anomaly-based Intrusion Detection Systems do not use any attack signatures, these systems are likely to produce false-positive results. Anomaly Based Intrusion Detection Systems are also able to detect new attacks. Intrusion detection systems are systems designed to detect these attacks, which are made up of various packages and data, which can be attacked or caught after computer system attacks against the computer system technology. Intrusion detection systems can be thought of as a kind of alarm system.

It is possible to divide them into categories in many different ways. For example: According to the Internet Security Systems (ISP) model, an intrusion detection system can be primarily active or passive. The latter may be host-based or network-based. When we combine these two systems, intrusion detection systems can be grouped as such:

- active / host-based,
- active / network-based,
- passive / host-based,
- passive / network-based.

Intrusion detection can be classified according to two analysis methods. A system needs to respond in real-time or close to an attack that is detected to be functional (for example, shaping firewall rules against an attack or warning the user from the command console). Passive systems usually record episodes and

then store them for review. There is a need for triggering mechanisms (in other words, to know the wrong and unusual usage of the system and network resources) to detect attacks. These are misuse attacks (signature-based attacks) and anomaly attacks.

Intrusion Detection is becoming re-created as Intrusion Prevention. These systems are being crafted for HIDS and NIDS environments, showing that vendors listen to security needs. These new technologies work by various means, such as intercepting application interface calls to operating systems and classifying the calling activity. If the Intrusion Prevention system thinks that the caller is inappropriate, the access can be denied, allowed, logged, or combined.

3.1 Network-Based IDS

A Network-Based IDS (NIDS) analyzes incoming packets over a network connection and analyzes packets on the data part of the attack. NIDS uses the abnormality detection of signatures to detect attacks. It alarms to report a real-time attack keeps a log of detailed information about the attack after the attack has occurred. Network-based intrusion detection systems display the traffic passing through the network's segment in the form of a data source. This is usually accomplished by bringing the network card into promiscuous mode to capture all traffic passing through it. Traffic to other segments of the network and other types of communication, such as phone lines, can not be captured and displayed. The network-based intrusion detection system mainly deals with packets passing through the network via a sensor. The package arriving at the detector must be checked against the existing signatures to decide what to do with the package. The filter at the start level specifies which packets are accepted and which packages are to be discarded or sent to the attack recognition module. If an attack is detected, the response module triggers the alarm to be generated in response to the attack. Encryption of the traffic between the sensor and the monitor, including sensors and viewers in a separate network, is essential for security. For a knowledgeable and experienced attacker, the traffic (alarms, status logs, other packets, etc.) between the sensor and the viewer is vital for attacking the network. Sensors and viewers can be included in a separate network to protect against DoS (Denial of Service) attacks. The other advantage is that the network on which the attack is detected differs from the network we are on. Network-based intrusion detection relies on acquired knowledge [6]. Symantec reported that IDS could generate 10-90% of false alarms depending on the level of tuning and customization [7]. Julich and Dacier [8] have pointed out that IDS could generate up to 99% false alarms.

3.2 Host-Based IDS

Host-based intrusion detection was a commonly used method in the early 1980s. Audit logs were held against potentially dangerous network activities. Today, this system is used; but "audit logs" are more sophisticated, automated, and real-time detection and response made easier. Software is used to view logs in host-based systems. The system, event, and security records on Windows NT systems, Syslog, and custom OS registry files are available on UNIX systems. Any changes to these files are to be compared to the existing security policy, and the response will be promptly answered. The host-based IDS displays real-time logs and responds in the same way. Some host-based IDS can also listen to port events and block access to specific private ports, thereby providing network security. The task of host-based intrusion detection systems; Listening to the traffic of the server on which the server is installed, recording files and transactions based on the attack/signature database on the server and customized for that server, and responding by detecting attacks. Host-Based Intrusion Detection Systems (HIDS) work by examining the log files of the server traffics based on the database on the server and notify a report to the relevant system administrator when an unexpected attack is detected. The essential rule in these systems is system compatibility. The compatibility of operating systems can be non-contingent.

Host-based intrusion detection systems are installed on various special servers and detect or prevent attacks on that server. It is the task of taking the configuration files of the systems they are in, tracking the files that the system records are kept in, examining the changes that may occur in the system's integrity, and preventing malicious use. They have difficulties complying with the systems they have built fully. The nature of the operating systems is incompatible with each other. This leads to the requirement that intrusion detection systems are explicitly written for that operating system and structured to the weaknesses. They are available for custom server software.

4. Literature Review

Anderson first described the concept of the intrusion detection system in 1980, and in 1987 by Denning's publication, the basic intrusion detection system was defined. The amount of data being produced by such Intrusion Detection Systems (IDS) exceeds by far the human capability of information processing [9]. Various researchers have given the following definitions on matter intrusion detection systems and technology in recent years.

According to Yang and others [10], IDS is a system that detects and identifies intrusion behavior or intrusion enterprises by monitoring and analyzing Ag

packets or system audit records in a computer system and then giving real-time intrusion warnings to system administrators.

According to Xuetao and others [11], intrusion detection technology is a crucial research area in the information system, which is open to attack and is an essential research direction for information technologies that prevent malfunctions from being exploited by malicious codes or codes.

According to Pikoulas and others [12], the intrusion detection system is a system that identifies threats aimed at any organization and then guarantees that the system is protected.

Jemini and others [13] have compared a network with an intrusion detection system to a house with installed burglar alarm systems. They both used different methods to detect an attacker from the inside. In addition, everyone has been alerted that the system and the attacker are alerting them.

From the above definitions, the definition of the intrusion detection system, in general, can be given as follows: It is a system aiming at detecting attackers who are infiltrating or leaking outside the system with various purposes such as accessing the system without permission, unauthorized use of the system resources, accessing and changing the personal information of the users, running or stopping the operation of the system, and users who misuse the limited system resources.

Intrusion detection systems can be divided into three main categories and subcategories. Network-based intrusion detection systems detect web-based attacks based on an intrusion detection system and host-based intrusion detection systems that detect attacks against a single computer system. Traditionally, intrusion detection systems detect misuse attacks and systems that see anomaly attacks. According to the attack detection technique, some studies assumed that they are in systems that detect identification/hybrid attacks, a mixture of misuse and abnormality models, as an additional category [14,15]. Also, detection of abnormality attacks can be decomposed by statistical abnormality test, artificial neural networks, full based on the detection of abnormality, data mining based on the detection of anomalies, immune-based abnormalities detection, and so on [10,16].

Intrusion detection systems are central and distributed according to their architectures [14,17]. Data analysis in centralized intrusion detection systems is done on a server independently of the number of servers monitored. This process can be done on servers in the intrusion detection systems prepared with distributed architecture. Though centralized architecture and intrusion detection systems have the advantage of

having direct access to the database, there is a severe drawback, such as the occurrence of bottlenecks. DDIS, AAFID, and NIDIA can be given to intrusion detection systems prepared with distributed architecture. Intelligent agents are usually used in structures used instead of the new generation distributed architecture. Intrusion detection systems can be classified as real-time or offline in terms of operational logic.

A STUDY USES XML-based SOAP, WSDL, and UDDI to utilize web services that allow machine-to-machine interoperability. M. Silva and others presented a multi-agent remote access intrusion detection system [17] that provides services for users who do not have a local intrusion detection system in their work. Multi-agent architecture and model-based architecture web services were used in the model they used. Due to the multi-agent structure, system flexibility is provided by agents sharing information in the system. Model-based architecture adds portability, interoperability, and reusability to the system. The design presented in this study consists of 6 layers, including monitoring, analysis, response, update, management, storage. The proposed system provides intrusion detection system services over the internet. Although users can easily access it, there is a disadvantage in its very intensive communication.

Data collection techniques in intrusion detection systems are implemented through sensors. These sensors are classified as internal and external sensors. Internal sensors embedded in the program being watched or working as part of them and those separate from the program are also referred to as external sensors. Advantages of external sensors; They can be easily added to the server quickly and easily separated from the server. The ability of an attacker to disable or change the sensor as easy to modify and creating delays is the disadvantage of external sensors. The advantages of internal sensors can be listed as minimal latency, ease of change, and difficulty in developing the server's weaknesses. However, it is listed as a low overhead to the server's performance, the necessity of developing the program to be monitored in the program's language, updating and developing the wrong implementation, and serious problems. Examples of external sensors are agents that monitor each server in distributed systems separately and report them in a hierarchical structure they find. Internal sensors developed for OpenBSD systems for internal sensors can be provided that do not require the additional load to detect different attacks in real-time [15]. Intrusion detection systems' quality should be evaluated according to their effectiveness, adaptability, and extensibility scales [15].

While intrusion detection systems detect attacks, they do not determine that they have failed successfully. Instead, this decision is left to the analyst and system

administrators. In such a case, the system administrator reviews the collected audit information, performs vulnerability scans, and checks the system for updates. Although these operations can be performed on small-scale networks, they are not practical in distributed networks having a large amount of control information.

Researchers have generally ignored the human factor by focusing on the machine component in the intrusion detection system. This shortcoming puts the advocating side in a disadvantageous position. Because the values of avoidance and assertion validation methods are not fully understood [16].

5. Verified Current Zero-Day Exploits of IDS Systems

The zero-Day vulnerability occurs when computer vulnerability is publicly announced. Once the Zero-Day Vulnerability occurs, all computers and computer users using that software are at risk. If the software's support team does not act fast enough to close the gap, hackers can turn this vulnerability into exploits and quickly share them among themselves. Of course, a competent team can perform a simple computer user or internet hackers. As a result, more hackers can easily manage to exploit this vulnerability.

Zero-Day Exploit transforms the vulnerabilities caused by the Zero Day Vulnerability into software or scripts by experienced internet hackers. When such vulnerabilities are turned into Zero-Day Exploit, all professional or inexperienced hackers can easily exploit the vulnerability and damage systems.

The preparation of Zero-Day Exploits is sometimes a complicated process, and sometimes it can be straightforward. Creating Zero-Day Exploits for operating systems such as Windows XP that have entirely lost support and have not received updates will be much easier. Microsoft has announced that no security updates will be offered for this operating system. All vulnerabilities for Windows XP will turn into Zero-Day Exploit from now on.

Zero-Day Attack attacks can be a kind of blessing for internet hackers who act early. A zero-day attack is the emergence of software vulnerability and hackers launching attacks using this vulnerability directly or as an exploit. Because although others have revealed these vulnerabilities, the first act of hackers will benefit from this vulnerability and will continue to use the exposure until closing the gap. Some examples of IDS and systems are declared as verified zero-day exploits in the table below. The hyperlinks can provide detailed information for each exploit.

Table 1. Some Examples for Verified Exploits Declared in the Exploit Data Base on the IDS

Date	Title	Type	Platform	Author
2009-09-21	Snort unified 1 IDS Logging - Alert Evasion & Logfile Corruption/Alert Falsify	DoS	Multiple	Pablo Rincón Crespo
2009-07-27	Magician Blog 1.0 - 'ids' SQL Injection	WebApps	PHP	Evil-Cod3r
2007-12-26	RunCMS 1.6 - Blind SQL Injection (IDS Evasion)	WebApps	PHP	sh2kerr
2007-10-27	Oracle 10g - 'LT.FINDRICSET' SQL Injection (IDS Evasion)	Local	Multiple	sh2kerr
2005-12-07	Appfluent Database IDS < 2.1.0.103 - Environment Variable Local Overflow	Local	Solaris	c0ntex
2002-05-17	Cisco IDS Device Manager 3.1.1 - Arbitrary File Read Access	Remote	Hardware	Andrew Lopacki
2001-09-05	Cisco Secure IDS 2.0/3.0 / Snort 1.x / ISS RealSecure 5/6 / NFR 5.0 - Encoded IIS Detection Evasion	Remote	Multiple	blackangels
2000-06-07	Computer Associates eTrust Intrusion Detection 1.4.1.13 - Weak Encryption	Local	Windows	Phate.net
1999-08-05	Network Security Wizards Dragon-Fire IDS 1.0 - Command Execution	Remote	Hardware	Stefan Lauda

Source: www.exploit.db

The information given in Table 1 is related to exploits available in the exploit database for the IDS system. The each of the exploits, there is a link demonstrating its information. For example, with the "Snort unified 1 IDS Logging - Alert Evasion & Logfile Corruption/Alert

Falsify" named exploit, the alert type and size are overwritten with the MAC addresses of the raw packet.

So with malformed packets (Eth/IP/TCP/Data with modified MAC addresses), the size and the type (and other information) can be set falsifying alerts for a later parsing process. For example, suppose an attacker builds malformed packets. In that case, so a signal is faked, the size is more extensive than 128M (the unified log limit size by default), snort will continue inserting alerts in the file. Still, when reading that alert, a parser

will try to jump 128M skipping the signals inserted after the falsified one. An attacker can also insert a complete list of falsified signals and malformed packets because the basic package is TCP data. You can fill with falsified UnifiedLog alert structures with binary data. Therefore you would need to adjust the packet headers to set the "size of the alert" (overwritten with the MACs of the packet), making that the parser read the following alert in the offset that the TCP data will overwrite with the list of falsified warnings.

6. Advantages and Disadvantages of NIDS and HIDS

According to the intrusion detection system, the categorization is performed single host-based or multi host-based because of data collection mechanism and activities monitoring. Network-based intrusion detection systems monitor the entire network to determine an attack or an attack condition. There is a distinction between network-based and host-based systems on "how data is collected" but not on "how and where data is processed" [15]. In general, network-based intrusion detection systems are based on signature detection, and host-based intrusion detection systems are based on anomaly detection [14,15]. The HIDS and NIDS approaches have advantages and disadvantages. Pahlevanzadeh and Sansudin also exhibited these advantages and disadvantages that they have stated in their work in Table 2.

Table 2. Comparison of HIDS and NIDS

NIDS	HIDS
The activity area is wide	The activity area is limited. It monitors private system activities.
It is better at detecting an attack from the outside. Notices that HIDS is missing	It is better at detecting intrusions from inside. HIDS notices that NIDS are missing.
The package header and the entire package will be examined.	It does not see package headers.
The reaction is close to real-time.	Reacts after any suspected entry.
Independent from host	Dependent to host
Dependent to bandwidth	Independent from bandwidth
Slows traffic on networks where IDS clients are located	Slow down IDS installed server computers
The payload detects network attacks after they are analyzed.	Detects local attacks before they damage the network.
It is not appropriate for carrying encrypted data and using the keying.	It is appropriate for carrying encrypted data and using the keying.
There is no overload	Overloaded
Have high false-positive value	Have low false positive value

In addition to the information given in Table 1, Bai and Kobayashi [15] point out that it is difficult to change the evidence left by the attacker for network-based intrusion detection systems and host-based intrusion detection systems are connected to the operating systems. However, they will not miss packets such as network-based systems in dense network traffic [18].

The goal of the NIDS is to detect an attack that is actively happening on a network. The emerging trend seems to blend the two approaches in what we now call a hybrid intrusion detection system [19]. The Hybrid IDS combines both signature and anomaly-based models to achieve higher detection rates with lower false positives.

In addition to the host and network-based intrusion detection systems, these systems can be considered a mix of host and network-based systems divided into three different categories [15]. These are PH-NIDS (Per Host Network-Based IDS), LB-NIDS (Load Balanced Network-Based IDS), FW-IDS (Firewall Based IDS). PH-NIDS analyzes network traffic based on the host and only incoming traffic. LB-NIDS uses load balancing and balances bandwidth using other network intrusion detection systems. FW-IDS Network-based intrusion detection system adds functionality to a firewall. There is hardly any packet loss, but there is a slowdown in the network.

7. Expectations from a sound intrusion detection system

The quality of intrusion detection systems is often assessed according to their effectiveness, adaptability, and extensibility characteristics. These parameters can be ordered as follows from a good and quality intrusion detection system other than the primary needs:

- Attack detection rates are at very high levels
- It can operate at high speed and can be used in real-time and applications
- Be able to display all events by following the most effective listening data in large quantities
- In the system where it is running, the processor memory, file, and network operations are at a minimum level of resource utilization
- To Alert the security analyst by instantly alerting them of any attack
- Be able to withstand the attack that may come to it
- Easy to set up and scalable
- No matter how high the density in the network traffic, the network packets are not lost
- It is a structure that does not cause faults and openings in its internal mechanism.
- The system must be very resistant to an attacker's deception.

8. Intrusion Detection Tools

Here we are analyzing some of the best known IDS tools to understand their benefits and advantages in comparison. Snort is a leader in open-source NIDS solutions. Snort uses signature-based intrusion detection and anomaly-based detection methods and can rely on user-created rules or update signatures from the database as emerging threats. Suricata is Snort's direct competitor, and it applies a security and anomaly-based approach based on signature-based detection methodology to detect attacks. Bro IDS uses an anomaly-based intrusion detection method. The language of Bro IDS is specific to network applications that are the NIDS. It is very effective in traffic analysis.

6.1 Snort

Snort is a recently developed network-based intrusion detection system that can perform abuse detection and real-time traffic analysis on IP networks. Snort is an intrusion detection system that works in the abuse detection model—initially presented as a rule-based penetration detection system in the intrusion detection model. Nowadays, it is also used for traffic analysis such as network data collection using plug-in programs detection of abnormalities in protocol headers. Snort consists of a multi-layer structure. It works with all the arrangements to detect specific attacks and output them in the desired format.

Snort, open-source, and free software distributed under the GNU license, was developed by Martin Roesch in 1988. Now, an attack developed by Sourcefire, which Martin Roesch has built, is the most widely used globally. It is capable of real-time traffic analysis and packet logging on IP networks, which can work seamlessly on many different platforms such as Linux, Windows, MAC, and FreeBSD Detection and prevention system software. Snort, which is generally signature-based, can also perform protocol and anomaly analysis by using a set of paid or unpaid rules downloaded from www.snort.org and www.emergingTreats.com. They also have a flexible rule/policy setup language that allows users to write their own rules for attack detection, software protocol analysis, content scanning/mapping, buffer overflow, port scanning, operating system fingerprint test.

When Snort is used as an Intrusion Detection System (IDS), two network interface cards are usually used. One of the interfaces is used to listen to the network and remotely access Snort and configure Snort. The interface that listens to the network is generally not assigned an IP address but all the switch ports to which it is connected or mirrored. Snort will listen to all packets passing through the switch with this method. Snort's architecture is based on performance, simplicity, and flexibility. It is built on four essential components:

packet decoder, preprocessor, detection engine, and logging/alarm.

6.2 Suricata

Suricata is an open-source intrusion detection and prevention system distributed with a GPLv2 license. The first beta version was released in December 2009, and the first stable version was released in June 2010. Snort's support of the rules became effective soon after being accepted. Suricata has come up with significant innovations in attack detection. These are the new HTTP normalization tool called HTP library and developed by Ivan Ristic from the Suricata project team. The most important feature of this new tool that allows parsing HTTP traffic is "security-aware." It can capture various techniques that attackers can use to bypass intrusion detection systems. However, the library has different parses for request line, request header, URL, username, response line, server response line, and cookie, "basic" and "digest" authentication operations related to the HTTP protocol. Another essential feature of Suricata is its ability to support multi-threaded operations. For architects with multiple processor units, the packet processing is distributed in different departments with different threads. Each CPU unit acts as a separate machine running on a single processor. Thus, load balance is achieved, and performance is improved.

The characteristics of Suricata are as follows:

- It can be used in operation modes such as intrusion detection systems (IDS), intrusion prevention systems (IPS).
- It is possible to record the traffic in PCAP format and then analyze it offline by monitoring the network traffic. It also works in UNIX socket mode for the analysis of PCAP files.
- Linux, FreeBSD, OpenBSD, Mac OS X, Windows, and almost all operating systems can work.
- The configuration file is in YAML format, making it easy to understand. Many programming languages are supported. With Suricata 2.0 stable version, YAML file is divided into desired parts and called from the main file.
- The IPv6 protocol is fully supported.
- TCP sessions perform operations such as tracking the session from beginning to end, queuing the stream, etc. It also has a separate module for reassembling the shredded packages.

A study based on a comparison of Snort and Suricata found that both systems are sound [20].

6.3 BRO

Bro is an open-source, UNIX-based, BSD-distributed intrusion detection system, network analysis, and monitoring tool. It was first codified in 1995 by Vern Paxson, Lawrence Berkeley National Laboratory (LBNL). It was functionally developed in 1996 and announced in an article published in 1998. By 2003, the project was supported by the National Science Foundation (NSF) and is now being developed at the International Computer Science Institute (ICSI) in Berkeley.

Bro is a complex network traffic analysis tool, unlike the classical rule-based IDS. Traffic analysis covers security and includes performance analysis and networking solutions.

The characteristics of Bro are as follows;

- Linux, FreeBSD, MacOS and UNIX-based operating systems.
- It can analyze real-time or offline.
- It uses the library "libpcap" to capture packages.
- Bro users offer clusters ("Bro Clusters") wherever traffic is concentrated and distributed, such as universities, research laboratories, and large-scale businesses. Bro runs on different servers, and they can communicate between themselves.

9. Conclusion

IDS systems become the most critical security systems for e-government and e-business applications [21]. One of the ways to identify hackers is to use and tightly tune intrusion detection systems (IDSs), which try to detect or predict the probability of an attack in various ways, such as controlling the network traffic and detecting those trying to attack by creating too much traffic on the network [22]. Session Initiation Protocol (SIP) packet replay attack, SIP packet insertion attack, TLS connection reset attack, flood attacks, and fake message attacks are the most known DoS attacks. Using a SIP-supported firewall against such attacks provides detailed network analysis and prevents attacks by adding SIP-oriented rules to IDS and IPS devices. Multiple packets sent simultaneously can be detected with these systems, which can warn admins. Restriction can be in the form of not accepting packets from users outside the network, or it can be in the form of limiting the number of packets coming over a single IP. In addition, during the attack on the server, the attack can be detected manually by monitoring the network packets with tools like "ngrep". [23].

While the number of software vulnerabilities discovered and publicly disclosed by white hats or experts is increasing every year, only a small portion, if not all, of these vulnerabilities are used in real-world attacks. Due to constraints on time and qualified resources,

organizations often look to ways to identify threatened vulnerabilities for patch prioritization. For this, robust threat intelligence is needed, which not every organization can do well and adequately [24]. Since we have found many zero-day exploits available in the exploit-DB database, it is highly recommended to tighten IDS and IPS tools and keep up to date with the latest vendor patches. Machine learning techniques are now widely used to perform effective attack detection, as attackers can quickly exploit techniques and zero-day vulnerabilities that bypass security measures and avoid direct detection. In this context, deep learning networks can play an essential role by analyzing network flows and classifying them as "normal" or "attacked". Various projects aim to design and implement tools for detecting zero-day threats (ZED-IDS, Zero Day Intrusion Detection System), and a deep learning architecture is used to detect DoS attacks [25, 26].

It is impossible to choose the most effective approach for IDS systems formed by very different methods. Still, the advantages and disadvantages of each IDS system are presented to the reader. It can be said that traces on Attack signature-based systems will increase in terms of the processing time in the future due to the day-to-day progress slowing down of such systems will be inevitable, and new investigations will eliminate this deficiency. More efficient signature-based intrusion detection systems should be developed. IDS and IPS systems should be used with firewall devices. These products are used together with the new generation Firewall devices, which enable the monitoring of the activity on the network and the analysis of the traffic to detect possible cyber-attacks, breaches, and threats. In this way, the performance problems that may arise are prevented and successful results by working more efficiently. Today, the complex structure of networks and the fact that they are connected to other networks, especially the internet, with many access points, make it easier for cyber attackers. It has become challenging to prevent complex network systems from increasing and developing attacks with technology development. It has become impossible to protect data and ensure information security with encryption or a stand-alone firewall.

Today, intrusion detection systems that apply artificial intelligence, machine learning, and data mining approaches are intensely confronted. Artificial intelligence plays a vital role in detecting intrusions and is widely considered the better way to adapt and build IDS. Nowadays, neural network algorithms have emerged as a new artificial intelligence technology applied to real-time problems [26]. As can be seen from the reviewed articles, researchers have concentrated on classifiers. There is also a question of how the intrusion detection systems run offline to show how they perform in real-time. A suggested way is to select real-time intrusion detection systems with faster and higher

detection rates by reducing the number of features by selecting only the critical components examined. In addition, more successful intrusion detection systems can be created by combining various categories of methods in the simplest terms using different 'fusion' approaches.

Another consequence of the studies examined is the need for up-to-date audit data sets. The data sets used in the studies are often very diverse and outdated. For this, it can be said that it is necessary to create quantitative and diversified data sets in terms of personal privacy. We believe that the methods that generate traffic data will be further developed to observe the real-time success of the intrusion detection systems presented in the literature and give us a more detailed interpretation of these systems.

Author's Contributions

Ahmet EFE: Guided the drafting and writing of the manuscript, checked and finalized the work.

Irem Nur ABACI: Drafted preliminary content.

Ethics

There are no ethical issues after the publication of this manuscript.

References

- [1]. Bahman Nikkhahan, Akbar Jangi Aghdam, and Sahar Sohrabi, "E-government security: A honeynet approach", *International Journal of Advanced Science and Technology* Volume 5, April, 2009 <http://www.sersc.org/journals/IJAST/vol5/5.pdf>
- [2]. Niva Das, Tanmoy Sarkar, "Survey on Host and Network Based Intrusion Detection System" Department of Information Technology, University of Calcutta, Kolkata Email: niva.cu@gmail.com *Int. J. Advanced Networking and Applications* Volume: 6 Issue: 2 Pages: 2266-2269 (2014) ISSN : 0975-0290
- [3]. Yousef Farhaoui, Ahmed Asimi, "Creating a Complete Model of an Intrusion Detection System effective on the LAN" (IJACSA) *International Journal of Advanced Computer Science and Applications*, Vol. 3, No. 5, 2012
- [4]. Zhitian Zhou, Congyang Hu, "Study on the E-government Security Risk Management", *International Journal of Computer Science and Network Security*, VOL.8 No.5, May 2008 Manuscript received May 5, 2008 Manuscript revised May 20, 2008.
- [5]. Wallner R., *Intrusion Detection Systems*, 2007, <http://www.kiv.zcu.cz/~ledvina/DHT/tugraz/IDS.pdf>
- [6]. Young S. and Aitel D., *The hacker's handbook: the strategy behind breaking into and defending networks*. CRC Press, 2003.
- [7]. Timm K., "Strategies to reduce false positives and false negatives in nids," *Tech. Rep.*, Access Date 10 Oct, 2015.
- [8]. Julisch K. and Dacier M., "Mining intrusion detection alarms for actionable knowledge," in *Proceedings of the eighth ACM SIGKDD international conference on Knowledge discovery and data mining-KDD 02*. Association for Computing Machinery (ACM), 2002.
- [9]. Chyssler T., Burschka S., Semling M., Lingvall T. and Burbeck K., "Alarm Reduction and Correlation in Intrusion Detection Systems".
- [10]. Yang W., Wan W., Guo L. and Zhang L.J., "An Efficient Intrusion Detection Model Based on Fast Inductive Learning", *International Conference on Machine Learning and Cybernetics*.
- [11]. Xuetao D., Chunfu J. and Fu Y., "A Typical Set Method of Intrusion Detection Technology Based on Computer Audit Data", *International Conference on Computational Intelligence and Security*.
- [12]. Pikoulas J., Buchanan W., Mannion M. and Triantafylopoulos K., "An Intelligent Agent Security Intrusion System", *9th Annual IEEE International Conference and Workshop on the Engineering of Computer-Based Systems*.
- [13]. Jemili F., Zaghdoud M. and Ben Ahmed M., "A Framework for an Adaptive Intrusion Detection System using Bayesian Network", *IEEE Intelligence and Security Informatics*.
- [14]. B. Pahlevanzadeh and A. Samsudin, "Distributed Hierarchical IDS for MANET over AODV+", *IEEE International Conference on Telecommunications and Malaysia International Conference on Communications*.
- [15]. Bai Y. and Kobayashi H., "Intrusion Detection Systems: Technology and Development", *17th International Conference on Advanced Information Networking Applications*.
- [16]. David J. Chaboya, Richard A. Raines, Rusty O. Baldwin, Barry E. Mullins, "Network Intrusion Detection: Automated and Manual Methods Prone to Attack and Evasion", *IEEE Security and Privacy*.
- [17]. Silva M., Lopez D. and Abdelouahab Z., "A Remote IDS based on Multi Agent Systems, Web Services and MDA", *International Conference on Software Engineering Advances*.
- [18]. Irfan Gul, M. Hussain, "Distributed Cloud Intrusion Detection Model" *International Journal of Advanced Science and Technology* Vol. 34, September, 2011 <https://pdfs.semanticscholar.org/9e13/4e4ea8319869f95cc4efab372fb5fbabe01.pdf>
- [19]. Hassen M. Alsafi, Wafaa Mustafa Abdulllah, Al-Sakib Khan Pathan, IDPS: An Integrated Intrusion Handling Model for Cloud, *Computer Science, Networking and Internet Architecture*, March 2012, <https://arxiv.org/abs/1203.3323>
- [20]. Chintan Kacha, Kirtee A. Shevade, "Comparison of Different Intrusion Detection and Prevention Systems" *International Journal of Emerging Technology and Advanced Engineering* Volume 2, Issue 12, December 2012) <https://pdfs.semanticscholar.org/08d2/5088d72857dd05467a3689ac8a36e838e724.pdf>
- [21]. Mahmood Khalel Ibrahim et al, "Secure E-Government Framework: Design and Implementation", *IJCSET/May 2013 / Vol 3, Issue 5*, 186-193
- [22]. Sajad Einy, Cemil Oz, Yahya Dorostkar Navaei, "The Anomaly- and Signature-Based IDS for Network Security Using Hybrid Inference Systems", *Mathematical Problems in Engineering*, vol. 2021, Article ID 6639714, 10 pages, 2021. <https://doi.org/10.1155/2021/6639714>
- [23]. Yüksel, M. , Öztürk, N. "SIP Saldırıları ve Güvenlik Yöntemleri" . *Bilişim Teknolojileri Dergisi 10* (2017): 301-310 <https://dergipark.org.tr/tr/pub/gazibtd/issue/30647/331042>



[24]. Almukaynizi M., Nunes E., Dharaiya K., Senguttuvan M., Shakarian J., Shakarian P. (2019) Patch Before Exploited: An Approach to Identify Targeted Software Vulnerabilities. In: Sikos L. (eds) *AI in Cybersecurity. Intelligent Systems Reference Library, vol 151. Springer, Cham.*
https://doi.org/10.1007/978-3-319-98842-9_4

[25]. Catillo, Marta, Rak, Massimiliano, and Villano, Umberto. 'Discovery of DoS Attacks by the ZED-IDS Anomaly Detector'. 1 Jan. 2019 : 349 – 365. *Journal of High Speed Networks*, DOI: [10.3233/jhs-190620](https://doi.org/10.3233/jhs-190620)

[26]. V. Kanimozhi, T. Prem Jacob, Artificial Intelligence based Network Intrusion Detection with hyper-parameter optimization tuning on the realistic cyber dataset CSE-CIC-IDS2018 using cloud computing, *ICT Express, Volume 5, Issue 3, 2019, Pages 211-214, ISSN 2405-9595,*
<https://doi.org/10.1016/j.ict.2019.03.003>.

Efficient Web-Based Application Development for Carbon Footprint Calculation: Example of Burdur Province

Mustafa Batar^{1*} 

¹Burdur Mehmet Akif Ersoy University, Department of Computer Engineering, 15030 Burdur, Turkey

*mbatar@mehmetakif.edu.tr

*Orcid: 0000-0002-8231-6628

Received: 1 August 2021

Accepted: 24 January 2022

DOI: 10.18466/cbayarfbe.977279

Abstract

With each passing year, people's consumption activities create permanent effects on nature. In this context, the carbon footprint has been determined as a way of expressing the magnitude of this impact. In addition, the carbon footprint is defined as a measure of the damage caused by human activities to the environment in terms of the amount of greenhouse gases produced and measured in units of carbon dioxide. In this study, an easy-to-use and effective carbon footprint calculation engine has been created for carbon footprint calculation. Also, this application has been designed and developed as a web-based application – <http://karbon-ayakizi.com/> (this site has been in active use between January 2020 and January 2021, but it is currently inactive). Furthermore, a real case study on the carbon footprint of an education institution located in the city centre of Burdur has been conducted, and so the accuracy and functionality of the developed application has been showed and demonstrated. For this purpose, natural gas consumption within Scope-1, electricity consumption within Scope-2, private personal cars, public transportation service vehicles and water consumption data within Scope-3 have been considered in carbon footprint measurement. In the light of these obtained numerical data, the efficiency and the reliability of the developed carbon footprint calculation engine – application – with its trustworthy results have been explained and showed in detail.

Keywords: Carbon footprint, calculation engine, web-based application, environmental pollution

1. Introduction

The ecological balance (environmental balance) is defined as the system that consists of the physical and biological elements of the natural environment and in which the mutual interactions between living and non-living things continue in a way that preserves the general character of the ecosystem [1]. One of the biggest factors in the deterioration of the ecological balance is defined as the traces left in nature because of some activities carried out by humanity while continuing its life, depending on various effects and factors such as the rapid increase in population, industrial and technology activities, global competition, consumption needs, unconscious and unlimited consumption understanding and mentality [2-4]. As a result of these traces, various problems on a global scale such as pollution of the natural environment, depletion of natural resources, global climate change, and increase in barren areas and the threat of extinction by decreasing some species arise. In this context, climate change, which is the most obvious environmental

problem, is caused by greenhouse gas emissions that reach the atmosphere because of human activities [5,6].

In recent years, many models, methods and indicators have been put forward in the quantitative calculation of the sustainability of societies and individuals. The “ecological footprint”, developed to measure the impact of individuals on natural ecosystems and their sustainability levels, is one of these indicator tools [2,7,8]. Depending on human consumption activities, the ecological footprint components are expressed in six basic areas in *Figure 1* as grassland footprint, forest area footprint, fishery area footprint, agricultural land footprint, built area footprint, and carbon footprint [9]. In addition, ecological footprint is defined as the fertile land and water area, biologically expressed in “global hectares” (gha), required to produce the resources consumed by an individual, community, institution, organization or activity and to remove the waste it generates, with current technology and resource management [9].

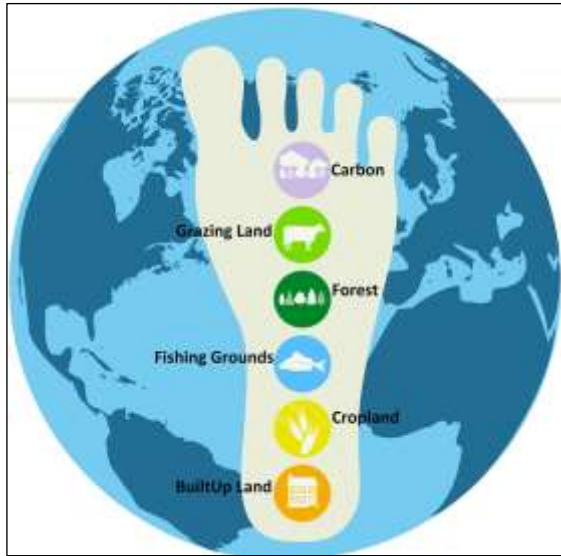


Figure 1. Ecological footprint components [9].

2. Carbon Footprint

The largest component of the ecological footprint is the carbon footprint [10]. As it is the largest component of the total footprint on a global scale, the carbon footprint constitutes the largest component of Turkey's total ecological footprint – 46% (1.24-1.36 gha per capita) [9] as shown in Figure 2. In addition, carbon footprint includes emissions from fossil fuels used in the country, emissions from the production process of products purchased from abroad, the country's share in international trade emissions and non-fossil fuel carbon emissions [9].



Figure 2. Turkey's ecological footprint components [9].

“People” as defined by the “Kyoto Protocol” [6] in Figure 3: leave a trace in nature as a result of the activities they carry out in transportation, heating, shelter, products, services and many other subjects [11]. Moreover, carbon footprint calculations are made in order to provide mandatory or voluntary greenhouse gas commitments of companies, institutions and organizations, to determine their effects on climate change and to participate in emission trading mechanisms.

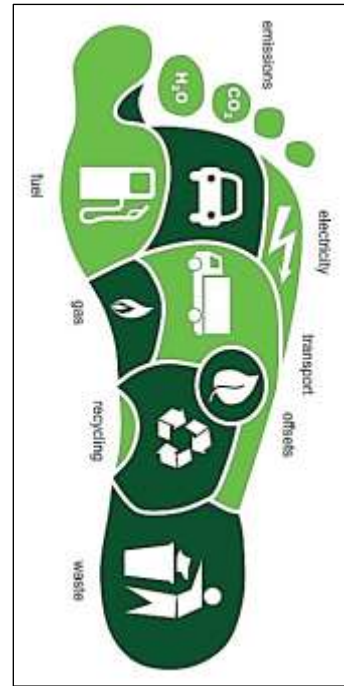


Figure 3. Carbon footprint [11].

In this way, in Table 1 [6] in the following, the greenhouse gases determined within the “Kyoto Protocol” have been shown and explained.

Table 1. Greenhouse gases by Kyoto Protocol [6].

Symbol	Given name	CO ₂	Main sources
CO ₂	Carbon dioxide	1	Combustion of Fossil Fuels, Forest Fires, Cement Production
CH ₄	Methane	21	Landfills, Production and Distribution of Oil and Natural Gas, Digestion of Farm Animals, Fermentation in Systems
N ₂ O	Nitrous oxide	310	Combustion of Fossil Fuels, Fertilizers, Nylon Production
HFC _s	Hydrofluorocarbons	140-11700	Refrigerator Gases, Aluminum Melting, Semi Conductor Production
PFC _s	Perfluorocarbons	6500-9200	Aluminum Production, Semiconductor Production
SF ₆	Sulfur Hexafluoride	23900	Electricity Transmission and Distribution Systems, Magnesium production

The carbon footprint, which can be formed personally and institutionally as a result of people's activities, may be calculated by grouping them in two [12] or three scopes [13-17]. In this context, Scope-1 includes activities that directly create carbon footprints. In this category, there are fossil fuels used by institutions and organizations for heating or energy needs and emissions

created by the fuels of the vehicles within the organization. Also, Scope-2 indirect carbon footprint includes emissions due to steam, cooling or hot water purchased by the institution from another institution or organization, and emissions caused by the electrical energy consumed by the institution. Moreover, Scope-3 is another indirect carbon footprint is the most difficult and troublesome to calculate, which does not have direct emissions from the institution or organization but originates from the activities of the institution. In this way, activities such as outsourced transportation services, emissions from the wastes of the institution or organization, and catering services taken from outside are included in this scope [18]. According to the data of the Wildlife Conservation Foundation [9], the footprint per capita in Turkey is 2.7 (gha). This figure is much more than the world average [19].

In the literature reviews on carbon footprint, which is an important concept in the preservation of ecological balance, studies on this subject in Turkey are more limited than studies conducted abroad, and various studies have been carried out in universities as educational institutions [6, 20-23] and there is no study on this subject in other educational institutions [11]. Furthermore, studies on the subject emphasize the need for the development of education, program and teaching materials and various subject-based applications for reducing carbon footprint values in terms of individual, social and institutional aspects [2].

3. Method

The universe of the study consists of education and training institutions in the city centre of Burdur. In this context, the sample of the research is one of the education and training institutions in the city centre of Burdur, using the convenient/accidental sampling method, considering that the sample is easily accessible and practical due to the limitations in terms of time, money and labour [24]. In *Figure 5*, the general boundaries of the educational institution, which has been considered as a sample, have been indicated visually. Also, the study has been done and carried out by applying the following steps in *Figure 4*.

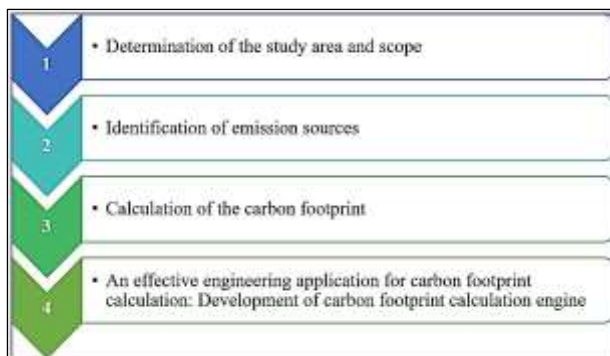


Figure 4. Steps for calculating carbon footprint.



Figure 5. The general boundaries of the education institution in Burdur [25].

The study, whose general boundaries have been indicated in *Figure 5*, located in the centre of Burdur, has been carried out. As of 2019-2020 academic year, there have been 27 school staff – 21 staff members, 2 administrators, 1 civil servant, 2 service personnel and 1 security – 244 students – primary, secondary, high school – in total. In addition, the distance of the institution to the city centre of Burdur is approximately 4.5 kilometres.

Emissions arising from the activities carried out directly or indirectly by the educational institution in the study are listed in the following:

Scope-1: Various sources that directly emit greenhouse gas emissions from the organization itself.

Scope-2: Emissions to the atmosphere associated with indirect consumption of energy such as purchased electricity, heat, steam and cooling.

Scope-3: Emissions arising from the activities of the organization but not under the control of the organization and caused by various sources that cannot be classified as Scope-2 emissions.

Within the framework of the scopes explained above, the emissions created by the natural gas consumption of the institution for fuel within Scope-1; electricity consumption for electrical energy within Scope-2; emissions arising from the transportation of students and employees (teachers, civil servants, servants, security guards, etc.) and water consumption are evaluated within Scope-3. However, it is not included in the carbon footprint measurement due to the lack of food service and consumption and the lack of data on chemicals/consumables purchased.

Scope-1, natural gas used for heating; Scope-2, electricity consumption; and Scope-3, it possible to calculate the data on water consumption annually and in order to provide more realistic information, the data of 2019 have been included in the scope of the study. In addition, the data of the institution regarding the emission sources included in the scope of the examination and research have been obtained from the institution administration on the basis of the relevant invoices. Moreover, private personal cars used for the transportation of students and employees (teachers, civil

servants, servants, security guards, etc.), and service vehicles in public transportation considered within Scope-3, have been determined and the emissions caused by these have been found out, revealed and calculated in detail.

4. Carbon Footprint Calculation Engine

In order to apply the carbon footprint calculation engine, the work-flow diagram has been determined and the study has been revealed and carried out in this way. Within the framework of this schedule – in Figure 6 –, the application has been planned, designed, developed, necessary tests have been carried out, the writing has been completed and then implemented into the life.

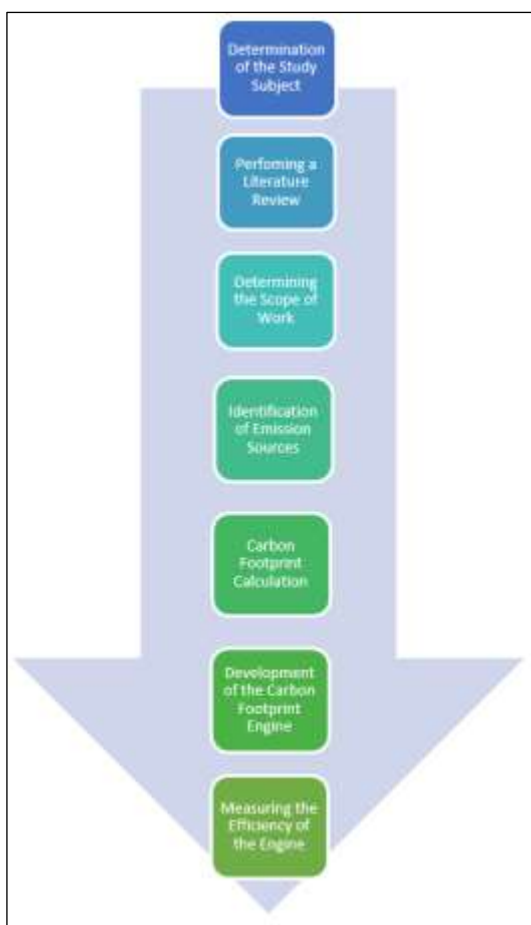


Figure 6. The schedule in work-flow diagram.

Scientific formulas for calculating and finding carbon emission values [11,26] have been explained in the following, and a carbon footprint calculation engine – application – has been designed and developed in the line with these specific formulas (formula 1 to 9).

$$EtCO_2/year \text{ (natural gas)} [11] \quad (1)$$

$$= (((\text{Natural gas usage (m}^3) * 0.67) * 0.001) * (56100 * 0.001) * 48 * 1) * 0.001$$

0,67=Average Density; 0,001=kg-ton; 56100=Emission Factor; 0,001=kg-ton; 48=Oxidation Factor; 1=Oxidation Factor; 0,001=ton-Gg

$$EtCO_2/year \text{ (electricity)} [11] \quad (2)$$

$$= ((\text{Electricity consumption (kWh)} * 0.4603 * 0.133) + (\text{Electricity consumption (kWh)} * 0.4603)) * 0.001$$

0,4603=Emission Factor; 0,133=Loss Factor; 0,4603= Emission Factor; 0,001=10⁻³

$$EtCO_2/year \text{ (gasoline liter)} [11] \quad (3)$$

$$= (((\text{Gasoline usage (liter)} * 0.735) * 0.001) * (69300 * 0.001) * 44.3 * 1) * 0.001$$

$$EtCO_2/year \text{ (gasoline km)} [11] \quad (4)$$

$$= (((\text{kilometer}/100) * 7.5 * 0.735) * 0.001) * (69300 * 0.001) * 44.3 * 1) * 0.001$$

0,735= Average Density; 0,001=kg-ton; 69300= Emission Factor; 0,001=kg-ton; 44,3= Oxidation Factor; 1= Oxidation Factor; 0,001=ton-Gg

$$EtCO_2/year \text{ (diesel liter)} [11] \quad (5)$$

$$= (((\text{Diesel use (liter)} * 0.83) * 0.001) * (74100 * 0.001) * 43 * 1) * 0.001$$

$$EtCO_2/year \text{ (diesel km)} [11] \quad (6)$$

$$= (((\text{kilometer}/100) * 7.5 * 0.83) * 0.001) * (74100 * 0.001) * 43 * 1) * 0.001$$

0,83= Average Density; 0,001=kg-ton; 74100= Emission Factor; 0,001=kg-ton; 43= Oxidation Factor; 1= Oxidation Factor; 0,001=ton-Gg

$$EtCO_2/year \text{ (water)} [11] \quad (7)$$

$$= (\text{Water consumption (m}^3) * 0.0014$$

0,0014= Emission Factor

$$EtCO_2/year \text{ (public transportation)} [11] \quad (8)$$

$$= (((((\text{Kilometer} * 0.13)/\text{number of people}) * 0.830 * 0.001) * (74100 * 0.001) * 43 * 1) * 0.001) * \text{number of people}$$

0,13=Diesel use; 0,830= Average Density; 0,001=kg-ton; 74100= Emission Factor; 0,001=kg-ton; 43= Oxidation Factor; 1= Oxidation Factor; 0,001=ton-Gg

$$\text{Number of Trees to be Planted Against Carbon Emission} [27] \quad (9)$$

$$= \text{Total Carbon Footprint (Ton)} / (((24 * 2.3) * 365) * 0.001)$$

While developing the carbon footprint calculation engine, Visual Studio Code platform (IDE) has been used in the web-based application. Also, PHP, HTML, CSS and JavaScript languages have been used through this platform. In addition, the main part of the site has been written in PHP, and CSS has been used for the design part. Moreover, functions for carbon footprint calculation formulas have been developed with the JavaScript language. Furthermore, HTML has been used for the basic texts on the site. In addition, in order to prevent errors in user input, relevant commands have been written so that character entries and number entries with minus (-) values that should not be in formulas have not been accepted. Before the designed and

developed site has been opened to internet access, necessary trials and tests have been carried out and applied in the local environment via the AppServ server. As a result of the successfully completed tests, the necessary domain (domain name) and hosting (domain service) transactions have been made and the engine link address <http://karbon-ayakizi.com/> (this site has been in active use between January 2020 and January 2021, but it is currently inactive) has been opened to internet access. Also, the interface for obtaining the necessary data from the user on the developed site has been showed in *Figure 7*; the interface for writing the outputs to the screen has been given in *Figure 8*; the interface for calculating the tree to be planted depending on the outputs has been showed in *Figure 9*. In addition, in *Figure 10* in the following, the source code fragment of the index of the developed site has been given in detail.

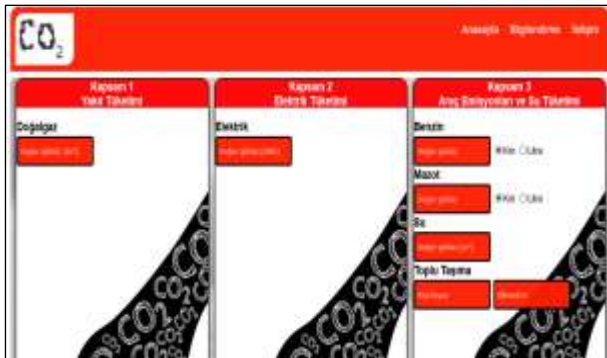


Figure 7. Interface for inputs in the site.



Figure 8. Interface for outputs via calculate button.



Figure 9. Interface for tree calculation via see button.

```

<!-- Header -->
<meta charset="utf-8">
<meta name="viewport" content="width=device-width, initial-scale=1">
<link href="static/style.css" type="text/css" rel="stylesheet">
<!-- /Header -->
<!-- Main Content -->
<div class="body">
  <div class="row">
    <form action="" method="POST">
      <div class="form-body">
        <div class="form-row">
          <div class="form-group">
            <input type="text" value="" class="form-control" placeholder="Doğalgaz (m3)"/>
          </div>
        </div>
        <div class="form-row">
          <div class="form-group">
            <input type="text" value="" class="form-control" placeholder="Elektrik (kWh)"/>
          </div>
        </div>
        <div class="form-row">
          <div class="form-group">
            <input type="text" value="" class="form-control" placeholder="Benzin (litre)"/>
          </div>
          <div class="form-group">
            <input type="text" value="" class="form-control" placeholder="Mazot (litre)"/>
          </div>
          <div class="form-group">
            <input type="text" value="" class="form-control" placeholder="Su (m3)"/>
          </div>
          <div class="form-group">
            <input type="text" value="" class="form-control" placeholder="Toplu Taşıma (Kisi-km)"/>
          </div>
        </div>
        <div class="form-row">
          <div class="form-group">
            <input type="button" value="Hesapla" class="btn btn-primary"/>
          </div>
        </div>
      </div>
    </form>
  </div>
  <div class="row">
    <div class="col">
      <table border="1">
| Kapsam | Doğalgaz | Elektrik | Benzin | Mazot | Su | Toplu Taşıma |
| --- | --- | --- | --- | --- | --- | --- |
| Kapsam 1 | 18.042 Ton | 5.215 Ton | 1.892 Ton | 26.446 Ton | 14 Ton | 6.595 Ton |
| Toplam | 73.991 Ton | | | | | |

```

Figure 10. Source code fragment of the site index.

5. Important Findings Regarding the Carbon Footprint Calculation Engine

In the study carried out in the 2019-2020 academic year, based on the 2018-2019 academic year, it has been stated that the natural gas consumption within Scope-1 has been approximately annually 38,000 m³ (as a result of the findings obtained from the monthly natural gas bills) in the light of the findings summarized in *Table 2* below, and it has been concluded that this consumption caused 69 tons of carbon emissions. In addition, when the electricity consumption in the Scope-2 calculation has been examined, it has been determined that the annual average is 19.000 kWh (as a result of the amounts obtained from the monthly electricity bills), and it has been stated that this electricity consumption causes around 10 tons of carbon emissions. Furthermore, when the annual use of gasoline and diesel products within Scope-3 has been examined, it has been calculated that these have been approximately 12,500 liters (~169,000 km, 30 gasoline cars in total) and 14,000 liters (~187,000 km, 28 diesel cars in total), respectively. It has been revealed that a total of 68 tons of carbon emissions have been exposed to the environment. Moreover, it has been stated that the annual water consumption and usage, which has been also included in Scope-3, has been approximately 1,600 m³ (in the light of the usage calculations obtained from the monthly water bills), and it has been calculated that it has caused around 2 tons of carbon emissions. When looked at the last parameter in Scope-3, which has been public transportation, it has been calculated that the vehicles serving the school travel an average of 200,000 km (23 diesel-powered public transportation vehicles for 20 people) annually and has caused approximately 69 tons of carbon emissions. In the light of the data that emerged, it has been concluded that the education institution within the province of Burdur has caused a total of about 216 tons of carbon emissions in the 2019-

2020 academic year - based on the 2018-2019 academic year – in Scope-1, Scope-2 and Scope-3 frameworks. Also, it has been calculated that approximately 11 trees (based on the rates specified in the TEMA foundation [27]) have been needed to control this emission and capture carbon. In this context, the carbon emission findings obtained as a result of the calculations have been summarized in *Table 2* in the following.

Table 2. Total carbon emission of the education institution in Burdur province.

Annually	Scope-1	Scope-2	Scope-3				Total
	Natural gas	Electricity	Gasoline	Diesel	Water	Public Transport	
Consumption/Use	38272 m ³	19173.48 kWh	12672 L	13962 L	1586 m ³	290834.4 km	215.83 ton EitCO ₂ /year
Output	69.05 ton	9.99 ton	28.59 ton	36.92 ton	2.22 ton	69.05 ton	
Total	69.05 ton	9.99 ton	136.78 ton				

6. Conclusion and Discussion

In the study, a web-based carbon footprint calculation engine has been designed and developed. In addition, the carbon footprint of an education institution located in the city centre of Burdur has been calculated as a real case study. In the light of the calculations made and the results obtained, the annual carbon emission of the education institution in Burdur province due to the fuel (natural gas) used for heating the institution in Scope-1 has been 69.05 tons; in Scope-2 the annual carbon emission due to electricity consumption has been 9.99 tons; in Scope-3, annual carbon emission based on vehicle emissions (gasoline and diesel) and water consumption has been 136.78 tons. Finally, the annual total carbon emission value of the institution has been 215.83 tons. In this context, it has been determined that at least 11 adult trees have to be located within the general boundaries of the institution for the absorption of this carbon value, according to the equation and the formula set by TEMA Foundation [27].

In addition to these, the study has provided both the calculation of the carbon footprint (individual and institutional) and the demonstration of how the damage to the environment could be improved – especially with tree planting. In this respect, a face-to-face meeting was held with the Burdur Forestry Operations Directorate within the scope of the study regarding the reduction of carbon emissions by planting trees and it was promised that planting could be done in each year in the areas included in the afforestation program. Also, some discussions on climate change were held at the World Economic Forum held in Davos, Switzerland on January 24, 2020, and it was set to goal of growing 1 trillion trees [28]. In this context, it has been clearly observed that the conducted research and the presented work have been valid and meaningful both in national and international framework. Within the scope of the study, the site <http://karbon-ayakizi.com/> (this site has been in

active use between January 2020 and January 2021, but it is currently inactive) has been designed and developed, and its effectiveness and trustworthy results have been showed with a specific case study.

7. Future Works

The designed and developed website <http://karbon-ayakizi.com/> has been extracted, created and emerged within the framework of case analysis based on the parameters that have been included in Scope-1, Scope-2 and Scope-3 that may cause carbon emissions within the framework of the carbon footprint of the education institution in Burdur province. In addition, it has been aimed to get a general domain name related to the site, and to enable people to reach it quickly and comfortably on the internet, and it has been also aimed to move forward in a forward-looking, cumulative and collective way that has been open to development and improvement. With the addition of all the parameters used in the carbon footprint calculation of this study, which emerged with a case analysis, in the light of the scientific formulas in the academic world, all users (individuals, institutions, organizations, companies, foundations, etc.) will calculate their own carbon footprints and as a result, it will be that people become more conscious (environmental, social, societal, etc.) related tree calculation, nature and environment. In addition to this goal, it will be able to create a large data set in the light of the information to be obtained. Moreover, various purposes related to the data set to be obtained with the help of artificial intelligence, machine learning and deep learning algorithms and methods, which are developed on the basis of mathematics, and which are very popular in the informatics world these days and will not lose their importance for many years. With the contribution of these techniques, operations such as classification, clustering, advice, prediction and ordering will be applied and carried out in this carbon footprint study in the future. In this context, the study will be able to calculate the carbon footprint (private & general), specify the required tree planting, and present a purposeful and detailed report in the light of the available data and information.

Acknowledgement

Thanks to the education institution located in the city centre of Burdur for doing a real case study and analysis in the carbon footprint engine in this study.

Author's Contributions

Mustafa Batar: Did all the work in the study (did literature review, created calculation engine, designed and developed application, did analysis and case study, did paper formatting, etc.)



Ethics

Author declares that there are no ethical issues related to publication of this manuscript. The performed study is out of scope of any ethical issues.

References

- [1]. Çepel, N. 1992. Elmalı sedir ormanlarının ekolojik önemi. *İstanbul Üniversitesi Orman Fakültesi Dergisi*; 42: 1-8.
- [2]. Ertekin, P. 2012. *Sürdürülebilir kaynak kullanımına yönelik çevre eğitimi uygulamalarının ilköğretim öğrencilerinin karbon ayak izi konusunda bilinçlenmeleri üzerine etkisi*. Yüksek Lisans Tezi, Muğla Sıtkı Koçman Üniversitesi Eğitim Bilimleri Enstitüsü, Muğla.
- [3]. Özer, B. 2012. *Türkiye elektrik sektöründe CO2 emisyonu azaltma potansiyeli üzerine senaryo analizleri*. Doktora Tezi, İstanbul Teknik Üniversitesi Fen Bilimleri Enstitüsü, İstanbul.
- [4]. Özsoy, C. E. 2015. Düşük karbon ekonomisi ve Türkiye'nin karbon ayak izi. *HAK-İŞ Uluslararası Emek ve Toplum Dergisi* 4: 198-215.
- [5]. Rana R., Ingraio C., Lombardi M., Tricase C. 2016. Greenhouse gas emissions of an agro-biogas energy system: Estimation under the renewable energy directive. *Science of The Total Environment*; 550:1182-1195.
- [6]. Özçelik, G. (2017). *Çanakkale Onsekiz Mart Üniversitesi Terzioğlu Kampüsü'nün enerji ve karbon ayak izi açısından değerlendirilmesi*. Yüksek Lisans Tezi, Çanakkale Onsekiz Mart Üniversitesi, Çanakkale.
- [7]. Jia, J., Zhao, J., Deng, H., Duan, J. 2010. Ecological footprint simulation and prediction by ARIMA model-A case study in Henan Province of China. *Ecological Indicators*; 10: 538-544.
- [8]. Lei, K., Hu, D., Wang, Z., Yu, Y., Zhao, Y. 2009. An analysis of ecological footprint trade and sustainable carrying capacity of the population in Macao. *The International Journal of Sustainable Development and World Ecology*; 16: 127-136.
- [9]. WWF, 2012. Türkiye'nin Ekolojik Ayak İzi Raporu. https://www.footprintnetwork.org/content/images/article_uploads/Turkey_Ecological_Footprint_Report_Turkish.pdf (accessed at 31.07.2021).
- [10]. Borucke, M., Moore, D., Cranston, G., Gracey, K., Iha, K., Larson, J., Lazarus, E., Morales, J. C., Wackernagel, M., Galli, A. 2013. Accounting for demand and supply of the biosphere's regenerative capacity: The National Footprint Accounts' underlying methodology and framework. *Ecological Indicators*; 24: 518-533.
- [11]. Üreden, A. 2019. *Sürdürülebilir yaşam için karbon ayak izi (Çankırı Karatekin Üniversitesi örneği)*. Yüksek Lisans Tezi, Çankırı Karatekin Üniversitesi Fen Bilimleri Enstitüsü, Çankırı.
- [12]. Jones, C. M., Kammen D. M. 2011. Quantifying carbon footprint reduction opportunities for U.S. households and communities. *Environmental Science and Technology*; 45: 4088-4095.
- [13]. Adanalı, K. Carbon management and model applications. 7th International Ankiros Foundry Congress, İstanbul, Turkey, 2014.
- [14]. Bekiroğlu, O. Sürdürülebilir kalkınmanın yeni kuralı: Karbon ayak izi. II. Elektrik Tesisat Ulusal Kongresi, İzmir, Türkiye, 2011.
- [15]. Kitzes J., Peller A., Goldfinger S., Wackernagel M., 2007. Current methods for calculating national ecological footprints accounts. *Science for Environment and Sustainable Society*; 4: 1-9.
- [16]. Mutlu, V., Özgür, C., Kaplan Ş. 2018. Determination of carbon footprint in rubber industry. *Bilge International Journal of Science and Technology Research*; 2: 139-146.
- [17]. Üreden, A., Özden, S. 2018. Kurumsal karbon ayak izi nasıl hesaplanır: teorik bir çalışma. *Anadolu Orman Araştırmaları Dergisi*; 4: 98-108.
- [18]. Turanlı, A. M. 2015. *Estimation of carbon footprint: A case study for Middle East Technical University*. MSc thesis, Middle East Technical University Graduate School of Natural And Applied Sciences, Ankara.
- [19]. WWF, Ekolojik ayak izi. https://www.wwf.org.tr/basin_bultenleri/raporlar/yaayan_gezegen_raporu/yasayangezegenraporu2014/ekolojikayakizi/ (accessed at 31.07.2021).
- [20]. Başoğul, Y. 2019. Determining the ecologic and carbon footprints of Adiyaman University faculty of engineering students. *The International Journal of Engineering and Science*; 8: 46-52.
- [21]. Eren, Ö., Parlakay, O., Hilal, M., Bozhüyük, B. 2017. Ziraat Fakültesi akademisyenlerinin ekolojik ayak izinin belirlenmesi: Mustafa Kemal Üniversitesi örneği. *Gaziosmanpaşa Üniversitesi Ziraat Fakültesi Dergisi*; 34: 138-145.
- [22]. Keleş, Ö. 2007. *Sürdürülebilir yaşama yönelik çevre eğitimi aracı olarak ekolojik ayak izinin uygulanması ve değerlendirilmesi*. Doktora Tezi, Gazi Üniversitesi Eğitim Bilimleri Enstitüsü, Ankara.
- [23]. Yaka, İ. F., Koçer, A., Güngör, A. 2015. Akdeniz University health services vocational determination of carbon footprint. *Electronic Journal of Machine Technologies*; 12: 37-45.
- [24]. Büyüköztürk, Ş., Çakmak, E., Akgün, Ö. E., Karadeniz, Ş., Demirel, F. 2018. *Eğitimde Bilimsel Araştırma Yöntemleri*. Ankara: Pegem Akademi.
- [25]. Google Maps, Burdur. <https://www.google.com/maps/place/Burdur,+Burdur+Merkez%2FBurdur/@37.7325713,30.2474,13z/data=!3m1!4m5!3m4!1s0x14c42c1038052bdd:0x7f33fbee17399f8b!8m2!3d37.718336!4d30.282333> (accessed at 20.02.2020).
- [26]. IPCC, Guidelines for National Greenhouse Gas Inventories. <https://www.ipcc-nggip.iges.or.jp/public/2006gl/index.html> (accessed at 31.07.2021).
- [27]. TEMA, TEMA diyor ki; ağaç dakin, küresel ısınmaya el koyun. <https://www.tema.org.tr/basin-odasi/basin-bultenleri/tema-diyor-ki-agac-dikin-kuresel-ismmaya-el-koyun> (accessed at 31.07.2021).
- [28]. INDEPENDENT Türkçe, Davos 2020 sona erdi: İklim değişikliğinin nasıl ele alınacağına dair kafa karışıklığı sürüyor. <https://www.indyturk.com/node/122876/d%C3%BCnya/davos-2020-sona-erdi-iklim-de%C4%9Fi%C5%9Fikli%C4%9Finin-nas%C4%B1-ele-al%C4%B1naca%C4%9F%C4%B1n-dair-kafa> (accessed at 31.07.2021).

Self-tuning Fuzzy PID Controller Design and Energy Management in DC Microgrid: Standalone and Grid Connected Mode

Ahmet Kaysal^{1*} , Selim Koroğlu² , Yüksel Oğuz³ 

¹Department of Electrical Engineering, Afyon Kocatepe University, Afyonkarahisar, Turkey.

²Department of Electrical Electronics Engineering, Pamukkale University, Denizli, Turkey.

³Department of Electrical Electronics Engineering, Afyon Kocatepe University, Afyonkarahisar, Turkey.

*akaysal@aku.edu.tr

*Orcid: 0000-0002-4142-0840

Received: 28 November 2020

Accepted: 28 November 2022

DOI: 10.18466/cbayarfbe.832874

Abstract

This paper presents a control system and energy management strategy (EMS) with a standalone and grid-connected mode in the microgrid. The microgrid is energized by distributed energy resources (DER) such as photovoltaic panels, wind turbines and lithium-ion batteries. The controller structure for regulating the voltage regulation in this microgrid consisting of renewable energy sources and an energy storage system is covered. Overshoot, rise time, settling time performances of designed self-tuning fuzzy proportional-integral-derivative (SFPID) controller and conventional proportional-integral-derivative (PID) controller examined comparatively. In addition, an EMS has been proposed for loads that fed in the microgrid. Here, the aim is to make maximum use of RESs as much as possible, maintain voltage regulation, and ensure continuity in the feeding of the critical load. The system switches between the standalone and grid-connected modes if necessary. A model of the microgrid's dynamic behavior is constructed, and it is simulated in the MATLAB[®]/Simulink environment. The proposed SFPID controller stabilizes the bus voltage and frequency oscillations within the allowable tolerance limits in a short time despite the disturbance effects on the generation and load side.

Keywords: Energy management system, fuzzy controller, microgrid, renewable energy system.

1 Introduction

In traditional power systems, energy production methods are largely based on fossil fuels, and the negative effects of these fuels on the environment have become quite alarming. In these systems, central power plants are preferred to meet the energy needs of consumers, and the network structure is interconnected. Therefore, high voltage transmission lines are required during the transmission of energy to the consumption centers. This is the reason for investment costs increase and transmission losses. The production of clean energy in distributed energy resources (DER) based on renewable energy systems (RES), such as photovoltaics (PV) and wind energy (WT), plays an important role due to the positive impact on the environment [1, 2]. In recent years, microgrid (MG) structures fed with alternative energy sources have been raised. The MG system has efficiency, ease of control, and network integration.

MGs are small community networks, and they have attracted much attention in recent years due to their advantages, such as reducing power losses in transmission lines, achieving maximum utilization from RES, and providing reliable energy to consumers. Typical MGs include PV arrays, WTs, energy storage systems (ESS), power DC/DC converters, DC/AC inverters, and local loads that can operate standalone or grid-connected mode in power systems [3]. MGs, which can operate both connected to the main grid and independent of the grid, have proven to be efficient in eliminating the negative effects of intermittent energy generation depending on weather and environmental conditions [4].

MGs are vital for managing existing energy sources, frequency and voltage control, and the smooth and optimum operation of the existing network. In an energy system, it is necessary to keep the amplitudes of the voltage of the load buses within certain operating limits in both steady-state and transient voltage stability events. In the literature, many methods such as fuzzy

logic controller [5], self-tuning fuzzy PI/PID (SFPID) controller [6-9], adaptive neuro-fuzzy controller [10], conventional PID controller [11], predictive power and voltage control [12, 13] are recommended for voltage control in MG. In addition, energy management and optimization have become the focus of research conducted on MGs. The control methods used in the optimum operation of MGs can generally be grouped into four classes such as centralized [14], decentralized [15], distributed and hierarchical control methods [16-18]. Three-level hierarchical control methodology is widely used, including primary, secondary and tertiary control levels [19, 20]. Ziouani et al. [21], a control strategy based on a hierarchical approach, is presented to operate MG, which continuously switches between island mode and grid-connected modes. In order to regulate the output voltage, the inner control is used to improve the stability in the primary control, amplitude, and frequency for active and reactive power-sharing. Mohamed et al. [22] developed a tertiary control algorithm for DC MG, and a laboratory-scale test was performed experimentally.

In this paper, the SFPID controller has been suggested to minimize voltage oscillations in a MG consisting of RES and ESS and improve the voltage response of the system. The designed controller is compared with the conventional PID controller. Furthermore, an energy management strategy (EMS) has been proposed to regulate power flow in MG. The suggested EMS ensures that the voltage and frequency in the MG are maintained at the specified limits and switches between the standalone and the grid-connected modes to ensure continuity in the supply of the critical load.

2 Configuration and Modeling of the Microgrid

PV arrays and WTs based on permanent magnet synchronous generators (PMSG) form renewable energy sources in the MG structure. A battery pack is available to provide the needed power in cases where the generated power cannot meet the load demand. Also, MG includes power electronic converters and dynamic loads used as interfaces in connecting these sources to the DC bus. These components are connected through a DC bus, as shown in Figure 1.

A 400V DC bus is created for RES and ESS. A converter is used when connecting the PV system to the DC bus. The wind turbine based on a PMSG is first converted to DC with the help of a three-phase rectifier and then connected to the DC bus via the boost converter. Here, taking changes in bus voltage and power as a reference and with the control of the boost converter, RES is worked at the maximum power point (MPP). The ESS is connected to the DC bus via the

bidirectional converter to perform charging and discharging according to the state of the energy. The SFPID controller has been suggested to minimize voltage oscillations between MG and AC loads and improve the system's voltage response. The EMS's integration among source, load, and network is carried out according to the priority of the loads. If the resources are insufficient to feed the critical load, the grid-connected mode is switched.

In the suggested MG structure, the total load is 9 kW and the critical power (P_{cr}) is defined as 2.5 kW, load2 (P_{L2}) 3.5 kW and load3 (P_{L3}) 3 kW. The installed power capacity of the system is a total of 11.1 kW, including PV generation system 6.1 kW and WT generation system 5 kW. The energy capacity of the ESS unit used as a storage device in the system is determined as 6 kWh.

2.1. Photovoltaic System

PV systems are one of the most important RES and convert irradiant energy directly into electrical energy. Since the electrical energy obtained from the PV system will vary depending on the sun's position, clouds and temperature changes, the operation of PV arrays at the MPP is important for system efficiency. In the boost converter structure, perturb and observe (P&O) technique provides working at the MPP. Figure 2 shows the boost converter structure, and Table 1 shows the electrical characteristic of the PV module.

Table 1. Electrical characteristics of the photovoltaic module (25 °C and 1000 W/m²).

Description	Symbol	Value
Maximum power (W)	P_{max}	305.23
Open circuit voltage (V)	V_{oc}	64.2
Voltage at MPP (V)	V_{mpp}	54.7
Cells per module	N_{cell}	96
Short-circuit (A)	I_{sc}	5.96
Current at MPP (A)	I_{mpp}	5.58
Diode saturation current (A)	I_0	$1.36e^{-11}$
Shunt resistance (Ω)	R_{sh}	420.55
Series resistance (Ω)	R_s	0.3778

The PV system consists of 20 modules, five parallel strings and four serial modules per string. As seen in the relationship between the P-V and I-V curves of the PV arrays in Figure 3, the installed capacity of the PV arrays is 25 °C cell temperature and 6105 W in the irradiance of 1 kW/m². The output voltage of the PV arrays from 218.8 V is increased to 400 V DC bus voltage with the boost converter.

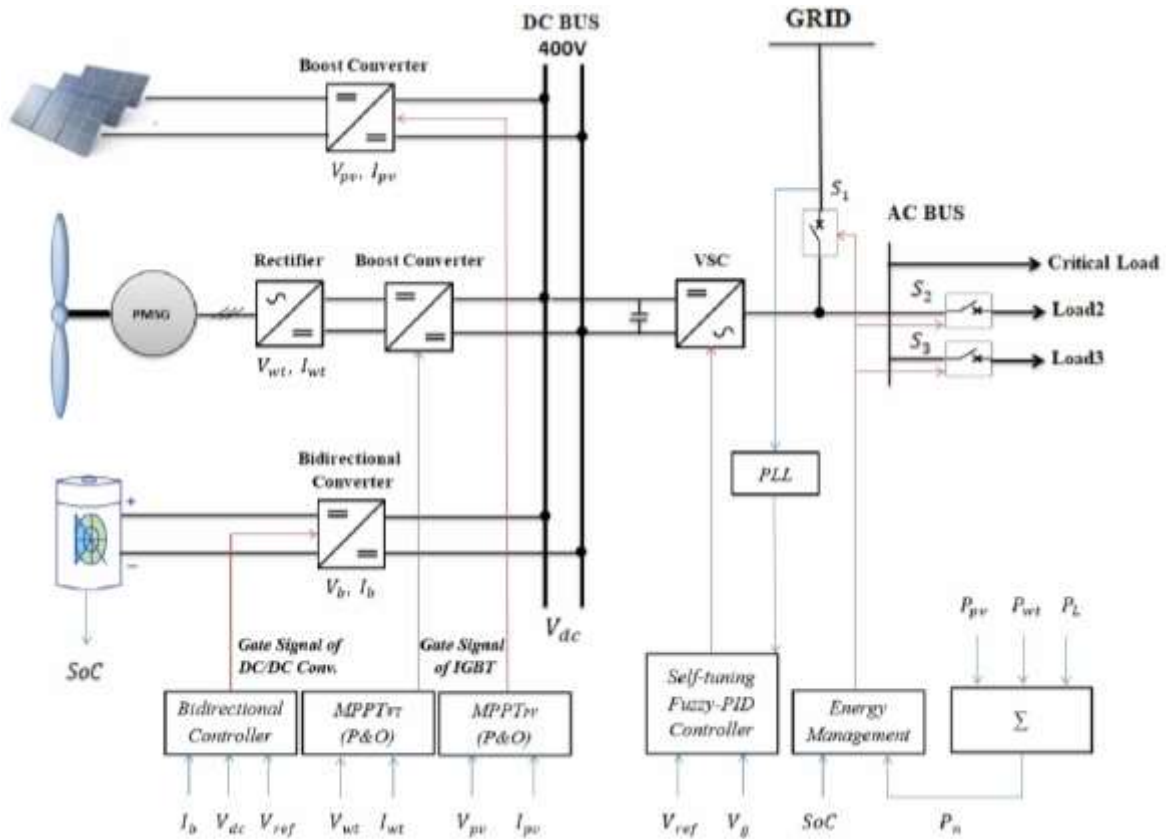


Figure 1. Microgrid power system architecture.

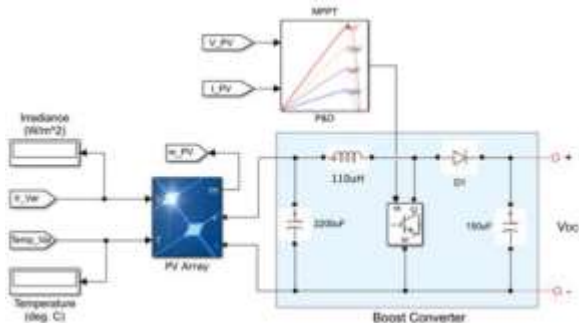


Figure 2. PV array and boost converter structure.

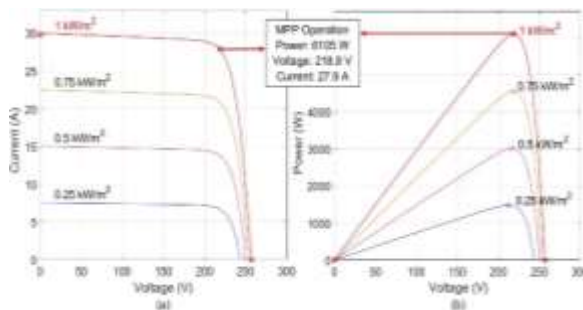


Figure 3. (a) I-V and (b) P-V curves of the solar simulator in 1 kW/m^2 irradiation.

2.2. Wind Energy System

One of the other essential RES is wind turbines. Many types of generators are used in wind turbines. One of them is PMSGs, which can be used directly in wind turbines without a gear system. For this generator type, the rotor magnetic flux is generated by permanent magnets; therefore, it has no brush mechanism. Since there are no rotor windings, there are no winding losses, and a high-power density can be achieved [23]. The WT, diode rectifier and MPPT controlled converter structure are shown in Figure 4. The technical characteristics of the PMSG are listed in Table 2.

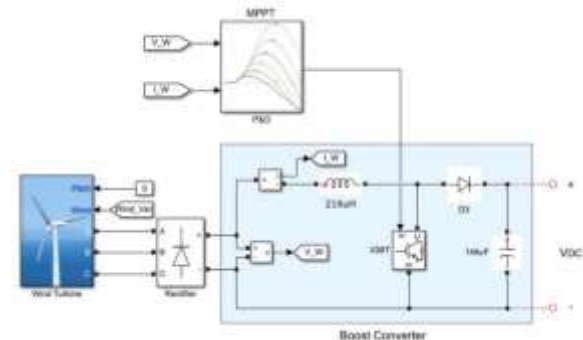


Figure 4. Wind turbine and boost converter structure.

Table 2. Technical characteristics of the PMSG.

Description	Symbol	Value
Nominal PMSG power (W)	P_n	5000
Nominal voltage (L-L) (V)	V_n	425
Stator resistance (Ω)	R_s	0.0918
Stator inductance (mH)	L_s	0.975
No. of pole pairs	p	4
Flux linkage (V.s)	ϕ_f	0.1688
Viscous damping (N.m.s)	F	0.0004924
Moment of inertia (kg. m ²)	J	0.003945

2.3. Energy Storage System

The ESS is connected to MG's DC bus with a bidirectional converter. The energy surplus obtained from RES and not used on the load side is stored in ESS. Energy stored is used to meet the demand of the load when the network is not sufficient or the network is not available. Thus, both the critical loads are not de-energized, and the control of the voltage and frequency components is provided within limits. According to the Coulomb Counting method, SOC is given in Equation (2.1).

$$SOC(t) = SOC(t - 1) + \int_0^t \frac{I_b}{C_b} dt \quad (2.1)$$

Where $SOC(t - 1)$ is the initial value of SOC right before I_b battery current is applied to the battery cell, C_b is the capacity of the battery and time t of the battery. Charging the battery is performed according to the limits determined in the control algorithm. These limits are important for the safety of the battery and are given in Equation (2.2).

$$SOC_{min} \leq SOC \leq SOC_{max} \quad (2.2)$$

SOC_{min} and SOC_{max} are the minimum and maximum charge states of the battery. These values are determined as 20% and 100%, respectively. The ESS structure is given in Figure 5, and the used system's technical characteristics are given in Table 3.

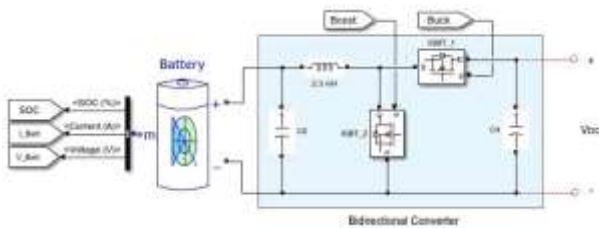


Figure 5. Battery and bidirectional converter structure.

Table 3. Technical specifications of the ESS.

Description	Symbol	Value
Maximum capacity (Ah)	Q	30
Nominal voltage (V)	V_n	200
Fully charged voltage (V)	V_f	232.8
Cut-off voltage (V)	V_c	150
Internal resistance (Ω)	R_i	0.0667
Nominal discharge current (A)	I_d	13.04

3. Voltage Source Converter and SFPID controller

The voltage source converter (VSC) converts the DC input voltage to a symmetrical AC output voltage at the desired amplitude and frequency. The inverter gain, also known as the modulation index, can be defined as the ratio of the AC output voltage to the DC input voltage [24]. The adjustable output voltage is obtained by controlling this gain parameter in the inverter with the suggested SFPID. The block diagram based on the SFPID controller is given in Figure 6.

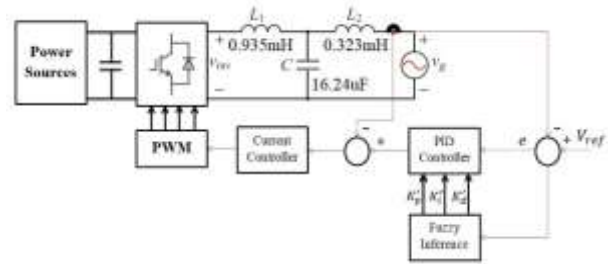


Figure 6. Block diagram of SFPID controller.

The feedback error of the fuzzy inference system is e and the derivative of the error is Δe . They are given in Equations (3.1) and (3.2).

$$e(t) = V_{ref}(t) - V_g(t) \quad (3.1)$$

$$\Delta e(t) = e(t) - e(t - 1) \quad (3.2)$$

Where $V_{ref}(t)$ represents reference input, $V_g(t)$ represents output signal. Feedback error e and Gaussian membership functions are used during the fuzzification of the derivative of the error Δe , and it is represented in Equation (3.3) [25].

$$f(x; \sigma, c) = \exp\left(-\frac{(c - x)^2}{2\sigma^2}\right) \quad (3.3)$$

Where the width of the fuzzy set is σ and the center of fuzzy set c . Thus, the input data e and Δe are converted to the appropriate linguistic value using the fuzzy Mamdani inference model. The fuzzy inference system linguistic variables are organized as negative big (NBB),

positive big (PBB), negative small (NSS), positive small (PSS) and zero (ZR). Rule bases are given in Table 4, and Table 5 and membership functions for input and output variables are given in Figure 7. In the next step of the fuzzy inference system, K_p' , K_d' and K_i' outputs are determined according to the rule base defined in Table 4 and Table 5. As an example;

IF $e(t)$ is NBB and $\Delta e(t)$ is ZR THEN K_p is PSS, K_d is NSS and K_i is NSS. All other cases are described similarly.

Table 4. The rule base of K_p and K_d

$e \setminus \Delta e$	NBB	NSS	ZR	PSS	PBB
NBB	PBB	PBB	PSS	PSS	ZR
NSS	PBB	PSS	ZR	ZR	NSS
ZR	PBB	ZR	ZR	ZR	NBB
PSS	PSS	ZR	ZR	NSS	NBB
PBB	ZR	NSS	NSS	NBB	NBB

Table 5. The rule base of K_i

$e \setminus \Delta e$	NBB	NSS	Z	PSS	PBB
NBB	NBB	NBB	NSS	NSS	ZR
NSS	NBB	NSS	ZR	ZR	PSS
ZR	NBB	ZR	ZR	ZR	PBB
PSS	NSS	ZR	ZR	PSS	PBB
PBB	ZR	PSS	PSS	PBB	PBB

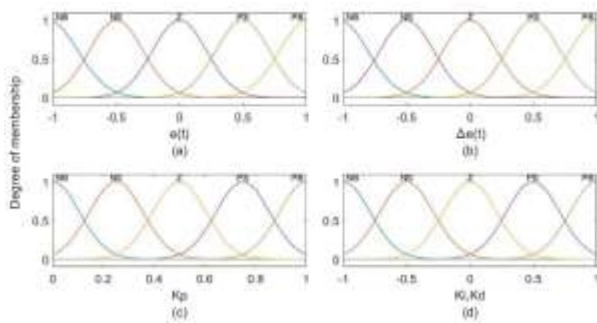


Figure 7. Gaussian membership functions for input variable (a) $e(t)$ (b) $\Delta e(t)$ and output variable (c) K_p gain (d) K_i and K_d gain.

Finally, the fuzzy output is converted to a sharp control signal in the defuzzification process. The centroid method defined in Equation (3.4) is used during this process.

$$x = \frac{\sum_{i=1}^n x_i \cdot \mu(x_i)}{\sum_{i=1}^n \mu(x_i)} \quad (3.4)$$

Where, x is the defuzzified value, x_i indicates the sample element, $\mu(x_i)$ is the membership function,

and n represents the number of elements in the sample. Thus, the best proportional gain constant K_p' , the integral gain constant K_i' and derivate gain constant K_d' outputs are obtained. These values are used as the multiplier in the calculation of PID coefficients. According to Equation (3.5)-(3.7), the PID controller parameters are updated.

$$K_p = K_{p0} * K_p' \quad (3.5)$$

$$K_i = K_{i0} * K_i' \quad (3.6)$$

$$K_d = K_{d0} * K_d' \quad (3.7)$$

Where, K_p' is proportional modification coefficient, K_i' is integral modification coefficient, K_d' is derivative modification coefficient. The initial values of the PID controller are calculated using transfer function-based Simulink PID Tuner. K_{p0} is initial proportional gain (0.02), K_{i0} is initial integral gain (0.6), and K_{d0} is initial derivative gain (0.0001). The control signal of the SFPID controller is defined as shown in Equation (3.8). Simulink block diagram of the MG is given in Figure 8.

$$U_{FPID} = K_p e(t) + K_i \int e(t) + K_d \frac{de(t)}{dt} \quad (3.8)$$

Finally, filtration is performed to bring the voltage at the inverter output closer to the form of a sinusoidal wave. An LCL filter was used for this purpose. As a result of the analyzes, calculated values of inductors L_1 and L_2 and capacitor C are 0.935mH, 0.323mH and 16.24 μ F, respectively (see Figure 6).

4. Energy Management System in DC Microgrid

The EMS provides coordination between MG's standalone mode and grid-connected modes. It also allows activation and de-activation of loads in a controlled manner. Depending on the state of the sources and loads, the power equation in MG should be defined as in Equation (4.1).

$$P_{pv} + P_{wd} = P_L \pm P_{batt} \quad (4.1)$$

Where, the P_{batt} represents battery power, P_{pv} , P_{wd} represent power generated by PV array and WT, respectively. P_L represents the total power of loads that are connected to MG. Similarly, the total load is defined by Equation (4.2).

$$P_{Cr} + P_{L2} + P_{L3} + P_{Loss} = P_L \quad (4.2)$$

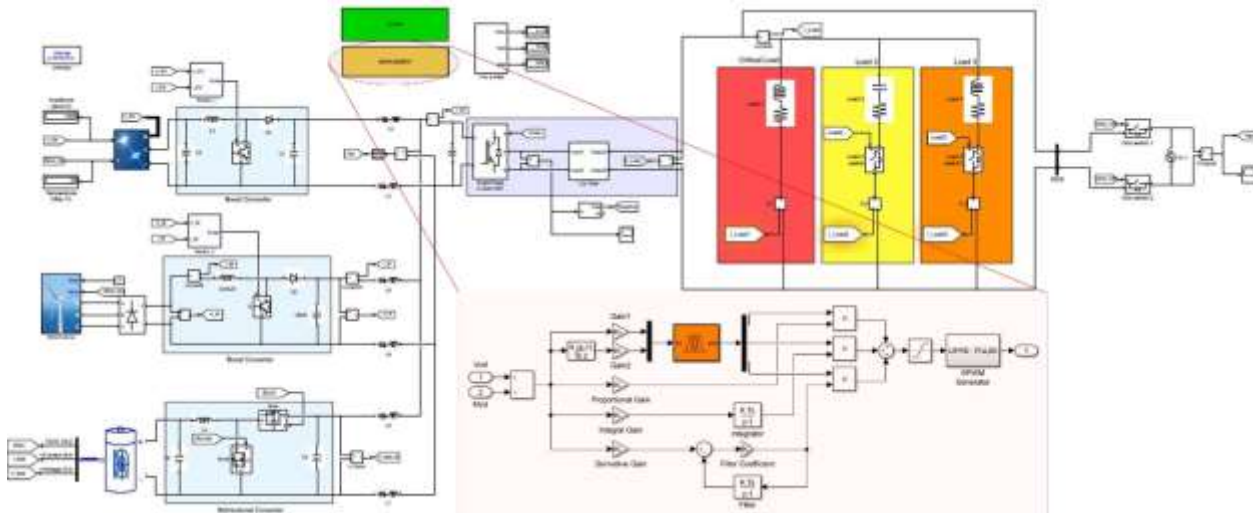


Figure 8. Simulink diagram of the MG architecture.

P_{cr} represents the critical load that must be active continuously. P_{L2} and P_{L3} are loads that can be controlled according to the load condition. The EMS flow diagram between power supplies and loads is shown in Figure 9.

In this case, scenarios related to SOC are given in Table 6. According to the flow diagram, if the total power produced by RES is insufficient to meet the demanded power, the battery supplies the energy as required. If SOC falls below 50%, it opens the S_2 circuit breaker, and so load2 is disabled. If SOC falls below 40%, it opens the S_3 circuit breaker, and so load3 is deactivated.

Table 6. MG transition strategy

Scenarios	Transition conditions	Events
1	$SOC < SOC_{max}$	Battery discharging, PV and WT are in MPPT
2	$SOC < 50\%$	Load2 shedding, PV and WT are in MPPT
3	$SOC < 40\%$	Load2 shedding, PV and WT are in MPPT
4	$SOC < SOC_{min}$	Pgrid \rightarrow ON
5	$SOC > SOC_{max}$	Pgrid \rightarrow OFF

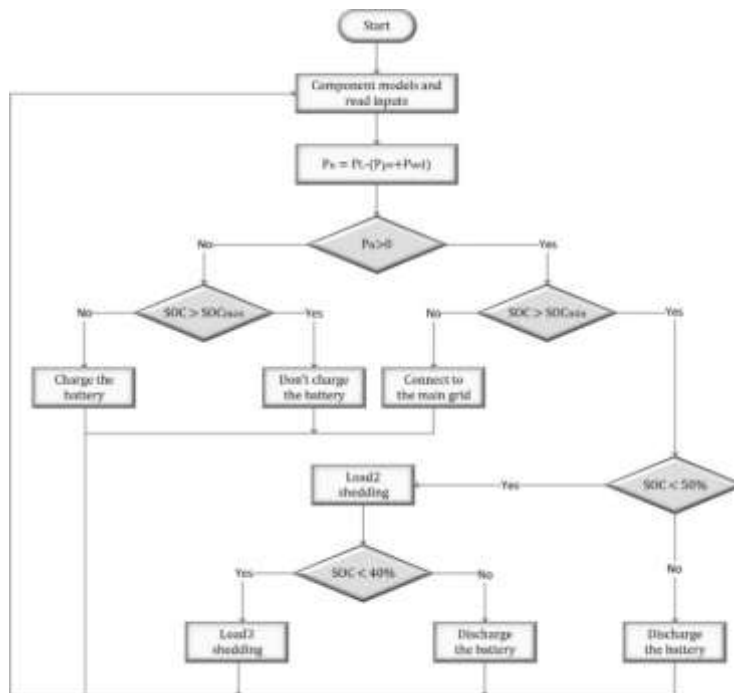


Figure 9. Flowchart of the proposed EMS.

If the SOC, which is determined as the safe range for the battery, falls below the SOC_{min} level, the power flow from the battery to the load is stopped. The grid is switched to connected mode, and the battery is charged in this case. If the production capacity of the power supplies is greater than the demanded load, the energy surplus is stored in the battery. When the battery reaches SOC_{max} level, excess energy is transferred to the grid.

5. Simulation Results and Discussion

In Figure 1, the block diagram is simulated in the DC MG MATLAB[®]/Simulink environment. A SFPID controller is designed for system voltage stability. The comparison of PID and SFPID controllers is given in Figure 10. The performance values for the PID and SFPID controllers are given in Table 7. Reference root mean square (RMS) value of output voltage in MG is 230 V. When a PID controller is used in the control structure of the VSC, the overshoot value of the output voltage is 244 V, and this value is 236 V when the SFPID controller is used. Similarly, for the PID controller, the rise time is 0.035s, and the settling time is 0.301s, while for the SFPID controller, these values are 0.021s and 0.075s, respectively. The results show that the proposed SFPID controller improves the overshoot 57.14%, rise time 40% and settling time 75.08% in performance criteria compared to the PID controller.

Table 7. Comparative performance analysis of PID and SFPID controllers.

Parameter	PID	SFPID
Overshoot (%)	6.087	2.609
Rise Time (s)	0.035	0.021
Settling Time (s)	0.301	0.075

The voltage and frequency stability of the MG on the standalone and grid-connected modes has been analyzed under variable production scenarios. In these scenarios, the solar radiation is 0.2-1 kW/m², and the wind speed is changed autonomously between 8-12 m/s. When the simulation is started, the SOC of the battery is 80%. The changes in the power flow between the source and the load are given in Figure 11. In the initial case, the solar panels produce 6.08 kW in 1 kW/m², the wind turbine produces 5.4 kW at 12 m/s, and the totally produced power is 11.08 kW. In this case, all loads with a total of 9 kW are operational. The surplus 2.26 kW power is transferred to ESS. When solar irradiance decreased to 0.25 kW/m² at second 2, the energy obtained from solar panels decreased to 1.59 kW. In this case, because the power supplies are insufficient to meet the demand power, 2.5 kW of power is met from ESS to meet the total load.

Since the SOC value of the battery falls below 50% of the limit value defined in the EMS in 5 s, load2 with the lowest priority level of 3.5 kW is disabled, and surplus 0.52 kW power is used to charge the ESS. It is assumed that wind speed is to fall to 8 m/s and the solar irradiance is 0.1 kW/m² in the 6th second. Since the power produced under these conditions could not meet the current demand load, the ESS in the charge state went into discharge mode with 4.33 kW power to meet the remaining load demand. When ESS continues discharge for a while, SOC falls below 40%, load3 with low priority was disabled and critical load continued to feed. Discharge operation is stopped because the battery charge falls below SOC_{min} level in the 10.2th second. In order to be ensured of feed of the critical load, EMS switched to grid-connected mode. When the system switches to the grid mode, all loads are supplied, and RES has charged ESS. As the SOC level of ESS reached to SOC_{max} in 14 s, the grid was deactivated and switched back to standalone mode. Thus, the supply of the loads continues to be provided by the RES.

The variation of DC bus current and voltage in MG is given in Figure 12 compared to PID and proposed SFPID controller. Voltage variation in the DC bus is shown in Figure 12 (a) for PID and SFPID controllers. In this system, it is desired that the DC link voltage remains at 400 V. In order to evaluate the change in the DC bus voltage during the simulation process generated in different scenarios, voltage regulation values maximum positive ε_k^+ and lowest negative ε_k^- were obtained according to Equation (5.1) [26].

$$\varepsilon_k^+ = \frac{\bar{u}_k - \min(u_k)}{\bar{u}_k} \cdot 100\% \quad (5.1)$$

$$\varepsilon_k^- = \frac{\bar{u}_k - \max(u_k)}{\bar{u}_k} \cdot 100\%$$

Where, \bar{u}_k is reference DC voltage and u_k is the DC voltage value at the time of operation. Maximum oscillation in the DC bus voltage has occurred in the 14th second due to changes in scenarios or load after the condition in which MG gets into a steady state. As seen in Figure 12 (a), considering the oscillation values that continued for 200 ms in the 14th s, the voltage regulation results obtained from the PID controller are 8.75% and 0% (ε_k^+ and ε_k^-), and the results obtained from the proposed SFPID controller are 4.85% and 0%, respectively. The variation of the DC bus current is shown in Figure 12 (b) for both controllers. Here, the DC current change of the system depending on the load is seen. The fluctuation of the DC bus current is seen to be high at the start. This is due to the voltage and current oscillations during the wind turbine operation.

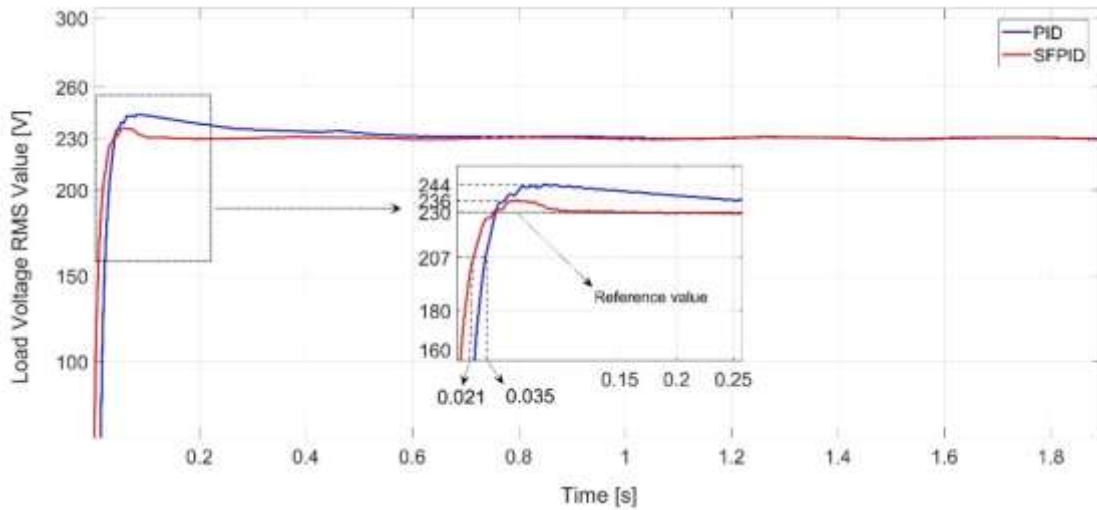


Figure 10. Comparative graphic of control methods.

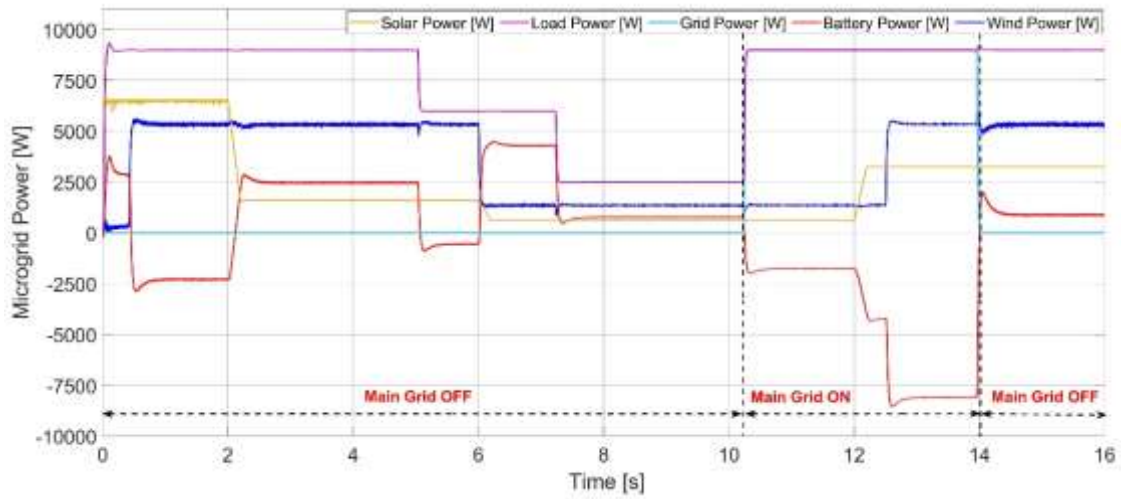


Figure 11. The power flow of DC MG based on proposed EMS.

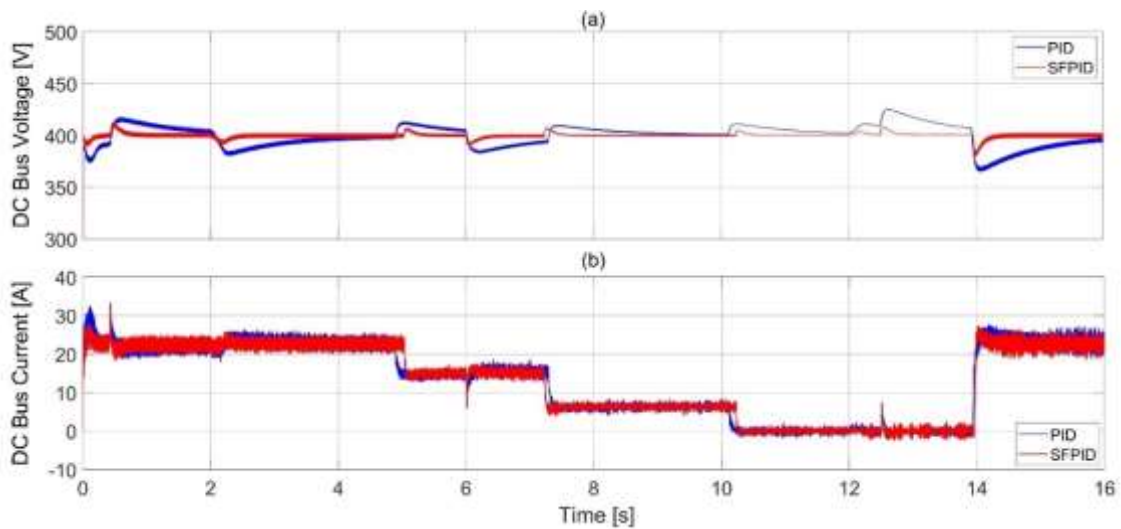


Figure 12. DC bus (a) Output voltage and (b) Output current variation graphs.

The graphs of the change in the maximum and RMS values of the load voltage during the simulation process (SFPID) in MG are given in Figure 13. Similarly, the biggest oscillation in the AC bus voltage after the steady-state of the MG occurred at 14s. Considering the maximum and minimum voltage values of the oscillation that continued for 150ms, the voltage regulation results ϵ_k^+ and ϵ_k^- are obtained as 0% and -1.74%, respectively (see Figure 13(b)). According to these results, it has been shown that the oscillations in the load voltage are within limits according to the EN

50160 standard [27]. The graph of the change in system frequency during the simulation process in MG is given in Figure 14. The changes in scenarios or load after the stabilization of MG, the maximum oscillation in the system frequency occurred at 14.38 s and lasted for 200 ms (10 cycles). This shows that the oscillations are within the limit values according to EN 50160 standard. Similarly, it has been observed that the SFPID controller greatly reduces oscillations in the system frequency relative to the PID controller.

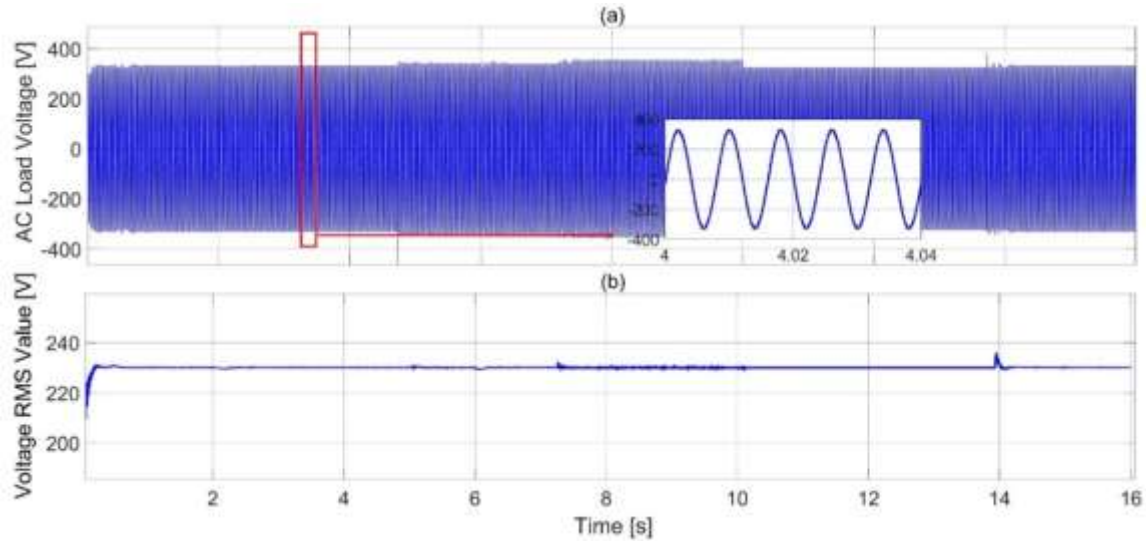


Figure 13. Graph of the AC load voltage change of MG (a) Maximum AC load voltage value (b) AC load voltage RMS value.

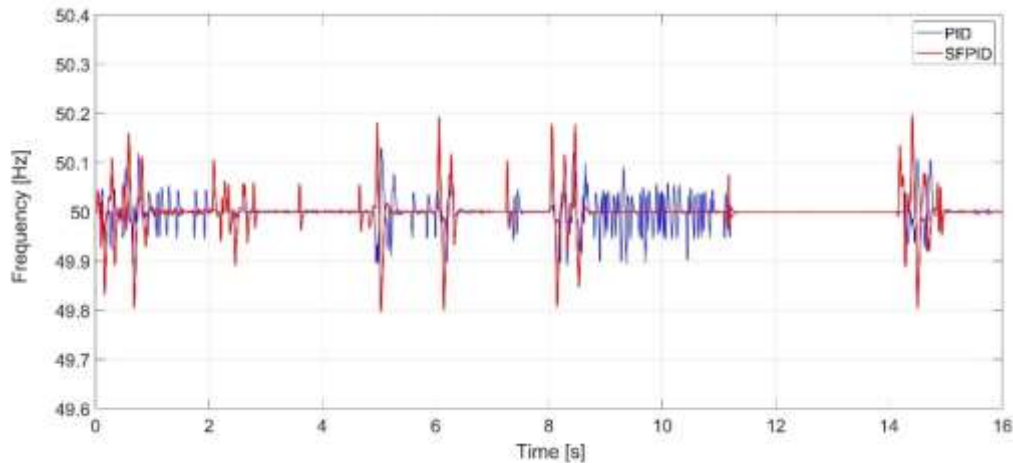


Figure 14. Effect of PID and SFPID controllers on system frequency.

Also, the total harmonic distortion (THD), a measure of the formal proximity between the output waveform and its main component, is one of the performance criteria that measures power quality. As seen from the graphics in Figure 15, THD_V and THD_I in the voltage and current are measured, and it is seen that they are within the limit values according to IEC 61000-4-7 standard [28]. A comparative graph of current and voltage harmonics of

SFPID and PID controller is shown in Figure 16. The THD is calculated as 3.54% and 3.29% for voltage and current when using the PID controller in the MG. On the other hand, THD for voltage and current in SFPID is 3.14% and 3.12%, respectively. The results clearly showed that the THD ratio is improved by 9.4% for voltage and 5.17% for current compared to the proposed SFPID controller with the PID controller.

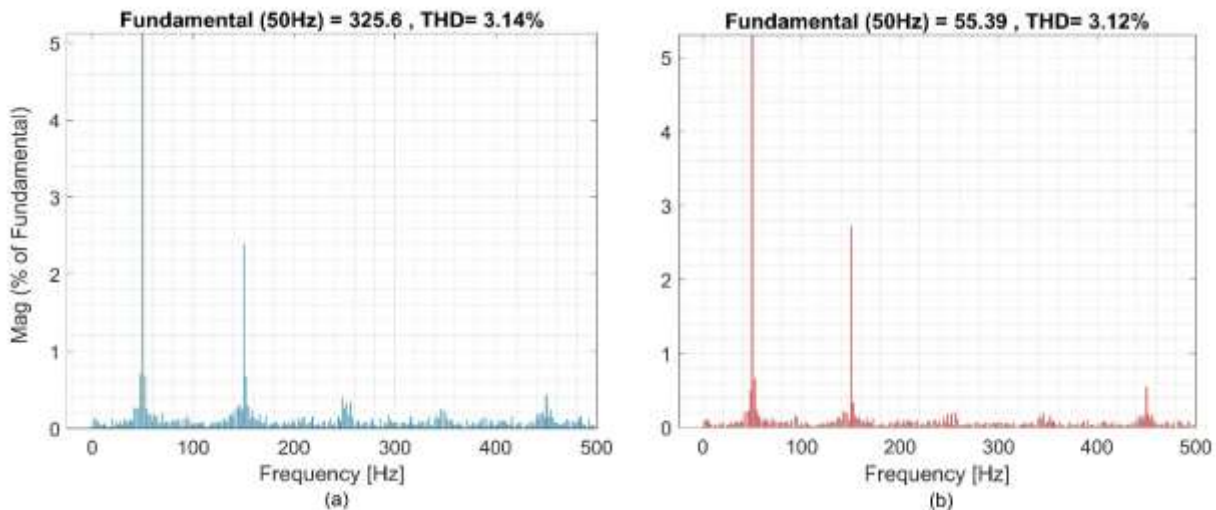


Figure 15. THD spectrum for SFPID controller (a) Load voltage (b) Load current.

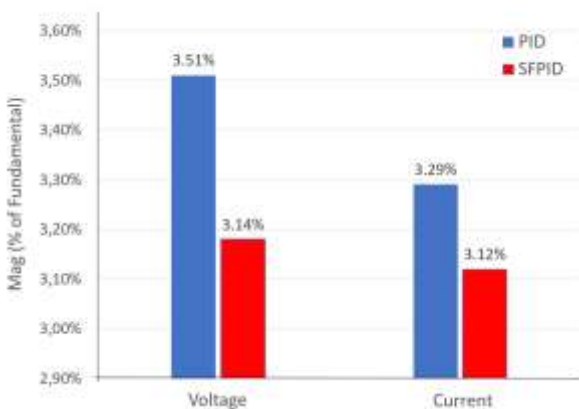


Figure 16. Comparison of voltage and current harmonics

6. Conclusion

In this study, a MG structure consisting of RES with ESS has been developed to operate in standalone and grid-connected modes. The aim is to make maximum use of RES. However, RES and ESS resources may be insufficient to feed the critical load, the worst-case scenario. In this case, MG switches between standalone and grid-connected modes to ensure continuous feed.

In the MG, the SFPID controller is designed for voltage regulation stability compared with traditional PID controllers. Results show that compared to the PID controller, the SFPID controller diminishes overshoot at voltage signal at the system output by 57.14%, shortens settling time by 75.08% and improves rise time by 40%. Thanks to the designed controller and suggested EMS system, the system performance is good and within limit values under all scenarios.

Future work will include a hierarchical control method and hardware implementation for several MGs and ESSs.

Author's Contributions

Ahmet Kaysal: Drafted and wrote the manuscript, performed the result analysis.

Selim K roglu: Supervised the manuscript's progress interpretation and helped in manuscript preparation.

Yüksel Oğuz: Assisted in analytical analysis on the structure, supervised the manuscript's progress.

Ethics

There are no ethical issues after the publication of this manuscript.




References

- [1]. Merabet, A, Tawfique, KA, Ibrahim, H, Beguenane, R and Ghias, AMYM. 2017. Energy Management and Control System for Laboratory Scale Microgrid Based Wind-PV-Battery. *IEEE Transactions on Sustainable Energy*; 8(1): 145-154.
- [2]. Bai, W and Lee, K. 2014. Distributed Generation System Control Strategies in Microgrid Operation. *IFAC Proceedings*; 47(3): 11938-11943.
- [3]. El-Bidairi, KS, Nguyen, HD, Jayasinghe, SDG, Mahmoud, TS, Penesis, I. 2018. A hybrid energy management and battery size optimization for standalone microgrids: A case study for Flinders Island, Australia. *Energy Conversion and Management*; 175: 192-212.
- [4]. Tummuru, NR, Mishra MK and Srinivas, S. 2015. An Improved Current Controller for Grid Connected Voltage Source Converter in Microgrid Applications. *IEEE Transactions on Sustainable Energy*, 6(2): 595-605.
- [5]. Bhosale, R and Agarwal, V. 2019. Fuzzy Logic Control of the Ultracapacitor Interface for Enhanced Transient Response and Voltage Stability of a DC Microgrid. *IEEE Transactions on Industry Applications*; 55(1):712-720.



- [6]. Kim, JY, Kim, HM, Kim, SK, Jeon, JH, Choi, HK. 2019. Designing an Energy Storage System Fuzzy PID Controller for Microgrid Islanded Operation. *Energies*; 4(9):1443-1460.
- [7]. Vigneysh, T and Kumarappan, N. Stability analysis and dynamic performance enhancement of autonomous microgrid using adaptive fuzzy PI controller, IEEE Congress on Evolutionary Computation (CEC), San Sebastian, 2017, pp. 1199-1206.
- [8]. Bayhan, S, Demirbas, S and Abu-Rub, H. 2016. Fuzzy-PI-based sensorless frequency and voltage controller for doubly fed induction generator connected to a DC microgrid. *IET Renewable Power Generation*; 10(8):1069-1077.
- [9]. Anantwar, H, LakshmiKantha, BR and Sundar, S 2017. Fuzzy self-tuning PI controller based inverter control for voltage regulation in off-grid hybrid power system. *Energy Procedia*; 117:409-416.
- [10]. Saroha, J, Singh, M and Jain, DK. 2018. ANFIS-Based Add-On Controller for Unbalance Voltage Compensation in a Low-Voltage Microgrid. *IEEE Transactions on Industrial Informatics*; 14(12):5338-5345.
- [11]. Chauhan, RK, Rajpurohit, BS, Hebner, RE, Singh, SN and Longatt, FMG. Design and analysis of PID and fuzzy-PID controller for voltage control of DC microgrid, IEEE Innovative Smart Grid Technologies, Asia, Bangkok, 2015, pp. 1-6.
- [12]. Hu, J, Shan, Y, Xu, Y, Guerrero, JM. 2019. A coordinated control of hybrid ac/dc microgrids with PV-wind-battery under variable generation and load conditions. *International Journal of Electrical Power & Energy Systems*; 104:583-592.
- [13]. Jayachandran, M, Ravi, G. 2019. Predictive power management strategy for PV/battery hybrid unit based islanded AC microgrid. *International Journal of Electrical Power & Energy Systems*; 110:487-496.
- [14]. Almada, JB, Leão, RPS, Sampaio, RF, Barroso, GC. 2016. A centralized and heuristic approach for energy management of an AC microgrid. *Renewable and Sustainable Energy Reviews*; 60:1396-1404.
- [15]. Tuckey, A, Zabihi, S and Round, S. Decentralized control of a microgrid, 19th European Conference on Power Electronics and Applications, Warsaw, 2017, pp. 1-10.
- [16]. Feng, X, Shekhar, A, Yang, F, Hebner RE and Bauer, P. 2017. Comparison of Hierarchical Control and Distributed Control for Microgrid. *Electric Power Components and Systems*; 45(10):1043-1056.
- [17]. Yazdani, M and Mehrizi-Sani, A. 2014. Distributed Control Techniques in Microgrids. *IEEE Transactions on Smart Grid*; 5(6):2901-2909.
- [18]. Sen, S, Kumar, V. 2018. Microgrid control: A comprehensive survey. *Annual Reviews in Control*; 45:118-151.
- [19]. Rajesh, KS, Dash, SS, Rajagopal, R, Sridhar, R. 2017. A review on control of ac microgrid. *Renewable and Sustainable Energy Reviews*; 71:814-819.
- [20]. Unamuno, E, Barrena, JA. 2015. Hybrid ac/dc microgrids—Part II: Review and classification of control strategies. *Renewable and Sustainable Energy Reviews*; 52:1123-1134.
- [21]. Ziouani, I, Boukhetala, D, Darcherif, AM, Amghar, B, El Abbassi, I. 2018. Hierarchical control for flexible microgrid based on three-phase voltage source inverters operated in parallel, *International Journal of Electrical Power & Energy Systems*; 95:188-201.
- [22]. Mohamed, AA, Elsayed, AT, Youssef, TA, Mohammed, OA. 2017. Hierarchical control for DC microgrid clusters with high penetration of distributed energy resources. *Electric Power Systems Research*; 148:210-219.
- [23]. Wu, B, Lang, Y, Zargari, N and Kouro, S. Power Conversion and Control of Wind Energy Systems; Hoboken, NJ, USA: John Wiley & Sons, 2011.
- [24]. Rashid, MH. Power Electronics Devices, Circuits and Applications, Prentice-Hall, Englewood Cliffs, New Jersey, 2003.
- [25]. Bingi, K, Ibrahim, R, Karsiti MN and Hassan, SM. Fuzzy gain scheduled set-point weighted PID controller for unstable CSTR systems, IEEE International Conference on Signal and Image Processing Applications, 2017, pp. 289-293.
- [26]. Santos, P, Fonte P and Luis, R. Improvement of DC Microgrid Voltage Regulation Based on Bidirectional Intelligent Charging Systems, 15th International Conference on the European Energy Market, Lodz, 2018, pp. 1-6.
- [27]. Seme, S, Lukač, N, Štumberger, B, Hadžiselimović, M. 2017. Power quality experimental analysis of grid-connected photovoltaic systems in urban distribution networks. *Energy*, 139:1261-1266.
- [28]. Oliveira, WR, Anésio, LF, Filho, JC. 2019. A contribution for the measuring process of harmonics and interharmonics in electrical power systems with photovoltaic sources. *International Journal of Electrical Power & Energy Systems*; 104:481-488.

Performing DoS Attacks on Bluetooth Devices Paired with Google Home Mini

Tuğrul Yüksel¹ , Ömer Aydın^{2*} , Gökhan Dalkılıç³ 

¹Dokuz Eylül University, Faculty of Engineering, Computer Engineering, İzmir Turkey

²Manisa Celal Bayar University, Faculty of Engineering, Electrical and Electronics Engineering, Manisa, Turkey

³Dokuz Eylül University, Faculty of Engineering, Computer Engineering, İzmir Turkey

*omer.aydin@deu.edu.tr

*Orcid: 0000-0002-7137-4881

Received: 7 January 2021

Accepted: 6 December 2022

DOI: 10.18466/cbayarfbe.856119

Abstract

In today's technology world, virtual personal assistants (VPAs) have become very common and most people have started making their homes smart, using these VPAs. Although different companies have different assistants, Google Home Mini (GHM) is our focus in this paper. The first device, Google Home, was released in November 2016 and then GHM was released after a year, in October 2017. GHM has many features such as playing music, setting reminders, setting kitchen timers, and controlling smart home devices. Although GHM might be reliable against cyber-attacks, devices that are paired with GHM could be attacked and these cyber-attacks can lead to severe problems. Cyber-attack issues become more important to us, specifically if the devices controlled by GHM are vital devices such as ovens, fire alarms, and security cameras. In this article, we represent the denial of service (DoS) attacks applied against devices that are paired with GHM. In this study, Bluedoser, L2ping, and Bluetooth DoS script, which are software in the Kali Linux platform, were used to perform DoS attacks, and some devices were used such as GHM, headphones, and two speakers as victim devices. Successful results were observed on Bluetooth headphones.

Keywords: Bluetooth attacks, Denial of service attack, Google Home, Security, Network attacks, Virtual personal assistant.

1. Introduction

Using virtual personal assistants (VPAs) like Google Home Mini (GHM) to make our home smart is possible nowadays and many people do it successfully. As of 2017, newly developed VPAs such as GHM were presented to the market, so the capabilities and usage of virtual assistants have been started to expand rapidly. Smart home devices, GHM, and at least one device that is capable of running GHM applications are required basically for designing a smart home. Most of today's VPAs can interpret human voices and can respond via their defined voice. These kinds of VPAs are also able to understand lots of questions, manage smart devices connected to them. Moreover, they can manage basic operations such as calendars, alarms, and email checking. People use VPAs for different reasons. Some of them think that VPAs have a big role in easing their lives. Almost half of the users utilize features of a VPA such as browsing the web, weather forecasts, and music.

Using VPA for online shopping and information is also possible.

Despite the advantages that a VPA provides to the user, there are serious security issues that are associated with using them. Although there is not much research on the use of VPAs, which is rapidly increasing, research continues in this area. The most important security issue is privacy. The questions we ask the VPA are stored on the servers and the responses we receive from the VPA are also sent to us by those servers. Although companies report that this data exchange remains confidential and the data is encrypted, our privacy may be compromised by another attacker during this data exchange between the server and the VPA.

1.1 Related Works

Zhang et al. (2018) reported a study that was a security analysis of popular VPAs and proved the vulnerability of VPAs against two new attacks [1]. They implemented two attacks that are called "voice

squatting" and "voice masquerading", on GHM and Amazon Echo. These attacks focused on the way VPAs work or misconceptions of users about VPA functionalities. These two attacks were the proofs of a realistic threat to VPAs, as understood by their studies and the real-world attacks they performed. Finally, they implemented a context-sensitive detector to reduce the voice masquerading threat with a 95% precision.

Alrawi et al. examined possible security issues in 45 smart home applications and IoT devices [2]. They determined that most users were the reason for the security vulnerabilities. Users endanger their security for various reasons. In particular, they do this by using home assistants and IoT devices at different security levels. There has been research that offers a simple and effective solution for such security vulnerabilities. That solution is regulating the multiple IoT and Home Assistant usage and explaining the relational relationships to the users.

In another study, Park et al. (2018) discussed data storing and security methods of a GHM [3]. There are a lot of research projects that have been done on the other virtual personal assistants for digital investigations and the related article produces another one about a GHM. They separated the study into three main sections: the device, the mobile app, and the network and they analyzed the results obtained. In conclusion, they reported that the GHM does not store much data in the mobile app. The data that is exchanged across the GHM, mobile app and the Google cloud is analyzed by using Wireshark. The vulnerability tests on ajp13 port (one of the five ports of Google Home Mini) are proceeded and it is realized that it is not exploitable.

Caputo et al. (2020) dealt with that critical information about the habits of the users, which use VPA. The critical information can be leaked using the features of the encrypted traffic, such as the throughput, the size of protocol data units, or the IP addresses [4]. In a related study, they showed the risks of using VPA via models developed by using exploiting machine learning techniques to classify traffic and implemented privacy leaking attacks automatically.

Çepik et al. made attempts to attack the network time protocol and exploits were tested [5]. The attack was carried out on a wireless connection established between a Google Home Mini device and an Internet of things device. They examined secure communication between an IoT device and the GHM [6-8]. They tried to determine whether the Blynk (blynk.cc) application accesses time information via the simple network time protocol (SNTP) [9] from the time server. Thus, they tested the possibility that an attacker could obtain this information and interrupt the secure connection.

Giese and Noubir developed a set of forensic IoT techniques [10]. They applied these reverse engineering techniques to the hardware and software of the Amazon

Echo Dot. They demonstrated that there is little protection of private user data. An attacker with physical access to such devices would be able to gain access to Wi-Fi credentials and can reach the sensitive information. They have shown that passwords and some sensitive information in the flash memory can be accessed even after the device is reset to factory settings. Finally, they proposed alternative secure designs and techniques to mitigate threats.

Yiğit tried to establish a secure connection using the AES algorithm between the NodeMCU and the Blynk in his study [11]. In this way, he aimed to prevent possible security vulnerabilities in the connection of the GHM with IoT devices.

There is increasing concern about the data collection and the security breaches of user privacy on devices like Amazon Echo and Google Home. Consumers sometimes unknowingly place too much trust in these devices. Ferraris et al. investigated the behavior of the devices such as Amazon Echo and Google Home in the smart home environment in terms of trust relationships [12]. As a result, they evaluated the effectiveness of the security controls provided and identified potentially related security issues. They defined a trust model to address the identified issues.

1.2 Aim and Contribution

Making a smart home or smart somewhere else is possible using GHM as told in the introduction section of the paper. This seems like a useful solution, but we have to be sure that the devices controlled via GHM are also secure. This paper focuses on the security of devices that are paired with the GHM via Bluetooth [13]. If the Bluetooth devices have some security weaknesses, the problem may become more vital. People can pair their vital devices such as an oven, security camera, or a fire alarm with GHM. The weakness(es) of those devices can cause irreversible damage and may harm people.

Our work aims to analyze the weaknesses of the devices and apply cyber-security attacks on them. To achieve our goal and simulate the attacks, the Ping of Death [14] attack, which is one of the DoS attacks, is used on the Kali Linux operating system. There are some customized tools for performing DoS attacks on the Kali Linux system. In our study, those tools are used for education research, and they shouldn't be used against someone else without permission. Attacking using those tools to someone is illegal and legal sanctions can be imposed on the attackers.

DoS attack is a type of cyber-attack in which a malicious attacker aims to render a computer or IoT device unavailable by interrupting the device's service [15]. DoS attack is launched from a single computer and

the computer is also the attacker's device. DoS attacks harm by overwhelming a victim machine with requests until normal traffic is unable to be processed, resulting in a denial of service to users. In this study, useful tools of Kali Linux were used to send requests and packages. In this paper, 2 Bluetooth speakers, 1 Bluetooth headphone, and GHM were used to achieve success. DoS attack was applied on those devices separately and different results were obtained. Three different Bluetooth devices were used as a victim because the results depend on the vulnerability of the devices. This study contributes to putting forth of risks of using a VPA and performing cyber-attacks using vulnerabilities of the devices. At the end of the study, results are presented and analyses are discussed. Attacks are performed on the victim devices one by one and software tools, which are used for cyber-attack, are applied on each victim device separately.

2. Materials

In our study, Bluetooth headphones, Bluetooth speakers, Kali Linux [16] operating system, and tools for DoS attack were used. GHM was used to pair victim devices via Bluetooth. Kali Linux, which includes tools for penetrating tests, was required as the operating system for performing DoS attacks. L2ping (linux.die.net/man/1/l2ping), Bluedoser (github.com/Anlos0023/bluedoser) and Bluetooth DoS Script (github.com/crypt0b0y/bluetooth-dos-attack-script) are used for performing DoS attacks on victims. In this section, the GHM, Kali Linux, and tools for attacking are explained.

2.1. Google Home Mini

GHM, developed by Google; which allows us to turn our devices into smart devices in our home, office, or elsewhere; is an assistant that takes voice commands. GHM is connected to Google services over the Internet. Thanks to its microphone, it detects our voice commands and executes the commands. While devices that are on the same network as the GHM can be managed, we can also manage Bluetooth devices with the GHM.

There are lots of features such as turning lights on and off with the GHM, playing music by pairing our Spotify account with the GHM, managing our Netflix account with voice, sending voice messages, ordering food, calling by voice, creating alarms and reminders, managing smart home devices, etc. To use all these opportunities, it is enough to download the GHM application, complete the setup phase of the GHM, and make sure that the GHM is connected to the internet. After the setup phase, users can make the GHM listen to themselves saying "Hey Google" and can say the command they want to it.

Before using the GHM smart assistant, the device should be reset to factory settings by holding down the reset button on the back of the GHM. Using the Bluetooth service of the GHM, the setup phase is completed through the GHM application, and the device is connected to the Wi-Fi access point. Thus, the GHM becomes ready to access its services over the Internet. Finally, assistant settings can be changed through the device application, users can introduce their voice to the assistant and the GHM detects the voice that is introduced. Figure 1 simply describes the working principle system.



Figure 1. Google Home Mini system.

2.2. Kali Linux

Kali Linux is a Debian (en.wikipedia.org/wiki/Debian) based Linux operating system developed for penetration tests and security audits. Penetration tests are used to find, analyze and report vulnerabilities in systems. With a lot of tools and components for cybersecurity, Kali Linux is a widely used operating system for performing penetration tests. In this study, DoS attacks were performed using l2ping, Bluedoser, and Bluetooth DoS script tools on the Kali Linux system.

Bluez (bluez.org) is a library that provides the Bluetooth layer and protocol requirements necessary for us to use Bluetooth on our Kali Linux operating system. Bluez is developed in a modular structure which can support more than one Bluetooth adapter and also it contains many useful modules. Bluez, which can run on almost all Linux systems, can be downloaded using the "sudo apt-get install bluez" command.

Hcitol (linux.die.net/man/1/hcitol) contains many useful commands such as "dev", "scan", "inq". To reach all commands and detailed descriptions, the "hcitol -h" command can be used on the terminal. Finding the media access control (MAC) addresses of Bluetooth devices during our attacks is the first step to do before starting any operation. "hcitol scan" command finds those MAC addresses with their device names.

2.2.1. L2ping

L2ping allows us to send packets to Bluetooth devices. During performing l2ping, we need to determine some

parameters such as "-i", "-s", "-f". The computer's Bluetooth adapter should be selected using the "-i" parameter. In this study, our Bluetooth adapter was hci0. By using the "-s" parameter, we can adjust the size of the packets to be sent. The target needs to be set by entering the victim's MAC address with the "-f" parameter.

2.2.2. Bluedoser

Bluedoser is a tool used to perform DoS attacks to disrupt the Bluetooth function. Bluedoser automatically tries to detect the surrounding Bluetooth devices and lists detected devices to the attacker with their MAC address. Then, the victim to be attacked is determined by finding from the list. Finally, a DoS attack can be initialized by entering the victim's MAC address into the interface.

Bluedoser performs a DoS attack using l2ping. The only difference is that Bluedoser attacks the victim using more than one thread instead of attacking by only one thread. That acts like sending packages from more than one terminal and the way used by Bluedoser disturbs the victim more periodically.

2.2.3. Bluetooth Dos Script

Bluetooth DoS script (BDS) is a script that works on only Linux systems and is used to perform Bluetooth DoS attacks. It is required by l2ping in the Kali Linux system to use BDS. The working principle of BDS is the same as Bluedoser, but the only difference is that BDS allows attackers to define thread count as a parameter. This parameter provides performing DoS attacks using a defined number of threads. Figure 2 explains how BDS uses it for attacking.

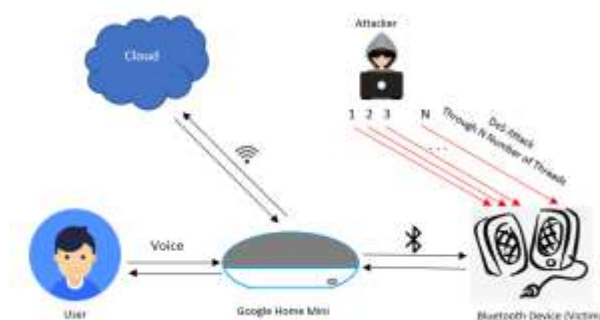


Figure 2. Performing DoS attack using BDS.

As soon as BDS attacks any unpaired Bluetooth device, it prevents other devices from connecting to the attacked victim device. For some devices that are not very secure, it may stop communicating with the corresponding device connected via Bluetooth. The security of the device to be attacked is the most important measure in the disconnection process via a DOS attack.

3. Proposed Work

First of all, the GHM application is downloaded to the device and the setup of the GHM proceeds through the application. After the GHM setup, we can integrate applications that support the GHM and many processes which we can do with our Gmail account. The GHM has a Bluetooth feature so that, we can pair Bluetooth devices in our house with the GHM and manage them by giving voice commands to the GHM. So, can we stop the services of these Bluetooth devices via DoS attacks? Especially if these Bluetooth devices have vital responsibilities such as fire alarms or security cameras, this issue becomes even more important for us. In this study, in addition to many studies on GHM security, we worked on DoS attacks against Bluetooth devices that are paired with the GHM. DoS attacks were applied based on the vulnerability of the Bluetooth devices. While the services of the non-secure devices were stopped, the Bluetooth connections of these devices with the GHM were also cut. In line with the results obtained, it is obvious that the devices to be connected with the GHM should also be secure.

Using l2ping, an attack was carried out on the Bluetooth headphone paired with the device. As the first step, as you can see in Figure 3, the parameters were adjusted, and then the attack was launched. Packets to be sent are set to 600 bytes, Bluetooth adapter and victim device MAC address are also set up. Only part of the MAC address can be read from Figure 3, the remaining is blackouted.

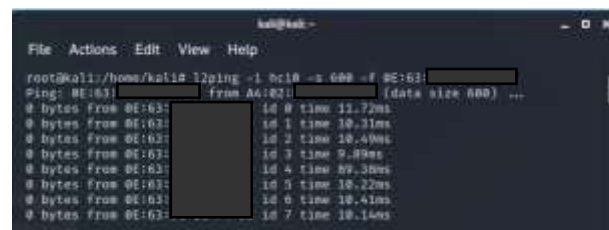


Figure 3. L2ping

The victim device's MAC address was searched using Bluedoser's user interface. After determining the victim device, the related MAC address with the victim was set up as the parameter. Then DoS attack using Bluedoser was started on the Bluetooth headphone.

The user interface of BDS is as you can see in Figure 4. BDS requires Victim MAC address, package size, and several threads as parameters. After the DoS attack starts, packets of 600 bytes are sent to the victim over 100 different threads. The number of threads for achievement depends on the victim and this count may



Figure 4. The user interface of BDS.

change for different devices to be attacked. This optimal thread number was found by performing lots of attacks on the victim and observing those trials.

4. Results and Discussion

L2ping attack was failed even though the Bluetooth headphone accepted the packets. During the attack, music was playing over the headphone and service couldn't be denied. While sending the packages to the GHM, the GHM doesn't accept the packages. When trying to send packages to the Bluetooth speakers, packages couldn't be received because the Bluetooth speaker already had a Bluetooth connection with the GHM.

In the attack on the Bluetooth connection between the GHM and the Bluetooth headphone using Bluedoser, expected success was not achieved and the Bluetooth connection could not be disconnected. The attack is performed on non-paired Bluetooth headphones and then it is tried to connect to the headphone via the GHM using Bluetooth. As a result, the GHM could not connect to the headphone.

In the attack on the Bluetooth connection between the GHM and the Bluetooth headphone using BDS, success was achieved and the Bluetooth connection was disconnected. Before the DoS attack, the GHM was playing music over the Bluetooth headphone as an output device. The GHM was changed the output device automatically after the DoS attack and it started to play music over itself. An optimal thread count was found for Bluetooth headphones and observations were plotted as a graph in Figure 5. Using 6 threads causes voice corruption on the headphone and using more than 6 threads provides disconnection of the Bluetooth connection between the headphone and the GHM. Using 7 threads offers the same result and using more than 7 threads is unnecessary, it just fatigues the attacker. The optimal thread number depends on the vulnerability of the Bluetooth device and this graph changes for different Bluetooth devices. Attacks should be performed again, and trials should be observed again to obtain a graph for another Bluetooth device.

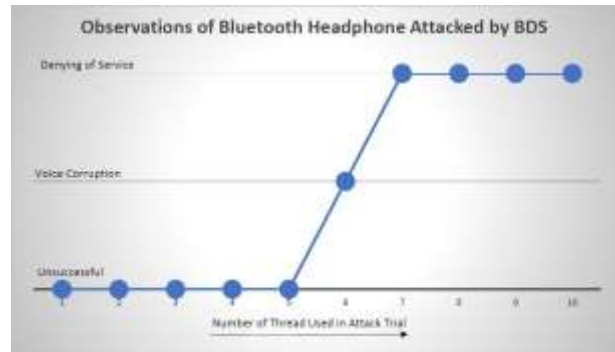


Figure 5. Optimal thread count for Bluetooth headphone.

We realized that we could not be successful in the DoS attack using l2ping, but we know that BDS uses l2ping and we succeeded in the DoS attack using BDS. This is because the BDS performs l2ping attacks over multiply defined threads and sends a suitable number of packages to the victim as much as possible to keep the victim busy. The optimal thread count parameter was found by observing different trials for Bluetooth headphones. Using at least 7 threads provided successful DoS attack results for our Bluetooth headphone.

5. Conclusion

In conclusion, attacks that were performed using l2ping, Bluedoser, and Bluetooth DoS script (BDS) were observed. No success was achieved using Bluedoser and l2ping against Bluetooth headphones and other Bluetooth speakers. Attack, which was performed using BDS against Bluetooth headphones, was able to disconnect Bluetooth service and victim headphone was denied of service.

We achieved success in performing a DoS attack on the device which supports more than one Bluetooth connection. Other devices didn't support more than one Bluetooth connection, so they didn't accept packets while the DoS attack has been performed. Future work aim is to find a way to perform DoS attacks on the other Bluetooth devices that don't support more than one Bluetooth connection. It is required to find more vulnerabilities for those devices and to discover new techniques against security risks.

Author's Contributions

Tuğrul Yüksel: Wrote the draft manuscript, prepare the system and made the experiments.

Ömer Aydın: Assisted in analysis on the structure, supervised the experiment's progress, made result interpretation, helped in manuscript preparation, made the manuscript ready for the journal, took part in the journal submission and following the journal process.

Gökhan Dalkılıç: Served as a consultant in the execution of the whole process. He supervised the process of the preparation of the manuscript, made criticism and made the proof reading in language.



Ethics

There are no ethical issues after the publication of this manuscript.

References

- [1]. Zhang, N, Mi, X, Feng, X, Wang, X, Tian, Y, Qian, F. 2018. Understanding and Mitigating the Security Risks of Voice-Controlled Third-Party Skills on Amazon Alexa and Google Home. <https://arxiv.org/pdf/1805.01525.pdf>
- [2]. Alrawi, O, Lever, C, Antonakakis, M, Monroe, F. 2019 SoK: Security Evaluation of Home-Based IoT Deployments. IEEE Symposium on Security and Privacy. San Francisco, Ca. 20-22 May 2019. Doi:10.1109/SP.2019.00013
- [3]. Park, M, James JI. 2018. Preliminary Study of a Google Home Mini. *Journal of Digital Forensics* 2018 June, 12(1). <https://arxiv.org/pdf/2001.04574>
- [4]. Caputo, D, Verderame, L, Ranieri, A, Merlo, A, & Caviglione, L. 2020. Fine- hearing Google Home: why silence will not protect your privacy. *Journal of Wireless Mobile Networks, Ubiquitous Computing, and Dependable Applications (JoWUA)*, 11(1), 35-53. <https://doi.org/10.22667/JOWUA.2020.03.31.035>
- [5]. Çepik, H, Aydın, Ö, Dalkılıç, G. 2020. Security Vulnerability Assessment of Google Home Connection with an Internet of Things Device. 7th International Management Information Systems Conference. İzmir, Turkey. 09-11.12.2020.
- [6]. Google Home specifications. Google Home Help. Google. Retrieved December 6, 2017.
- [7]. Demmitt, J. 2015. "Google's Nest Labs plans top-secret project at new Seattle engineering center". Geekwire.
- [8]. Statt, N, Bohn, D. 2019. Google Nest: Why Google finally embraced Nest as its smart home brand". The Verge. Retrieved October 9, 2019.
- [9]. Mills, D. 1995. Simple network time protocol (SNTP). RFC 1769, University of Delaware.
- [10]. Giese, D, Noubir, G. 2021. Amazon echo dot or the reverberating secrets of IoT devices. In Proceedings of the 14th ACM Conference on Security and Privacy in Wireless and Mobile Networks, 13-24.
- [11]. Yiğit, E. 2021. Secure Connection between Google Home and IoT Device. *Journal of Emerging Computer Technologies*, 1(1), 18-20.
- [12]. Ferraris, D, Bastos, D, Fernandez-Gago, C, El-Moussa, F. 2021. A trust model for popular smart home devices. *International Journal of Information Security*, 20(4), 571-587.
- [13]. Sheppard, M. The Bluetooth basics. In: Bing B (ed) *Wireless local area networks: the new wireless revolution*, John Wiley & Sons, New York, 2002, pp 191-202.
- [14]. Yihunie, F, Abdelfattah, E, Odeh, A. In Analysis of ping of death DoS and DDoS attacks, IEEE Long Island Systems, Applications and Technology Conference (LISAT), Farmingdale, USA, 2018, pp 1-4. IEEE.
- [15]. Huegen, C. A. 1998. Network-Based Denial of Service Attacks. *IEEE Transactions on Information Theory*.
- [16]. Singh, A. 2013. Instant Kali Linux. Packt Publishing Ltd.

Radar Absorber Fabric Design Based on Periodic Arrays of Circular Shaped Conductive Patches

Muhammet Hilmi Nisancı^{1*} , Baha Kanberoglu¹ , Yılmaz Çiğdem¹ , Fatih Özkan Alkurt² ,
Muharrem Karaaslan² 

¹ Department of Electrical and Electronics Engineering Department, Sakarya University, Sakarya, 54055, Turkey,

² Department of Electrical and Electronics Engineering Department, Iskenderun Technical University, Iskenderun, Hatay, Turkey

* nisanci@sakarya.edu.tr

* Orcid : 0000-0002-8210-7260

Received: 13 April 2021

Accepted: 19 January 2022

DOI: 10.18466/cbayarfbe.915217

Abstract

In this study, the design and electrical tests of polarization-independent radar absorber fabric containing an array of circular shaped conductive patches positioned on a neoprene fabric are presented. The proposed absorber has an overall thickness of 1.57 mm and a unit cell dimension of $8.75 \times 8.75 \text{ mm}^2$, which is $< \lambda/3$, where λ is the free-space wavelength at 9.33 GHz. In the designs, electrical performance of the radar absorber fabric is numerically studied in both planar and conformal structures. Furthermore, the two-dimensional (2D) surface current distribution at the resonant frequency is examined to better understand the operating principles of the proposed structure. Finally, a prototype of the radar absorber is manufactured using neoprene fabric with relative permittivity of 3.18, loss tangent of 0.93, and the frequency dependent reflection parameter values are measured by using the free space measurement technique to validate the numerical results. A good agreement between the measurement and numerical results is obtained.

Keywords: Radar absorber fabric, metamaterials, frequency selective surfaces.

1. Introduction

Radars are commonly used for detecting, locating, tracking, and recognizing of the air, land and sea vehicles such as ships, aircraft and space crafts for both civilian and military purposes [1]-[4]. Radar Absorbing Materials (RAM) which convert the incident electromagnetic energy into thermal energy should be used to make harder to detect of these vehicles by radars [5]-[7]. The traditional RAMs based on frequency selective surface (FSS) are include periodically arranged of conductive patches located on a dielectric substrate. In the literature various FSS designs with different unit element geometries are proposed to reduce the electromagnetic energy reflected back to the radar [8]-[10].

In [11], a thin absorber which consists of a single resistive FSS layer and a dielectric superstrate is designed to operate in the frequency range of approximately 3.3 to 20 GHz with 88.26% bandwidth. In the designs, square patches are used as the unit cell

elements to simplify the derivation of the equivalent circuit model. The three-layer ultrathin RAM which includes an FSS with double square loops is considered in [12]. In order to improve the absorption performance of the considered structure micro-split gaps are opened in the middle of the outer square loops. In this way, the -10dB absorption bandwidth is increased to 14.1 GHz. Another design is shown in [13], where a tunable circuit analog absorber is proposed for the first time. The basic idea of the tunable circuit analog absorbers is replacing the conventional ground plane by a varactor tunable FSS. The RAMs can be also used for conformal surface applications. For this purpose, in [14], a Jaumann absorber with a low-pass FSS back layer is applied to the curved wing-front end to efficiently reduce the monostatic radar cross-section for both TE and TM polarizations over 2–16 GHz.

Recently fabric-based radar absorbers are becoming more popular for their low processing cost, flexibility, light weight and easy fabrication [15].

In the proposed study a polarization-independent radar absorber fabric is designed to operate in the center frequency of the X-band.

This paper is organized as follows. Section 2 describes the design procedure and numerical analysis of the proposed model. Section 3 details the manufacturing and measurement processes. Moreover, this section compares the measurement results with numerical results in the frequency range of interest. Finally, Section 4 presents the evaluation and conclusions of the paper.

2. Radar Absorber Fabric Design and Operating Principle

In this study, radar absorber fabric design with circular shaped conductive patch array providing polarization-independent absorption characteristic for both TE and TM modes under different incident angles due to the symmetrical shape of the patches is considered. As shown in Figure 1, the proposed structure has four design parameters; the radius of the circular patches r , the thickness of the fabric positioned between the conductive patches t , the side length of the unit element h and the relative permittivity of the fabric positioned between the conductive patches ϵ_r . The design parameter values of the absorber fabric are obtained by using CST Microwave Studio optimization tools for 9.33 GHz center frequency value as listed in Table 1 [16].

Table 1. Design parameter values of radar absorber fabric with circular shaped patch array

Parameter	Description	Value
r	the radius of the circular patches	3 mm
t	the thickness of the fabric positioned between the conductive patches	1.5 mm
h	the side length of the unit element	8.75 mm
ϵ_r	the relative dielectric permittivity of the fabric	3.5

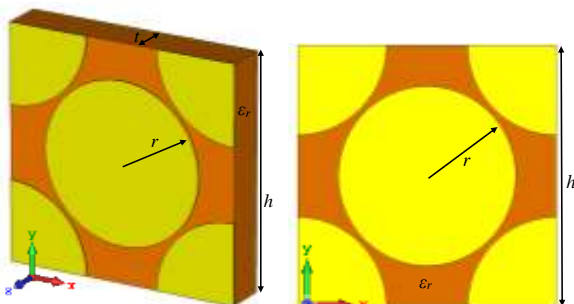


Figure 1. Design parameters of the radar absorber fabric with a circular shaped patch array

In the simulations, the open boundary condition is used along z-direction whereas electric and magnetic boundary conditions are respectively used along the x and y-directions to eliminate all tangential electric and magnetic fields. Furthermore, the unit element model illustrated in Figure 1 is excited with a pure TEM mode by two 50 Ω waveguide ports which are located over xy planes at equal distances from the panel along the z-axis.

The frequency dependent transmission (T), reflection (R) and absorption (A) coefficient values obtained from numerical analysis are compared in Figure 2. It is observed from the comparison given in Figure 2, the amplitude values of the reflection and absorption coefficients are respectively minimum and maximum at the center operating frequency of 9.33 GHz, while the transmission coefficient values are equal to zero throughout the frequency range due the ground plane used in the designs.

$$T + R + A = 1 \quad (2.1)$$

Considering Eq. (1), the sum of the amplitude values of the frequency dependent transmission, reflection and absorption coefficients should be equal to 1. While the transmission parameter values are zero due to the ground plane, the reflection and absorption coefficients should be symmetrical with respect to each other. Therefore, in this study, only reflection coefficient values are taken into consideration in the numerical analysis.

The effect of various incidence angles and polarizations of the electromagnetic wave on the electrical performance of the radar absorber fabric is also considered in this study. For this purpose, numerical analysis is performed for the angle of incidence of the electromagnetic wave between 0° – 60° with 15° angle steps and the obtained frequency dependent reflection parameters are compared in Figure 3.

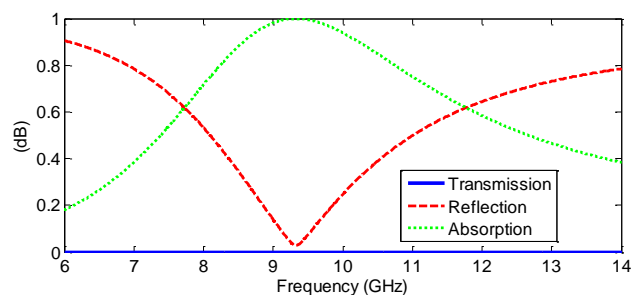


Figure 2. Numerically obtained frequency dependent transmission (T), reflection (R) and absorption (A) coefficient values of the radar absorber fabric

It can be seen from Figure 3 that the operating frequency value of the radar absorber fabric shifts towards higher frequencies depending on the increase in the incidence angle.

To examine the electrical performance of the radar absorber fabric against different polarizations of the electromagnetic wave, the angle of the wave with the x -axis is changed with 15° steps between 0° – 60° and the obtained frequency dependent reflection parameters are compared in Figure 4. From the comparison given in Figure 4, the proposed radar absorber fabric design shows a polarization independent characteristic.

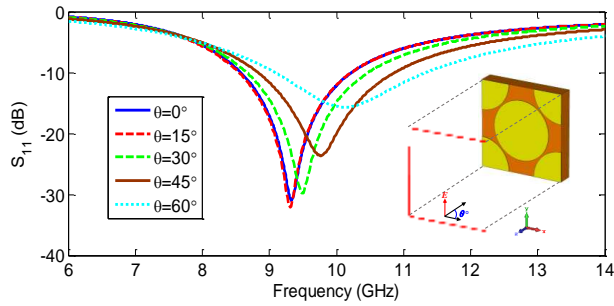


Figure 3. Numerically obtained frequency dependent reflection coefficient values of the radar absorber fabric for various incidence angle of electromagnetic wave

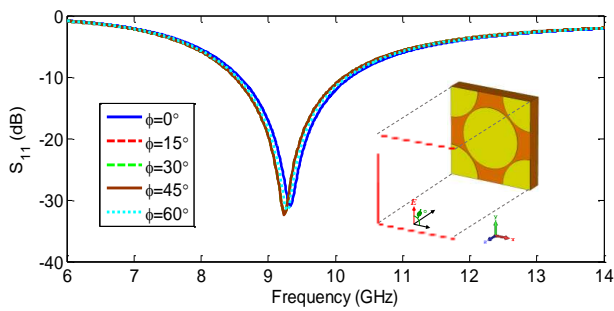


Figure 4. Numerically obtained frequency dependent reflection coefficient values of the radar absorber fabric various polarizations of the electromagnetic wave

In order to investigate the electrical performance of the proposed structure, 2D surface current density at the operating frequency of the radar absorber fabric with normal electromagnetic wave excitation ($\phi=0^\circ, \theta=0^\circ$) is considered. As can be clearly seen from Figure 5, conductive circular patches resonate at operating frequency.

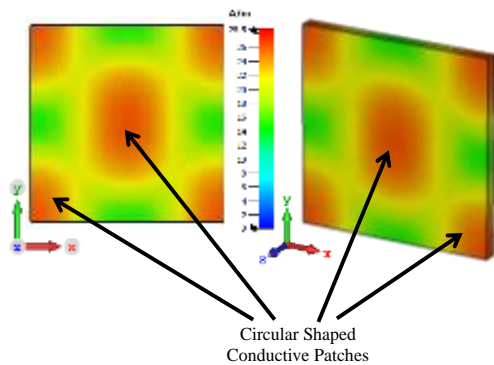


Figure 5. 2D surface current distribution at the center operating frequency of the radar absorber fabric

After the 2D surface current density of the proposed structure is studied, several simulations are implemented to investigate the effect of the design parameter values on the electrical performance of the radar absorber. For this purpose, only one design parameter value is varied while the others are fixed as shown in Table 2.

Table 2. Design parameter values used in the parameter analysis of radar absorber fabric

Model	r	t	h	ϵ_r
Ref. Model	3 mm	1.5 mm	8.75 mm	3.5
Model-1	2.94 mm	1.5 mm	8.75 mm	3.5
Model-2	3.06 mm	1.5 mm	8.75 mm	3.5
Model-3	3 mm	1.3 mm	8.75 mm	3.5
Model-4	3 mm	1.7 mm	8.75 mm	3.5
Model-5	3 mm	1.5 mm	8.55 mm	3.5
Model-6	3 mm	1.5 mm	8.95 mm	3.5
Model-7	3 mm	1.5 mm	8.75 mm	2.5
Model-8	3 mm	1.5 mm	8.75 mm	4.5

The first parameter to be studied is the radius of the circular patches r . As can be clearly seen from Figure 6, the center of the operating frequency moves to 9.86, 9.33, and 8.62 GHz by varying r as 2.94, 3, and 3.06 mm, respectively.

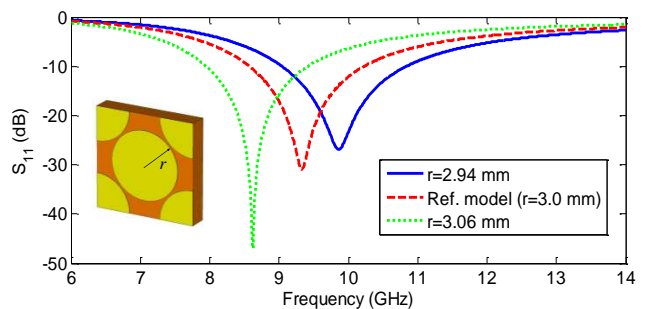


Figure 6. Numerically obtained reflection coefficient results of the proposed radar absorber as the function of the r .

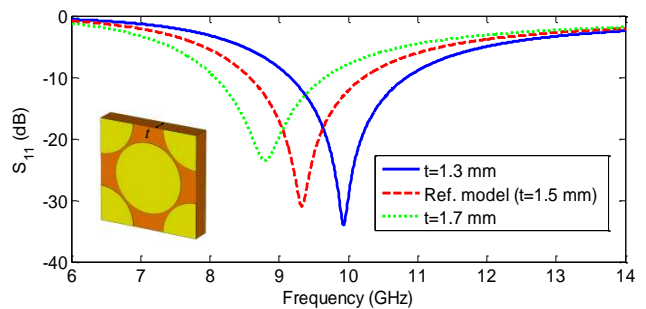


Figure 7. Numerically obtained reflection coefficient results of the proposed radar absorber as the function of the t .

In order to investigate the effect of the thickness of the fabric positioned between the conductive patches and ground plane on the operating frequency, t is varied from 1.3 mm to 1.7 mm with an increment of 0.2 mm. Figure 7 confirms that the operating frequency is inversely proportional to t .

The effect of the unit cell dimension on the reflection coefficient values of the radar absorber fabric is compared in Figure 8 under varying the values of h . As depicted in in Figure 8, the center of the operating frequency values are obtained as 8.55, 9.33, and 9.8 GHz for the unit cell dimension values of 8.55, 8.75, and 8.95 mm, respectively.

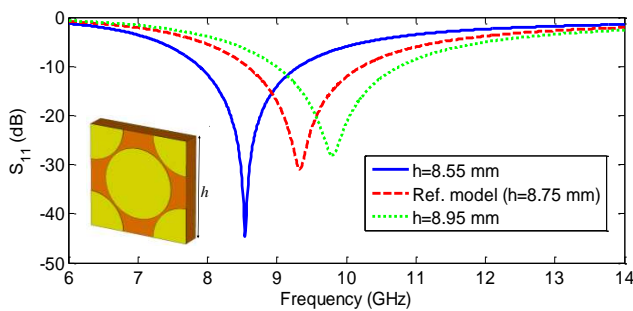


Figure 8. Numerically obtained reflection coefficient results of the proposed radar absorber as the function of the h .

Finally, the effect of the relative dielectric permittivity of the fabric ϵ_r on the electrical performance is considered. According to Figure 9, the operating frequency is inversely proportional to the relative dielectric permittivity value of the fabric.

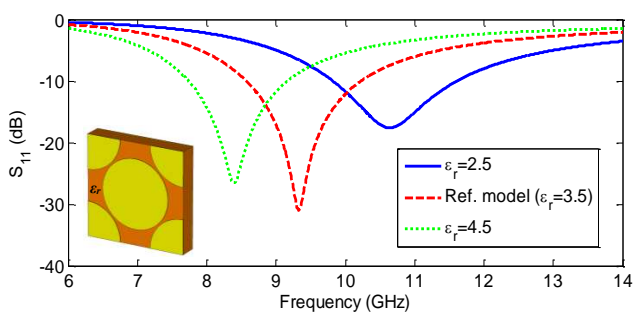


Figure 9. Numerically obtained reflection coefficient results of the proposed radar absorber as the function of the ϵ_r .

Before starting the manufacturing process of the radar absorber fabric, the electrical performance of the absorber fabric on the conformal structures is considered. For this purpose, the designed absorber fabric is placed on a cylindrical conformal structure which has an average inner radius of 8.8 cm as shown in Figure 10 and numerical analyzes are performed by applying periodic boundary conditions along the vertical axis. In the numerical analysis, reflection parameters are obtained by using waveguide port. It can be observed

from the frequency dependent reflection parameters given in Figure 11 that the center operating frequency does not change when the absorber fabric is positioned on conformal structures, but the amplitude of the reflection coefficients decreases at higher frequencies.

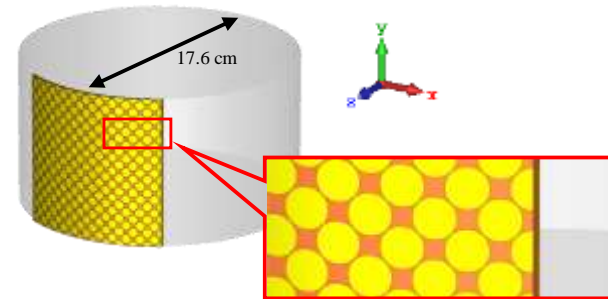


Figure 10. Radar absorber fabric placed on the curved structure

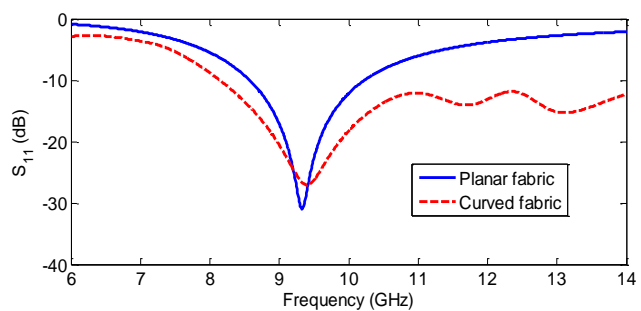


Figure 11. Comparison of the numerically obtained frequency dependent reflection coefficient values of the conformal radar absorber fabric with the planar fabric

3. Manufacturing Process and Experimental Verification

In order to experimentally verify the numerical analysis results, the prototype of the radar absorber fabric is manufactured. As schematically shown in Figure 12, the grounding conductor and circular shaped patch arrays are manufactured using conductive fabric with a shielding efficiency of 70–90 dB in the frequency range of 10 MHz –30 GHz consisting of 62% polyester, 25% copper and 13% nickel, while 1.5 mm thick neoprene fabric is used for the dielectric substrate.

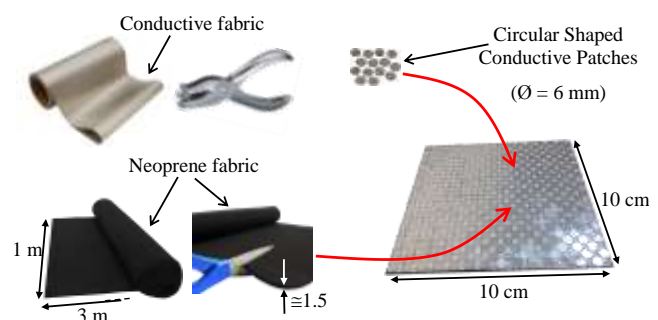


Figure 12. Prototype production stages of radar absorber fabric

After the manufacturing process is completed, the electrical performance of the radar absorber fabric is started by measuring the frequency dependent complex dielectric permittivity of the neoprene fabric. As shown in Figure 13, Agilent N5234A PNA-L microwave vector network analyzer (VNA) with an operating frequency range of 10 MHz to 43.5 GHz is used together with the Agilent 85070E dielectric measurement kit. The obtained measurement results of the neoprene fabric for the frequency range of 6–12 GHz are given in Figure 14.

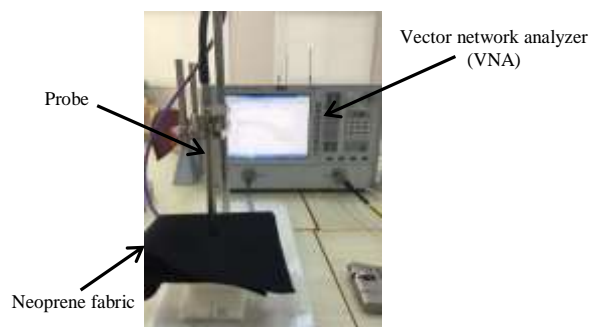
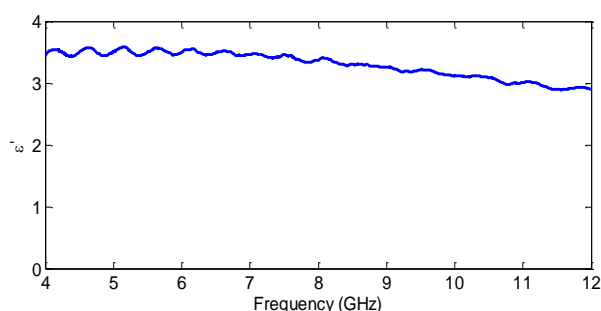
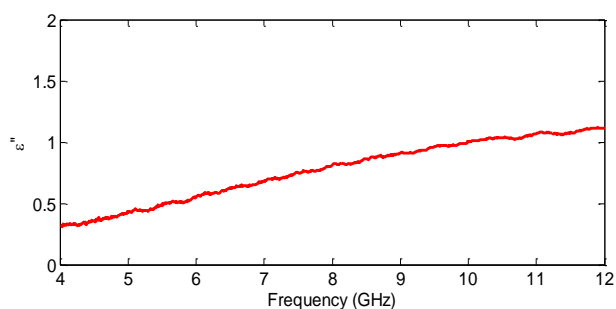


Figure 13. Measurement setup of frequency dependent complex dielectric permittivity of neoprene fabric



(a)



(b)

Figure 14. Frequency dependent complex dielectric permittivity of neoprene fabric (a) real and (b) imaginary parts

It can be observed from Figure 14 that the real and imaginary parts of the relative permittivity value of the neoprene fabric at the center operating frequency are 3.18 and 0.93, respectively. The obtained values

confirm that the electrical characteristic of the neoprene fabric is similar to the substrate used in the simulations. After the complex relative permittivity values of the neoprene fabric is verified by measurements, frequency dependent reflection coefficient values of the planar radar absorber fabric are measured. For this purpose, the free space measurement setup shown in Figure 15 is used [17]. In the measurements a horn antenna which has excellent radiation characteristics in the operating frequency range of 3 GHz to 18 GHz is located 20 cm far from the proposed structure and connected through semi rigid coaxial cable to the VNA.



Figure 15. Frequency dependent reflection parameter measurements of planar radar absorber fabric

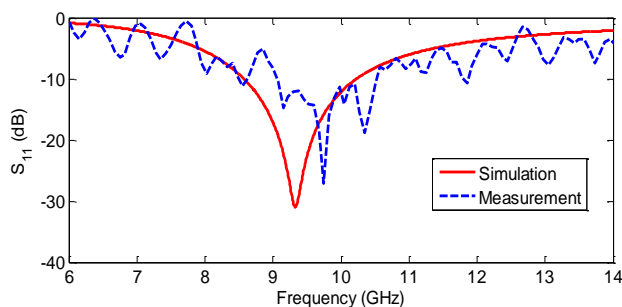


Figure 16. Comparison of the numerically obtained reflection coefficient values of the planar radar absorber fabric with the measurements

The reflection coefficient values obtained from the measurements are compared with the numerical results in Figure 16. It can be clearly seen from Figure 16 that the measurement results are consistent with the numerical results.

In order to obtain the electrical performance of the cylindrical conformal absorber fabric, as shown in Figure 17, the proposed structure is placed on a paper roll with an average radius of 8.5 cm and reflection coefficient values are obtained in the frequency range of 6-14 GHz. The reason for using a paper roll in measurements is that it has a conformal surface and has a dielectric permittivity of close to 1 which is equal to free space.

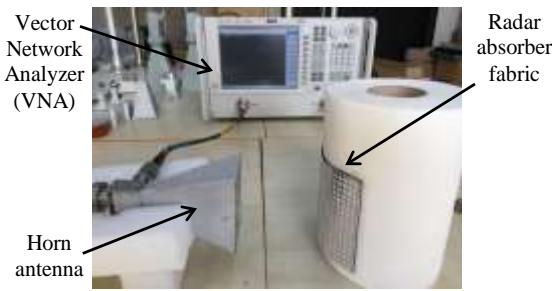


Figure 17. Frequency dependent reflection coefficient measurements of cylindrical conformal surface absorber fabric

The frequency dependent reflection coefficient values obtained from measurements are compared with the numerical analysis results in Figure 18.

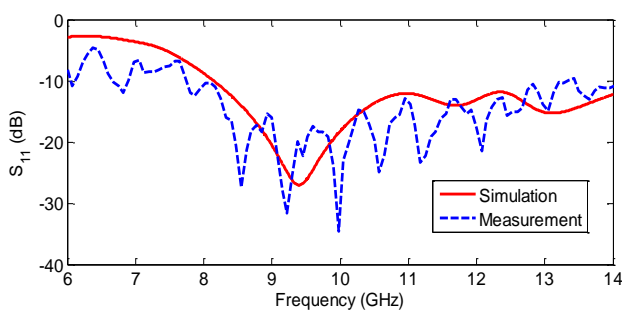


Figure 18. Comparison of the numerically obtained reflection coefficient values of the conformal radar absorber fabric with the measurements

It can be seen from the comparison given in Figure 18 that the measurement results are in good agreement with the numerical analysis results.

Finally, the electrical performance of the proposed radar absorber fabric is compared with previously published studies in terms of unit cell dimensions, material used in the manufacturing process, the operating frequency values and the polarization insensitivity. As it can be observed from Table 3, the proposed absorber represents a polarization insensitivity up to 60° and good miniaturization as well as flexibility for conformal applications.

Table 3. Electrical performance of the proposed radar absorber fabric compared with previously published studies

Ref. No.	Unit cell (mm ²)	Material	Oper. Freq. (GHz)	Pol. Insens.
[15]	30x30	Fabric	9, 9.8	0°–60°
[18]	26x26	FR4	28	0°–40°
[19]	11x11	FR4	10	Not ment.
[20]	16x16	Graph.	11.6	Not ment.
This study	8.75x8.75	Fabric	9.33	0°–60°

4. Conclusion

In this study, radar absorber fabric with a circular shaped conductive patch array which has a central operating frequency of 9.33 GHz is designed. In the designs, the electrical performance of the radar absorber fabric is numerically studied considering the different incident angle and polarization of the electromagnetic wave. In the numerical analysis, the angle of incidence of the electromagnetic wave is changed between 0°–60° with 15° angle steps. It is observed from the numerical results that the operating frequency value of the absorber fabric shifted towards high frequencies due to the increase in the incident angle whereas the operating frequency value does not change for the different polarizations of the electromagnetic wave. In order to deeply analyze the electrical performance of the radar absorber fabric 2D surface current distribution at the operating frequency value for normal electromagnetic wave excitation ($\phi=0^\circ$, $\theta=0^\circ$) is examined. Within the scope of numerical analysis, the electrical performance of the conformal structure obtained by placing the planar radar absorber fabric on the cylinder surface with an inner radius of 8.8 cm is analyzed and it is observed that the central operating frequency value has shifted 60 MHz towards the high frequency. In order to experimentally verify the numerical analysis results of both the planar and conformal radar absorber fabrics, the prototype of the proposed structure is produced, and the frequency dependent reflection coefficients are obtained by using the free space measurement technique. The measurement results of the planar radar absorber fabric are consistent with the numerical results whereas the measurement results of the cylindrical conformal radar absorber fabric are in good agreement with the numerical results. Consequently, the proposed absorber represents good miniaturization as well as flexibility for conformal applications and a polarization insensitivity up to 60° both for TE and TM modes.

Author's Contributions

Muhammet Hilmi Nisancı: Drafted and wrote the manuscript, carried out the manufacturing process of the radar absorber fabric, performed the numerical analysis.

Baha Kanberoğlu: Drafted and wrote the manuscript, performed the numerical analysis.

Yılmaz Çiğdem: Assisted the manufacturing process of the radar absorber fabric and performed the numerical analysis.

Fatih Özkan Alkurt: Performed the experiment to verify the numerical analysis results.

Muharrem Karaarslan: Supervised the experiment's progress and analysed the obtained results.

Ethics

There are no ethical issues after the publication of this manuscript.







References

- [1]. Jayalakshmi, C. G.; Inamdar, A.; Anand, A.; Kandasubramanian, B. J., 2019. Polymer matrix composites as broadband radar absorbing structures for stealth aircrafts. *Journal of Applied Polymer Science.*, 136: 1-21.
- [2]. Laws, K. E; Vesecky, J. F.; Lovellette, M. N.; Paduan, J. D. Ship tracking by HF radar in coastal waters, OCEANS 2016 MTS/IEEE Monterey; Monterey, CA, USA, 2016, pp. 1-8.
- [3]. Lee, R. J.; Steele, S. L. 2014. Military Use of Satellite Communications, Remote Sensing, and Global Positioning Systems in the War on Terror. *Journal of Air Law and Commerce*, 79(1), 69-80.
- [4]. Dzvonnkovskaya, A.; Gurgel, K.; Rohling, H.; Schlick, T. Low power High Frequency Surface Wave Radar application for ship detection and tracking. 2008 International Conference on Radar; Adelaide, SA, Australia, 2008, pp. 627-632.
- [5]. Zhukov, P. A.; Kirillov, V. Y. The Use of Radar Absorbing Materials for Electronic Devices. International Youth Conference on Radio Electronics, *Electrical and Power Engineering (REEPE)*; Moscow, Russia, 2020, pp. 1-5.
- [6]. Mitrano, C.; Balzano, A.; Bertacca, M.; Flaccavento, M.; Mancinelli, R. CFRP-based broad-band Radar Absorbing Materials. IEEE Radar Conference; Rome, Italy, 2008, pp. 1-6.
- [7]. Perini, J; Cohen, L. S., 1993. Design of broad-band radar-absorbing materials for large angles of incidence. *IEEE Transactions on Electromagnetic Compatibility*, 35(2), 223-230.
- [8]. Terracher, F.; Berginc, G. Thin electromagnetic absorber using frequency selective surfaces. IEEE Antennas and Propagation Society International Symposium. Transmitting Waves of Progress to the Next Millennium. 2000 Digest. Held in conjunction with: USNC/URSI National Radio Science Meeting; Salt Lake City, UT, USA, 2000, pp. 846-849.
- [9]. Ming-liang, W.; Sheng-jun, Z.; Jia-qi, L.; Wei, L.; Xue-mei, L.; Liang, X. W. FSS design research for improving the wide-band stealth performance of radar absorbing materials. International Workshop on Metamaterials (Meta); Nanjing, China, 2012, pp. 1-4.
- [10]. Varadan, V. V. Radar Absorbing Applications of Metamaterials. IEEE Region 5 Technical Conference; Fayetteville, AR, USA, 2007, pp. 105-108.
- [11]. Lv, X.; Withayachumnankul, W.; Fumeaux, C. 2019. Single-FSS-Layer Absorber with Improved Bandwidth–Thickness Tradeoff Adopting Impedance-Matching Superstrate. *IEEE Antennas and Wireless Propagation Letters*, 18(5), 916-920.
- [12]. Xu, H.; Bie, S.; Xu, Y.; Yuan, W.; Chen, Q.; Jiang, J., 2016. Broad bandwidth of thin composite radar absorbing structures embedded with frequency selective surfaces. *Composites Part A: Applied Science and Manufacturing*, 80, 111-117.
- [13]. Bakshi, S. C.; Mitra, D. A Reconfigurable FSS Backed Continuously Tunable CAA Inspired Absorber. IEEE Indian Conference on Antennas and Propagation (InCAP); Hyderabad, India, pp. 1-4, 16-19 Dec. 2018.
- [14]. Motevasselian, A.; Jonsson, B. L. G., 2011. Partially Transparent Jaumann-Like Absorber Applied to a Curved Structure. *International Journal of Antennas and Propagation*, 2011, 1-7.
- [15]. J. Tak, J.; Choi, J., 2017. A Wearable Metamaterial Microwave Absorber. *IEEE Antennas and Wireless Propagation Letters*, 16, 784-787.
- [16]. CST Studio Suite 2019, available at www.3ds.com.
- [17]. Yan, M.; et al. 2014. A Novel Miniaturized Frequency Selective Surface with Stable Resonance. *IEEE Antennas and Wireless Propagation Letters*, 13, 639-641.
- [18]. Bilal, R. M. H; et al., 2021. Wideband Microwave Absorber Comprising Metallic Split-Ring Resonators Surrounded With E-Shaped Fractal Metamaterial. *IEEE Access*, 9, 5670-5677.
- [19]. Yoo, M.; Lim, S., 2013. Wideband metamaterial absorber using an RC layer. Asia-Pacific Microwave Conference Proceedings (APMC), 1227-1229.
- [20]. Olszewska, M., 2013. A broadband metamaterial absorbing panel with a resistive pattern made of ink with graphene nanoplatelets. European Microwave Conference, 1039-1042.



A Review: The Physical, Nutritional, Bioactive Properties and Health Benefits of Jujube Fruit

Fadime Begüm Tepe^{1*} , Raci Ekinci² , Çetin Kadakal² , Nizam Mustafa Nizamlioğlu³ 

¹Department of Food Technology, Şebinkarahisar Vocational School of Technical Science, Giresun University, Giresun, Turkey

²Department of Food Engineering, Faculty of Engineering, Pamukkale University, Denizli, Turkey

³Department of Food Engineering, Faculty of Engineering, Karamanoğlu Mehmetbey University, Karaman, Turkey

* begumotag@gmail.com

* Orcid : 0000-0003-4989-5354

Received: 11 April 2021

Accepted: 11 March 2022

DOI: 10.18466/cbayarfbe.913267

Abstract

Jujube (*Ziziphus jujuba* Mill.), which grows in tropical and sub-tropical regions of world and has been commercially cultivated in China for 4000 years. Jujube is a juicy and crispy fruit, resembling a large olive and tasting like an apple. Moreover, jujube has been used for treatment of several diseases in traditional Chinese medicine. Jujube has antioxidant, anticancer, hepatoprotective, anti-inflammatory, antimicrobial activities due to bioactive components such as phenolic compounds, saponins, polysaccharides and ascorbic acid. It is also a valuable fruit in terms of its nutrient content including carbohydrates, proteins, vitamins and minerals. In recent years, the tendency towards natural therapies has increased, due to increase in incidence of certain diseases and adverse effects of drugs used in the treatment of such diseases. Jujube could be considered as a natural therapeutic material because of bioactive and nutritional properties. The aim of present review is to introduce jujube fruit in terms of chemical composition, effects on health and bioactive properties.

Keywords: bioactive properties; health benefits; jujube; nutritional value

1. Introduction

Jujube (*Ziziphus jujuba* Mill.), belonging to *Rhamnaceae* family, has been grown for 4000 years and has more than 700 cultivars in China [1]. The jujube is naturally spread in some regions of Russia, India, North Africa, Southern Europe, Middle East and Anatolia [2,3]. Jujube is called different names among cultures such as Chinese jujube, Tsao, Azufaifo, Chinese date, Dara, Unnap, Annap, and Hünnap [4,5].

China, the only exporter, produces 90% of jujube in the world [6,7]. In Turkey, statistical data has been compiled since 2013 by Turkey Statistical Institute. According to records, jujube production has increased from 142 tonnes in 2013, to 1760 tonnes in 2021 [8].

Jujube is a crispy and juicy fruit with a single hard stone, which resembles a large olive in size of approximately 4x6 cm, and tastes similar to an apple [9,10].

The color of jujube fruit changes from yellow to red-brown during maturation. Generally, jujube is consumed as fresh or dried fruit, but it also has a variety of consumption types such as tea, alcoholic beverages, pickles, jam, compote or candy in some cultures [11].

Jujube has been used in Traditional Chinese Medicine for thousands of years because of nutritional and bioactive properties [9, 12]. Recently, some researchers have indicated that jujube fruits are good source of vitamins (especially vitamin C) and minerals (calcium, iron and potassium as well as the content of carbohydrates, proteins and fatty acids [10,13,14]. The jujube, which is rich in phenolic compounds, has many bioactive properties such as antioxidant, anticancer, anti-inflammatory, hepatoprotective and sedative activities [9,15,16,17].

The purpose of the study is to review the jujube fruit in terms of physical features, nutritional values and bioactive properties.

2. Physical features

Jujube plant is a small deciduous tree with thorny branches and can reach 5-10 m height. Jujube has shiny-green leaves with 2-7 cm wide and 1-3 cm broad. Yellowish green, small flowers of jujube are 5 mm wide [18]. Also, there is one stone in the fruit [19]. Jujube fruits have ovoid and elongated shape like an olive. Jujube, a mild climate plant, can grow wild as well as cultivation for commercial purpose in garden. The growth rate of jujube trees is slower than other fruit trees.

The growing season of jujube is divided into 5 stages. Stage I is bud burst to leafing stage during early April-early May. Stage II is flowering to fruit set stage during mid-May-late June. Fruit formation stage is the third stage, and it occurs between late June-late July. During early August-early September, fruit maturation stage proceeds and then between October and March, dormancy stage continues [9].

Soil type does not have large effects on jujube growth because jujube trees are resistant to salinity and alkalinity. It is not necessary to provide large amount of water since jujube trees are better adapted to arid regions than other fruit trees [9]. Sandy, permeable, moist, and lime-rich soil with sufficient humus for jujube cultivation is more suitable [20]. Although jujube trees adapt to many climates, it needs summer heat for the formation of high-quality fruits.

3. Nutritional properties

Jujube fruit is a good source of vitamins, minerals, phenolic components, carbohydrates. Nutritional values and bioactive components of jujube depend on maturity stage and genotype [15].

Jujube contains approximately 85% carbohydrates, 57-77% reducing sugar, 0.57-2.79% soluble fibre, 5.24-7.18% insoluble fibre, 4.75-6.86% protein, 0.37-1.02% lipid, and 2.26-3.01% ash in dry weight [21]. In general, fructose, glucose and sucrose are the major sugars [22, 23]. Foods, which are rich in fructose, may be considered as potential food source for diabetic diets. So, jujube may be helpful for diabetics because of high fructose content [22]. Some researchers have indicated that sugar content and composition may differ based on cultivar, agro-climatic conditions and habitat [21]. Hernandez et al. [5] found that fructose, glucose, and sucrose levels of jujube ranged from 4.8 to 5.7 g/100 mL, 3 to 3.9 g/ 100 mL, 1.6 to 9.4 g/100 mL, respectively. Hernandez et al. [5] have indicated that the differences in the content of sugar depend on only cultivar because they grow at similar conditions. In another study, predominant sugars of jujube were defined as fructose, glucose, and sucrose. It was indicated that with the increasing maturity level, content

of total sugar increased, then at the last stage of maturation, it decreased. Content of total sugar was determined as 817.42, 6061.23 and 4807.33 mg/100 g fresh weight at the first, fourth and last (sixth) stage of maturation, respectively. Additionally, it was reported that sucrose content increased with maturation despite of no sucrose content at initial stages [23].

There is limited information about protein and amino acid content of jujube. Amino acid profile of jujube at eight maturation stage was investigated by Choi et al. [24]. It was stated that protein content of jujube decreased from 42.1 to 4.6 g protein/100 g dry weight during maturation. Asparagine was reported to be major amino acid. Additionally, total free amino acids/protein (%) increased from 3.4 to 62.4 during maturation. Hernandez et al. [5] reported that protein content of jujube is ranged from 3.7% to 5.8% in dry weight and the usage of jujube in unbalanced plant-based diet might be helpful for remedy protein deficiency. Free amino acid composition of fresh, dried and stored jujube was showed by Pu et al. [25] The results demonstrated that fresh jujube contains approximately 26 g/kg free amino acid. The major amino acid was proline (17117.4 mg/kg), followed by threonine (3794.7 mg/kg) and serine (1151.4 mg/kg). Free amino acid content was stated to decrease as a result of Maillard reactions during drying [26].

Organic acids are indicators for fruit maturation, flavor, nutrition and acceptance of fruits [27]. Different types and amounts of organic acids in jujube were reported to be found depending on fruit's maturity stage, genotype, cultivation regions and climates [22,28]. According to the results of Gao et al. [22], while malic (294-740.3 mg/100 g fresh weight), citric (39.4-196.6 mg/100 g fresh weight) and succinic (0-177.9 mg/100 g fresh weight) acid were the organic acids in jujube cultivars. They have also indicated that the concentration of each organic acids differed dependent on cultivar. In a study, oxalic, tartaric, malic, lactic, and ascorbic acid were detected in jujube with different cultivar and maturity stage. Ascorbic (280.4-250.3 mg/L in white maturity; 312.9-319.2 mg/L in red maturity) and malic acid (106.1-130.7 mg/L in white maturity; 268.2-305.6 mg/L in red maturity) were reported to be major organic acids. They have stated that only oxalic acid content decreased with maturity from 92.3 to 45.3 mg/L, while the others reached maximum amount in the red maturity stage. This study has shown that maturity stage has important effect on organic acid content [15]. Although, Hernandez et al. [5] determined succinic acid (0.84-5.53 g/100 mL) as main organic acid, citric (0.30-0.77 g/100 mL), ascorbic (0.41-0.64 g/100 mL) and malic acid (0.21-0.31 g/100 mL) were reported to be detected in jujube fruits by other researchers. Some researchers have demonstrated that tartaric, malic, citric and succinic acid may exist in jujube fruits, but predominant organic acid was malic acid followed by tartaric acid.

At the different maturation stages, content of each organic acid was stated to be different [23]. Wu et al. [23] have also indicated that organic acids are the markers for fruit acceptability.

Li et al. [21] have reported that jujube has low lipid content (0.37-1.02%). Total lipid amount of fresh jujube fruits was observed between 0.06-0.1% by San and Yildirim [29]. They detected 19 different fatty acid and indicated that oleic (14.27-18.84%), linoleic (17.39-34.20%), palmitic (13.21-17.84%) and palmitoleic (7.27-18.86%) acid were predominant fatty acids in 4 jujube cultivars. These differences may result from jujube cultivars, chemical composition of jujube, geographical and climatic conditions.

Vitamins are essential micronutrients because they cannot be synthesized in human body. Therefore, it is a necessity to meet the need for vitamins with diet [30]. Vitamins have vital functions and lack of vitamins can cause various health problems [31]. Ascorbic acid (vitamin C), a water-soluble vitamin, has scavenging free radical activity and is a chelating and reducing agent [32]. Jujube is one of the richest fruits in terms of vitamin C [10]. Recommended nutrient intakes (RNIs) for vitamin C were stated that 45 mg/day for an adult man [33]. As recommended by FAO/WHO, one jujube fruit would meet the daily requirements for the complex vitamin C for an adult man [14]. In a study, ascorbic acid content of jujube was reported to be as 310.32 mg/100g fresh weight at the beginning of maturation and then decreased with maturation to 199.58 mg/100 g. It was indicated that ascorbic acid content of jujube is higher than most reported fruits as source of vitamin C such as kiwi, strawberry, lemon [23,34]. Cosmulescu et al. [15] have reported that ascorbic acid content of two different jujube cultivars were 280.4-250.3 mg/L at the white maturity stage, 321.9-319.2 mg/L at the red maturity stage. Most of studies indicate the highest ascorbic acid value at matured stage [35]. Wojdylo et al. [14] have stated that ascorbic acid content of four different jujube cultivars was ranged from 387 to 555 mg/100 g fresh weight. Gao et al. [22] have also indicated that hardness of fruit was significantly correlated with vitamin C content. Li et al. [21] have found that the amounts of other water-soluble vitamins were 0.04-0.09 mg/100 g for thiamine (B1), 0.05-0.09 mg/100 g for riboflavin (B2) and 192-359 mg/100 g for vitamin C. According to FAO, recommended daily riboflavin intake is 1.1 mg/day for female and 1.3 mg/day for male and recommended daily thiamin intake is 1.1 mg/day for female and 1.2 mg/day for male. Thus, one fresh jujube fruit wouldn't meet daily recommended intake.

Dietary minerals have great important roles in prevention of several diseases. Many researches show that jujube is one of the mineral-richest fruits. Hernandez et al. [5] determined four macro- (potassium, calcium, magnesium, sodium) and four micro-elements

(iron, zinc, copper, manganese) in jujube. It was reported that potassium content of jujube was ranged from 11.9 to 17.3 g/kg dry weight as the highest mineral content [5]. Similarly, Wang et al. [36] have noticed the same result for potassium (13.1 g/kg). Calcium content of jujube was reported to be ranged from 0.23 to 0.72 g/kg and jujube might be considered as calcium source [36]. Jujube was found also rich in micro-elements such as iron (10.2-17.3 mg/kg dry weight), zinc (4.0-5.1 mg/kg dry weight), copper (0.5-1.2 mg/kg dry weight), manganese (0.2-2.9 mg/kg dry weight) by Hernandez et al. [5]. Li et al. [21] have stated that jujube is considered as rich fruit in terms of minerals and potassium (79.2-458 mg/100g fresh weight), calcium (45-118 mg/100g fresh weight), phosphor (59.3-110 mg/100 g fresh weight) and manganese (24.6-51.2 mg/100g fresh weight) have been defined as major minerals in the tested jujubes. Iron (4.68-7.90 mg/100 g fresh weight), sodium (3.22-7.61 mg/100 g fresh weight), zinc (0.35-0.63 mg/100 g fresh weight) and copper (0.19-0.42 mg/100 g fresh weight) were also detected by Li et al. [21].

Phenolic content of fruits plays a key role with regard to improving sensory quality and resistance to some stress conditions [37,38]. Phenolic compounds also show bioactive properties such as antioxidant, anticancer, anti-inflammatory and antiallergic [39]. Ecological conditions, harvest and post-harvest conditions, maturity stage and process conditions of fruits have effects on the phenolics in terms of amount and quality [38]. In general, catechin, epicatechin and rutin are the main flavonoids; caffeic, gallic, chlorogenic and ferulic acid are the main phenolic acids of the jujube fruits [39,29,12,23,24]. Choi et al. [24] identified the flavonoids of jujube as epicatechin, procyanidin B2, kaempferol-glucosyl-rhamnoside, quercetin-3-galactoside, quercetin-3-robinobioside, quercetin-3-rutinoside. Phenolic content of jujube changes during maturation. It was observed that total flavonoid content of jujube decreased with maturity stage from 26.52 to 0.35 g/100 g dry weight [24]. Seven phenolic compounds (catechin, epicatechin, caffeic acid, ferulic acid, p-hydroxybenzoic acid, chlorogenic acid and rutin) were defined in jujube fruits by San and Yildirim [29]. San and Yildirim [29] have also indicated that predominant phenolic compounds of fruits were catechin (2.46-3.74 mg/100 g fresh weight) and rutin (0.88-3.60 mg/100 g fresh weight). Gao et al. [40] have reported that flavanoid content of different jujube cultivars were ranged from 159.3 to 230.3 mg rutin equivalent (RE)/ 100 g fresh weight. Phenolic content of jujube fruit (600.4 Gallic acid equivalent (GAE)/100 g fresh weight) have been reported to be higher than common fruits which are known for their high total phenolic contents such as cranberry (507 mg GAE/100 g fresh weight), red grape (182 mg GAE/100 g fresh weight), strawberry (147.8 mg GAE/100 g fresh weight) [40].

4. Bioactive Properties

4.1 Antioxidant properties

Antioxidants are defined as substances that greatly delay or inhibit the oxidation of materials that can easily be oxidized [41]. Antioxidant substances are divided into two groups as natural or synthetic. Natural antioxidants are extractable compounds which exist in plant and animal tissues or occur during the food processing such as fermentation and heat treatment. Important natural antioxidants include tocopherols, flavonoids, polyphenols, phenolic acids, vitamin C, carotenoids and selenium [42].

Jujube is a very rich fruit in terms of flavonoids and phenolic components. Gao et al. [22] have stated that jujube have more antioxidant activity (AA) than common antioxidative fruits such as pomegranate, guava and sweetsop. In their study trolox equivalent antioxidant capacity (TEAC), total phenolic (TPC) and total flavonoid content (TFC) of jujube fruits were ranged from 1.74 to 7.75 mmol Trolox equivalent (TE)/100 g fresh weight, 275.6 to 541.8 mg GAE/ 100 g fresh weight and 62 to 284.9 mg RE/100 g fresh weight, respectively. The authors have also indicated that higher AA was found in fruits which have higher antioxidant substances such as flavonoid and phenolic content and during the maturation, AA, TPC and TFC decreased [22].

Kou et al. [43] studied fifteen matured jujube cultivars in terms of bioactive compounds and AA. They have demonstrated that AA of jujube mainly depends on ascorbic acid, polyphenols and proanthocyanidins. In the study, AA of methanol extracts of jujube fruits was reported to be ranged from 1.04 to 1.91 mM TE/100 g fresh weight as DPPH values and 224.6 to 406.2 mg ascorbic acid equivalent (AAE)/100 g fresh weight as Ferric Reducing/Antioxidant Power (FRAP) values by Kou et al. [43].

Some researchers have investigated that jujube in the green maturity stage have higher DPPH scavenging activity, FRAP value and phenolic content than ripe jujube [44]. The DPPH radical scavenging activity and FRAP activity were found between 76.01-91.84% in green pulp and 0-85.11% in ripe pulp, respectively; 126.12 and 163.02 mmol FeSO₄/g dry weight in green pulp and 0-148.18 mmol FeSO₄/g dry weight in ripe pulp, respectively. Furthermore, a positive correlation between AA and TPC was reported by Siriamornpun et al. [44].

Cosmulescu et al. [15] have investigated those AA and bioactive compounds of two different jujube cultivars at four maturity stages from white to red maturity. During the maturation, TPC, TFC and AA were reported to be decreased from 1269.6-1643.4 to 475.3-529.5 to mg GAE/100 g, 34.6-48.5 to 19.9-26.7 mg QE/100 g,

1566.4-1661.4 to 1154.6-1164.7 mg AAE/100 g, respectively. They have indicated that TPC, TFC and AA decreased with maturity for two varieties and genotype has effect on amount and composition of bioactive compounds [15].

Four maturity stages of jujube fruits were analyzed in terms of antioxidant capacity and chemical components by Wang et al. [45] and pulp and peel of fruits were separately investigated. The results showed that peel of fruits have higher antioxidant capacity, total phenolic and flavonoid content than the pulp. At green maturity stage, all of these values were the highest level. However, these values significantly decreased during maturation [45]. Wu et al. [23] analyzed that the effect of maturation on some physicochemical properties and AA of jujube. It was stated that maturation levels were identified by red surface area percentage. This study showed that AA, total phenolic, total flavonoid and proanthocyanidin content decreased during the maturation. Epicatechin and cinnamic acid were reported to be found as the dominant phenolic compounds.

Choi et al. [24] determined AA of jujube by 4 methods; Folin Ciocalteu Reducing Capacity (F-C), DPPH Radical Scavenging Assay, ABTS Radical Scavenging Assay and Ferric Reducing/Antioxidant Power (FRAP) Assay. While F-C and FRAP assay were significantly correlated with each other ($r=0.985$), DPPH assay was weakly correlated with other methods ($r=0.8$). These AA methods have different principles such as FRAP and F-C assay detect only electron transfer antioxidants, ABST and DPPH detect electron transfer and hydrogen transfer antioxidants.[46] Therefore, differences between results of these methods may result from different precisions to a variety of antioxidative molecules. To explain the effect of AA in jujube, correlations between different compounds and antioxidant capacity results were calculated by Wojdylo et al. [14]. The results showed that content of ascorbic acid and polyphenolic compounds such as quercetin derivatives, polymeric procyanidins and flavonols related to antioxidant capacity ($r>0.8$). Zhang et al. [12] have investigated antioxidant capacities of the ethanolic extract of different tissues of jujube and it was noticed that flavonoid content of peel is higher than in the seed and pulp. Besides, antioxidant capacity was reported to be related to TPC and TFC in the study ($r>0.98$). In another study, AA and TPC of jujube pulp and peel were investigated by Xue et al. [47] The results of study showed that TPC and AA of jujube peel were found to be higher than pulp in three jujube cultivars. Xue et al. [47] have also reported that antioxidant capacity was measured by three different methods (DPPH, FRAP, TEAC) and all results of these three methods were highly correlated with each other.

There are studies on the relation between AA and peel color of Jujube. In literature, in this context, relation between antioxidant capacity and peel color of jujube was investigated by Xie et al. [48] It was reported that peel color may be an indicator for polyphenol content and antioxidant capacity. The L value represents lightness, and it indicates freshness of fruits [49]. Xie et al. [48] have reported that L values decreased from 87.24 to 58.77 during maturation. A value, which expresses redness, increased gradually from 0.53 to 17.03 during maturation. The b value, represent of yellowness, increased at the beginning of maturation, and then decreased. TPC of jujube peel decreased during maturation, while total flavonoid and proanthocyanidin content of jujube peel increased at first maturation stage and then decreased. It was indicated that higher L value is related to higher content of total phenolics, and it means that jujube would be at the first stage of maturation (unripe). The higher b value is related to higher content of flavonoids and proanthocyanidins which means jujube would be mid-mature. The higher a value related with higher content of total phenolics which means jujube would be fully mature.

4.2 Antimicrobial activity

In recent years, many microorganisms, which cause infections and contagious disease, have developed resistance against antibiotics because of antibiotics' misuse. For this reason, several researchers have indicated requirement of defining novel compounds having antibiotic effect [50]. Antimicrobial activity of fruits depends on cultivar and composition of fruit, species of target microorganism, processing and storage conditions. Proteins, lipids, pH, salts and temperature effect on antimicrobial activity of phenolic substances in fruits [51].

Özkan [52] have reported that jujube has antibacterial activity against gram positive bacterias. The highest antibacterial activity was identified against *Staphylococcus aureus* with 2 mg/mL (methanolic extract of jujube) minimum inhibitory concentration. Similarly, Abd-Alrahman et al. [53] and Ahmad and Beg [54] have stated that jujube extracts have antimicrobial effects on gram positive bacteria such as *S.aureus*. On the other hand, no or poor antimicrobial effects on gram negative bacteria such as *Escherichia coli* was reported by Abd-Alrahman et al. [53] and Ahmad and Beg [54].

4.3. Anticancer activity

It is known that *Ziziphus* species have been used for treatment several diseases such as diabetes, liver complaints, obesity, insomnia, and cancer in Traditional Chinese Medicine [1,9,64]. In cell culture studies, it was reported that *Ziziphus* extracts have anticancer activities on several tumor cell line [55]. It was stated that triterpenic acids were effective bioactive components on

cancer [56]. Additionally, polysaccharides of jujube may show antitumor activity by different mechanisms such as inducing the apoptosis of tumor cells, prevention of oncogenesis and spread of tumor cells, improving immune response to tumors [57,58,59,60,7]. Choi et al. [24] have investigated some chemical properties, antioxidative and cancer cell inhibitory effects of jujube fruits at eight maturity level. Cancer cell inhibitory effect was determined by using MTT (3-(4,5-dimethylthiazol2-yl)-2,5-difeniltetrazolyum-bromür) method. This method is based on measurement the color change of MTT test solution with the cell viability. MTT solution with yellow color is reduced by alive cells to formazan components with purple color, then the absorption is measured. In the study, two normal cell line and three carcinogenic cell line were treated with four doses of the jujube fruits at different maturity levels. Cervical cancer cells were dose-dependently inhibiting all maturity levels, in contrast with normal lung and lung cancer cells inhibition decreased with maturation. It was also noticed that cancer cell inhibition effects of jujube were related to flavonoid content and AA.

Anticancer activity of dried jujube fruit was investigated by Vahedi et al. [61] Jurkat leukemia cell line, HeLa epitheloid cervix and HEP-2 larynx carcinoma cell line was treated by water extract of dried jujube fruit. MTT results showed that jujube has dose-dependently cytotoxic effects on these cell lines [61]. Huang et al. [62] have demonstrated that jujube fruit extracts have anticancer activity in HepG2 hepatocellular carcinoma cell line by inducing apoptosis. In a study, the antiproliferative effects of different extracts obtained from jujube fruit on MCF7 and SKBR3 breast cancer cell lines were investigated. The highest antiproliferative activity was found in the fraction which is rich in triterpenic acid and protocatechuic acid [55]. Antiproliferative activity of deproteinized polysaccharides (DPP) of jujube fruits was evaluated by Hung et al. [63] DPP showed dose- and time-dependent antiproliferative activity against melanoma cells. Hoshyar et al. [64] have proved the in vitro anticancer activity of aqueous jujube extract against breast cell line. Additionally, in vivo experiments showed that due to decreasing the adverse effects of N-Methyl-N-Nitrosourea (NMU) carcinogenesis, jujube fruit could be helpful for treatment of breast cancer. They also indicated that this anticancer effect could be related to AA of jujube. In a study, it was demonstrated that aqueous extracts of two different varieties jujube have cytotoxic effect on leukemic cell line with 375 and 852 µg/mL IC₅₀ (the half maximal inhibitory concentration) values [44].

4.4. Other health benefits

The liver has important role in the body because of functions in biotransformation and detoxification [65]. Therefore, protection of liver or curing liver injuries

with natural sources have been evaluated by many researchers [66]. The hepatoprotective effect of water extracted jujube was investigated and protocatechuic acid, vanillic acid, p-coumaric acid, catechol, p-hydroxybenzoic acid were indicated as the main phenolic compounds by Liu et al. [67] In vivo experiments in mice with alcohol-induced liver damage showed that oral administration of water extracted jujube decreased the level of total cholesterol and triglyceride, activities of serum hepatic AST (aspartate aminotransferase), ALT (alanine aminotransferase) and LDH (lactate dehydrogenase). Alcohol-induced liver damage cause to increasing of these parameters in the serum. Decreasing level of these parameters with oral administration of jujube indicated that jujube has therapeutic and protective effects against alcohol-induced liver damage. In another study, the researchers have shown that jujube fruits extracts have hepatoprotective effects in relation to modulate the oxidative stress in hepatic injury [68]. Selim et al. [69] have investigated effects of jujube and honey on the human hepatocarcinogenesis. The study run with 50 patients who have chronic hepatitis C. Patients were treated with 4 g jujube and 1 g honey three times per day for three months. Results showed that the treatment decreased the level of some parameters related to the disease such as ALT, AST, alkaline phosphatase (ALP), bilirubin. It may be considered the potential of using jujube for natural therapy against hepatocarcinogenesis due to results of the study.

In Traditional Chinese Medicine, jujube has been used for some therapeutic purposes. Mostly encountered problems such as insomnia and anxiety have been treated with jujube [64,70]. Sedative and hypnotic effects of jujube have been associated with decreasing the monoaminergic system activity [71]. Jiang et al. [71] have indicated that most effective sedative and hypnotic functions of jujube were a result of existing saponins. Another disease, which may be treated by jujube, is Alzheimer's Disease. Alzheimer's is memory loss caused by loss of cholinergic neurons of the nucleus basalis of Meynert (NBM) and cortical cholinergic deficiency [72]. Because jujube has activator effect on choline acetyltransferase due to oleamide content, jujube may be useful for therapy of Alzheimer's [73]. Rabiei et al. [72] have indicated that jujube has effects on memory repairing and restoring behavioral disorders produced by NBM lesion.

Nucleotide and flavonoids are specific bioactive components of jujube. For instance, cAMP (cyclic Adenosine Monophosphate) in jujube has important roles in several physiological processes such as neuroprotective effects, antimelancholic properties [74,75]. Additionally, some studies showed that jujube increased the cAMP level in plasma and hippocampus of animals [76]. cAMP has also an important role in gene expression, inhibition of cell proliferation, heart

diseases, allergic diseases [77]. Kou et al. [43] found that the amount of cAMP in jujube ranged from 17.38 to 193.93 $\mu\text{g/g}$ fresh weight.

5. Conclusion

Prevalence of many diseases such as cancer, diabetes, liver diseases, vitamin or mineral insufficiency has increased around the world. Medical treatments and drugs have some adverse effect. Therefore, interest in natural therapeutics has increased. Jujube is one of the richest fruits in nutritional and bioactive compounds. In the current paper, nutritional values and health benefits of jujube were reviewed. In the light of the previous researches,

- The jujube fruit has high phenolic content. Jujube extracts may be used for natural antioxidant extracts because of high phenolic content.
- The jujube is a rich source of ascorbic acid, strong antioxidant substance. Therefore, it may be beneficial to investigate usage potential of jujube as natural vitamin C supplement.
- The knowledge of total phenolics, polysaccharides, triterpene acids, organic acids may be useful for understanding the bioactivity of jujube. Due to bioactive compounds, jujube fruits have a potential medicinal value.

Health benefits of jujube such as anticancer, antioxidant, antidiabetic and hepatoprotective activities have been indicated by previous researches. Further studies are needed to better understanding of curing potential of jujube.

Author's Contributions

Fadime Begüm Tepe: Drafted and wrote the manuscript

Raci Ekinci: Supervised the manuscript

Çetin Kadakal: Supervised the manuscript, checked the English grammar of the manuscript and edited.

Mustafa Nizam Nizamhoğlu: Edited of the manuscript.

Ethics

There are no ethical issues after the publication of this manuscript.

References

- [1]. Guo, S., Duan, J. A., Tang, Y. P., Zhu, Z. H., Qian, Y. F., Yang, N. Y., Shang, E. X., & Qian, D. W. (2010). Characterization of nucleosides and nucleobases in fruits of ziziphus jujuba by UPLC-DAD-MS. *Journal of Agricultural and Food Chemistry*, 58(19), 10774–10780. <https://doi.org/10.1021/jf102648q>
- [2]. Reich, L. (1991). Uncommon fruits worthy of attention: a gardener's guide. Addison-Wesley.



- [3]. Yaşa, F. (2016). Composition of the jujube fruit grown in Turkey and changes in the composition of the jujube fruit during drying. MSc Thesis. Pamukkale University, Denizli, Turkey.
- [4]. Akbolat, D., Ertekin, C., Menges, H. O., Ekinçi, K., & Erdal, I. (2008). Physical and nutritional properties of jujube (*Zizyphus jujuba* Mill.) growing in Turkey. *Asian Journal of Chemistry*, 20(1), 757–766.
- [5]. Hernández, F., Noguera-Artiaga, L., Burló, F., Wojdyło, A., Carbonell-Barrachina, Á. A., & Legua, P. (2016). Physico-chemical, nutritional, and volatile composition and sensory profile of Spanish jujube (*Zizyphus jujuba* Mill.) fruits. *Journal of the Science of Food and Agriculture*, 96(8), 2682–2691. <https://doi.org/10.1002/jsfa.7386>
- [6]. Zheng, H., Lu, H., Zheng, Y., Lou, H., & Chen, C. (2010). Automatic sorting of Chinese jujube (*Zizyphus jujuba* Mill. cv. 'hongxing') using chlorophyll fluorescence and support vector machine. *Journal of Food Engineering*, 101(4), 402–408.
- [7]. Ji, X., Peng, Q., Yuan, Y., Shen, J., Xie, X., & Wang, M. (2017). Isolation, structures and bioactivities of the polysaccharides from jujube fruit (*Zizyphus jujuba* Mill.): A review. *Food Chemistry*, 227, 349–357. <https://doi.org/10.1016/j.foodchem.2017.01.074>
- [8]. Turkish Statistical Institute. Production of Fruits, Beverage and Spice Crops. <https://data.tuik.gov.tr/Bulten/Index?p=Bitkisel-Uretim-Istatistikleri-2021-37249>
- [9]. Gao, Q. H., Wu, C. Sen, & Wang, M. (2013). The Jujube (*Zizyphus Jujuba* Mill.) fruit: A Review of current knowledge of fruit composition and health benefits. *Journal of Agricultural and Food Chemistry*, 61(14), 3351–3363. <https://doi.org/10.1021/jf4007032>
- [10]. Pareek, S. (2013). Nutritional composition of jujube fruit. *Emirates Journal of Food and Agriculture*, 463–470.
- [11]. Wojdyło, A., Figiel, A., Legua, P., Lech, K., Carbonell-Barrachina, Á. A., & Hernández, F. (2016). Chemical composition, antioxidant capacity, and sensory quality of dried jujube fruits as affected by cultivar and drying method. *Food Chemistry*, 207, 170–179. <https://doi.org/10.1016/j.foodchem.2016.03.099>
- [12]. Zhang, H., Jiang, L., Ye, S., Ye, Y., & Ren, F. (2010). Systematic evaluation of antioxidant capacities of the ethanolic extract of different tissues of jujube (*Zizyphus jujuba* Mill.) from China. *Food and Chemical Toxicology*, 48(6), 1461–1465. <https://doi.org/10.1016/j.fct.2010.03.011>
- [13]. Wang, B. N., Cao, W., Gao, H., Fan, M. T., & Zheng, J. Bin. (2010). Simultaneous determination of six phenolic compounds in jujube by LC-ECD. *Chromatographia*, 71(7–8), 703–707. <https://doi.org/10.1365/s10337-010-1485-1>
- [14]. Wojdyło, A., Carbonell-Barrachina, Á. A., Legua, P., & Hernández, F. (2016). Phenolic composition, ascorbic acid content, and antioxidant capacity of Spanish jujube (*Zizyphus jujuba* Mill.) fruits. *Food Chemistry*, 201, 307–314. <https://doi.org/10.1016/j.foodchem.2016.01.090>
- [15]. Cosmulescu, S., Trandafir, I., Nour, V., Achim, G., Botu, M., & Iordanescu, O. (2018). Variation of bioactive compounds and antioxidant activity of jujube (*Zizyphus jujuba*) fruits at different stages of ripening. *Notulae Botanicae Horti Agrobotanici Cluj-Napoca*, 46(1), 134–137. <https://doi.org/10.15835/nbha46110752>
- [16]. Abedini, M. R., Erfanian, N., Nazem, H., Jamali, S., & Hoshyar, R. (2016). Anti-proliferative and apoptotic effects of *Zizyphus Jujube* on cervical and breast cancer cells. 6(2), 142–148.
- [17]. Rajopadhye, A., & Upadhye, A. S. (2016). Estimation of Bioactive Compound, Maslinic Acid by HPTLC, and Evaluation of Hepatoprotective Activity on Fruit Pulp of *Zizyphus jujuba* Mill. Cultivars in India. 2016.
- [18]. Golmohammadi, F. (2013). Medicinal plant of Jujube (*Zizyphus jujuba*) and its indigenous knowledge and economic importance in desert regions in east of Iran: situation and problems. *Journal of Engineering Technology and Applied Sciences*. 3(6), 493–505.
- [19]. Sharma, R., Rana, J.C (2017). Nutritional composition and value added products of Chinese ber (*Zizyphus jujuba* Mill.) growing in Northern hill regions of India. *Indian Journal of Natural Products and Resources*. 7(4), 323-327.
- [20]. Tümen, G., Sekendiz, O.A. (1989). Balıkesir ve merkez köylerinde halk ilacı olarak kullanılan bitkiler. VIII. Bitkisel İlaç Hammaddeleri Toplantısı, Bildiri Kitabı. 347-354.
- [21]. Li, J.W., Fan, L.P., Ding, S.D., Ding, X.L. (2007). Nutritional composition of five cultivars of Chinese jujube. *Food Chemistry*. 10, 454-460.
- [22]. Gao, Q.H., Wu, C.S., Yu, J.G., Wang, M., Ma, Y.J., Li, C.L. (2012). Textural characteristic, antioxidant activity, sugar, organic acid, and phenolic profiles of 10 promising jujube (*Zizyphus jujuba* Mill.) selections. *Journal of Food Science*. 77(11), 1218-1225.
- [23]. Wu, C.S., Gao, Q.H., Guo, X.D., Yu, J.G., Wang, M. (2012). Effect of ripening stage on physicochemical properties and antioxidant profiles of a promising table fruit 'pear-jujube' (*Zizyphus jujuba* Mill.). *Scientia Horticulturae*. 148, 177-184.
- [24]. Choi, S.H., Ahn, J.B., Kim, H.J., Im, N.K., Kozukue, N., Levin, C.E., Friedman, M. (2012). Changes in free amino acid, protein, and flavonoid content in jujube (*Zizyphus jujube*) fruit during eight stages of growth and antioxidative and cancer cell inhibitory effects by extracts. *Journal of Agricultural and Food Chemistry*, 60, 10245-10255.
- [25]. Pu, Y., Ding, T., Wang, W., Xiang, Y., Ye, X., Li, M., Liu, D. (2018). Effect of harvest, drying and storage on the bitterness, moisture, sugars, free amino acids and phenolic compounds of jujube fruit (*Zizyphus jujuba* cv. Junzao). *Journal of the Science of Food and Agriculture*. 98(2), 628-634.
- [26]. Malgorzata, W., Konrad, P.M., Zielinski, H. (2016). Effect of roasting time of buckwheat groats on the formation of Maillard reaction products and antioxidant capacity. *Food Chemistry*. 196, 355-358.
- [27]. Serradilla, M.J., Martín, A., Ruiz-Moyano, S., Hernández, A., López-Corrales, M., de Guía Córdoba, M. (2012). Physicochemical and sensorial characterisation of four sweet cherry cultivars grown in Jerte Valley (Spain). *Food Chemistry*. 133(4), 1551-1559.
- [28]. Poyrazoglu, E., Gokmen, V., Artik, N. (2002). Organic acids and phenolic compounds in pomegranates (*Punica granatum* L.) grown in Turkey. *Journal of Food Composition Analysis*. 14, 567–75.
- [29]. San, B., Yildirim, A.N. (2010). Phenolic, alpha-tocopherol, beta-carotene and fatty acid composition of four promising jujube (*Zizyphus jujuba* Miller) selections. *Journal of Food Composition and Analysis*. 23, 706-710.
- [30]. Xiao, H.W., Pan, Z., Deng, L.Z., El-Mashad, H.M., Yang, X.H., Mujumdar, A.S., Gao, Z.J., Zhang, Q. (2017). Recent developments and trends in thermal blanching—A comprehensive review. *Information Processing in Agriculture*. 4(2), 101-127.
- [31]. Chirkin, V., Karpov, S., Selemenev, V., Shumskiy, N. (2013). Determination of fat-soluble vitamins in foods, vitamin and mineral formulations, feed premixes, and blood serum by reversed-phase HPLC. *Journal of Analytical Chemistry*. 68(8), 820-825.
- [32]. Bendich, A., Machlin, L.J., Scandurra, O., Burton, G.W., Wayner, D.D.M. (1986). The antioxidant role of vitamin C. *Advances in Free Radical Biology & Medicine*. 2, 419-444.

- [33]. Food and Agriculture Organization of the United Nations. Human Vitamin and Mineral Requirements. <http://www.fao.org/3/a-y2809e.pdf>.
- [34]. Frenich, A.G., Torres, M.H., Vega, A.B., Vidal, J.M., Bolanos, P.P. (2005). Determination of ascorbic acid and carotenoids in food commodities by liquid chromatography with mass spectrometry detection. *Journal of Agricultural and Food Chemistry*. 53(19), 7371-7376.
- [35]. Moradinezhad, F., Setayesh, F., Mahmoodi, S., Khayyat, M. (2016). Physicochemical properties and nutritional value of jujube (*Ziziphus jujuba* Mill.) fruit at different maturity and ripening stages. *International Journal of Horticultural Science and Technology*. 3(1), 43-50.
- [36]. Wang, Y.G., Ma, Y.L., Liu, X.F., Wang, X.L., Wang, Y.L., Ren, H.W. (2014). Composition analysis and nutritional evaluation of *Ziziphus jujuba* Mill. Cv. Xiaokou. *Modern Food Science and Technology*. 30, 23.
- [37]. Lancaster, J.E., Reay, P.F., Norris, J., Butler, R.C. (2000). Induction of flavonoids and phenolic acids in apple by UV-B and temperature. *The Journal of Horticultural Science and Biotechnology*. 75(2), 142-148
- [38]. Davik, J., Kjersti Bakken, A., Holte, K., Blomhoff, R. (2006). Effects of genotype and environment on total anti-oxidant capacity and the content of sugars and acids in strawberries (*Fragaria x ananassa* Duch.). *The Journal of Horticultural Science and Biotechnology*. 81(6), 1057-1063.
- [39]. Hudina, M., Liu, M., Veberic, R., Stampar, F., Colaric, M. (2008). Phenolic compounds in the fruit of different varieties of Chinese jujube (*Ziziphus jujuba* Mill.). *The Journal of Horticultural Science and Biotechnology*. 83(3), 305-308.
- [40]. Gao, Q.H., Wu, P.T., Liu, J.R., Wu, C.S., Parry, J.W., Wang, M. (2011). Physico-chemical properties and antioxidant capacity of different jujube (*Ziziphus jujuba* Mill.) cultivars grown in loess plateau of China. *Scientia Horticulturae*. 130(1), 67-72.
- [41]. MacDonald-Wicks, L.K., Wood, L.G., Garg, M.L. (2006). Methodology for the determination of biological antioxidant capacity in vitro. A review. *Journal of the Science of Food and Agriculture*. 86, 2046-2056.
- [42]. Madhavi, D.L., Deshpande, S.S., Salunkhe, D.K. (1996). Food Antioxidants, Technological, toxicological and health perspectives. Markel Dekker, Newyork
- [43]. Kou, X., Chen, Q., Li, X., Li, M., Kan, C., Chen, B., Zhang, Y., Xue, Z. (2015). Quantitative assessment of bioactive compounds and the antioxidant activity of 15 jujube cultivars. *Food Chemistry*. 173, 1037-1044.
- [44]. Siriamornpun, S., Weerapreeyakul, N., Barusrux, S. (2015). Bioactive compounds and health implications are better for green jujube fruit than for ripe fruit. *Journal of Functional Foods*. 12, 246-255.
- [45]. Wang, C., Cheng, D., Cao, J., Jiang, W. (2013). Antioxidant capacity and chemical constituents of chinese jujube (*Ziziphus jujuba* mill.) at different ripening stages. *Food Science and Biotechnology*. 22(3), 639-644.
- [46]. Prior, R.L., Wu, X., Schaich, K. (2005). Standardized methods for the determination of antioxidant capacity and phenolics in foods and dietary supplements. *Journal of Agriculture and Food Chemistry*. 53, 4290-4302.
- [47]. Xue, Z., Feng, W., Cao, J., Cao, D., Jiang, W. (2009). Antioxidant activity and total phenolic contents in peel and pulp of Chinese jujube (*Ziziphus jujuba* Mill) fruits. *Journal of Food Biochemistry*. 33(5), 613-629.
- [48]. Xie, P.J., You, F., Huang, L.X., Zhang, C.H. (2017). Comprehensive assessment of phenolic compounds and antioxidant performance in the developmental process of jujube (*Ziziphus jujuba* Mill.). *Journal of Functional Foods*. 36, 233-242.
- [49]. Zhan, X., Yang, M., Yuan, L., Gong, Y., Xie, Y., Peng, Q., Ye, S., Li, Q., Li, Z. (2016). Prying into the limit of CIE value for TPE-based blue AIEgens in organic light-emitting diodes. *Dyes and Pigments*. 128, 60-67.
- [50]. Ceylan, Ş., Saral, Ö., Özcan, M., Harşit, B. (2017). Determination of antioxidant and antimicrobial activities of bilberry (*Vaccinium myrtillus* L.) extracts in different solvents. *Artvin Coruh University Journal of Forestry Faculty*. 18(1), 21-27.
- [51]. Sağdıç, O. (2003). Sensitivity of Four Patogenic Bacteria to Turkish Thyme and Oregano Hydrosols. *Lebensmittel-Wissenschaft und -Technologie*. 36, 467-473.
- [52]. Özkan, H. İ. (2017). The examination of some biochemical components of jujube fruit (*Ziziphus jujuba* mill.) and its antibacterial, hypoglycaemic and total antioxidant activities. MSc Thesis, Balıkesir University.
- [53]. Abd-Alrahman, S.H., Salem-Bekhit, M.M., Elhalwagy, M.E. (2013). Chemical composition and antimicrobial activity of *Ziziphus jujuba* seeds extract. *Journal of Pure and Applied Microbiology*. 7, 379-385.
- [54]. Ahmad, I., Beg, A.Z. (2001). Antimicrobial and phytochemical studies on 45 Indian medicinal plants against multi-drug resistant human pathogens. *Journal of Ethnopharmacology*. 74(2), 113-123.
- [55]. Plastina, P., Bonofiglio, D., Vizza, D., Fazio, A., Rovito, D., Giordano, C., Barone, I., Catalano, S., Gabriele, B. (2012). Identification of bioactive constituents of *Ziziphus jujube* fruit extracts exerting antiproliferative and apoptotic effects in human breast cancer cells. *Journal of Ethnopharmacology*. 140, 325-332.
- [56]. Tahergorabi, Z., Abedini, M.R., Mitra, M., Fard, M.H., Beydokhti, H. (2015). "Ziziphus jujuba", A red fruit with promising anticancer activities. *Pharmacognosy Reviews*. 9(18), 99.
- [57]. Wasser, S.P. (2002). Medicinal mushrooms as a source of antitumor and immunomodulating polysaccharides. *Applied Microbiology and Biotechnology*. 60(3), 258-274
- [58]. Moradali, M.F., Mostafavi, H., Ghods, S., Hedjaroude, G.A. (2007). Immunomodulating and anticancer agents in the realm of macromycetes fungi (macrofungi). *International Immunopharmacology*. 7(6), 701-724.
- [59]. Ren, L., Perera, C., Hemar, Y. (2012). Antitumor activity of mushroom polysaccharides, A review. *Food & Function*. 3(11), 1118-1130.
- [60]. Yan, J.K., Wang, W.Q., Wu, J.Y. (2014). Recent advances in *Cordyceps sinensis* polysaccharides, Mycelial fermentation, isolation, structure, and bioactivities, A review. *Journal of Functional Foods*. 6, 33-47.
- [61]. Vahedi, F., Najafi, M.F., Bozari, K. (2008). Evaluation of inhibitory effect and apoptosis induction of *Zyzyphus Jujube* on tumor cell lines, an in vitro preliminary study. *Cytotechnology*. 56, 105-111.
- [62]. Huang, X., Kojima-Yuasa, A., Norikura, T., Kennedy, D.O., Hasuma, T., Matsui-Yuasa, I. (2007). Mechanism of the anti-cancer activity of *Ziziphus jujuba* in HepG2 Cells. *The American Journal of Chinese Medicine*. 35(3), 517-532.
- [63]. Hung, C.F., Hsu, B.Y., Chang, S.C., Chen, B.H. (2012). Antiproliferation of melanoma cells by polysaccharide isolated from *Ziziphus jujuba*. *Nutrition*. 28, 98-105.



- [64]. Hoshyar, R., Mohaghegh, Z., Torabi, N., Abolghasemi, A. (2015). Antitumor activity of aqueous extract of *Ziziphus jujube* fruit in breast cancer. An in vitro and in vivo study. *Asian Pacific Journal of Reproduction*. 4(2), 116-122.
- [65]. Cemek, M., Aymelek, F., Büyükkuroğlu, M.E., Karaca, T., Büyükben, A., Yılmaz, F. (2010). Protective potential of Royal Jelly against carbon tetrachloride induced-toxicity and changes in the serum sialic acid levels. *Food and Chemical Toxicology*. 48(10), 2827-2832.
- [66]. Liu, G., Liu, X., Zhang, Y., Zhang, F., Wei, T., Yang, M., Wang, K., Wang, Y., Liu, N., Cheng, H., Zhao, Z. (2015). Hepatoprotective effects of polysaccharides extracted from *Ziziphus jujube* cv. Huanghetanzao. *International Journal of Biological Macromolecules*. 76, 169-175.
- [67]. Liu, N., Yang, M., Huang, W., Wang, Y., Yang, M., Wang, Y., Zhao, Z. (2017). Composition, antioxidant activities and hepatoprotective effects of the water extract of *Ziziphus jujuba* cv. Jinsixiaozao. *RSC Advances*. 7(11), 6511-6522.
- [68]. Shen, X., Tang, Y., Yang, R., Yu, L., Fang, T., Duan, J.A. (2009). The protective effect of *Ziziphus jujube* fruit on carbon tetrachloride-induced hepatic injury in mice by anti-oxidative activities. *Journal of Ethnopharmacology*. 122(3), 555-560.
- [69]. Selim, M.M., Kashwaa, F.A.A., Mohammed, M.S., El-Houseini, M. (2017). Protective role of magic fruit and honey bee against human hepatocarcinogenesis. *Archives in Cancer Research*. 5(4), 159.
- [70]. Zhao, J., Li, S.P., Yang, F.Q., Li, P., Wang, Y.T. (2006). Simultaneous determination of saponins and fatty acids in *Ziziphus jujube* (Suanzaoren) by high performance liquid chromatography-evaporative light scattering detection and pressurized liquid extraction. *Journal of Chromatography A*. 1108, 188-194.
- [71]. Jiang, J.G., Huang, X.J., Chen, J., Lin, Q.S. (2007). Comparison of the sedative and hypnotic effects of flavonoids, saponins, and polysaccharides extracted from Semen *Ziziphus jujube*. *Natural Product Research*. 21(4), 310-320.
- [72]. Rabiei, Z., Rafieian-Kopaei, M., Heidarian, E., Saghaei, E., Mokhtari, S. (2014). Effects of *Ziziphus jujube* extract on memory and learning impairment induced by bilateral electric lesions of the nucleus basalis of meynert in rat. *Neurochemical Research*. 39(2), 353-360.
- [73]. Heo, H.J., Park, Y.J., Suh, Y.M., Choi, S.J., Kim, M.J., Cho, H.Y., Chang, Y.J., Hong, B., Kim, H.K., Kim, E., Kim, C.J., Kim, B.G., Shin, D.H. (2003). Effects of oleamide on choline acetyltransferase and cognitive activities. *Bioscience, Biotechnology, and Biochemistry*. 67(6), 1284-1291.
- [74]. Chen, J., Liu, X., Li, Z., Qi, A., Yao, P., Zhou, Z., Dong, T.T.X., Tsim, K.W.K. (2017). A review of dietary *Ziziphus jujuba* fruit (jujube), Developing health food supplements for brain protection. *Evidence-Based Complementary and Alternative Medicine*. <https://doi.org/10.1155/2017/3019568>.
- [75]. Chi, Y. F., Zhang, Z. (2009). Antimelancholic medicine prepared from jujube cAMP materials, European: CA 2707192.
- [76]. Tian, J.S., Gao, S., Cui, Y.L., Wang, Q.S., Liu, L.P., Zhang, Z.G. (2010). The cyclic AMP content with time variation after oral administration of the extract of *Fructus Jujubae* in mice. *Chinese Journal of Experimental Traditional Medical Formulae*. 16(7), 102-104.
- [77]. Sharma, R., Sharma, S., Siddiqui, S. (2000). Physiology of fruit ripening in jujube-a review. *Haryana Journal of Horticultural Sciences*. 29(1/2), 1-5.

Boron Removal from Colemanite Mine Wastewater by Coagulation using Zinc Hydroxide—A Factorial Optimization Study

Mustafa Korkmaz^{1*} , Cengiz Özmetin¹ , Elif Özmetin¹ , Elif Çalgan¹ , Öznur Ziyanak¹ 

¹Balıkesir University, Engineering Faculty, Environmental Engineering Department, Çağış Campus, Balıkesir Turkey

* korkmazm@balikesir.edu.tr

* Orcid: 0000-0001-8424-6339

Received: 2 July 2021

Accepted: 25 February 2022

DOI: 10.18466/cbayarfbe.951542

Abstract

In this study, boron removal from synthetic solutions and colemanite mine wastewater by coagulation method using in-situ generated zinc hydroxide from zinc chloride salt was investigated. The parameters for Jar test experiments were solution pH (8-12), concentration (50-750 mg/L), temperature (12-40°C), and zinc chloride dosage (1.0204-10.204 g). The saturation pH of zinc hydroxide is 8.93. The boron adsorption capacity reached to maximum value at pH value of 9 and this pH was selected as optimum value. Boron adsorption capacity increased with increasing concentration due to increasing driving force of concentration. High dosages increased the removal percentage. The adsorption of boron to zinc hydroxide had exothermic nature. The optimum conditions obtained from synthetic solutions were applied to the colemanite mine wastewater by 2² factorial designs. The maximum boron adsorption capacity of zinc hydroxide from colemanite mine wastewater was calculated as 43.57 mg/g. The used material and process was promising for boron mine wastewater. The end product of removal from mine wastewater may be used in zinc borate production by solid-state reactions by calcinations.

Keywords: Boron removal, coagulation, colemanite mine wastewater, factorial design, zinc hydroxide.

1. Introduction

Turkey has 61% of the world borate amount and its underground boron richness forms from colemanite, ulexite, pandermite, tincal and kernite minerals [1]. Boron has an average 5-50 ppm concentration in the earth crust [2]. The two of boron chemicals used as boron source in the industrial applications are boric acid and borax. While colemanite deposits of Turkey are located in Bigadiç, Mustafa Kemal Paşa and Kırka regions, the borax deposits are located in Eskişehir region [3]. The excavated colemanite minerals in Bigadiç region are waited in water for swelling of attached soils from the surface of colemanite mineral and these washing waters contain about 382 mg/L boron [4]. The general wastewater of Bigadiç colemanite mine is stored in Çamköy dam and has 627.36 mg/L boron concentration. The boric acid is produced from the reaction of colemanite ore (Ca₂B₆O₁₁·5H₂O) with sulphuric acid and gypsum is produced as solid waste from this reaction [5]. The boric acid production plant located in Bandırma District in Turkey discharges 2,750-3,500 mg/L boron containing wastewater [6].

Borax production in Bandırma plant is formed from the reaction of colemanite mineral with Na₂CO₃ and NaHCO₃ salts. The solid form of CaCO₃ is filtered from mother solution and borax is crystallized [7]. The removal of boron from the wastewater of Bandırma boric acid plant and Bigadiç colemanite mine (Çamköy dam) is necessary because boron is toxic at higher concentrations than needed for humans, animal and plants. For humans, daily intake of boron by drinking water and diet is expected in the range of 0.2–0.6 and 1.2 mg/day, respectively [8]. The tolerable limit value of boron in the irrigation water has been reported as maximum 4 mg/L for asparagus, palm, sugarbeet, clover, onion and etc. [9].

Boron removal from wastewaters is possible by physico-chemical methods. The most investigated methods for boron removal are reverse osmosis, electrocoagulation, ion exchange, coagulation, electro dialysis, solvent extraction and adsorption. These mentioned processes are not capable of production economically valuable end product such as zinc borate except electrocoagulation in which zinc electrodes are

used. Therefore, coagulation with zinc chloride is advantageous for production of zinc borate [10]. Kluckzka and coworkers studied the comparison of activated carbon, zirconium oxide and aluminum oxide and the boron adsorption capacities of the adsorbents were about 0.8, 0.4, 0.4 mg/g for aluminum oxide, activated carbon and zirconium oxide, respectively [11]. In an ion exchange study, Öztürk and coworker reported the optimum pH value as 9 for boron ion exchange reaction with the Dowex 2×8 resin [12]. Lee et al. has reported that the fraction of polyborate ions in solution is higher at 10 °C than 60 °C temperature for boron concentration of 1,000 mg/L [13]. Sayiner and coworkers have reported that the metal hydroxide forming in the electrocoagulation process was of a high adsorption capacity for anion and cations [14]. In another electrocoagulation study reported by Yilmaz and coworkers, the optimum conditions for boron removal from geothermal water were determined as pH (8), 6.0 mA/cm² current density and 333 (Kelvin) temperature [9]. Vasudevan and coworkers reported that the equilibrium data between boron and zinc hydroxide flocs from electrocoagulation process fitted to the Langmuir isotherm suggesting monolayer coverage of boric acid molecules [15]. The boron removal performance of CPA2 reverse osmosis membrane at pH 9 was reported as 61% and 45% at 500 mg/L and 15,000 mg/L NaCl concentrations [16]. Hu et al. reported the performance of a new prepared reverse osmosis membrane for boron removal from waters [17]. Yazıcıgil and coworker determined that the current density was an important operation parameter in electrodialysis process because it transports the ions from one cell to the other through the membrane via driving force of current density and the best removal efficiency was obtained at high current density [18]. The solvent extraction can be applied with organics containing diols.

In the literature, a few studies intending boron removal by chemical coagulation have been reported. In the reported studies, the performance of polyaluminum chloride (PAC) [19], alum [20], aluminum chloride [21] and ferric chloride [22] were tested; however, zinc hydroxide has not been reported in the literature for boron removal from wastewater by coagulation method. The colemanite mine wastewater (The wastewater of Çamköy dam) had about 627.36 mg/L boron. As the zinc chloride addition to boron solution after pH adjustment will cause to residual zinc cation, the pH adjustment after zinc chloride addition is advantageous due to zero zinc concentration at pHs above 8.93. This process enables to production of zinc borate.

2. Materials and Methods

The process was coagulation as the formation of zinc hydroxide and binding of boron on it were occurred simultaneously, but as a result there was a binding process and therefore it can be mentioned for adsorption

process. The pure zinc cations did not remove boron and only in-situ formed zinc hydroxide adsorbed boron. Therefore, boron adsorption capacities of the zinc hydroxides could be calculated. A coagulation-flocculation process was conducted for boron removal from synthetic solutions and colemanite mine wastewater using in-situ generated zinc hydroxide from zinc chloride. The experiments were carried out by applying Jar Test experiments. The zinc chloride (Carlo Erba product) had ≥98% purity and this purity percentage was taken into consideration when the zinc chloride amounts (1, 2.5, 5, 7.5, 10 g) were being calculated. The working boron solutions were prepared using solid boric acid (Merck Product). The boron solutions were prepared at 50-750 mg/L concentrations and solid zinc chloride salt was added and mixed for dissolution and then pHs of the solutions were adjusted on a magnetic stirrer. Thus, zinc hydroxide flocs became formed in the boric acid solutions. The temperature of the solutions was controlled by a temperature-controlled water circulator. The solution containing both of boron and zinc hydroxide in batch jacketed reactors were placed to the Jar Test apparatus and 2.5-5 min rapid mixed for coagulation at 120 rpm and 27.5-30 min slow mixed for flocculation at 30 rpm. At the end of the reaction, the formed flocs were allowed for settling during one hour and 10 mL boron solution was taken from clear portion of the solutions and boron analysis was done by potentiometric method. Boron analysis procedure was as follows [23]: A volume of 5 mL of solution was pipetted into 100 mL beaker and a volume of 50 mL of pure water was added and pH of the solution was adjusted to 7.6 and mannitol was added to the solution up to pH of the solution became stable. Then, the solution was titrated with 0.02 N KOH solution up to the solution pH became again 7.6. 1 mL 0.02 N KOH solution is equal to 0.6964 mg B₂O₃. The spent base volumes in the titration were recorded for boron concentration calculation and also the standardization factors for base solution were measured against 500 mg/L boron solution daily. The obtained optimum conditions from the synthetically prepared solutions were applied to the colemanite mine wastewater as a function of dilution (1 and 20-fold) and coagulant dosage (7.5 and 12.5 g). The characterization of colemanite mine wastewater was as follows: 713 mg/L sulphate, 627.36 mg/L boron, pH (8.50), conductivity 2,137 (µS/cm), total hardness 658.8 (mg CaCO₃/L) and suspended solids (9 mg/L). The used base and acid solutions had 4 M concentration for KOH and 20% (v/v) for concentrated HCl. Throughout the whole experiments the pure water had 22.5 °C temperature. The experimental setup is given in Figure 1. The results of time dependent experiments are given in Figure 2 and optimum time was determined as 32.5 min. The flocculation time was determined as 30 min because the classical flocculation process requires 20-30 minutes to mature the flocs for healthy settling [24]. The boron removal was depended on flocculation. The

approximate base volumes requiring for pH adjustment in synthetic solutions were (10.9-17.3 mL for pH range of 8-12), (10.35-17.5 mL for concentration interval of 50-750 mg/L), (12.3-13 mL for 12-40 °C) and (7.2-40.6 mL for 1.0204-10.2040 g coagulant dosage). The raw solutions throughout the experiments had 500 mL volume. The spended base volumes (10 M KOH) for colemanite mine wastewater in pH adjustment to 9 were around 15 mL for 7.5 g zinc chloride and 25 mL for 12.5 g zinc chloride at 12 °C. Boron adsorption capacities were calculated by the following equation:

$$Q_e(\text{mg/g}) = \frac{((C_0 \times V_1 / 1000) - (C \times V_2 / 1000))}{M} \quad (1)$$

$Q_e(\text{mg/g})$, Boron adsorption capacity, C_0 is initial boron concentration (mg/L), V_1 is the solution volume before base addition (mL), C is the boron concentration at the end of the reaction (mg/L), and V_2 is the solution volume at the end of base addition (mL). M is the mass of zinc hydroxide (g) The saturation pH value for completely precipitation of zinc cations in the reactors was 8.93 and to avoid residual zinc cation after precipitation of zinc hydroxide, the minimum operation pH was selected as 9. The residual zinc concentrations for 2.5510 g zinc chloride at pH values of 9,10,11 and 12 and at pH 10 for 10.2040 g zinc chloride were zero. Residual zinc concentration at pH 8 was 224.7 mg/L. Therefore, after the pH 8 study, the taken solution pH was raised to 9-10 and the solution refiltered and then boron analyzed. For this operation the floc amount is very low.

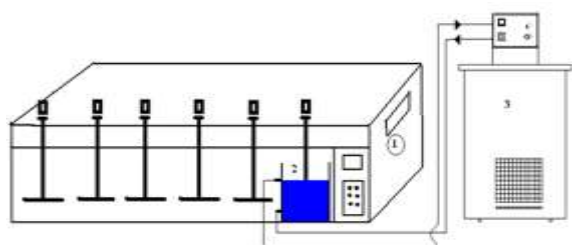


Figure 1. 1-) Jar test apparatus, 2-) Jacketed batch reactor, 3-) Temperature controlled water circulator.

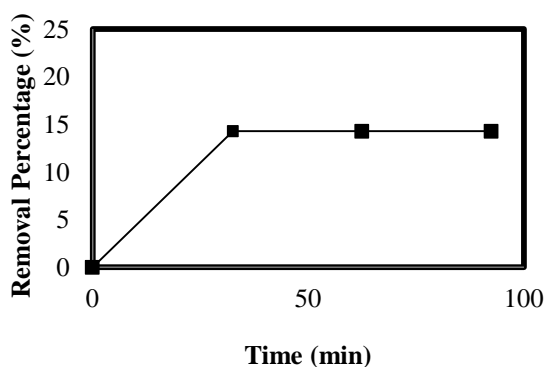


Figure 2. Time effect on removal of boron (pH=10, 22.5 °C, zinc chloride:2.5510g, 250 B-mg/L).

3. Results and Discussion

3.1. pH Effect on Boron Removal

The initial solution pH limits the performance of technologies such as adsorption, reverse osmosis, electro-dialysis, electro-coagulation and etc. Solution pH affects the formation of metal hydroxides in the solution phase when chemical coagulation process is applied. For instance, the aluminum hydroxide is dominate at pH range of 5.5-10 based on aluminum concentration and aluminum hydroxide plays main role in electro-coagulation of boron [21]. Boron removal by zinc hydroxide was studied at pH range of 8-12. The results are given in Figure 3. The experimental parameters were as follows: Temperature (22.5 °C), boron concentration (250 mg/L), zinc chloride amount (2.551 g). The adsorption capacity of zinc hydroxide reached to maximum value at pH 9. The boric acid starts to convert to monoborate anion at pHs above 7 and turns completely to monoborate at pHs above 11 for boron concentration below 270 mg/L [13].

The adsorption capacities belonging to pH effect were 12.38, 20.78, 9.75, 8.59, 5.88 mg/g for 8,9,10,11,12 pHs. The removal percentages were 18.87, 31.80, 16.28, 14.76, 11.63% for 8,9,10,11,12 pHs, respectively. In this study, the dominate form of boron was boric acid and monoborate anion at pH value of 9 [13]. Boron ions adsorbed onto $Zn(OH)_2$ flocs during the removal. The zinc cations were existing at pH below 8.93 and are toxic. For instance, the residual zinc concentration was 224.7 mg/L for pH 8. Adsorption capacity of fresh zinc hydroxide flocs increased at pH 9 due to presence of boric acid molecules and monoborate anions against competitive hydroxyl ions. Boron removal for in-situ formed iron hydroxide was reported as pH (7) and for in-situ formed aluminum hydroxide was reported to reach to maximum value at pH (8) [25,26].

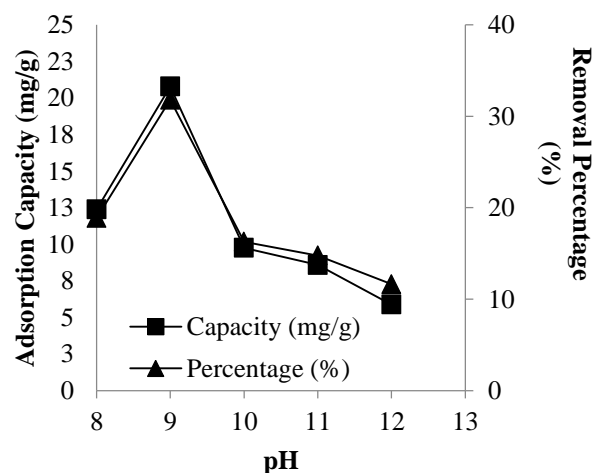


Figure 3. pH effect on removal of boron (250 mg-B/L, 22.5 °C, zinc chloride:2.5510g).

3.2. Concentration Effect on Boron Removal

The polyborates are not present at concentrations below 270 mg/L boron; however, the molar fraction of polyborates rises by concentration increase above 270 mg/L boron [13]. The studied experimental parameters were as follows: Temperature (22.5 °C), pH (10), and zinc chloride amount (2.551 g). The results are given in Figure 4. Boron adsorption capacity change was studied at concentration range of 50-750 mg/L and the capacity increased with increasing concentration. Boron reacts as mainly monoborate anion and boric acid with $Zn(OH)_2$ at pH 10 for boron concentration below 250 mg/L and polyborates were adsorbed on zinc hydroxide floccs at 500-750 mg/L [13]. The adsorption capacities were 5.03, 5.70, 9.75, 26.54 and 42.60 mg/g for 50, 100, 250, 500 and 750 mg/L concentrations, respectively. The removal percentages were 38, 22.49, 16.28, 21.71, 20.71 for concentrations of 50, 100, 250, 500 and 750 mg/L. The high percentage of 750 mg/L than 250 mg/L can be attributed to polyborate formation. The reason of increase of adsorption capacity at high boron concentrations was the low zinc hydroxide-to-boron ratio or high driving force of concentration [4]. Boron adsorption capacity of in-situ formed iron hydroxide was increased with concentration increase [25].

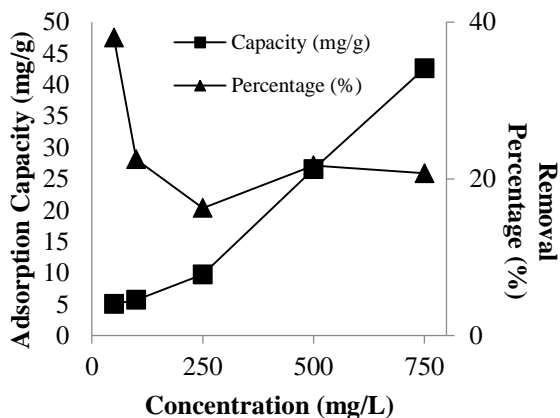


Figure 4. Concentration effect on removal of boron (pH 10, 22.5 °C, zinc chloride:2.5510g).

3.3. Dosage Effect on Boron Removal

The coagulant dosage is important parameter to obtain the maximum removal yield and it should be determined before operation of coagulation-flocculation process. The zinc chloride dosages between 1.0204 and 10.204 g were applied for boron removal from synthetic solutions. The experimental parameters were as follows: Temperature (22.5 °C), pH (10), concentration (250 mg/L). The results are given in Figure 5. Boron adsorption capacities were 9.95, 9.75, 13.76, 12.25 and 9.05 mg/g for 1.0204, 2.551, 5.102, 7.653, and 10.204 g coagulant dosages. Thus, optimum dosage was determined as 5.102 g. The differences in these results

can be attributed to the effective ion-to-adsorbent ratio. The removal percentages were 7.14, 16.28, 42.06, 56.35, 56.35% for 1.0204, 2.551, 5.102, 7.653, and 10.204 g coagulant dosages. The increase of removal percentages with dosage increase was the result of adsorbent active surface increase [1]. Boron adsorption capacity of in-situ iron hydroxide increased with dosage decrease [25].

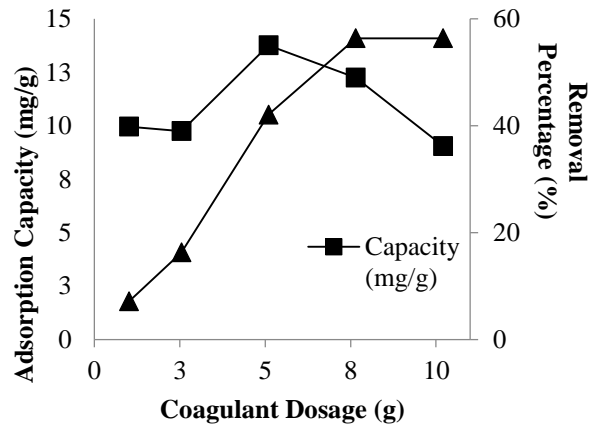


Figure 5. Dosage effect on removal of boron (250 B-mg/L, 22.5 °C, pH 10).

3.4. Temperature Effect on Boron Removal

Polyborate molar fraction increases by decreasing temperature for boron concentration above 270 mg/L [13]. The experimental parameters were as follows: Zinc chloride dosage (2.551 g), pH (10), concentration (250 mg/L). The results are given in Figure 6. Boron adsorption capacities were 12.38, 9.75, 2.99 and 0 mg/g for 12, 22.5, 30, 40 °C temperatures. Boron reacted with $Zn(OH)_2$ species as monoborate anion and boric acid for all the temperatures. The coagulation was exothermic process suggesting the increasing trend of removal yield with decreasing temperature. The removal percentage values for 12, 22.5, 30, 40 °C temperatures were 18.87, 16.28, 6.78 and 0%. Similarly, boron removal by in-situ formed iron hydroxide was reported as exothermic process [25].

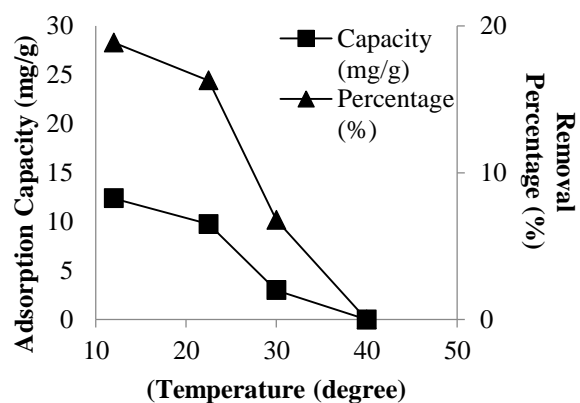


Figure 6. Temperature effect on removal of boron (250 mg-B/L, zinc chloride 2.5510 g, pH 10)

3.5. 2² Factorial Design of Experiments

A factorial experimental design was applied to colemanite mine wastewater with 627.36 mg/L concentration. The design of experiments is a well-known approach for optimization of independent factors. The factorial design of experiments analyzes the responses for changing parameters from low value to the high value. If the limits of parameter levels have been determined before; for example, by traditional classical experiments, the analysis of data set by factorial design will be helpful for establishment of interaction effects belonging to experimental factors. To determine the main (i.e pH or coagulant dosage) and interaction effect (i.e., pH*coagulant dosage) of parameters for boron removal by zinc hydroxide, the four factorial experiments (2²) were carried out. For the present study, the effect of parameters such as dilution factor (1 and 20-fold) and coagulant dosage (7.5 and 12.5 g) were optimized by 2² factorial design using Minitab 16.0 programme. The response used in the statistical analysis was the adsorption capacity (mg/g) of the zinc hydroxide. The number of experiments in the experimental matrix was calculated by the equation of $a^{k_1} \times b^{k_2} = 2^1 \times 2^1 = 4$ where a and b are the number of levels and k₁ and k₂ are the number of factors [4, 27]. The P values (confidence constants) were used as control parameter to check the reliability of the developed statistical model, individual and interaction effects of the parameters. In general, the larger the magnitude of t (Student t-test) and the smaller the value of p, the more significant is the corresponding coefficient term [4, 27]. The general regression model equation is given as follows.

$$\text{Zn(OH)}_2 \text{ (Capacity mg/g)} = b + b_1X_1 + b_2X_2 + b_3X_1X_2 \quad (2)$$

Here; b, b₁, b₂, b₃ are model constants and X₁, X₂ and X₁X₂ are coded factors representing coagulant dosage, dilution factor and dosage-dilution interaction, respectively.

The low and high levels of parameters are given in Table 1. The low and high levels of coagulant dosage (zinc chloride) were 7.5 and 12.5 g while the low and high levels of dilution factor were 1 and 20-fold. The factors and their levels were determined according to preliminary experiments conducted on synthetic solutions. The optimum results (T=12°C, pH=9) determined by synthetic solution experiments were applied to colemanite mine wastewater with 627.36 mg/L concentration. The factorial matrix of experimental design is given in Table 2. The ANOVA analysis (student-t test and confidence levels, p) was performed and is given in Table 3. The confidence limit value (p) for main and interaction effects of parameters was selected as 88% (p<0.12). The optimized factors were abbreviated to be dilution factor (D) and coagulant dosage (CD). The regression model for boron removal

from colemanite mine wastewater by coagulation method was obtained as follows:

$$\text{Capacity (mg/g)} = 52.8534 - 1.4040\text{CD} - 1.8384\text{D} \quad (3)$$

The regression model was developed according to uncoded factors. The results of ANOVA analysis are given in Table 3. According to analysis of ANOVA, only model constant and dilution were found as important parameter and the coagulant dosage was above confidence level (p<0.12). The importance sequence of the parameters and interactions were as follows: dilution and dosage factor. R-Sq, R-Sq(adjusted) values were calculated as 97.09 and 91.26% respectively by Minitab 16.0 programme. The Pareto chart is given in Figure 7. The limit value of the Pareto chart for confidence level was calculated as 5.242 by the programme and the statistically insignificant parameter was dosage. The dilution-dosage interaction factor distorted the fitness of the regression model to the data; therefore, this term was omitted in the analysis in the programme. The maximum boron adsorption capacity of zinc hydroxide from colemanite mine wastewater was calculated as 43.57 mg/g and 92.48% removal was obtained at 20-fold dilution and 12.5 g zinc chloride dosage. Although the boron concentration of colemanite mine wastewater was high from 250 mg/l, the removal percentage of 7.5 g dosage for mine water (627.36 mg/L, initial pH=9, 12 °C) was found as high from synthetic solution (7.6530 g dosage, pH=10 and 250 mg/L concentration, 22.5 °C, Figure 4). This result can be attributed to the formation of polyborates at high concentration and initial pHs and temperatures differences for mine water and synthetic solutions. The removal percentage of 750 mg/L is high than 250 mg/L for synthetic solution (Figure 4) and this result can be related with the polyborate formation. Also, the content of mine water may cause to these results. The residual boron concentrations from colemanite mine wastewater at 7.5-12.5 g dosages and 20 fold dilutions were 4.72-2.36 mg/L, respectively and these values are suitable for usage as irrigation water of mine water.

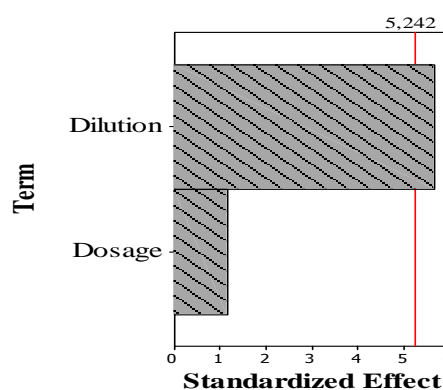


Figure 7. Pareto graphic of analysis

Table 1. Low and high levels of parameters for optimization

Parameters	Abbreviation	Low Level	High Level
Zinc Chloride			
Coagulant Dosage (g)	CD	7.5	12.5
Dilution (Fold)	D	1	20

Table 2. Experimental matrix for optimization and responses (pH:9, temperature:12 °C, concentration: 627.36 mgB L⁻¹)

Experimental Parameters			Adsorption capacity (mg/g)	Removal Percentage (%)
Run	Dosage (g) ZnCl ₂	Dilution (Fold)	Analyzed data by Minitab*	Unanalyzed data by Minitab**
1	7.5	1	43.57*	75.19**
2	7.5	20	2.47*	84.96**
3	12.5	1	30.38*	87.22**
4	12.5	20	1.62*	92.48**

1 fold dilution: (627.36 mg/L/1) and 20 fold dilution: (627.36 mg/L/20)

Table 3. Factorial fitness to boron removal from colemanite mine wastewater (pH:9, temperature:12 °C, concentration: 627.36 mgB L⁻¹)

Term	Effect	Model Coefficients (Uncoded Units)	T	p
Constant		52.8534	6.32	0.100
CD	-7.02	-1.4040	-1.1	0.459
D	-34.93	-1.8384	-5.6	0.111

T:Student T-test, p-value: Statistically confidence value

3.6 Economical Evaluation of Treatment and Comparison with Conventional Coagulants

The kilogram price of commercial zinc chloride, iron chloride and aluminum chloride are \$1, \$0.5, \$0.22. In the study, the zinc chloride was used as raw material for preparation of zinc hydroxide in reactor body and for this purpose 10 M KOH was used. The prices of metal chlorides are very low and their boron removal performances close to each other. In our previous studies, the boron removal performances of iron and aluminum chlorides were studied [25,26]. For instance, boron removal was 44.7 % at 250 mg/L boron solution for 2.5 g/515 mL aluminum chloride at pH=8 and boron removal was 29.71% at 250 mg/L boron solution for 2.5 g/520 mL iron chloride at pH=7 [25,26]. In this study, boron removal was 50.4% at 250 mg/L boron solution for 2.551/510 mL zinc chloride at pH=10. The removal performances of coagulants in the basis of (price)/ (% removal × gram total coagulant amount) was in the sequence of 0.00506, 0.00123, 0.00421 (\$)/(%

removal×gram coagulant) for zinc, aluminum, iron chlorides. Therefore, the advantage sequence of the coagulants was aluminum, iron and zinc chlorides. The treated colemanite mine wastewater is a big problem in Bigadiç boron mine in Balıkesir city and region underground water quality. Also, the solid waste of treatment may be used in zinc borate production by calcination or solid-state reactions [10]. Therefore, this produced zinc borate will contribute an economical value to Turkey and this treatment will solve the environmental problem of the wastewater

4. Conclusion

Boron removal by coagulation from synthetically prepared solutions and colemanite mine wastewater was studied using in-situ generated zinc hydroxide from zinc chloride salt. The results of the study were summarized as follows. The optimum initial solution pH was determined as 9 and the coagulation process had exothermic nature. Boron adsorption capacity increased with increasing concentration and maximum capacity was obtained at 5.1020 g zinc chloride dosage for synthetic solutions. The results obtained from the synthetically prepared solutions were applied to colemanite mine wastewater supplied from the Bigadiç colemanite mine in Balıkesir city of Turkey. The maximum adsorption capacity for optimum conditions in mine wastewater (7.5 g zinc chloride dosage and 1-fold dilution) was obtained as 43.57 mg/g at pH of 9 and 12°C temperature. The experimental factors were optimized by factorial design approach and while dilution factor was statistically important, coagulant dosage was statistically unimportant for boron removal. And also, the treated water can be reused in mine field due to low boron content.

Author's Contributions

Mustafa Korkmaz: Performed the experiment, result analysis and manuscript preparation.

Cengiz Özmetin, Elif Özmetin, Elif Çalgan, Öznur Ziyanak: Helped in manuscript preparation.

Ethics

There are no ethical issues after the publication of this manuscript.

References

- [1]. Korkmaz, M., Özmetin, C., and Fil, B.A. 2016. Modelling of Boron Removal from Solutions Using Purolite S 108 in a Batch Reactor. *CLEAN–SoilAir Water*; 44: 949–958.
- [2]. Vanlı, Ö. 2007. Removal of Pb, Cd, B Elements From Soil By Chelate Assisted Phytoremediation Method. Istanbul Technical University, Institute of Science and Technology, Master in Science Thesis, Istanbul.



- [3]. Bayar, D. 2001. Boron removal from aqueous solution by adsorption and experimental design”, Osman Gazi University, Institute of Science and Technology, Master in Science Thesis, Eskişehir.
- [4]. Korkmaz, M., Fil, B.A., Özmetin, C., and Yaşar, Y. 2014. Full factorial design of experiments for boron removal from Colemanite mine wastewater using PuroLite S 108 resin. *Bulgarian Chemical Communications*; 46:594–601.
- [5]. Özmetin, C., Aydın, Ö., Kocakerim, M.M., Korkmaz, M., and Özmetin, E. 2009. An empirical kinetic model for calcium removal from calcium impurity-containing saturated boric acid solution by ion exchange technology using Amberlite IR-120 resin. *Chemical Engineering Journal*; 148: 420–424.
- [6]. Yılmaz, A.E. 2009. The Boron Removal from industrial wastewater by electrocoagulation method”, Atatürk University, Institute of Science and Technology, Ph.D. Thesis, Erzurum.
- [7]. Dural, E. 1998. Researching of production wastes of borax and boric acid fabrics of Etibank in Bandırma area bletoused in glaze composition (1000 °C-1200 °C). Anadolu University, Institute of Science and Technology, Master in Science Thesis, Eskişehir.
- [8]. Kutlu, M., Aydoğan, G., and Mumcu, E. 2007. Mutagenicity analysis of water samples from Seydisuyu (Kırka, Turkey) stream under the influence of boron production complex, *Food and Chemical Toxicology*; 45:2064–2068.
- [9]. Yılmaz, A.E., Boncukcuoğlu, R., Kocakerim, M.M., Yılmaz, M.T., and Paluluoğlu, C. 2008. Boron removal from geothermal waters by Electrocoagulation. *Journal of Hazardous Materials*; 153:146–151.
- [10]. Kipcak, A. S., Acarali, N. B., Derun, E. M., Tugrul, N., and Piskin, S., 2013. Low temperature solid-state zinc borate synthesis from ZnO and H₃BO₃. *International Journal of Materials and Metallurgical Engineering*; 7:,285-289.
- [11]. Kluczka, J., Ciba, J., Trojanowska, J., Zolotajkin, M., Turek, M., and Dydo, P. 2007. Removal of boron dissolved in water. *Environmental Progress*; 26:71–77.
- [12]. Öztürk, N., and Köse, T.E. 2008. Boron removal from aqueous solutions by ion-exchange resin: Batch studies. *Desalination*; 227: 233–240.
- [13]. Na, J.W., and Lee, K.J., 1993. Characteristics of boron adsorption on strong-base anion-exchange resin. *Annals of Nuclear Energy*; 20:455–462.
- [14]. Sayiner, G., Kandemirli, F., and Dimoglo, A. 2008. Evaluation of boron removal by electrocoagulation using iron and aluminum electrodes. *Desalination*; 230:205–212.
- [15]. Vasudevan, S., Lakshmi, J. and Sozhan, G. 2013. Electrochemically assisted coagulation for the removal of boron from water using zinc anode. *Desalination*; 310:122–129.
- [16]. Oo, M.H., and Song, L. 2009. Effect of pH and ionic strength on boron removal by RO membranes. *Desalination*; 246: 605–612.
- [17]. Hu, J., Pu, Y., Ueda, M., Zhang, X., and Wang, L. 2016. Charge-aggregate induced (CAI) reverse osmosis membrane for sea water desalination and boron removal. *Journal of Membrane Science*; 520:1–7.
- [18]. Yazicigil, Z., and Öztekin, Y. 2006. Boron removal by electrodialysis with anion-exchange membranes. *Desalination*; 190:71–78.
- [19]. Karakaş, Z.K., Yılmaz, M.T., Boncukcuoğlu, R., and Karakaş, İ.H. 2013. The Effect of the pH of the Solution in the Boron Removal using Poly aluminium Chloride (PAC) Coagulant with Chemical Coagulation Method. *Journal Selcuk University Natural and Applied Science*; 2; 339–346.
- [20]. Karcıoğlu, Z., Yılmaz, M.T., and Yılmaz, A.E. 2012. Boron Removal From Industrial Waste Waters By Using Aluminum Sulfate Coagulant With Chemical Methods. *Iğdır University Journal of the Institute of Science and Technology*; 2:15–22.
- [21]. Yılmaz, A.E., Boncukcuoğlu, R., and Kocakerim, M.M. 2007. A quantitative comparison between electrocoagulation and chemical coagulation for boron removal from boron-containing solution. *Journal of Hazardous Materials*; 149:475–481.
- [22]. Golder, A.K., Dhaneesh, V.S., Samanta, A.N. and Ray, S.2008. Removal of nickel and boron from plating rinse effluent by electrochemical and chemical techniques. *Chemical Engineering Technology*; 31:143-148.
- [23]. Foote, F.J.1932. Determination of boron in waters: Method for direct titration of boric acid. *Industrial&Engineering Chemistry Analytical Edition*; 4:39–42.
- [24]. Davis, M.L. Water and wastewater engineering design principles and practice; The McGraw-Hill Companies, Inc., (2010).
- [25]. Özmetin, C., Korkmaz, M. 2019. Full factorial design of experiments for boron removal by iron hydroxide from colemanite mine wastewater. *Balıkesir Üniversitesi Fen Bilimleri Enstitüsü Dergisi*; 21(1):244-253.
- [26]. Korkmaz, M., Özmetin, C., Özmetin, E., Ziyanak, Ö. 2020. Boron removal by coagulation using Al(OH)₃ and factorial optimization of data for boron mine wastewater. *Balıkesir Üniversitesi Fen Bilimleri Enstitüsü Dergisi*; 22(2): 687-697.
- [27]. Kavak, D. 2011. Boron adsorption by clinoptilolite using factorial design. *Environmental Progress&Sustainable Energy*; 30: 527–532.

The Effect of Coating Parameters of Active Layer on the Performance of Polymer Solar Cells

Esma Yenel^{1*} 

¹Konya Technical University, School of Technical Science, Department of Electricity and Energy, Konya Turkey

*esmayenel@gmail.com

*Orcid: 0000-0003-1348-6399

Received: 8 October 2021

Accepted: 20 January 2022

DOI: 10.18466/cbayarfbe.992952

Abstract

In this study, Glass / ITO / PEDOT / Polymer / Al organic solar cell structures were obtained by using glass/indium doped tin oxide (Glass/ITO) transparent metal oxide substrates, PEDOT:PSS and P3HT:PCBM polymer photoactive layer and their performance depending on spin rate and coating technique were investigated. The polymer layer was coated using the spin coating method. Al metal was coated by the physical vapor deposition method. By keeping the concentration of the photoactive layer constant, the effects of different spin coating rates, beside static and dynamic coating technique on the power conversion efficiency of the cells and their stability were compared. Electrical characterization of organic solar cells was performed under a solar simulator in a glove box system. By applying voltage between -0.5 V and +1.5 V, I-V (current-voltage) measurements of the solar cells were taken in the light and dark. The power conversion efficiencies of organic solar cells coated at 800rpm, 1000rpm and 2000rpm spin coating speeds, respectively, were observed to be 2.34%, 2.08% and 1.98%. When the average efficiency values are considered, static coating at 800 rpm gives more reproducible results in comparison with the other average efficiency values. The average efficiency values for static coating at 800 rpm is observed to be %2.

Keywords: Energy, Organic solar cell, Photovoltaic, Polymer solar cell,

1. Introduction

Recently organic solar cells have gained great attention due to their easy fabrication, low cost and flexibility. Organic photovoltaics consist of two organic-based materials compressed between two metal electrodes. The most common type of device is a combination of the donor (p) and acceptor (n) materials. In addition, it is possible to change the chemical structures of the materials, as well as to increase the efficiency with additional materials. In normal type organic solar cells, active P3HT:PCBM layers are produced between a transparent ITO (indium tin oxide) or FTO (fluorine tin oxide) glass and an Al back electrode.

While simple photovoltaic (PV) devices based on organic materials have limited power conversion efficiency (PCE), typically below 0.1%, over time, including dye/dye, polymer/dye, polymer/polymer, and

polymer/fullerene blends showed higher efficiency and have become interesting for researchers. Due to the high electron carrier capability of fullerene, polymer/fullerene mixtures have become a subject of interest in recent years [1]. In polymer solar cells, poly (3-hexylthiophene) (P3HT) and phenyl C61-butyric acid methyl ester (PCBM) are the most widely used materials with improved efficiency. PCBM is a fullerene derivative material. Due to its high electron mobility, it is used as an acceptor material in organic solar cells. P3HT is a commercially available and has a wider absorption spectrum than polyphenylene vinylene (PPV) derivatives that make them another widely used material in this technology.

In conventional organic solar cells, poly (ethylene-dioxythiophene) (PEDOT) solution is coated on the conductive substrate. PEDOT is a thiophene derivative but has poor solubility in water. It is mixed with

polystyrene sulfonate (PSS) to increase the solubility in water and it becomes a proper form for the solution process. Combining with PSS also provides high conductivity which is a requirement for organic solar cells. An active layer is coated on PEDOT:PSS film which improves the quality of the ITO or FTO coated surfaces. The active layer is generally composed of polymer-fullerene derivatives. The typical structure of organic solar cell is shown in **Hata! Başvuru kaynağı bulunamadı..**

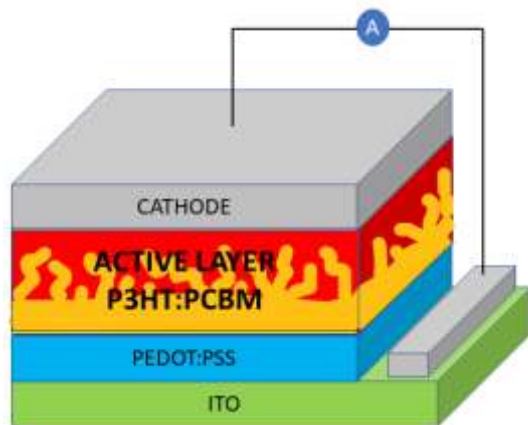


Figure 1. Schematic presentation of a typical organic solar cell.

Photocurrent generation in polymer solar cells consists of 4 steps: light absorption, exciton diffusion, separation of excitons into charge carriers, and charge collection. First, the incident light is absorbed by the active layer and excited molecules are formed in the active layer. The excitations spread in the active layer and dissociate at the interface with different electron affinities to form free charge carriers. Finally, the charge carriers are transported by moving towards the anode and cathode due to the chemical potential difference [2]. There are generally 2 different types of structures for photoactive layer. The heterojunction structure is generally formed by coating the mixture of donor-acceptor materials on a substrate as a mixture. Unlike bulk inorganic semiconductors, organic semiconductor materials do not directly produce free charge carriers by light absorption, but strongly form electron-hole pairs called excitons [3]. Since the exciton diffusion length is typically around 10-20 nm in conjugated polymers, the optimum distance of the exciton diffusion length in donor-acceptor (D/A) interface must be approximately 10-20 nm. For this reason, in bulk-heterojunction structure active contact area, its length and film structure play an important role in charge separation and transport [4]. Therefore, the size of the active contact area has critical importance on

performance. An ideal donor-acceptor configuration should be perfect for efficient exciton dissociation and charge transport (Figure).

The size of the active contact area depends on the optimum microphase separation. While microphase separation can usually be achieved by heat treatment, some methods can be applied during the production process to facilitate this separation. Microphase separation occurs due to the tendency of p and n-type (P3HT and PCBM) semiconductor molecules in mixture to come together. However, the duration of the heat treatment and the applied temperature are important parameters and may vary depending on the ambient conditions. It has been shown in previous studies that the mixing ratios of semiconductor, thermal annealing and type of solvent play a critical role in the performance of organic solar cells [6]. Zhao et al. [5] worked on the 70 nm thick P3HT:PCBM (1:0.8) and exposed them to 120, 130, 140, 150 °C for different periods of time. While the efficiency was 0.74% in the cell without any heat treatment, it was observed that the efficiency increased to 2.54% after 3 minutes of heat treatment at 130 °C. On the other hand, the cell with a thickness of 250 nm of the active layer, the highest value was obtained at 150 °C for 3 minutes. Another parameter that affects solar cell performance is the P3HT/PCBM solvent. P3HT/PCBM dissolves well in solvents such as toluene, chloroform, chlorobenzene. However, solvent evaporation during spin coating is an important factor. Wang et al. examined the effects of mixtures prepared with different solvents and observed that 1,2-dichlorobenzene and chlorobenzene solvents were the best compared to other solvents [7]. They even found very good results with a mixture of two solvents [8].

However, active layer thickness is also a critical parameter and directly affects cell efficiency. Iakobson et al. reported that the thicker the photo active layer, the larger short circuit current (J_{sc}) and photon to current conversion efficiency (PCE). PCE increases more than twice within the studied range[9]. Further increase of the photo active layer thickness leads to increase in roughness. Light harvesting ability increases with increasing film thickness but it results in larger charge diffusion lengths and thus recombination losses [10–12]. Here we have to notice that thicker films do not mean better performance. Because there is a thickness limit for charge diffusion length and optimum thickness must be considered for the best efficiency. Farrokhifar et al showed that more than 90 nm thickness FF value dramatically decreases due to more and more light harvesting which leads an increase of hole density. As

well-known larger holes and excitons leads lower mobility of charge carriers and thus efficiency decreases [10].

In addition to the charge diffusion distance, thickness is also important in microphase separation. On the other hand, the morphological structure of the film is another factor and varies depending on the coating speed and technique.

In this study, besides the coating speed of the active layer, the effect of dynamic or static coating on the performance was investigated. The reproducibility tests of the prepared solar cells were carried out and optimum production conditions were determined over the average efficiency values.

2. Materials and Methods

2.1. Preparation of Solar Cells

ITO coated glasses, which allow light to pass through the active layer easily due to their transparency, are cut in 1.5 cm x 1.5 cm lengths. All glasses were washed with Hellmanex solution in an ultrasonic bath for 10 minutes. Then washing process was continued with water, acetone and propanol, respectively. The cleaned glasses were dried with nitrogen gas and exposed to oxygen plasma for 5 minutes.

PEDOT:PSS was filtered before coating. P3HT:PCBM ratio was adjusted to be 1:0.7. P3HT:PCBM was prepared by dissolving them in chlorobenzene/dichlorobenzene (1:1) solvents. It was incubated overnight on a magnetic stirrer at 45°C. PEDOT:PSS (70 μ l) was statically coated for 40 seconds at 4000 rpm. PEDOT:PSS coated glasses were dried at 120 °C for 10 minutes. Coating was carried out by statically or dynamically by dropping 50 μ l of 2% P3HT:PCBM solution on PEDOT:PSS coated ITO glass. P3HT:PCBM (cb/dcb) solutions were dynamically and statically coated with three different coating speeds of 800, 1000, 2000rpm under the same conditions. Static coating refers to dropping the perovskite solution onto film before spinning while dynamic refers to dropping the solution during spinning. The coated films were heat treated at 150 °C for 10 minutes. Finally, 80 nm Al electrodes were coated by physical vapor deposition technique under 5×10^{-6} torr pressure with an evaporation rate of 0.1 $\text{Å}/\text{s}$ - 5 $\text{Å}/\text{s}$. Figure 3 shows fabrication steps for organic solar cells. After the steps in Figure 1, solar cells with ITO/PEDOT:PSS/P3HT:PCBM/Al concepts were fabricated.

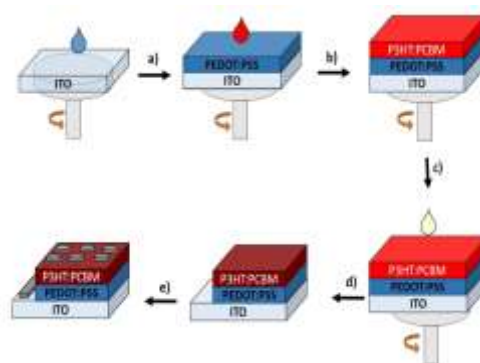


Figure 1. Scheme of preparation of organic solar cells

2.2. IV characterization of solar cells

Electrical characterization of organic solar cells was carried out in the glove box system (from MBraun company) under a solar simulator (Atlas, AM 1.5) by applying voltage between -0.5 V and +1.5 V, I-V (current-voltage). The results were calculated with home-made software. The software provide us all required data such as efficiency, FF, I_{sc} and V_{oc} etc for graphs. Measurements of the solar cells were taken in the light and in the dark. I-V results were evaluated according to the coating speed and static or dynamic coating technique by keeping the active layer mixing ratio and temperature constant.

3. Results and Discussion

Thin films of P3HT/PCBM (1:0.7) prepared in dichlorobenzene (DCB) and chlorobenzene (CB) were prepared separately at 800, 1000, 2000 rpm and compared with each other. Compared to coatings with high rotational speed and coatings with low rotational speed, the film thickness of the higher spin rates will be thin. Thin films absorb light less than thick films [13]. In this study, it is thought that since the cells coated with 800 rpm will be thicker and thus they will absorb more light. A photo of organic solar cells coated in different thicknesses prepared for this work is given in Figure 2.

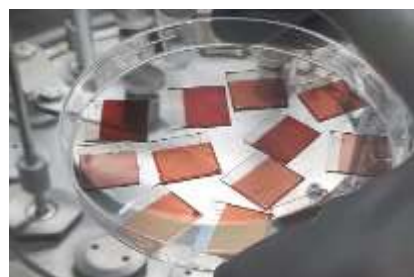


Figure 2. The photo of fabricated solar cells (except for top metal contacts)

The IV graphs of fabricated solar cells are given in Figure 3. In this graph, the best performance for each concept is given. The letter (S or D) at the beginning of the names given in the graphic indicates static or dynamic coating, while the number next indicates the coating speed (rpm). As can be clearly seen in Figure 3, the highest efficiency value was obtained with the dynamic coating technique at 800 rpm, while the lowest efficiency value was observed with the static coating at 2000 rpm (Table 1). In table 1, the last column shows the average values which are obtained from the arithmetic average of all fabricated devices.

Table 1. Characteristics of solar cells

Cell Description	J_{sc} (mA/cm ²)	V_{oc} (mV)	FF	V_{mp} [mV]	Efficiency [%]	Average efficiency (%)
S800	7,52	550	0,42	350	2,15	2,00
D800	7,63	550	0,45	350	2,34	1,87
S1000	7,75	500	0,46	300	2,22	1,92
D1000	7,37	450	0,43	300	1,87	1,79
S2000	5,67	400	0,48	250	1,36	1,18
D2000	6,11	400	0,48	250	1,48	1,37

Considering the static and dynamic coating technique as a basis, different film formations can be obtained according to the viscosity of the solution. While the dynamic coating is expected to give a more uniform morphology in films with low viscosity, ripples are expected on the film surface in the opposite case. The better yields at low coating rates show that both the concentration and the viscosity of the active layer solution are good. On the other hand, another result that supports this situation is the reproducibility values in static and dynamic coatings at low speed. Although the dynamic coating gave the highest efficiency value at 800 rpm, it was observed that the static coating gave more reproducible results at 800 rpm in case reproducibility test results were considered and evaluated.

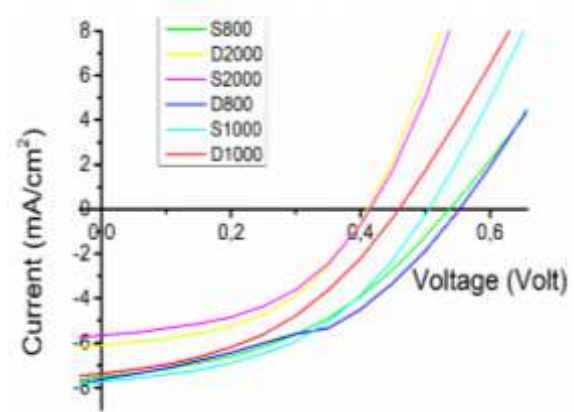


Figure 3. IV curves of solar cells

Looking at Figure 4 shows the reproducibility test results of all cell concepts. As it is known, one of the most critical parameters in solution-based thin-film device technologies such as organic solar cells, organic

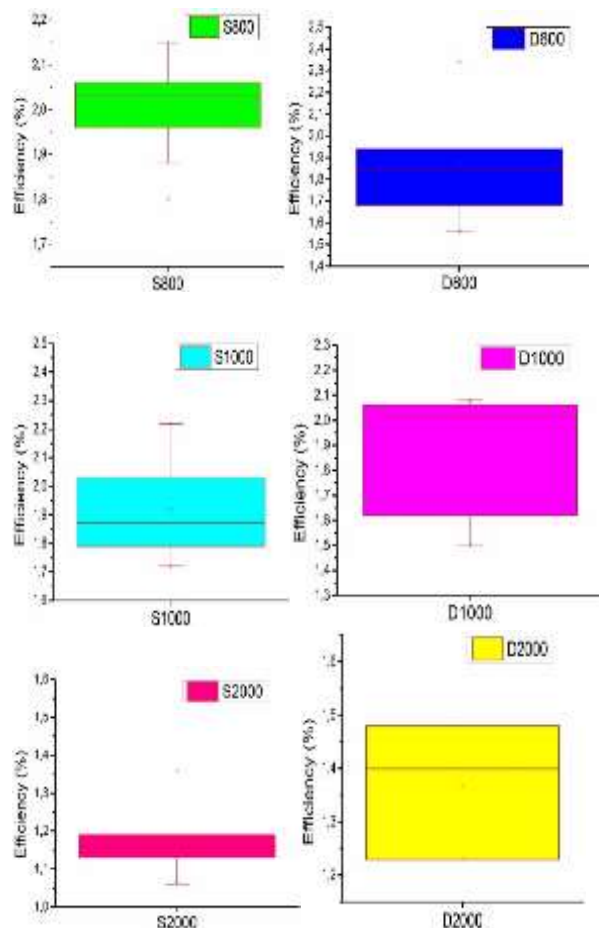


Figure 4. Reproducibility of solar cells.



4. Conclusion

As well-known, stability and reproducibility are critical parameters for organic solar cells. Many researchers focused to improve those parameters with different approaches. In this study, we focused on process optimization for coating parameters to achieve both high efficiency and reproducibility. As a result, using a mixture of chlorobenzene and dichlorobenzene as the solvent given in the experimental part, solvent concentration at the level of 2% and static coating at 800 rpm are the best parameters for reproducible and highly efficient solar cells.

Author's Contributions

Esma Yenel: Drafted and wrote the manuscript, performed the experiment and result analysis.

Ethics

There are no ethical issues after the publication of this manuscript.

References

- [1]. Spanggaard H, Krebs FC. (2004). A brief history of the development of organic and polymeric photovoltaics. *Solar Energy Materials and Solar Cells*. 83(2-3): 125-146. DOI: 10.1016/j.solmat.2004.02.021.
- [2]. Sims L, Egelhaaf HJ, Hauch JA, Kogler FR, Steim R. (2012). Plastic solar cells. *Comprehensive Renewable Energy*. 1(1): 439-480. DOI: 10.1016/B978-0-08-087872-0.00120-7.
- [3]. Gledhill SE, Scott B, Gregg BA. (2005). Organic and nano-structured composite photovoltaics: An overview. *Journal of Materials Research*. 20(12): 3167-3179. DOI: 10.1557/jmr.2005.0407
- [4]. Halls JJM, Pichler K, Friend RH, Moratti SC, Holmes AB. (1996). Exciton diffusion and dissociation in a poly(p-phenylenevinylene)/C60 heterojunction photovoltaic cell. *Applied Physics Letters*, 68(22): 3120-3122. DOI: 10.1063/1.115797.
- [5]. Zhao Y, Duan LP, Liu JT, Xu Q, Ni ZH. (2013). Optimisation of thermal annealing parameters for different thickness of active layers based on polymer/fullerene bulk heterojunction solar cells. *Materials Research Innovations*. 17(SUPPL. 1). DOI: 10.1179/1432891713Z.000000000207.
- [6]. Hoppe H, Sariciftci NS. (2008). Polymer solar cells. *Advances in Polymer Science*. 214(1): 1-86. DOI: 10.1007/12_2007_121.
- [7]. Wang W, Guo S, Herzig EM, Sarkar K, Schindler M, Magerl D. (2016). Investigation of morphological degradation of P3HT:PCBM bulk heterojunction films exposed to long-term host solvent vapor. *Journal of Materials Chemistry A*. 4(10): 3743-3753. DOI: 10.1039/C5TA09873D.
- [8]. Kadem BY, Al-Hashimi MK, Hassan AK. (2014). The effect of solution processing on the power conversion efficiency of P3HT-based organic solar cells. *Energy Procedia*. 50: 237-245. DOI: 10.1016/j.egypro.2014.06.029.
- [9]. Iakobson OD, Gribkova OL, Tameev AR, Nunzi JM. A common optical approach to thickness optimization in polymer and perovskite solar cells. *Scientific Reports* 2021; 11(1): 1-6. DOI: 10.1038/s41598-021-84452-x.
- [10]. Farrokhifar M, Rostami A, Sadoogi N. Opto-electrical simulation of organic solar cells. *Proceedings - UKSim-AMSS 8th European Modelling Symposium on Computer Modelling and Simulation, EMS 2014* 2014: 507-512. DOI: 10.1109/EMS.2014.73.
- [11]. Liu L, Li G. Thickness optimization of organic solar cells by optical transfer matrix. *Proceedings of the IEEE Conference on Nanotechnology* 2011: 332-336. DOI: 10.1109/NANO.2011.6144456.
- [12]. Malti I, Chiali A, Sari NC. Numerical study of electrical behavior of P3HT/PCBM bulk heterojunction solar cell. *Applied Solar Energy (English Translation of Geliotekhnika)* 2016; 52(2): 122-127. DOI: 10.3103/S0003701X16020195.
- [13]. Sariciftci NS, Braun D, Zhang C, Srdanov VI, Heeger AJ, Stucky G. (1993). Semiconducting polymer-buckminsterfullerene heterojunctions. Diodes, photodiodes, and photovoltaic cells. *Applied Physics Letters*; 62(6): 585-587. DOI: 10.1063/1.108863.





General Atom-Bond-Connectivity Index of Graphs

Seda Kinaci^{1*}

¹Vocational School, Tarsus University, Takbaş Mh. Kartaltepe Sk. Tarsus, Mersin. Turkey

*sedakinaci@tarsus.edu.tr

* Orcid: 0000-0002-5334-5091

Received: 28 July 2021

Accepted: 20 January 2022

DOI: 10.18466/cbayarfbe.975636

Abstract

The Atom-bond-connectivity index ABC of a graph G is determined by d_i and d_j . In this paper, sharp results for the general ABC index which has chemical applications are found using different methods. These new results for ABC index are investigated in terms of its edges, its vertices and its degrees. In particular, some relations for general ABC index are obtained involving different Topological indices; Randić index, Zagreb index, Harmonic index and Narumi-Katayama index. Indeed, general ABC index is improved by the help of the maximum and minimum degrees.

Keywords: Atom-Bond-Connectivity index, Topological indices, Generalization.

1. Introduction

A topological index is a popular number involved to graph which is used in chemical graph theory, particularly. Topological index also contributes to the design of pharmacologically active compounds and the identification of environmentally hazardous substances. The most important topological indices base on vertex and edge distances. Randić index is used to model the arms of the carbon atom framework of the alkanes. Randić index is described as [2]

$$R(G) = \sum_{v_i v_j \in E(G)} \frac{1}{\sqrt{d_i d_j}}$$

where $v_i v_j$ indicates the edge of the graph G and d_i is the degree of the vertex v_i . During many years, different indices are improved. Among them, first and second Zagreb indices are recognized by [4,7]

$$Z_1(G) = \sum_{v_i v_j \in E(G)} (d_i + d_j), Z_2(G) = \sum_{v_i v_j \in E(G)} (d_i d_j).$$

Another topological identifier is the Harmonic index that has a prominent place is described in [11]

$$H(G) = \sum_{v_i v_j \in E(G)} \frac{1}{d_i + d_j}$$

A survey of properties of Harmonic index is given in [10,13]. Also the modified Narumi-Katayama index is introduced in [8],

$$NK^*(G) = \prod_{i \in V(G)} (d_i)^{d_i} = \prod_{v_i v_j \in E(G)} (d_i d_j).$$

Nowadays, it is found the atom-bond connectivity index ABC which is a good example of linear and branched alkanes with tensile energy of cycloalkanes. ABC index is an important degree based topological index in [9] such that

$$ABC = ABC(G) = \sum_{v_i v_j \in E(G)} \sqrt{\frac{d_i + d_j - 2}{d_i d_j}}$$

The ABC index plays a significant role in temperature studies in alkanes. [1,3,6] For example, ABC index of ethene (C_2H_4) is $4\sqrt{\frac{2}{3} + \frac{2}{3}}$.

Recently, much attention is being paid to the general ABC index ABC_α is described as

$$ABC_\alpha = ABC_\alpha(G) = \sum_{v_i v_j \in E(G)} \left(\frac{d_i + d_j - 2}{d_i d_j}\right)^\alpha$$

The narrative order of this study is as follows: In Section 2, some results for general ABC index of graphs with some fixed parameters are obtained. In the sequel, some special bounds are outlined and some inequalities using the vertices, the edges and the degrees are

improved. In addition, some novel results for the general ABC index of graphs are pointed out related to Randic index, Zagreb index, Harmonic index and Narumi-Katayama index.

2. Main Results

Let G be a simple, finite, connected graphs with the vertex set $V(G)$ and the edge set $E(G)$. In this section, $\sum_{i,j \in E(G)}$ and $\prod_{i,j \in E(G)}$ is represented by \sum_{ij} and \prod_{ij} respectively.

The article [12] is referred to reader for a classical lemma, the Ozeki's inequality. Also, the following lemma is used to find the bound on general ABC index.

Theorem 2.1. [10] If $\alpha \geq 1$ is an integer and $0 \leq x_1 \leq \dots \leq x_k \leq k - 1$, then

$$(k - 1)^{1-\alpha} \sum_{j=1}^k (x^j)^\alpha \leq \left(\sum_{j=1}^k (x^j)^{\frac{1}{\alpha}} \right)^\alpha$$

For details, see [5,14,15].

2.2. On The General ABC Index For $\alpha = 1$ and $\alpha = 2$

In this subsection, G may have several connected components but G does not contain isolated vertices. Here, general ABC index for $\alpha = 1$ is found by adding an edge to G and by deleting an edge from G . Also, special inequalities for general ABC index are established associated with different topological indices.

Theorem 2.2. Let i and j be nonadjacent vertices of graph G and let $G + ij$ be the graph obtained from G by adding edge ij to it. Then,

- i) $ABC_1(G + ij) \leq ABC_1(G); d_i \geq 2,$
- ii) $ABC_1(G + ij) \geq ABC_1(G); 0 \leq d_i \leq 2.$

Proof: Let $d_i = \mu$ and $d_j = \rho$. For $x, y > 0$,

$$\frac{(\mu + 1) + \rho - 2}{(\mu + 1)y} - \frac{\mu + \rho - 2}{\mu\rho} = \frac{-\rho + 2}{\mu\rho(\mu + 1)}$$

There are two cases in this expression: i) $\rho \geq 2,$
 ii) $0 < \rho \leq 2.$

Let i_1, i_2, \dots, i_k be the neighbours of i in G for $k = d_i$ and let j_1, j_2, \dots, j_l be the neighbours of j in G for $l = d_j$. Let $\alpha = 1$ in general ABC index.

i) For $\rho \geq 2$; the inequality gives

$$ABC_1(G + ij) - ABC_1(G) = \frac{(d_i+1)+(d_j+1)-2}{(d_i+1)(d_j+1)} + \sum_{m=1}^k \left[\frac{(d_i+1)+d_{i_m}-2}{(d_i+1)(d_{i_m})} - \frac{d_i+d_{i_m}-2}{d_i d_{i_m}} \right] + \sum_{n=1}^l \left[\frac{(d_j+1)+d_{j_n}-2}{(d_j+1)(d_{j_n})} - \frac{d_j+d_{j_n}-2}{d_j d_{j_n}} \right] \leq 0$$

ii) Similarly case (i), $ABC_1(G + ij) - ABC_1(G) \geq 0$ for $0 < \rho \leq 2.$

Theorem 2.3. Let i and j be nonadjacent vertices of graph G and let $G - ij$ be the graph obtained from G by deleting edge ij to it. Then,

- i) $ABC_1(G) \geq ABC_1(G - ij); d_i \leq 2,$
- ii) $ABC_1(G) \leq ABC_1(G - ij); d_i \geq 2.$

Proof: Let $d_i = \mu$ and $d_j = \rho$. For $x > 1, \rho > 0$,

$$\frac{\mu + \rho - 2}{\mu\rho} - \frac{(\mu - 1) + \rho - 2}{(\mu - 1)\rho} = \frac{-\rho + 2}{\mu\rho(\mu - 1)}$$

There are two cases in the above expression:

- i) $\rho \geq 2,$ ii) $\rho \leq 2.$

Let i_1, i_2, \dots, i_k be the neighbours of i in G for $k = d_i$ and let j_1, j_2, \dots, j_l be the neighbours of j in G for $l = d_j$, similar to Theorem 3.1.

Let $\alpha = 1$ in general ABC index.

i) For $\rho \geq 2$; the inequality shows

$$ABC_1(G) - ABC_1(G - ij) = \sum_{m=1}^k \left[\frac{d_i + d_{i_m} - 2}{d_i(d_{i_m})} - \frac{(d_i - 1) + d_{i_m} - 2}{(d_i - 1)d_{i_m}} \right] + \sum_{n=1}^l \left[\frac{d_j + d_{j_n} - 2}{d_j(d_{j_n})} - \frac{(d_j - 1) + d_{j_n} - 2}{(d_j - 1)d_{j_n}} \right] - \frac{(d_i - 1) + (d_j - 1) - 2}{(d_i - 1)(d_j - 1)} \leq 0$$

ii) Similarly case (i), $ABC_1(G) - ABC_1(G - ij) \geq 0$ for $\rho \leq 2.$

Theorem 2.4. Let G be a nontrivial graph with the minimum degree δ and the maximum degree Δ . Then,

$$ABC_1(G) \geq \frac{\delta m}{\Delta} + (\delta^2 - 2)R^2(G)$$

Proof: It is seen that $(d_i - \delta)(\Delta - d_j) \geq 0$. Thus, $\Delta d_i + \delta d_j \geq d_i d_j$. It is implies that

$$d_i d_j + \Delta \delta \geq \frac{\Delta}{\delta} (d_i + d_j - 2) + \frac{2\Delta}{\delta}$$

Therefore, the inequality gets $1 + \frac{\Delta \delta}{d_i d_j} \leq \frac{\Delta}{\delta} \frac{d_i + d_j - 2}{d_i d_j} + \frac{2\Delta}{\delta} \frac{1}{d_i d_j}$. That is; $\frac{\delta m}{\Delta} + (\delta^2 - 2) \sum_{ij} \frac{1}{d_i d_j} \leq \sum_{ij} \frac{d_i + d_j - 2}{d_i d_j}$. By the definition of $ABC_\alpha(G)$ for $\alpha = 1$ and $R(G)$, $ABC_1(G) \geq \frac{\delta m}{\Delta} + (\delta^2 - 2)R^2(G).$



Theorem 2.5. Let G be a nontrivial, regular graph with m edges. Then,

$$ABC_1(G) \geq m \frac{2(NK^*(G))^{\frac{1}{2m}} - 2}{NK^*(G)}$$

Proof: By the Aritmetic-Geometric Mean inequality,

$$\begin{aligned} \frac{1}{m} \sum_{ij} \left(\frac{d_i + d_j - 2}{d_i d_j} \right) &\geq \frac{1}{m} \frac{\sum_{ij} (d_i + d_j) - 2m}{\sum_{ij} d_i d_j} \\ &\geq \frac{1}{m} \frac{\sum_{ij} 2\sqrt{d_i d_j} - 2m}{\sum_{ij} d_i d_j} \\ &\geq \frac{2(\prod_{ij} d_i d_j)^{\frac{1}{m}} - 2}{\prod_{ij} d_i d_j} \\ &\geq \frac{2(NK^*(G))^{\frac{1}{2m}} - 2}{NK^*(G)} \end{aligned}$$

Hence,

$$ABC_1(G) \geq m \frac{2(NK^*(G))^{\frac{1}{2m}} - 2}{NK^*(G)}$$

Theorem 2.6. Let G be a graph with n vertices and m edges. Then,

$$ABC_2(G) \leq \frac{H^2(G) - 4M_2(G) - H(G) + 4m}{M_2(G)^2}$$

Proof: Using the definition of $ABC_\alpha(G)$ for $\alpha = 2$; $ABC_2(G)$ is obtained as follows:

$$\begin{aligned} ABC_\alpha(G) &= \sum_{ij} \left(\frac{d_i + d_j - 2}{d_i d_j} \right)^\alpha \\ &\leq \frac{\sum_{ij} (d_i^2 + d_j^2) - 2 \sum_{ij} d_i d_j - 4 \sum_{ij} (d_i + d_j) + \sum 4}{\sum_{ij} (d_i d_j)^2} \\ &\leq \frac{\sum_{ij} (d_i + d_j)^2 - 4 \sum_{ij} d_i d_j - \sum_{ij} (d_i + d_j) + 4m}{M_2(G)^2} \\ &= \frac{H^2(G) - 4M_2(G) - H(G) + 4m}{M_2(G)^2} \end{aligned}$$

2.2. On The General ABC Index

In this subsection, ABC index is generalized and some relations for general ABC index are obtained consepting the degrees.

Theorem 2.7. Let G be a nontrivial graph with $x, y \in \mathbb{R}$. Then,

$$\begin{aligned} ABC_{x+y}(G)ABC_{x-y}(G) - \sigma_{x,y} &\leq ABC_x(G) \\ &\leq \sqrt{ABC_{x+y}(G)ABC_{x-y}(G)} \end{aligned}$$

with

$$\sigma_{x,y} = \begin{cases} 2^{x-2}n^2 \left(\left(\frac{\delta-1}{\delta^2} \right)^x - \left(\frac{\Delta-1}{\Delta^2} \right)^x \right) & ; \text{if } |x| \geq |y| \\ 2^{x-2}n^2 \left(\left(\frac{\Delta-1}{\Delta^2} \right)^{\frac{x+y}{2}} \left(\frac{\delta-1}{\delta^2} \right)^{\frac{x-y}{2}} - \left(\frac{\delta-1}{\delta^2} \right)^{\frac{x+y}{2}} \left(\frac{\Delta-1}{\Delta^2} \right)^{\frac{x-y}{2}} \right) & ; \text{if } |x| < |y| \end{cases}$$

Proof: The Cauchy-Schwarz inequality gives that

$$\begin{aligned} \sum_{ij} \left(\frac{d_i + d_j - 2}{d_i d_j} \right)^\alpha &= \sum_{ij} \left(\frac{d_i + d_j - 2}{d_i d_j} \right)^{\frac{x+y}{2} + \frac{x-y}{2}} \\ &\leq \sum_{ij} \left(\left(\frac{d_i + d_j - 2}{d_i d_j} \right)^{x+y} \right)^{\frac{1}{2}} \sum_{ij} \left(\left(\frac{d_i + d_j - 2}{d_i d_j} \right)^{x-y} \right)^{\frac{1}{2}} \\ &= \sqrt{ABC_{x+y}(G)ABC_{x-y}(G)} \end{aligned}$$

In this expression, there are four cases:

- 1) If $x + y \geq 0$ then, $\left(\frac{2\Delta-2}{\Delta^2} \right)^{\frac{x+y}{2}} \leq \left(\frac{d_i+d_j-2}{d_i d_j} \right)^{\frac{x+y}{2}} \leq \left(\frac{2\delta-2}{\delta^2} \right)^{\frac{x+y}{2}}$.
- 2) If $x + y \leq 0$ then, $\left(\frac{2\delta-2}{\delta^2} \right)^{\frac{x+y}{2}} \leq \left(\frac{d_i+d_j-2}{d_i d_j} \right)^{\frac{x+y}{2}} \leq \left(\frac{2\Delta-2}{\Delta^2} \right)^{\frac{x+y}{2}}$.
- 3) If $x - y \geq 0$ then, $\left(\frac{2\Delta-2}{\Delta^2} \right)^{\frac{x-y}{2}} \leq \left(\frac{d_i+d_j-2}{d_i d_j} \right)^{\frac{x-y}{2}} \leq \left(\frac{2\delta-2}{\delta^2} \right)^{\frac{x-y}{2}}$.
- 4) If $x - y \leq 0$ then, $\left(\frac{2\delta-2}{\delta^2} \right)^{\frac{x-y}{2}} \leq \left(\frac{d_i+d_j-2}{d_i d_j} \right)^{\frac{x-y}{2}} \leq \left(\frac{2\Delta-2}{\Delta^2} \right)^{\frac{x-y}{2}}$.

Let $(x + y)(x - y) \geq 0$. By the Ozeki's inequality, it is seen that

$$\begin{aligned} \sum_{ij} \left(\left(\frac{d_i + d_j - 2}{d_i d_j} \right)^{\frac{x+y}{2}} \right)^2 \sum_{ij} \left(\left(\frac{d_i + d_j - 2}{d_i d_j} \right)^{\frac{x-y}{2}} \right)^2 \\ - \left(\sum_{ij} \left(\frac{d_i + d_j - 2}{d_i d_j} \right)^{\frac{x+y}{2}} \right) \left(\sum_{ij} \left(\frac{d_i + d_j - 2}{d_i d_j} \right)^{\frac{x-y}{2}} \right)^2 \\ \leq \frac{n^2}{4} \left(\left(\frac{2\delta-2}{\delta^2} \right)^{\frac{x+y}{2}} \left(\frac{2\delta-2}{\delta^2} \right)^{\frac{x-y}{2}} \right. \\ \left. - \left(\frac{2\Delta-2}{\Delta^2} \right)^{\frac{x+y}{2}} \left(\frac{2\Delta-2}{\Delta^2} \right)^{\frac{x-y}{2}} \right) \end{aligned}$$

and thus,

$$\begin{aligned} ABC_{x+y}(G)ABC_{x-y}(G) - ABC_x(G) &\leq \\ 2^{x-2}n^2 \left(\left(\frac{\delta-1}{\delta^2} \right)^x - \left(\frac{\Delta-1}{\Delta^2} \right)^x \right). & \end{aligned}$$

It follows that

$$ABC_{x+y}(G)ABC_{x-y}(G) - \sigma_{x,y} \leq ABC_x(G).$$

Let $(x + y)(x - y) < 0$. It is represented that

$$ABC_{x+y}(G)ABC_{x-y}(G) - ABC_x(G) \leq \frac{n^2}{4} \left(\left(\frac{2\Delta - 2}{\Delta^2} \right)^{\frac{x+y}{2}} \left(\frac{2\delta - 2}{\delta^2} \right)^{\frac{x-y}{2}} - \left(\frac{2\delta - 2}{\delta^2} \right)^{\frac{x+y}{2}} \left(\frac{2\Delta - 2}{\Delta^2} \right)^{\frac{x-y}{2}} \right)$$

And thus,

$$ABC_{x+y}(G)ABC_{x-y}(G) - 2^{x-2}n^2 \left(\left(\frac{\Delta-1}{\Delta^2} \right)^{\frac{x+y}{2}} \left(\frac{\delta-1}{\delta^2} \right)^{\frac{x-y}{2}} - \left(\frac{\delta-1}{\delta^2} \right)^{\frac{x+y}{2}} \left(\frac{\Delta-1}{\Delta^2} \right)^{\frac{x-y}{2}} \right) \leq ABC_x(G).$$

Hence,

$$ABC_x(G) \geq ABC_{x+y}(G)ABC_{x-y}(G) - \sigma_{x,y}.$$

Theorem 2.9. Let G be a nontrivial graph with m edges, maximum degree Δ and $2\Delta \leq m - 1$. For any integer $4\alpha \geq 1$,

$$ABC_\alpha(G) \leq \delta^\alpha R_\alpha(G) + \alpha \delta^{\alpha-2} R_{\alpha-1}(G).$$

Proof: It is seen that $(d_i - \delta)(d_j - \delta) \geq 0$. Hence, $(d_i d_j + \delta^2) \geq \delta(d_i + d_j - 2)$. That is; $\left(\frac{d_i d_j}{\delta^2} + 1\right)^\alpha \geq \delta^{-\alpha} (d_i + d_j - 2)^\alpha$.

By the Bernoulli inequality for $x \geq -1$, it gives that

$$\delta^{-\alpha} (d_i + d_j - 2)^\alpha \leq \left(\frac{d_i d_j}{\delta^2} + 1\right)^\alpha \leq 1 + \alpha \frac{d_i d_j}{\delta^2}. \text{ Thus, } \frac{(d_i + d_j - 2)^\alpha}{(d_i d_j)^\alpha} \leq \frac{\delta^\alpha + \alpha \delta^{\alpha-2} d_i d_j}{(d_i d_j)^\alpha} \\ \left(\frac{d_i + d_j - 2}{d_i d_j}\right)^\alpha \leq \frac{\delta^\alpha}{(d_i d_j)^\alpha} + \frac{\alpha \delta^{\alpha-2}}{(d_i d_j)^{\alpha-1}}. \\ \sum_{ij} \left(\frac{d_i + d_j - 2}{d_i d_j}\right)^\alpha \leq \delta^\alpha \sum_{ij} \frac{1}{(d_i d_j)^\alpha} + \alpha \delta^{\alpha-2} \sum_{ij} \frac{1}{(d_i d_j)^{\alpha-1}}.$$

Therefore,

$$ABC_\alpha(G) \leq \delta^\alpha R_\alpha(G) + \alpha \delta^{\alpha-2} R_{\alpha-1}(G).$$

3. Conclusion

ABC index is an important estimation index in chemical graph theory. In this paper, some effects for the **ABC** index and the general **ABC** index are formed by the help of degrees and different topological indices. This paper aims to contribute to the use of the **ABC** index.

Author's Contributions

Seda Kınacı: Prepared and wrote the draft, proved the theorems.

Ethics

In the creation of this article, ethical violations were taken into account and acted within this framework.

References

- [1]. Ahmadi, M.B., Dimitrov, D., Gutman, I., Hosseini, S.A., Disproving a conjecture on trees with minimal atom-bond connectivity index, *MATCH Communications in Mathematical and in Computer Chemistry* 72, 685-698, 2014.
- [2]. Randić, M., On characterization of molecular branching, *Journal of the American Chemical Society* 97, 6609-6615, 1975.
- [3]. Bianchi, M., Cornaro, A., Palacios, J.L., Torriero, A., New upper bounds for the ABC index, *MATCH Communications in Mathematical and in Computer Chemistry* 76, 117-130, 2016.
- [4]. Borovičanić, B., Furtula, B., On extremal Zagreb indices of trees with given domination number, *Applied Mathematics and Computation* 279, 208-218, 2016.

- [5]. Büyükköse, S., Altınk, E., Yalçın, F., Improved Bounds for the Extremal Non-trivial Laplacian Eigenvalues, *Gazi University Journal of Science*, 28, (1), 65-68, 2015.

- [6]. Das, K.C., Atom-bond connectivity index of graphs, *Discrete Applied Mathematics* 158, 1181-1188, 2010.

- [7]. Das, K.C., On comparing Zagreb indices of graphs, *MATCH Communications in Mathematical and in Computer Chemistry* 63, 433-440, 2010.

- [8]. Ghorbani, M., Songhori, M., Gutman, I., Modified Narumi-Katayama index, *Kragujevac J. Sci.* 34, 5764, 2012.

- [9]. Gutman, I., Degree-based topological indices, *Croatica Chemica Acta* 86, 351-361, 2013.

- [10]. Josić, M.R., Josić, M.S., New Results on the Harmonic Index and Its Generalizations, *MATCH Communications in Mathematical and in Computer Chemistry* 78, 387-404, 2017.

- [11]. Fajtlowicz, S., On conjectures of Graffiti-II, *Congressional Number* 60, 187-197, 1987.

- [12]. Kaya Gök, G., Some Bounds on the Distance-Sum-Connectivity Matrix, *Journal of Inequalities and Applications*, 171, 2018.






- [13]. Wua, R., Tanga, Z., Deng, H., A lower bound for the harmonic index of a graph with minimum degree at least two, *Filomat* 27, 51-55, 2013.

- [14]. Kaya Gök, G., On the topological matrix and topological indices, *AKCE International Journal of Graphs and Combinatorics* 1, 252-258, 2020.

- [15]. Bapat, R.B., Graphs and Matrices, Indian Statistical Institute, New Delhi 110016, India, 2010.



Phytochemistry, Biological Activity and Toxicity of Botanical Dietary Supplement: KL21

Çinel Kösal Karayıldırım¹ , Adem Güner² , Gürkan Yiğittürk³ , Altuğ Yavaşoğlu⁴ , N. Ülkü Karabay Yavaşoğlu^{1*} 

¹Ege University, Science Faculty, Biology Department, İzmir, Turkey

²Giresun University, Science and Literature Faculty, Biology Department, Giresun, Turkey

³Muğla Sıtkı Koçman University, Medicine Faculty, Histology and Embryology Department, Muğla, Turkey

⁴Ege University, Medicine Faculty, Histology and Embryology Department, İzmir, Turkey

* ulku.karabay@ege.edu.tr

* Orcid: 0000-0002-7483-0184

Received: 25 June 2021

Accepted: 20 January 2022

DOI: 10.18466/cbayarfbe.957203

Abstract

The use of nutritional supplements has grown conspicuously over the last decades. The present study aimed to design, develop, and optimize the toxicological and biological procedures to perform the quantitative determination of botanical dietary supplement KL21 which is a novel product containing extract form 21 plant species in different amounts. The concentrations of phenolics in KL21 were 11.90 and 258.58 mg for ethanol extract, 3.58 and 86.42 mg for methanol extract, respectively. Carvacrol is a major component of the extracts according to GC-MS analysis. DPPH activity of methanol extract was higher than that of the ethanol extract. Both extracts showed similar relative antioxidant activity according to ABTS+ assay. Only methanol extract exhibited antimicrobial activity. KL21 ethanol extract exhibited inhibitory activity with 50% growth inhibitory concentration of 92.09 µg/mL, 95.47 µg/mL and 44 µg/mL on MCF-7, HeLa and HEK-293 cells respectively. KL21 demonstrated no mutagenic activity with the Salmonella strains. The in vivo toxicity test results indicated that KL21 had no significant adverse effects. Dose-dependent KL21 treatment seemed nontoxic due to biochemical, hematological values. No histological damage in the liver was observed in the tissues. These results suggested that KL21 polyherbal formulation is a natural source of antioxidant with antimicrobial activities and has therapeutic potential in a safe range.

Keywords: Antioxidant activity, Biochemical and hematological analyses, Dietary supplement, Phenolic and flavonoid contents, Toxicity

1. Introduction

Herbal drugs have been used for thousands of years in the worldwide especially they were extensively gained attention on last decades [1, 2]. Numerous herbal ingredients are now used to treat various diseases or health problems [3]. Additionally, there are many polyherbal formulations which can widely have used such as dietary supplements and treatment agents. Moreover, these formulations are source of vitamins, minerals and antioxidant compounds [4]. Because of herbs are source of polyphenolic compounds these formulations are widely used for anti-carcinogenic, anti-viral, anti-inflammatory effects. Also, the quality of polyherbal formulations depends on the composition and concentration of relevant natural compounds. For

these reasons, the quality control studies and toxicological investigations are most important parameters to determine the safety use of polyherbal formulations [5]. Nowadays, many studies that focused on adverse effects of herbal drug combinations results regarding the risk of herbal drug combinations induced adverse effects such as liver injury because of these herbs were contaminated by heavy metals, microbial toxins, pesticides, polycyclic aromatic hydrocarbons and fumigants. These factors can accumulate during the production and manufacturing of herbs and may have adverse effects on consumer health. Recently, the practice on herbal medicine is increasingly used in various diseases with the expectation of reducing drug toxicity, alleviating adverse effects and minimizing recruitment periods. Considering this situation,

reliability and efficiency of these herbal formulations are one of the important health problems for last decade. It is important to find new combinations and also to determine their toxicological level to improve the outcome for patients.

In this study, KL21 was used as a prototype which consisting of *Achillea millefolium* L. (Asteraceae), *Equisetum arvense* L. (Equisetaceae), *Urtica dioica* L. (Urticaceae), *Thymus vulgaris* L. (Lamiaceae), *Viscum album* L. (Viscaceae), *Acorus calamus* L. (Acoraceae), *Rosmarinus officinalis* L. (Lamiaceae), *Solidago vigaurea* L. (Asteraceae), *Silybum marianum* L. (Asteraceae), *Curcuma longa* V. (Zingiberaceae), *Lavandula stoechas* L. (Lamiaceae), *Fumaria officinalis* L. (Papaveraceae), *Taraxacum officinale* L. (Asteraceae), *Cichorium intybus* L. (Asteraceae), *Zingiber officinale* R. (Zingiberaceae), *Peganum harmala* L. (Nitrariaceae), *Juniperus communis* L. (Cupressaceae), *Nigella sativa* L. (Ranunculaceae), *Hypericum perforatum* L. (Hypericaceae), *Valeriana officinalis* L. (Valerianaceae), *Melissa officinalis* L. (Lamiaceae). Standardized KL21 product is approved as a botanical dietary supplement by The Republic of Turkey, Ministry of Agriculture and Forestry. However, there is no information about chemical composition profile and biological activities of KL21. The aim of this study was to assess the total phenolic and flavonoid content, antioxidant capacity and antimicrobial efficacy of KL21 polyherbal formulation. Additionally, it was aimed to analyze the toxicological profile and to investigate histological changes in liver. It allowed acquiring data about this product's therapeutic potential in a safe range.

2. Materials and Methods

2.1. Plant material

KL21 is a novel product containing extract form 21 plant species in different amounts. It is a mixture of *A.millefolium* L. (63 mg), *U.dioica* L. (63 mg), *E.arvense* L. (63 mg), *T.vulgaris* L. (99 mg), *V.album* L. (13 mg), *A.calamus* L. (13 mg), *R.officinalis* L. (27), *S.vigaurea* L. (13 mg), *S.marianum* L. (50 mg), *C.longa* V. (27 mg), *L.stoechas* L. (27 mg), *F.officinalis* L. (27 mg), *T.officinale* L. (27 mg), *C.intybus* L. (27 mg), *Z.officinale* R. (27 mg), *P.harmala* L. (13 mg), *J.communis* L. (27 mg), *N.sativa* L. (13 mg), *H.perforatum* L. (4 mg), *V.officinalis* L. (4 mg), *M.officinalis* L. (13 mg) in a hydroxypropylmethyl cellulose capsule (amount of 1 capsule). Merely, all quality control studies of KL21 have been done by Naturin Nutraceuticals Products Company, Izmir, Turkey. Ethanol and methanol extracts of KL21 were separately prepared.

2.2. Determination of total phenolic and flavonoid contents

The total phenolic compound was determined spectrophotometrically utilizing Folin–Ciocalteu reagent [6]. The total flavonoid compound content was measured as quercetin equivalence [7]. Volatile constituents were determined by Shimadzu QP 2010 plus Gas chromatography Mass spectrometry equipped with Rtx-CL capillary standard non-polar column compose of 100% dimethyl polysiloxane. Approximately 1 g of KL21 extracts were taken into a screw cap vial and 10 mL of acetone was added then 1 µL ethanolic and methanolic solutions were analyzed by GC-MS. The identification of the extracts was performed by Wiley 7 Library data provided by the software of the GC-MS.

2.3. Total antioxidant capacity

The antioxidant capacity of KL21 extracts were determined according to DPPH radical-scavenging activity and ABTS⁺ (Sigma-Aldrich Co., USA) radicalcation decolorisation assays. DPPH assay was performed with 1000 µL of the extracts and 4 mL methanol solution of DPPH. After 30 minutes of incubation at room temperature, the absorbance was read against a blank at 517 nm. Inhibition of a free radical by DPPH in percent was calculated. According to decolorisation assays, ABTS with potassium persulfate generates blue/green ABTS⁺. The radical formed shows a maximum absorbance at 734 nm. The total antioxidant activity percentage (TAA%) was calculated [8].

2.4. Minimum inhibitory concentration test

The bactericidal activity test was evaluated using the following four-gram negative test organisms which are *Escherichia coli* ATCC 11230, *Klebsiella pneumoniae* ATCC 13883, *Salmonella typhimurium* CCM 583, *Pseudomonas aeruginosa* ATCC 27853 and four-gram positive test organisms which are *Staphylococcus aureus* ATCC 6538P, *Staphylococcus epidermidis* ATCC 12228, *Bacillus cereus* ATCC 7064, *Enterococcus faecalis* ATCC 29212. Moreover, the fungicidal activity test was performed using the vegetative cells of *Candida albicans* NCPF 3179 and the spores of *Aspergillus brasiliensis* NCPF 2275. Strains were obtained from Biomerieux® (France) and Microbiologics® (USA). Gentamycin (CAS: 1405-41-0, Sigma Aldrich Co., USA) and Nystatin (CAS: 1400-61-9, Sigma Aldrich, Co., USA) were used as a positive control (NCCLS, 2015).

2.5. Cytotoxicity test

According to cell viability, modified MTT test was performed to determine the cytotoxic effects of KL21 extracts [9]. Human breast adenocarcinoma, Human lung adenocarcinoma, Human colon adenocarcinoma, Human cervix adenocarcinoma and Human embryonic kidney cell lines were maintained in flasks at 37 °C in incubator. The broth was treated with different dilutions (0.1 mg/mL, 1 mg/mL and 10 mg/mL) of KL21 and incubated for 72 hours. Inhibition of cell growth was calculated as IC₅₀ (50 % effective concentration). The results were measured at 570 nm with an UV spectrophotometer. GraphPad Prism (San Diego, USA) was used for the calculation of KL21 causing a 50 % inhibition in comparison to untreated controls.

2.6. The Ames Salmonella/microsome mutation test

Ames MPFtm mutagenicity assay (Xenometrix Inc. Switzerland) was conducted on 4 strains of *Salmonella typhimurium*, tester strains TA98, TA100, TA 1535 and TA 1537 according to the OECD Guideline 471 [10]. TA98 and TA 1537 strains are used for the detection of frameshift mutations and TA100 and TA1535 for base pair substitutions. Genotypes of the strains were checked by Xenometrix Inc. Study design was performed w/wo S9, strain-specific positive control chemicals and bacteria are exposed to 6 concentrations of ethanol and methanol extracts of KL21. Bacterial growth which is mutagenicity is measured colorimetrically by a color change (pH drop) from purple to yellow.

2.7. Animals and experimental design

The study was approved by the Ege University, Local Ethical Committee of Animal Experiment (24.02.2012, 2012-032). Ethical guidelines for investigation of experimental pain unconscious animals were considered all *in vivo* experiments [11]. Mice purchased from the KOBAY Laboratory (Izmir, Turkey). During the study, all animals were weighed daily.

2.7.1. Single dose oral toxicity test

Up-and-Down-Procedure (UDP) was conducted on 5 animals according to OECD Guidelines No: 425 [12]. Doses of KL21 which were applied 175, 500 and 2000 mg/kg. During the lethality period, body weight data and toxicity signs were observed individually. The total observations period was 14 days according to method.

2.7.2. Subacute toxicity test

Repeated dose 28-day oral toxicity study was conducted on male ($n=20$) and female ($n=20$) Swiss albino mice according to OECD Guidelines No: 407 [13].

After acclimation period healthy male and female mice were assigned randomly to groups (300, 600 and 900 mg/kg KL21 and control). All mice were sacrificed end of the study and liver weights were recorded after; liver/body weight ratios were calculated. Blood samples were collected before and end of the study for hematological and biochemical analyses. Routine protocols were performed for evaluation of histological analyses.

2.8. Statistics

All experimental results were the means of experiments performed in triplicate and the data in the tables and figures represent the mean values \pm standard deviations ($n=3$). $p<0.05$ was considered to be statistically significant.

3. Results

3.1. Total phenolic and flavonoid compounds analysis

Total phenolic and flavonoid compound contents of KL21 extracts were demonstrated. The highest contents of these compounds were seen in KL21 ethanol extract (Table 1). GC-MS analysis of the KL21 extracts led to identification and quantification of compounds. Nine compounds were identified constituting 99.9% of the total extracts (Table 2; Fig 1 and 2). Carvacrol has been reported a common major component (45.091% for ethanol extract; 42.414% for methanol extracts).

Table 1. Content of flavonoid and total phenolic compounds of KL21 extracts

Extracts	Phenolic Content (GAE mg /g)	Flavonoid Content (QE mg /g)
Ethanol	258.58 \pm 0.02	11.09 \pm 0.02
Methanol	86.42 \pm 0.03	3.58 \pm 0.02

* GAE: Gallic acid equivalent; QE: Quercetin equivalent

Table 2. Chemical composition of the KL21 extracts

Retention Time (min.)	Compounds	Composition of KL21 Extracts (%)	
		Ethanol	Methanol
7.32	Carvacrol	45.091	42.414
7.98	Eugenol	0.954	0.974
8.57	α -Curcumine	1.495	1.479
8.89	β -Sesquiphellandrene	0.615	0.508
10.94	α -Asarone	8.665	6.230
11.36	β -Tumerone	17.721	11.780
11.75	α -Tumerone	9.143	6.398
15.33	Hexadecanoic acid	6.056	12.409
18.30	Linolenic acid	10.259	17.807

The other most plentiful compounds were identified as β -Tumerone (17.721%), Linolenic acid (10.259%), α -Tumerone (9.143%), α -Asarone (8.665%) and Hexadecanoic acid (6.056%) for ethanol extract. Similarly, Linolenic acid (17.807%), Hexadecanoic acid (12.409%), β -Tumerone (11.780%), α -Tumerone (6.398%) and α -Asarone (6.230%) were identified for most abundant components of methanol extract.

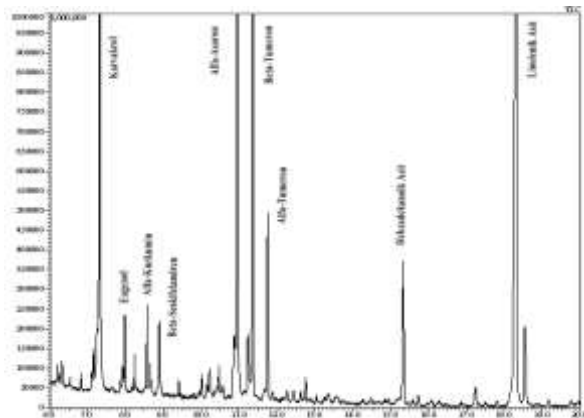


Figure 1. GC-MS chromatogram of KL21 ethanol extract

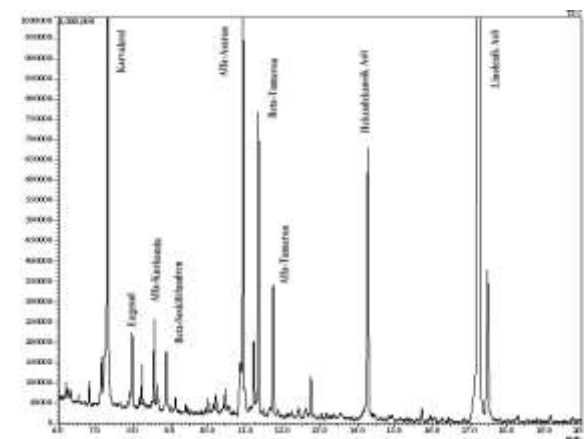


Figure 2. GC-MS chromatogram of KL21 methanol extract

3.2. Antioxidant capacity test

The antioxidant activities of KL21 extracts are demonstrated in Tables 3 and 4. According to DPPH method, methanol extract exhibited higher antioxidant activity than ethanol extract. The extract (0.25 mg/mL) displayed 40.82 % inhibition in the test. Additionally, it has exhibited similar antioxidant effect of α -tocopherol (36.89 mg/mL). Besides the IC_{50} value of methanol extract of KL21 was calculated as 0.294 mg/mL. However, IC_{50} value of ethanol extract was determined as 14.173 mg/mL. These data were demonstrated that lower IC_{50} value indicates higher antioxidant activity (Table 3). Also, both extracts showed similar relative antioxidant activity with antioxidant capacity according to ABTS⁺ assay (Table 4).

Table 3. DPPH radical scavenging activity of KL21 extracts

Extract (mg/mL)	Inhibition (%)	a-Tocopherol equivalent antioxidant activity values (μ g/mL)	IC_{50} (mg/mL)
0.25	40.82 \pm 0.04	36.89 \pm 0.01	
Methanol 0.50	74.86 \pm 0.03	67.66 \pm 0.01	0.294
1	90.66 \pm 0.04	81.94 \pm 0.03	
0.25	0.41 \pm 0.05	22.31 \pm 0.04	
Ethanol 0.50	2.92 \pm 0.01	32.22 \pm 0.02	14.173
1	4.67 \pm 0.02	42.16 \pm 0.03	

* Data expressed as mean \pm SD, IC_{50} : concentrations of extracts for 50% inhibition of DPPH free radicals

Table 4. Total antioxidant activity of KL21 extracts by ABTS assay

Extract (0.125 mg/mL)	ABTS Inhibition (%)	RRA
Ethanol	72.80 \pm 0.02	0.53 \pm 0.02
Methanol	71.70 \pm 0.02	0.52 \pm 0.02

* Data expressed as mean \pm SD, RAA, relative antioxidant activity (TAA% extract/TAA % standard antioxidant compound)

3.3. Antimicrobial activity

In general, there was major differences activity between methanol and ethanol extracts. Methanol extract was active against the tested microorganism with MIC values ranging from 32 to 64 μ g/mL. However, ethanol extract had no activity at the highest concentration (256 μ g/mL) (Table 5).

Table 5. Minimum inhibitor concentration values of KL21 extracts

Microorganism	MIC (mg/mL)			
	Extract		Gentamicin	Nystatin
	Methanol	Ethanol		
<i>S. aureus</i>	32	128	1	-
<i>S. epidermidis</i>	32	128	1	-
<i>S. typhimurium</i>	32	128	1	-
<i>E. coli</i>	32	256	1	-
<i>B. cereus</i>	64	256	4	-
<i>K. pneumoniae</i>	64	256	4	-
<i>E. faecalis</i>	32	256	16	-
<i>P. aeruginosa</i>	32	128	2	-
<i>C. albicans</i>	64	256	-	4
<i>A. brasiliensis</i>	64	256	-	8

3.4. Cytotoxicity test

The MTT results indicated that only ethanol extract inhibits cancer cell proliferation in a dose-dependent manner. The ethanol extract's IC₅₀ values were found to be 92.09 µg/mL and 95.47 µg/mL for 48 h treatment on MCF-7 and HeLa cell lines respectively. 44 µg/mL of ethanol extract and 49 µg/mL dose of methanol extract showed marked cytotoxicity on HEK-293 cell line.

3.5. The *Salmonella*/microsome mutagenicity assay

The mean number of positive yellow wells per 6 doses was calculated from the triplicates and the fold increases above the baseline were determined for each dose of KL21 polyherbal formulation extracts. According to results no mutagenic evidence was determined for maximum dose 5000 µg/mL of KL21 ethanol and methanol extracts (Fig 3 and 4).

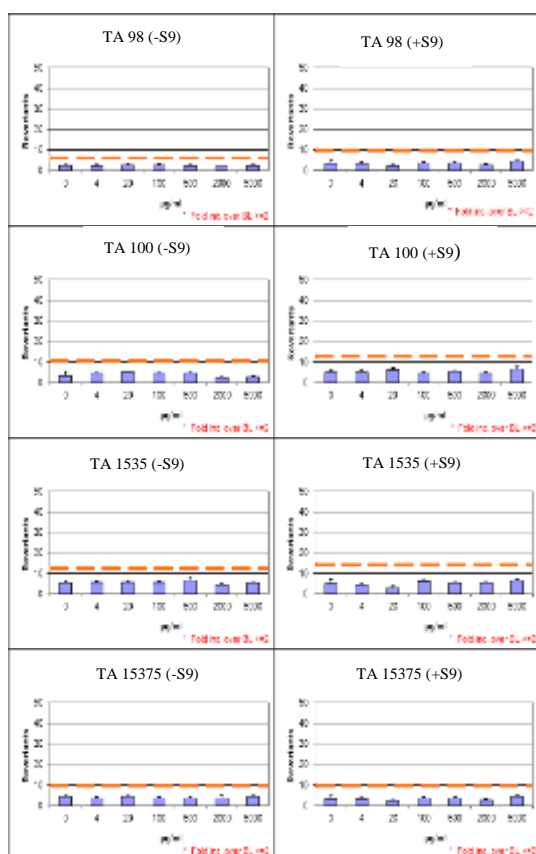


Figure 3. *S. typhimurium* mutagenicity test results of KL21 ethanol extract

3.6. In vivo toxicity test results

Each animal was observed daily throughout the entire 14-day single-oral-dose toxicity test period. There is no abnormal clinical signs or lethality, as well as the observation day and time were recorded (Table 6).

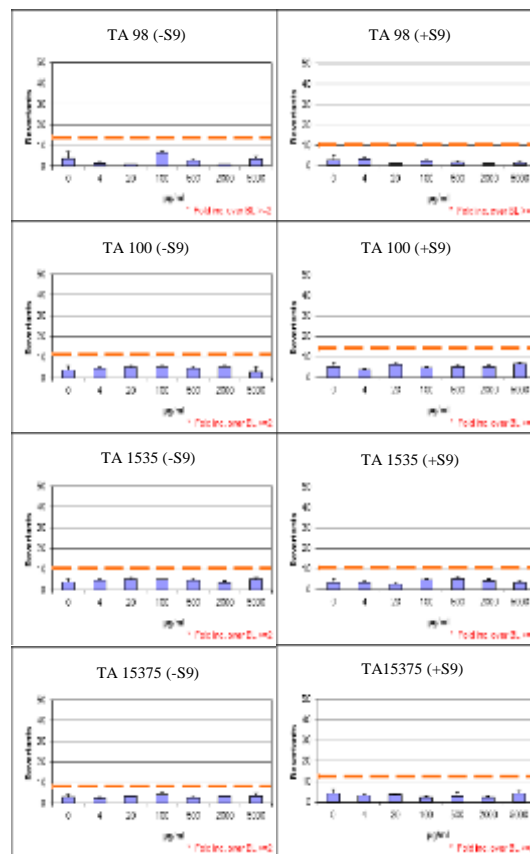


Figure 4. *S. typhimurium* mutagenicity test results of KL21 methanol extract

Table 6. Dose-dependent single dose oral toxicity test result

Step	Include (I) Exclude (E)	Dose (mg/kg)	Response (X) Non-response (O)	Log ₁₀ Dose
1	I	175	O	2.2430
2	I	550	O	2.7404
3	I	2000	O	3.3010
4	I	2000	O	3.3010
5	I	2000	O	3.3010
6	E			
7	E			
8	E			

Calculated maximum LD₅₀ value ≥ 2000 mg/kg

The LD₅₀ is greater than 2000 mg/kg because more than three animal survive.

According to subacute toxicity test results, there was no significant change in body weight gains of the treatment groups in comparison with control groups (Table 7). There were also no important differences in absolute and relative weights of organs of KL21 treated mice when compared with control (p<0.05) (Table 8). There were no significant differences in both biochemical and hematological parameters compared to KL21 treated and control groups in male and female mice (p<0.05). According to comparison between the pre-treatment (day 0), post-treatment (day 28) and control values of female and male mice, it was demonstrated that there were no toxicological significant differences (p<0.05) (Table 9-12).

Hematoxylin-eosin-stained sections of liver tissue were examined for routine histological parameters. According to results histological appearance of liver tissue was evaluated normal in all groups. Regular appearance of vena centralis, vena interlobular, hepatic artery, bile

ducts, sinusoids, eosinophilic cytoplasm, hepatocytes formations and nucleus alterations were also observed in the liver of all treated mice. Additionally, there were no numeric increases of Kupffer cells which were observed (Fig 5 and 6).

Table 7. Body weights of male and female mice of control and KL21 treated groups

Groups	Sex	Body Weight (g) (mean ± SD)				
		Day 0	Day 7	Day 14	Day 21	Day 28
Control	M	24.2 ± 1.16	24.6 ± 1.53	25.1 ± 1.28	28.8 ± 2.61	29.1 ± 2.56
	F	24.1 ± 1.02	25.7 ± 0.74	25.8 ± 0.70	28.5 ± 1.18	28.6 ± 1.15
300 mg/kg	M	24.3 ± 0.99	24.8 ± 1.44	25.0 ± 1.46	28.5 ± 1.69	28.7 ± 1.71
	F	24.4 ± 0.84	25.7 ± 0.57	25.7 ± 0.48	26.9 ± 0.82	27.2 ± 0.85
600 mg/kg	M	24.0 ± 1.22	25.9 ± 0.89	26.4 ± 0.43	27.4 ± 2.70	27.8 ± 2.29
	F	23.4 ± 0.54	24.4 ± 1.33	24.8 ± 1.14	26.5 ± 1.99	27.1 ± 1.59
900 mg/kg	M	24.6 ± 1.51	25.3 ± 0.88	25.8 ± 0.48	27.7 ± 1.09	27.8 ± 0.61
	F	24.4 ± 0.59	25.7 ± 0.91	26.1 ± 0.50	26.1 ± 1.78	26.5 ± 1.56

* Data expressed as mean ± SD, Statistically significant from the control (p<0.05)

Table 8. Organs weights and relative organs weights of male and female mice of control and KL21 treated groups

Groups	Sex	Liver Weight (g)	Relative Liver Weight (g)	Kidney Weight (g)	Relative Kidney Weight (g)	Testicle (g)	Relative Testicle Weight (g)
Control	M	1.54 ± 0.18	0.0528 ± 0.0026	0.38 ± 0.05	0.0131 ± 0.0012	0.16 ± 0.04	0.0055 ± 0.0011
	F	1.47 ± 0.22	0.0517 ± 0.0087	0.32 ± 0.02	0.0109 ± 0.0006	-	-
300 mg/kg	M	1.55 ± 0.15	0.0543 ± 0.0083	0.41 ± 0.01	0.0145 ± 0.0011	0.16 ± 0.01	0.0056 ± 0.0004
	F	1.45 ± 0.11	0.0535 ± 0.0038	0.32 ± 0.06	0.0117 ± 0.0011	-	-
600 mg/kg	M	1.57 ± 0.05	0.0564 ± 0.0028	0.40 ± 0.05	0.0142 ± 0.0015	0.14 ± 0.02	0.0051 ± 0.0006
	F	1.43 ± 0.07	0.0529 ± 0.0056	0.30 ± 0.06	0.0108 ± 0.0016	-	-
900 mg/kg	M	1.56 ± 0.10	0.0561 ± 0.0083	0.39 ± 0.02	0.0139 ± 0.0011	0.15 ± 0.02	0.0053 ± 0.0004
	F	1.46 ± 0.12	0.0553 ± 0.0070	0.39 ± 0.03	0.0112 ± 0.0016	-	-

* Data expressed as mean ± SD, Statistically significant from the control (p<0.05)

Table 9. Biochemical profile of female mice

Parameters	Pre-treatment period (Day 0)				Post-treatment period (Day 28)			
	Control	300 mg/kg	600 mg/kg	900 mg/kg	Control	300 mg/kg	600 mg/kg	900 mg/kg
ALB (g/dL)	3.9±0.6	3.7±0.4	4.1±0.1	4.1±0.2	3.3±0.1	3.0±0.1	3.0±0.4	3.4±0.1
ALP (U/L)	81.2±4.7	82.2±5.2	81.6±9.1	80.6±4.1	87.2±2.7	86.4±6.6	84.8±5.7	86.0±2.4
ALT (U/L)	61.0±7.5	57.0±12.9	58.4±16.1	60.6±14.6	57.4±2.0	56.6±2.5	55.6±4.3	55.8±3.4
AMY (U/L)	841±204	833±190	800±198	802±167	918±67	916±76	906±97	909±78
TBIL (mg/dL)	0.3±0.1	0.3±0.1	0.3±0.1	0.3±0.1	0.2±0.1	0.2±0.1	0.2±0.05	0.2±0.1
BUN (mg/dL)	12.0±1.8	12.2±1.6	12.6±3.2	12.8±2.7	10.2±1.6	10.8±1.3	10.6±0.8	10.8±1.6
Ca (mg/dL)	10.3±0.8	10.4±0.6	10.0±0.8	9.9±0.4	10.6±0.3	10.2±0.5	9.8±0.4	9.7±0.1
Phos (mg/dL)	8.3±1.4	8.1±1.6	8.2±1.3	8.3±1.4	8.1±0.7	8.2±1.6	8.1±0.8	8.8±0.5
Cre (mg/dL)	0.2±0.1	0.2±0.1	0.3±0.0	0.2±0.0	0.1±0.1	0.2±0.1	0.2±0.1	0.2±0.1
GLU (mg/dL)	214±53	216±19	214±16	215±54	223±8	227±17	226±9	222±12
Na (mmol/L)	136.4±3.7	135.2±1.7	135.8±1.9	135.0±3.2	142.0±1.5	142.2±5.2	142.4±4.6	142.0±5.0
K (mmol/L)	6.1±1.6	6.1±1.8	6.0±1.4	6.0±2.0	5.2±0.1	5.2±0.1	5.2±0.3	5.1±0.4
TP (g/dL)	5.4±0.4	5.3±0.5	5.7±0.4	5.5±0.5	6.2±0.2	6.2±0.4	6.3±0.2	6.2±0.3
GLOB (g/dL)	2.2±0.7	2.3±0.6	2.4±0.5	2.8±0.4	2.8±0.5	2.8±0.3	2.8±0.4	2.7±0.1
BA (umol/L)	3.8±2.1	4.0±1.5	3.4±1.8	3.6±2.4	3.2±0.3	3.8±0.3	2.4±0.8	2.0±0.7
Chol (mg/dL)	90.2±9.5	92.8±4.5	96.4±9.4	89.4±16.5	94.8±6.4	95.0±9.1	130.0±11.9	125.8±3.4

* Data expressed as mean ± SD, Statistically significant from the control (p<0.05)

Table 10. Biochemical profile of male mice

Parameters	Pre-treatment period (Day 0)				Post-treatment period (Day 28)			
	Control	300 mg/kg	600 mg/kg	900 mg/kg	Control	300 mg/kg	600 mg/kg	900 mg/kg
ALB (g/dL)	3.4±0.6	3.7±0.4	3.6±0.4	3.5±0.5	3.1±0.1	2.8±0.2	2.8±0.1	3.0±0.2
ALP (U/L)	88.8±7.9	85.2±4.9	89.6±12.2	86.6±7.4	87.6±14.3	89.4±7.8	87.6±3.3	88.4±2.7
ALT (U/L)	64.0±8.2	63.2±6.9	61.8±10.1	58.6±8.9	63.8±3.4	61.2±3.7	62.2±1.7	62.0±2.5
AMY (U/L)	826±78	821±57	818±11	827±30	919±75	917±81	911±90	914±92
TBIL (mg/dL)	0.2±0.1	0.2±0.1	0.2±0.1	0.2±0.1	0.2±0.1	0.2±0.1	0.2±0.1	0.2±0.1
BUN (mg/dL)	11.6±3.1	11.0±2.5	11.4±2.6	11.8±4.0	11.4±1.5	11.0±1.0	11.0±1.8	10.6±1.6
Ca (mg/dL)	10.4±0.6	10.4±0.4	10.2±0.4	10.1±0.3	10.4±0.4	10.1±0.3	10.1±0.4	9.9±0.3
Phos (mg/dL)	8.3±1.2	8.2±1.5	8.5±1.3	8.1±1.6	8.1±0.6	8.20±1.07	8.7±0.7	7.9±1.2
Cre (mg/dL)	0.3±0.1	0.3±0.1	0.3±0.1	0.3±0.1	0.2±0.1	0.20±0.07	0.2±0.0	0.1±0.1
GLU (mg/dL)	213±9	212±8	213±9	211±13	227±5	226±11	227±11	288±8
Na (mmol/L)	137.8±1.1	136.0±1.4	135.6±2.1	136.0±2.5	141.4±2.3	136.0±1.4	142.4±2.3	144.0±23.3
K (mmol/L)	5.3±0.8	5.2±0.4	5.2±0.4	5.2±0.3	5.3±0.4	5.2±0.4	5.3±0.3	5.3±0.2
TP (g/dL)	5.7±0.3	5.5±0.4	5.7±0.5	5.6±0.6	6.3±0.1*	5.5±0.4	6.3±0.1	6.3±0.1
GLOB (g/dL)	2.2±0.6	2.2±0.5	2.3±0.5	2.3±0.5	2.9±0.2	2.2±0.5	2.9±0.1	2.8±0.3
BA (umol/L)	4.0±1.5	3.8±1.3	4.2±1.4	4.0±2.0	4.1±0.1	3.8±0.2	4.0±0.7	3.3±0.1
Chol (mg/dL)	89.8±5.4	89.0±2.5	86.0±6.5	85.0±11.6	89.4±5.7	88.2±1.9	132.0±6.7	138.0±16.1

* Data expressed as mean ± SD

Statistically significant from the control (p<0.05)

Table 11. Hematological profile of female mice

Parameters	Pre-treatment period (Day 0)				Post-treatment period (Day 28)			
	Control	300 mg/kg	600 mg/kg	900 mg/kg	Control	300 mg/kg	600 mg/kg	900 mg/kg
WBC (10 ⁹ cell/L)	8.7±2.3	8.7±2.1	8.5±1.81	8.4±1.5	8.6±1.1	8.2±1.1	8.3±1.1	8.5±1.3
LYM (10 ⁹ cell/L)	5.4±1.3	5.5±1.2	5.3±1.32	5.1±1.4	5.9±0.8	5.8±0.9	5.9±1.4	5.7±1.11
MON (10 ⁹ cell/L)	0.2±0.1	0.3±0.1	0.2±0.2	0.2±0.1	0.3±0.1	0.2±0.1	0.2±0.2	0.2±0.1
NEU (10 ⁹ cell/L)	1.3±0.8	1.4±0.8	1.7±1.0	1.4±1.0	1.7±1.02	1.7±0.9	1.7±1.0	1.7±1.0
RBC (10 ¹² cell/L)	8.1±0.9	8.1±1.1	8.1±1.1	8.2±0.9	8.5±1.3	8.6±1.2	8.3±1.3	8.5±1.0
HGB (g/L)	14.5±0.5	14.5±1.1	14.1±1.2	14.2±1.1	13.9±1.3	13.9±1.1	13.6±1.3	13.8±1.1
HCT (%)	38.6±3.6	40.1±2.6	39.5±3.6	37.9±3.9	39.4±3.9	39.9±4.1	38.1±2.8	38.9±3.6
MCV (fl)	48.0±3.3	47.4±2.7	47.8±1.9	46.8±2.1	48.6±2.9	48.4±2.8	48.8±3.3	48.2±2.6
MCH (pg)	12.2±0.7	12.1±0.8	11.8±0.7	11.9±0.8	11.9±0.7	11.8±0.7	11.9±0.2	11.7±0.6
MCHC (g/dL)	28.1±2.1	28.1±2.3	27.5±2.2	28.0±2.4	28.4±1.1	28.8±0.8	28.2±2.5	28.0±1.5
RDWc (%)	18.5±0.8	18.3±0.4	18.5±0.5	18.2±0.7	18.9±0.4	18.7±0.4	18.7±0.6	18.9±0.9
PLT (10 ⁹ cell/L)	294.6±25.1	292.0±33.4	282.4±85.4	293.2±69.1	343.8±45.1	311.8±35.8	358.6±42.0	381.8±21.8
PCT (%)	0.1±0.1	0.1±0.1	0.2±0.1	0.1±0.1	0.1±0.1	0.1±0.1	0.1±0.1	0.1±0.0
MPV (fl)	7.4±0.7	7.5±0.9	7.3±0.7	7.2±1.1	7.4±0.5	7.3±1.1	7.3±0.7	7.2±1.1
PDWc (%)	36.6±2.7	34.2±2.3	34.3±2.1	34.1±1.5	34.5±0.6	34.9±1.1	34.9±1.0	34.2±1.6

* Data expressed as mean ± SD

Statistically significant from the control (p<0.05)

Table 12. Hematological profile of male mice

Parameters	Pre-treatment period (Day 0)				Post-treatment period (Day 28)			
	Control	300 mg/kg	600 mg/kg	900 mg/kg	Control	300 mg/kg	600 mg/kg	900 mg/kg
WBC (10 ⁹ cell/L)	8.8±1.5	8.9±0.2	8.6±0.4	8.6±0.5	9.8±1.1	9.9±0.3	9.6±0.3	9.9±0.3
LYM (10 ⁹ cell/L)	5.4±0.9	5.5±0.6	5.4±0.6	5.9±0.6	6.3±0.8	6.4±0.8	6.5±0.9	6.3±0.92
MON (10 ⁹ cell/L)	0.2±0.1	0.2±0.1	0.2±0.1	0.2±0.1	0.3±0.1	0.3±0.1	0.3±0.1	0.3±0.1
NEU (10 ⁹ cell/L)	1.8±0.6	1.8±0.1	1.8±0.2	1.8±0.5	1.5±0.5	1.5±0.4	1.5±0.3	1.5±0.3
RBC (10 ¹² cell/L)	8.9±0.4	8.8±0.1	8.8±0.1	8.7±0.3	9.4±1.1	9.5±0.9	9.4±0.8	9.4±0.5
HGB (g/L)	13.8±0.2	13.7±0.2	13.7±0.3	13.9±0.4	13.6±1.1	13.4±0.8	13.3±1.1	13.4±0.8
HCT (%)	39.7±2.3	38.9±1.9	39.3±1.4	39.1±3.2	40.8±1.5	40.4±1.6	40.8±1.9	40.5±1.5
MCV (fl)	79.2±1.4	49.0±2.5	49.2±5.4	49.0±1.5	48.0±1.3	48.0±2.1	48.0±2.2	48.2±1.9
MCH (pg)	11.9±0.4	11.6±0.4	11.6±0.4	11.6±0.4	11.7±0.3	11.8±0.4	11.8±0.3	11.7±0.4
MCHC (g/dL)	29.9±1.5	29.6±1.2	29.6±1.0	28.7±2.1	30.5±1.1	30.6±0.8	30.4±1.2	30.7±1.6
RDWc (%)	18.9±1.6	18.5±0.9	18.5±0.9	18.5±0.9	20.6±1.9	20.1±1.5	20.3±1.5	20.1±1.0
PLT (10 ⁹ cell/L)	287.2±7.3	287.2±6.4	288.2±8.7	288.8±8.5	286.8±45.8	289.0±7.0	287.0±9.2	287.8±8.2
PCT (%)	0.2±0.1	0.2±0.1	0.2±0.1	0.2±0.1	0.2±0.1	0.2±0.1	0.2±0.1	0.2±0.1
MPV (fl)	7.1±0.5	7.2±0.3	7.1±0.3	7.24±0.5	7.3±1.7	7.8±2.1	7.9±1.8	7.7±1.6
PDWc (%)	35.4±1.4	35.8±2.5	35.3±2.9	35.6±2.2	34.9±2.3	35.3±1.8	35.7±2.5	35.4±1.7

* Data expressed as mean ± SD

Statistically significant from the control (p<0.05)

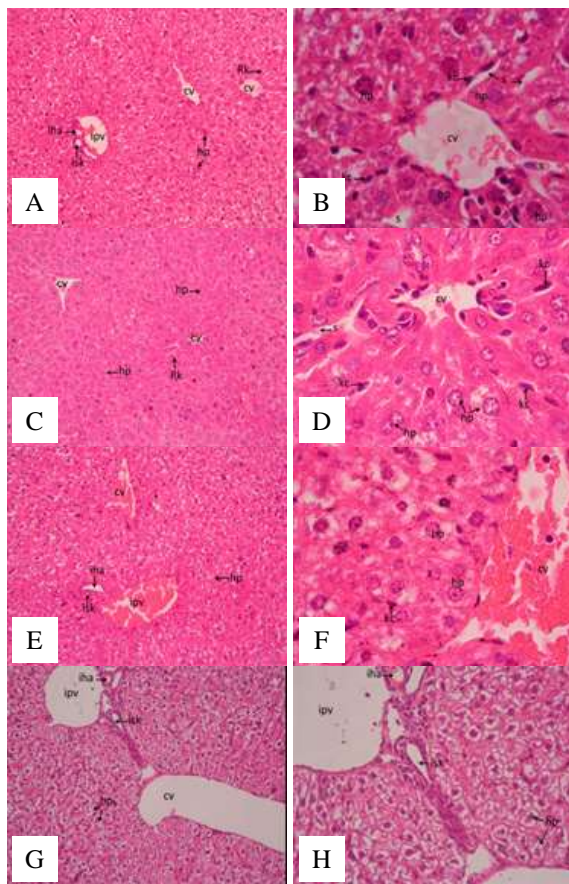


Figure 5. Histologic effects of Polyherbal formulation KL21 on liver of female mice. The liver sections of mice were stained with haematoxylin and eosin (H & E). Liver section of normal control group (Ax20, Bx100) and dose groups which were 300 mg/kg (Cx20, Dx100), 600 mg/kg (Ex20, Fx100) and 900 mg/kg (Gx20, Hx100) showing normal visible central veins (cv), sinusoids (sn), hepatocytes (hp), remark cords (Rk), interlobular portal vein (ipv), interlobular hepatic artery (iha), interlobular bile ducts (isk) and sinusoids (s). kc: Kupffer cells.

4. Discussion

New trends in drug discovery emphasize on natural sources with biological effective properties. Many people prefer to use them because they are safe which are derived from phenolic and flavonoid compounds [14]. Advantages of herbal drugs are decreased adverse effects, short time efficacy, induced immune system and positive economic outcomes on health expenditure [15]. Therefore, they are associated with conventional drugs or utilized significantly instead of them. For all these reasons it is necessary to determine their toxicological profile and verification for common implementation of safety data before marketing. The first step of this study was determined the phenolic and flavonoid contents, biological properties such as antioxidant and antimicrobial activities of KL21 extracts

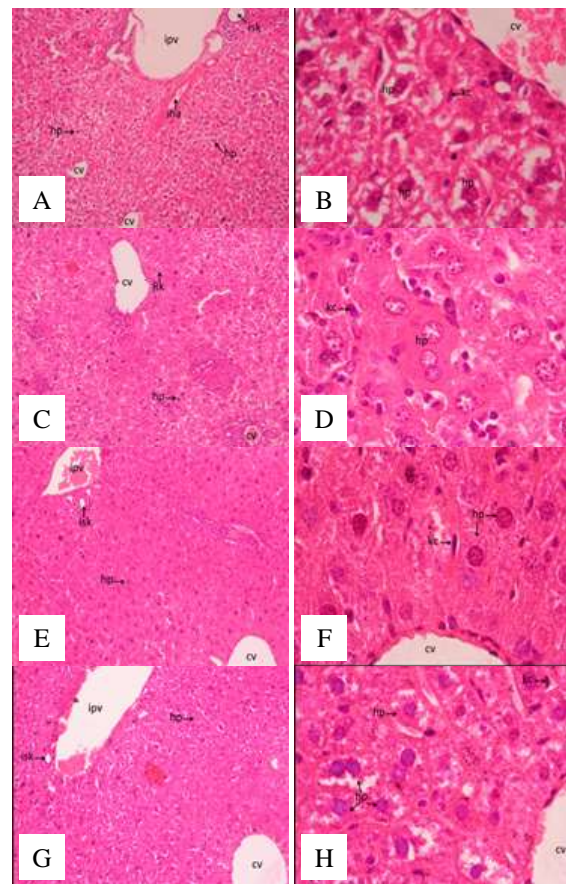


Figure 6. Histologic effects of Polyherbal formulation KL21 on liver of male mice. The liver sections of mice were stained with haematoxylin and eosin (H & E). Liver section of normal control group (Ax20, Bx100) and dose groups which were 300 mg/kg (Cx20, Dx100), 600 mg/kg (Ex20, Fx100) and 900 mg/kg (Gx20, Hx100) showing normal visible central veins (cv), sinusoids (sn), hepatocytes (hp), remark cords (Rk), interlobular portal vein (ipv), interlobular hepatic artery (iha), interlobular bile ducts (isk). kc: Kupffer cells.

Quercetin equivalent flavonoid content and gallic acid equivalent phenolic content of the ethanol extract was calculated as 11.09 and 258.58 mg/g respectively, while 86.42 mg/g and 3.58 mg/g were calculated in methanol extract. The results clearly demonstrated that ethanol extract had a high flavonoid and phenolic compound in comparison with methanol extract. It is already known that phenolic and flavonoid compounds are the major plant component with a high antioxidant capacity [8]. Therefore, considering the important role of polyphenolic and flavonoid compounds in the prevention and therapeutically of diseases, it is important to determine herbal formulations ingredients before activity studies. Bioactive ingredients are very important because of efficacy and safety of herbal formulations depends on phytochemical composition [16]. According to GC-MS analysis in our study, the major seconder compound in both extracts was

carvacrol. These results were in agreement with those reported in previous published papers that phenolic compounds. Phenolic compounds especially carvacrol demonstrate various pharmacological activities such as anti-inflammatory, anti-angiogenic and anti-cancer activities [17]. The most commonly used antioxidant methods are ABTS⁺ and DPPH conducted on both extracts. The results indicated that both extracts exhibited higher antioxidant capacity according to two analyzed methods. The phenolic components show multi-different biological activities [18]. According to MIC values of antimicrobial activity test, only methanol extract exhibited antimicrobial efficacy. Conversely, ethanol extract did not display antimicrobial activity against all bacteria included fungi which are tested microorganisms. This data suggested that the solvent type used in the extraction had a great impact on MIC values. There are experiments which emphasized it is important to consider that both polar and nonpolar compounds may find in extracts; thus, the microbial efficacy may be due to presence of components with variable polarities [19]. In the other hand, higher amount of linolenic acid in methanol extract was detected in comparison with ethanol extract [20].

Cytotoxicity of the KL21 extracts was tested on MCF-7, A549, CaCo-2, HEK-293 and HeLa cells. The tested extracts had no cytotoxic effects on A549 and Caco-2 cell lines. Our data showed that the 48 h IC₅₀ of ethanol and methanol extracts were 44 and 49 µg/mL on HEK-293 human kidney cells respectively. Additionally, it was demonstrated that ethanol extract was significantly toxic for cancer cell lines which were MCF-7 (92.09 µg/mL) and Caco-2 (95.47 µg/mL). Cytotoxic effects on cancer cell lines were affected by different solvent types of the polyherbal formulation including polar and non-polar constituents. This allows also the different phytochemical profile and biological activities due to extraction solvent [21]. Previously there were suggested that many herbal formulations exhibited cytotoxicity against various cancer cell lines [22]. Genetic toxicity testing has moved towards the earlier stages of drug discovery in order to identify genotoxic liabilities of new compounds in the pipeline.

Ames test is designed to detect genetic damage such as gene mutations which may reflect pharmaceuticals, including herbal preparations. According to test, both extracts of KL21 had no genotoxic potential in four *Salmonella* strains. This data exhibited specific approach to perform reduced risk assessment of KL21. However, Gumiganghwal-tang (GGT) is an herbal prescription made from nine different herbs and its extract acted as a genotoxic material [23]. Similarly, Pyungwi-san (PWS) is a mixture of six herbs and PWS extract exhibits genotoxicity. As a result of this it is important to determine herbal medicinal products (HMPs) genotoxicological profile and this may be a pre-condition for registration or marketing authorization.

The single dose oral toxicity up and down procedure permits estimation of an LD₅₀ with a confidence interval and the results allow a substance to be ranked and classified according to the Globally Harmonised System for the classification of chemicals which cause acute toxicity. The concept of the up-and-down animal testing approach was first step to determination of toxicity of the test material. According to the oral acute toxicity test, mice administered KL21 doses up to 2000 mg/kg did not exhibit mortality in 24 h. This result exerted the orally administered KL21 could be considered practically non-toxic. Likewise, Ojeok-san (OJS) is a widely used herbal formula in traditional Korean Japanese herbal medicine. The lethal dose of OJS with a 50 % mortality rate was over 2000 mg/kg [24]. Kai-Xin-San (KXS) is traditional Chinese medicine (TCM) formula and LD₅₀ of KXS was over 32.59 g/kg for mice which is relatively safe for oral medication [25]. In the assessment and evaluation of the toxic characteristics of the herbal formulation, the determination of oral toxicity using repeated doses carried out after initial information on toxicity has been obtained by single dose oral toxicity test. Herbal formulations may cause various side effects due to their complex chemical compounds. Because of this reason it is important to determine their toxicological background. The subacute toxicity study allowed identifying KL21 chemical compounds with toxic potential such as organ toxicity, which may warrant further in-depth investigation. Therefore, this study provides information on the possible health hazards likely to arise from repeated exposure over a relatively limited period of time. However, after 28 days' observation period, it was identified that KL21 has no adverse effects in the highest volume used. There is not any sign of observable toxicity was detected during the experimental period. During study, there was no any significant change in body and absolute/relative weights of organs compared to the normal groups. This result is important evidence to evaluate the toxicity of KL21 because of body weight changes such as decreases or increases are associated with toxic effects of chemicals, synthetic or herbal drugs. Moreover, hematological and biochemical analysis of metabolites was not significantly altered between control and treatment groups. Previously it has been reported to there are many acute, subacute and chronic toxicity studies to exerted safety evaluation of herbal formulations [26, 27]. The effects of KL21 were evaluated by histopathological examination of hepatic tissue sections using H&E staining. The highest dose of KL21 (900 mg/kg) did not causes any hepatic damage results in fibrotic changes in the hepatic tissues.

5. Conclusion

In conclusion, the results provide important information regarding the biological activity of KL21, thus, this data offer information critical for herbal drug development and emphasize to importance of determining the quality

criteria of natural product formation stage after manufacturer process. These findings indicated that KL21 due to its antioxidant capacities may be useful in the obviation of aging-related and various inflammatory diseases for human welfare. It was also undertaken to evaluate *in vitro* and *in vivo* toxicological profile of KL21 polyherbal formulation as a botanical dietary supplement. It is important to provide scientific evidence showing that the formulation is safe and efficacious in human's welfare.

Acknowledgement

The study is supported by Ege University, Faculty of Science (Project Number is 2012/FEN/067).

Author's Contributions

Çinel Köksal Karayıldırım: Performed the project, research design all experiments and wrote the manuscript.

N. Ülkü Karabay Yavaşoğlu: Helped to data interpretation and statistical analysis and wrote the manuscript.

Adem Güner: Supported the antioxidant test

Gürkan Yiğittürk and Altuğ Yavaşoğlu: Supported the histological tests

Ethics

There are no ethical issues after the publication of this manuscript.

References

- [1]. Bae, W.J., Kim, D.H., Lee, W.W., Kim, Y.H., Son, C.G., Characterizing the human equivalent dose of herbal medicines in animal toxicity studies, *Journal of Ethnopharmacology*, 2015, vol. 162, pp. 1-6. <https://doi.org/10.1016/j.jep.2014.12.023>
- [2]. Bansal, A., Chhabra, A., Rawal, K.R., Sharma, S., Chemometrics: A new scenario in herbal drug standardization, *Journal of Pharmaceutical Analysis*, 2014, Vol. 4, pp. 223-233. <https://doi.org/10.1016/j.jpha.2013.12.001>.
- [3]. Arsul, A.V., Ganjiwale RO, Yeole PG. Phytochemical and Pharmacological Standardisation of Polyherbal Tablets for Hepatoprotective Activity Against Carbon Tetrachloride Induced Hepatotoxicity, *International Journal of Pharmaceutical Sciences and Drug Research*, 2010, 2(4), pp. 265-268.
- [4]. Oh, J.S., Cho, H.J., Son, G.C., Systematic review of the incidence of herbal drug-induced liver injury in Korea, *Journal of Ethnopharmacology*, 2015, 159, pp. 253-256. <https://doi.org/10.1016/j.jep.2014.11.027>
- [5]. Kleinwächter, M., Paulsen, J., Bloem, E., Schnug, E., Dirk, Selmar., Moderate drought and signal transducer induced biosynthesis of relevant secondary metabolites in thyme (*Thymus vulgaris*) greater celandine (*Chelidonium majus*) and parsley (*Petroselinum crispum*), *Industrial Crops and Products*, 2015, 64, pp. 158-166. <https://doi.org/10.1016/j.indcrop.2014.10.062>
- [6]. Meda, A., Lamien, C.E., Romito, M., Millogo, J., Nacoulma, O.G., Determination of the total phenolic, flavonoid and praline contents in Burkina Fasan honey, as well as their radical scavenging

activity, *Food Chemistry*, 2005, Vol. 91, 3, pp. 571-577. <https://doi.org/10.1016/j.foodchem.2004.10.006>

[7]. Chang, C.C., Yang, M.H., Wen, H.M., Chern, J.C., Estimation of total flavonoid content in propolis by two complementary colorimetric methods, *Journal of Food and Drug Analysis*, 2002, Vol.10, no.3, pp. 178-182.

[8]. Ince, I., Kayalar, H., Elgin, G., Koksall, C., Yavasoglu, N.U., Antioxidant, anti-inflammatory activities and acute toxicity of the polyherbal formulation: Romix®, *Pharmaceutical Biology*, 2012, 50(6), pp. 720-726 <http://doi.org/10.3109/13880209.2011.622287>

[9]. Mosmann, T., Rapid colorimetric assay for cellular growth and survival: application to proliferation and cytotoxicity assays, *J. Immunol. Methods*, 1983, 65(1-2), pp. 55-63. [http://doi.org/10.1016/0022-1759\(83\)90303-4](http://doi.org/10.1016/0022-1759(83)90303-4)

[10]. OECD Guidelines for the testing of chemicals No: 471. *Bacterial Reverse Mutation Test*, 1997, pp.1-11.

[11]. Zimmermann, M., Ethical guidelines for investigations of experimental pain in conscious animals, *Pain*, 1983, 16 (2), pp. 109-110 [http://doi.org/10.1016/0304-3959\(83\)90201-4](http://doi.org/10.1016/0304-3959(83)90201-4)

[12]. OECD Guidelines for the testing of chemicals No: 425. Acute Oral Toxicity – Up-and-Down-Procedure (UDP), 2008, pp. 1-27.

[13]. OECD Guidelines for the testing of chemicals No: 407. Repeated Dose 28-day Oral Toxicity Study in Rodents, 1995, pp. 1-13.

[14]. Skalli, S. and Bencheikh, S.R., Pharmacovigilance of herbal medicines in Africa: Questionnaire study, *Journal of Ethnopharmacology*, 2015, 171, pp. 99-108 <http://doi.org/10.1016/j.jep.2015.05.033>

[15]. Yang, Y., Zhang, Z., Li, S., Ye, X., Li, X., He, K., Synergy effects of herb extracts: Pharmacokinetics and pharmacodynamic basis, *Fitoterapia*, 2014, 92, pp. 133-147 <http://doi.org/10.1016/j.fitote.2013.10.010>

[16]. Govindaraghavan, S. and Sucher, J.N., Quality assessment of medicinal herbs and their extracts: Criteria and prerequisites for consistent safety and efficacy of herbal medicines, *Epilepsy & Behavior Case Reports*, 2015, 52, pp. <http://doi.org/363-371>. <http://doi.org/10.1016/j.yebch.2015.03.004>.

[17]. Wang, S., Zheng, Z., Weng, Y., Yu Y., Zhang, D., Fan W., Dai R., Hu Z., Angiogenesis and anti-angiogenesis activity of Chinese medicinal herbal extracts, *Life Sciences*, 2004, 74(20), pp. 2467-2478 <http://doi.org/10.1016/j.lfs.2003.03.005>

[18]. Gahlaut, A., Chhillar, K.A., Evaluation of antibacterial potential of plant extracts using resazurin based microtiter dilution assay, *International Journal of Pharmacy and Pharmaceutical Sciences*, 2013, Vol.5(2), 376.

[19]. Awodele, O., Akindele, A.J., Aniete, J., Adeyemi, O.O., Preliminary antimicrobial evaluation of DAS-77®- A polyherbal medicine, *Journal of Herbal Medicine*, 2013, 3 pp. 52-56. <https://doi.org/10.1016/j.hermed.2013.01.002>

[20]. Kelber, O., Wegener, T., Steinhoff, B., Staiger C., Wiesner J., Knöss W., Kraft K., Assessment of genotoxicity of herbal medicinal products: Application of the “bracketing and matrixing” concept using the example of *Valeriana radix* (valerian root), *Phytomedicine*, 2014, 21(8-9), pp. 1124–1129 <http://doi.org/10.1016/j.phymed.2014.04.003>

[21]. Li, D., Zang, R., Yang, T.S., Wanga, J., Wang, X., Cell-based high-throughput proliferation and cytotoxicity assays for screening traditional Chinese herbal medicines, *Process Biochemistry*, 2013, 48, pp. 517-524 <https://doi.org/10.1016/j.procbio.2013.02.005>



- [22]. Shin, W.J., Park, J.H., Kwon, M., Son, G.C., Scientific evaluation of the chronic toxicity of the herbal medicine CGX in beagle dogs. Daejeon: Elsevier, 2010,48(2), pp. 743-749 <http://doi.org/10.1016/j.fct.2009.12.008>
- [23]. Shin, S.I., Seo, S.C., Ha, K.H., Lee, Y.M., Huang, S.D., Huh I.J., Shin K.H., Genotoxicity assessment of Pyungwi-san (PWS), a traditional herbal prescription, *Journal of Ethnopharmacology*, 2012, Vol. 133(2), pp. 696-703 <https://doi.org/10.1016/j.jep.2010.10.050>
- [24]. Ha, H., Lee, K.J., Lee, H.Y., Seo S.C., Kim, H.J., Lee, Y.M., Koh, S.W., Shin, K.H., Evaluation of safety of the herbal formula Ojeok-san: Acute and sub-chronic toxicity studies in rats, *Journal of Ethnopharmacology*, 2010, 131(2), pp. 410-416 <http://doi.org/10.1016/j.jep.2010.07.011>
- [25]. Mu, H.L., Huanga, X.Z., Liua, P., Hua, Y., Gao, Y., Acute and subchronic oral toxicity assessment of the herbal formula Kai-Xin-San, *Journal of Ethnopharmacology*, 2011, 138(2), pp. 138-357 <http://doi.org/10.1016/j.jep.2011.08.033>
- [26]. Wills, J.P. and Asha, V.V., Acute and subacute toxicity studies of *Lygodium flexuosum* extracts in rats, *Asian Pacific Journal of Tropical Biomedicine*, 2012, Vol.2(1), pp. 200-202 [https://doi.org/10.1016/S2221-1691\(12\)60159-2](https://doi.org/10.1016/S2221-1691(12)60159-2)
- [27]. Kim, J.Y.E., Chen, Y., Huang, J.Q., Li, M.K., Naumovski, R.V., Poon J., Chan K., Roufogalis, D.B., McLachlan, A., Mo, L.S., Yang, D., Yao, M., Liu, Z., Liu, J., Li, Q.G., Evidence-based toxicity evaluation and scheduling of Chinese herbal medicines, *Journal of Ethnopharmacology*, 2013, 146(1), pp. 40-61 <http://doi.org/10.1016/j.jep.2012.12.027>



Long-term Stability of Cationic Phytosphingosine Nanoemulsions as Delivery Systems for plasmid DNA

Selen Isar¹ , Yiğit Şahin² , Hasan Akbaba¹ , Ayşe Nalbantsoy³ , Gülşah Erel Akbaba⁴ ,
Yücel Başpınar^{1*} 

¹ Department of Pharmaceutical Biotechnology, Faculty of Pharmacy, Ege University, İzmir, Turkey.

² Department of Biotechnology, Graduate School of Natural and Applied Sciences, Ege University, İzmir, Turkey.

³ Department of Bioengineering, Faculty of Engineering, Ege University, İzmir, Turkey.

⁴ Department of Pharmaceutical Biotechnology, Faculty of Pharmacy, Izmir Katip Çelebi University, İzmir, Turkey.

* yucel.baspinar@ege.edu.tr

* Orcid: 0000-0003-2069-9659

Received: 4 June 2021

Accepted: 11 March 2022

DOI: 10.18466/cbayarfbe.948114

Abstract

Gene delivery systems like cationic nanoemulsions are in general not ready to use for any time. Thus, delivery systems for genetic materials like nucleic acids have to be prepared freshly before application. This study is focused on the preparation and characterization of cationic nanoemulsions using phytosphingosine for plasmid DNA delivery. Repurposing of cationic agents guided us to phytosphingosine, previously used for enhanced interaction with negatively charged surfaces. It was reported that phytosphingosine may act anti-apoptotic, but without using it in an appropriate delivery system like nanoemulsions. This gap attracted our interest in preparing and characterizing long-term stable cationic nanoemulsions and their cytotoxic effects on MDA-MB-231 and MCF-7 breast cancer cells using phytosphingosine. The cationic nanoemulsions 1, 2, and 3 were prepared and characterized in terms of droplet size, polydispersity index, zeta potential, long-term stability after storage at 25 and 40 °C, complexation with pDNA, release and cytotoxicity on MDA-MB-231 and MCF-7 cells. The CNEs showed appropriate properties like a small droplet size (<200 nm), a narrow size distribution and a high zeta potential (>+30 mV). Unfortunately, each cationic nanoemulsion showed some disadvantages. Cationic nanoemulsion 1 decreased the viability of cancer cells to only 25 %. Phase separation was observed for cationic nanoemulsion 2 after storage of six months at 40 °C. And cationic nanoemulsion 3 was not able to form a complex with pDNA.

To sum up, cationic nanoemulsion 1 is more appropriate than the other cationic nanoemulsions for delivering pDNA.

Keywords: cationic nanoemulsion, stability, pDNA, complexation, phytosphingosine, cytotoxicity.

1. Introduction

Large and hydrophilic free nucleic acids are negatively charged, which disables their cellular uptake. Furthermore, they are biologically not stable and degradation by nucleases in the blood is occurring. Drug delivery systems like viral or non-viral vectors are useful tools for improved delivery of nucleic acids and they can protect nucleic acids

from degradation. Loading anionic nucleic acids onto cationic delivery systems resulted in an enhanced binding on the cell surface and enhanced entrance of genetic material into the cell by endocytosis [1, 2]. Easy manufacturing, low immune response, cost-effectiveness, and safety are some of the advantages of non-viral vectors, representing alternative drug delivery systems to viral delivery of nucleic acids [3-7].

Cationic nanoemulsions (CNEs) were proposed for more than three decades as delivery system for nucleic acids [8-10]. CNEs are dispersed systems composed of an oil phase and an aqueous phase. Both phases are normally not miscible, thus the dispersed system is thermodynamically not stable. The inner oil phase of oil-in-water (O/W) emulsions can be stabilized by non-ionic surfactants (Tween 80, Poloxamer etc.) and additionally a cationic lipid like didodecyl-dimethylammonium bromide (DDAB) can be used [11]. A cationic lipid or agent in the formulation is required due to the formation of a complex with anionic nucleic acids through electrostatic interactions. The first cationic emulsion for the delivery of a plasmid through a portal vein injection in mice was composed of castor oil and 3-b[N-(N0,N0-dimethylaminoethane)-carbamoyl] cholesterol [8]. After its application, higher amounts of the gene product in the liver were observed, compared to traditional cationic liposomes. Oral, parenteral, and intranasal application and dilution with water are some of the advantages of NEs. Diazepam[®] Lipuro, Disoprivan[®], Etomidat[®] Lipuro, Intralipid[®], Lipofundin[®], Propofol 1%/2% Fresenius and Stesolid[®] are some examples of NEs available in the market.

Phytosphingosine (PS) is an important point of this study and was investigated as a complexation agent for plasmid desoxyribonucleic acid (pDNA) in CNEs with appropriate properties. PS is one representative of sphingoid bases, which are constituents of ceramides in the stratum corneum. PS is known to have antibacterial activity against epidermal and mucosal bacterial infections [5-Schuh] and antimicrobial and antiinflammatory activity and efficacy on acne vulgaris [12]. In addition, PS induced apoptosis-like cell death in *Neurospora crassa*, caspase-independent apoptosis in *Aspergillus nidulans* and is a potent inducer of apoptosis [13-16]. Furthermore, PS induced mitochondria-involved apoptosis and cell-cycle arrest in Jurkat cells, reduced cytochrome *c* release independently of caspase activation [17]. Moreover, PS dephosphorylated Akt to inhibit pro-growth signal, protein phosphatase inhibitor attenuated PS-induced Akt dephosphorylation and overexpression of mitochondria-localized anti-apoptotic protein Bcl-2 prevented PS apoptotic stimuli [17]. It was reported that PS caused a strong induction of caspase-8 activity and caspase-independent Bax translocation to the mitochondrial in Jurkat (human T-cell lymphoma) and NCI-H460 (human non-small cell lung cancer) cells [18]. Besides, PS induced activation of caspase 9 and 3, cytochrome *c* release from mitochondria and mitochondrial translocation of Bax from the cytosol without changes in the protein levels of Bcl-2,

Bcl-xL, and Bax [19]. These studies have in common that PS was not investigated in a delivery system like NE, which is a serious lack.

For manufacturing CNEs, the cationic compound is crucial for the positive charge and gene delivery systems using cationic agents are expected to be non-toxic, but potent to deliver the cargo to the target to a high extent. Within the last decades, several cationic agents have been studied for the complexation and delivery of nucleic acids. This study aims to point out PS and PS-Hydrochloride (PSHCl), which has a higher aqueous solubility than PS, as cationic agents in cationic nanoemulsions (CNEs) for delivery of pDNA. In that context, the effects of PS and PSHCl on particle properties, complexation and cytotoxicity among others were investigated.

The challenge of using PS is to find an appropriate solvent. The low aqueous solubility of PS is disabling its use in simple aqueous formulations. Due to this PS was used in previous studies in NEs for dermal [20, 21] and oral [22] application. This is the first study about using PS as a cationic agent in CNEs with appropriate properties for delivering pDNA. A previous study about the preparation a CNE using PS and Peceol was not appropriate due to phase separation after storage of 1 month at 40 °C [23].

This study is focused on the preparation and characterization of three CNEs as non-viral vectors for plasmid DNA delivery and one blank NE (OD-NE) as a control for the cytotoxicity studies. For that purpose, the CNEs were prepared by microfluidization and characterized in terms of particle properties like droplet size (DS), size distribution (polydispersity index, PDI), zeta potential (ZP) and cytotoxicity using human embryonic kidney (HEK 293) and the two breast cancer cell lines, MDA-MB-231 and MCF-7. Formation of complexes with pDNA and SDS release studies were only performed with the CNEs.

2. Material and Methods

2.1 Materials

Phytosphingosine (PS; 2S-amino-1, 3S, 4R-octadecanetriol) and PS-Hydrochloride (PSHCl) were gifts from Evonik (Essen, Germany). Polysorbate 80 (Tween 80, Merck, Germany) and lecithin from soybean 90% (Applichem, Darmstadt, Germany) were chosen as surfactants. Octyldodecanol (OD; Eutanol[®] G, Caesar and Lorenz GmbH, Hilden, Germany) as an oil compound was purchased.

The plasmid pEGFP-C1 from Invitrogen, California, USA was used as a model. The pDNA was amplified in *Escherichia coli DH5a* strain. Maxiprep plasmid DNA purification kit from Invitrogen (USA) was performed to purify plasmid. After obtaining pDNA, restriction enzyme digestion and visualized by agarose gel electrophoresis was performed to check plasmid unity. Moreover, the purity and the concentration of the plasmid were measured at 260/280 nm wavelengths by UV/Vis spectrophotometer. The concentration of pDNA was adjusted to 100 µg/mL and stored at -20°C until use.

2.2 Methods

2.2.1 Preparation of Cationic Nanoemulsions

The CNEs were prepared with microfluidization method by using Microfluidizer ML100L.

The CNEs were prepared using 0.5% PS (CNE 1 and 3) and PSHCl (CNE 2), respectively, 20% OD (CNE 1 and 2) and 5% OD (CNE 3), 2% lecithin and Tween 80, at 25 °C, by investigating the microfluidization duration of 1, 2, 3, 4, 5, 6, 8 and 10 minutes. An intermediate pressure between 500 and 700 bar, namely 600 bar, was chosen for the preparation of the CNEs, due to the fact that the CNEs will be blank, without a drug, and thus less pressure input into the NE system could be sufficient for obtaining CNEs with appropriate long-term properties.

The composition of the CNEs is given in Table 1. The CNEs were prepared by microfluidization as described in the literature [22, 24].

Table 1: Composition of the cationic nanoemulsions.

Compound	CNE 1	CNE 2	CNE 3
oil phase			
	%	%	%
	(w/w)	(w/w)	(w/w)
octyldodecanol	20	20	5
PS	0.5	-	0.5
lecithin	2	2	2
aqueous phase			
PS-HCl	-	0.5	-
Tween 80	2	2	2
bidistilled water	ad 100	ad 100	ad 100

Briefly, for CNE1 and 3 the oil phase was prepared by adding the cationic agent PS to OD at approximately 100 °C and stirred with a magnetic stirrer until complete solvation was obtained. After that, the surfactant lecithin was added and stirred until complete solvation was achieved at approximately 50 °C. The aqueous phase was

obtained by solving the surfactant Tween 80 and in bidistilled water at 25 °C.

For CNE2, the oil phase was prepared by solving the surfactant lecithin at 50 °C. The aqueous phase was obtained by solving PSHCl and Tween 80 in bidistilled water at 25 °C.

Afterwards, the oil phase was added to the aqueous phase and a pre-emulsion was obtained by using the high-speed stirrer Silverson L5M with 10000 rpm for 5 min and subjected afterwards to the Microfluidizer ML100L. The CNEs were prepared at 25 °C with 600 bar and different microfluidization durations (1, 2, 3, 4, 5, 6, 8 and 10 min) by microfluidization to obtain CNEs (Figure 1).



Figure 1: Photograph of the prepared cationic nanoemulsions.

2.2.2 Droplet Size and Zeta Potential Measurements of Particle Characterization of Cationic Nanoemulsions

The DS, PDI and ZP of the CNEs were measured directly after the preparation (d0). The mean DS and PDI were determined by Zetasizer Nano ZS (Malvern Instruments, Malvern, UK) per photon correlation spectroscopy with dynamic light scattering (DLS) and the ZP, representing the surface charge of particles, was determined by measuring the electrophoretic mobility. 20 µl of the sample was added to 20 ml bidistilled water and measured. The Helmholtze Smoluchowski equation was applied for the calculation of the ZP [25]. The CNE with appropriate properties like a small DS of less than 300 nm, a narrow size distribution (PDI <0.3) and especially a high ZP of >+30 mV was investigated according to the aimed formation of a complex with pEGFP-C1 (pDNA).

2.2.3 Complexation Studies of Cationic Nanoemulsion-pDNA

After freshly preparing the CNEs, their complex formation ability with pDNA was evaluated by the use of different relations of CNEs and pDNA,

shown with gel retardation assay. The augmenting amount of CNEs (0.5 - 5 μ l, 1:10 diluted) was added into the constant amount of pDNA solution (1 μ l of 100 ng/ml plasmid stock solution) and shaken on a bench-top shaker for 30 min to complete the binding of pDNA onto the CNEs *via* electrostatic interaction.

The resultant CNE:pDNA complexes were characterized by gel retardation assay [26]. The agarose gel electrophoresis (1% agarose/1xTAE, w/v) was carried out for 60 min under the voltage of 80 V and imaged *via* a gel documentation system (Vilber Lourmat, France). The CNE:pDNA complexes were freshly prepared before each use for further studies.

2.2.4 SDS Release Studies of pDNA from Cationic Nanoemulsion-pDNA Complex

SDS release studies of pDNA by agarose gel electrophoresis are necessary to provide that the cargo is released to reach the target. After forming the CNE-pDNA complex, SDS was immediately added and incubated for 10 min at 25 °C. Following the addition of glycerine, the samples were loaded on 1 % agarose gel electrophoresis.

SDS was added immediately after complex formation. Following 10 minutes incubation at 25°C, samples were loaded on 1% agarose gel for electrophoresis. Six CNE:pDNA ratios were tested – 0.5:1, 1:1, 2:1, 3:1, 4:1 and 5:1 (v/v).

The resultant CNE:pDNA complexes were characterized by gel retardation assay [26]. The agarose gel electrophoresis (1% agarose/1xTAE, w/v) was carried out for 60 min under the voltage of 80 V and imaged *via* a gel documentation system (Vilber Lourmat, France). The CNE:pDNA complexes were freshly prepared before each use for further studies.

2.2.5 Cytotoxicity Studies

The cytotoxicity studies of the freshly prepared CNEs were performed using non-cancerous HEK 293 (human embryonic kidney cells) cells and the two breast cancer cells MDA-MB-231 (human breast adenocarcinoma) and MCF-7 (human breast adenocarcinoma). Cells are cultured in DMEM/F12 (1:1) medium which supplemented with 10% fetal bovine serum (FBS) and 0.1% Pen-Strep (10.000 Units/mL penicillin and 10.000 μ g/mL Streptomycin) at 37°C and 5% CO₂ with humidified conditions. Cells were inoculated into 96-well plates (1x10⁵ cells per mL) and then incubated for 24 h at 37°C, 5% CO₂ and humidified conditions. Then, the medium was removed, the

cells were washed and treated with 3 different concentrations of CNE 1, CNE1:pDNA complex, CNE 2, CNE2:pDNA complex and CNE 3. In addition, OD-NE, PS, PSHCl and Doxorubicin (DOXO) were used as a control. After 48 h incubation, 20 μ l of MTT (3-(4,5-dimethylthiazol-2-yl)-2,5-diphenyltetrazolium bromide) solution is added and the plates are incubated for 4 h [27]. More after, media was discarded from wells and 150 μ l dimethyl sulfoxide was added on each well. For determining the optical density (OD), plates are placed in a spectrophotometer at 570 nm wavelength. Experiments were carried out at least in triplicate.

After OD was determined, cells viability (%) was calculated with the formula below:

%Viable cells: [(absorbance of treated cells)-(absorbance of blank)] / [(absorbance of control)-(absorbance of blank)] X 100 [28].

In the end, IC₅₀ values calculating by fitting viability (%) data to sigmoidal curve on Graphpad Prism 9 software.

2.2.6 Statistical Analysis

GraphPad Prism v6.01 software was used for statistical analysis of all data. P < 0.05 was considered to be statistically significant. Results are expressed as means \pm SD. For analysis between groups, a two-way ANOVA was performed followed by multiple comparison to compare differences between groups. Measurements and experiments were carried out at least in triplicate.

3. Results and Discussion

3.1 Preparation, Droplet Size and Zeta Potential Measurements of Cationic Nanoemulsions

In previous studies, it was shown that the formulation parameter like the type and concentration of the used compounds were more effective than the process parameters like preparation temperature, pressure and duration during the development of NEs were investigated [20-22].

Based on these findings, the CNEs were composed of 0.5% PS (CNE 1 and 3) or PSHCl (CNE 2), 5 % (CNE 3) and 20% OD (CNE 1) and 2% lecithin and 2% Tween 80, respectively [23, 29].

Previously, Peceol was used to solve PS and prepare CNEs. Unfortunately, phase separation occurred after storage of 1 month at 40 °C. Additionally, the ZP significantly decreased from +48.7 mV at the beginning to +12.8 mV after storage of 6 months at 25 °C, showing that this

formulation was not appropriate to form a complex with pDNA in the long term. An appropriate delivery system for nucleic acids should have a long-term ZP $>+30$ mV enabling its use in due time. Otherwise, the formulation must be prepared every time freshly, which could be interpreted as waste. Providing a DS <300 nm and PDI <0.3 , they come second, so the ZP, caused by the cationic agents PS and PSHCl, is more crucial for complexation and delivering plasmid DNA. The effects of the used compounds and of the microfluidization duration from 1-10 minutes on DS, PDI and ZP were studied to optimize the preparation of the CNEs.

With increasing the microfluidization duration from 1 to 10 minutes, the DS of CNE 1 (Figure 2a) decreased, from 159 nm (1 min) to 114 nm (10 min), just like the PDI slightly decreased from 0.09 (1 min) to 0.08 (10 min) (Figure 2a), and the ZP decreased from +43.2 mV (1 min) to +36.6 mV (10 min) (Figure 2b). Increasing the microfluidization duration resulted in a decrease of DS, PDI and ZP, but not all of these effects are desired. Due to the fact that the ZP is more crucial than DS and PDI, a microfluidization duration of 1 minute is appropriate. Similar results were observed by Isar et al. 2020 [23].

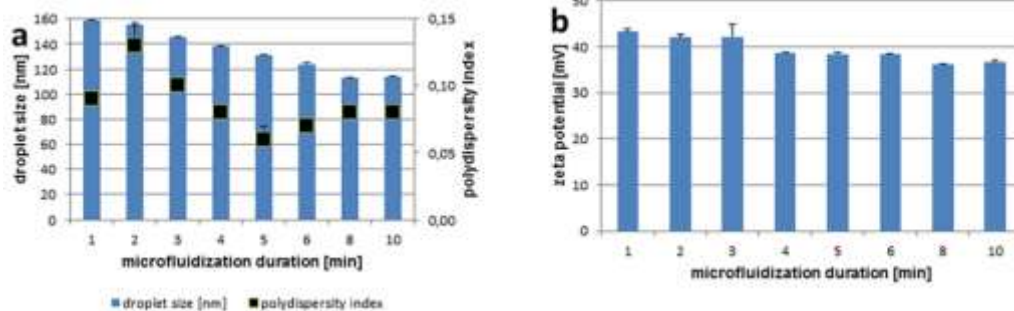


Figure 2 The droplet size, polydispersity index, and zeta potential results of CNE 1 with increasing microfluidization duration.

The DS of CNE 2 decreased from 113 nm (1 min) to 87 nm (10 min) (Figure 3a), the PDI decreased from 0.12 (1 min) to 0.08 (10 min) (Figure 3a), and the ZP first increased from +42.8 mV (1 min) to +50.1 mV (2 and 3 min), then decreased to +43.6 mV (10 min) (Figure 3b). Due to the fact that the

highest ZP was obtained after a microfluidization duration of 2 minutes (+50.1 mV), with a DS of 102 nm and a PDI of 0.09, this is an appropriate microfluidization duration for CNE 2.

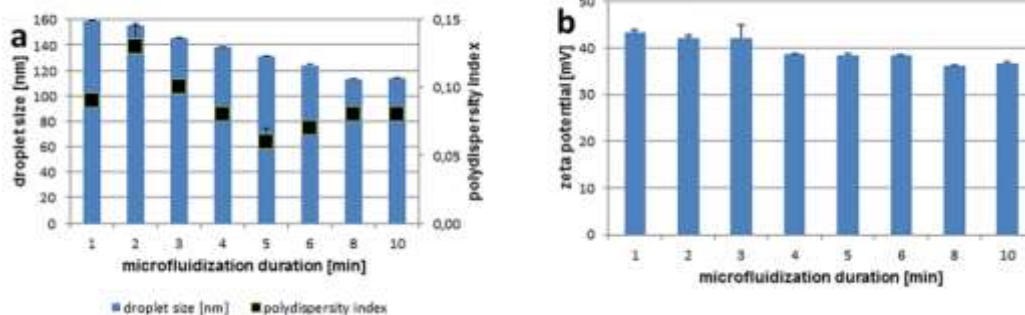


Figure 3: The droplet size, polydispersity index, and zeta potential results of CNE 2 with increasing microfluidization duration.

For CNE 3, the DS decreased from 188 nm (1 min) to 151 nm (10 min) (Figure 4a), but the PDI increased from 0.19 (1 min) to 0.23 (10 min) (Figure 4a), just like the ZP increased from +31.7 mV (1 min) to +35.4 mV (10 min) (Figure 4b). Here, a microfluidization duration of 1 minute is not sufficient to obtain a formulation with a maximum ZP. Increasing the

microfluidization duration to 2 minutes resulted in a ZP of +34.1 mV.

A higher ZP was obtained after a microfluidization duration of 2 minutes (+34.1 mV) with a DS of 184 nm and a PDI of 0.19, this is the optimal duration. Further increase of the microfluidization duration did not result in ZPs with significant differences, so a microfluidization duration of 2 minutes is appropriate.

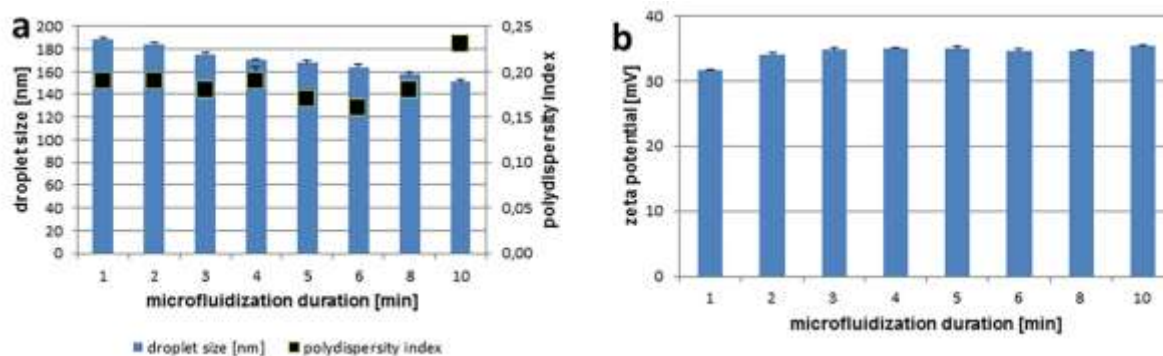


Figure 4: The droplet size, polydispersity index, and zeta potential results of CNE 3 with increasing microfluidization duration.

Comparing the formulation properties of the CNEs showed that for CNE 1 the complexation agent PS was dissolved in the inner oil phase, additionally containing OD and lecithin, whereas for CNE 2, the complexation agent PSHCl was used in the outer aqueous phase, containing Tween 80. The difference between CNE 1 and CNE 3 is based on the concentration of the inner oil phase. CNE 1 contained 20 % OD and 5% OD was used for CNE 3, leading to a formulation with a smaller DS (159 nm) and PDI (0.09) but higher ZP (+43.2 mV) when 20% OD was used, compared to CNE 3, with a DS of 184 nm, a PDI of 0.19 and a ZP of +34.1 mV.

The smallest DS of 102 nm, lowest PDI of 0.09 and highest ZP of +50.1 mV were observed for CNE 2, where PSHCl was used as complexation agent in the outer aqueous phase. Since the particle properties of CNE 1 and CNE 2 seem to be more beneficial compared to CNE 3, it can be supposed that CNE 3 is probably not suitable for our purpose of complexation pDNA.

CNE 1 showed after storage of up to 12 months at 25 and 40 °C no significant changes of DS and PDI (Table 2). The DS of 159 nm at the day of preparation increased to 176 nm and 180 nm after storage of 12 months at 25 and 40 °C, respectively.

Table 2: The droplet size, polydispersity index, and zeta potential results of cationic nanoemulsion 1 after storage of 12 months at 25 and 40 °C.

storage time and temperature	DS [nm ± SD]	PDI [± SD]	ZP [mV± SD]
d0	159 ± 1.3	0.09 ± 0.01	43.2 ± 1.3
d7, 25 °C	160 ± 2.1	0.12 ± 0.05	39.6 ± 1.2
d7, 40 °C	159 ± 1.7	0.13 ± 0.03	38.2 ± 1.7
d14, 25 °C	168 ± 2.5	0.08 ± 0.02	36.0 ± 1.9
d14, 40 °C	165 ± 0.6	0.09 ± 0.01	32.9 ± 0.3
d28, 25 °C	164 ± 1.2	0.10 ± 0.01	39.9 ± 1.3
d28, 40 °C	161 ± 0.3	0.10 ± 0.01	19.6 ± 0.4
m3, 25 °C	169 ± 3.2	0.09 ± 0.02	33.9 ± 0.9
m3, 40 °C	182 ± 5.3	0.06 ± 0.02	20.1 ± 0.2
m6, 25 °C	176 ± 3.1	0.09 ± 0.01	32.4 ± 0.7
m6, 40 °C	185 ± 3.5	0.04 ± 0.01	19.4 ± 0.4
m9, 25 °C	171 ± 2.8	0.12 ± 0.01	35.4 ± 0.8
m9, 40 °C	180 ± 1.7	0.07 ± 0.03	19.9 ± 0.4
m12, 25 °C	176 ± 2.7	0.09 ± 0.05	33.8 ± 0.8
m12, 40 °C	180 ± 1.7	0.07 ± 0.03	19.9 ± 0.4

The ZP decreased from 43.2 mV to 33.8 mV after storage of 12 months at 25 °C, still more than the aimed 30 mV, and to 19.9 mV after storage of 12 months at 40 °C (Table 2). Thus, even after

storage at 25 °C, CNE 1 is a ready to use formulation for further studies, without the need for fresh preparation.

The DS of CNE 2 showed no significant changes over 28 days, however storage at 40 °C caused an increase from 102 nm to 160 nm (Table 3). Finally, DSs of 179 nm and 203 nm were observed after storage of six and nine months at 25 °C, respectively. After storage of six months at 40 °C phase separation was observed. The PDI was very constant over nine months, at 25 °C. Just like

the DS, the ZP was stable after storage of 28 days at 25 °C with values of 50.1 mV at the beginning and 48.3 mV after 28 days. Unfortunately, the ZP decreased after storage of 28 days at 40 °C to 39 mV, but remained between 38.3 and 41.8 mV, even after storage of three months at 25 and 40 °C, six and nine months at 25 °C (Table 3). The stability studies for storage of 12 months are ongoing.

Table 3: The droplet size, polydispersity index, and zeta potential results of cationic nanoemulsion 2 after storage of nine months at 25 °C and three months at 40 °C.

storage time and temperature	DS [nm ± SD]	PDI [± SD]	ZP [mV± SD]
d0	102 ± 0.4	0.09 ± 0.01	50.1 ± 0.4
d7, 25 °C	124 ± 1.1	0.09 ± 0.03	52.6 ± 2.3
d7, 40 °C	123 ± 0.7	0.07 ± 0.01	50.1 ± 1.3
d14, 25 °C	122 ± 1.8	0.09 ± 0.03	50.3 ± 1.8
d14, 40 °C	125 ± 0.6	0.07 ± 0.01	47.7 ± 0.2
d28, 25 °C	131 ± 1.9	0.10 ± 0.01	48.3 ± 0.5
d28, 40 °C	160 ± 2.6	0.05 ± 0.02	39.0 ± 0.5
m3, 25 °C	155 ± 4.1	0.08 ± 0.02	38.6 ± 0.8
m3, 40 °C	155 ± 2.0	0.07 ± 0.03	41.8 ± 0.3
m6, 25 °C	179 ± 2.7	0.08 ± 0.02	40.0 ± 1.2
m9, 25 °C	203 ± 5.1	0.09 ± 0.02	38.3 ± 0.3

Storage of CNE 3 at 25 and 40 °C over a period of three months had no negative effect on DS, which was 184 nm at the beginning and 164 nm and 171 nm after three months (Table 4). A decrease of the PDI from 0.19 to 0.07 and 0.06, respectively, after storage three months at 25 and 40 °C was observed. The reason for that decrease is probably based on a more compact structure and size distribution with increasing storage time.

A slight decrease of DS is an indicator for this, too. The ZP revealed stable values of 34.1 mV at the beginning and 34.4 mV after storage of three months at 25 °C. Unfortunately, storage at 40 °C had non-beneficial effects on ZP, resulting in a decrease from 34.1 mV to 12.4 mV (Table 4), which is not appropriate. The stability studies for storage of 6 months and further are ongoing.

Table 4: The droplet size, polydispersity index, and zeta potential results of cationic nanoemulsion 3 after storage of three months at 25 and 40 °C.

storage time and temperature	DS [nm ± SD]	PDI [± SD]	ZP [mV± SD]
d0	187 ± 3.3	0.19 ± 0.02	34.1 ± 0.7
d7, 25 °C	179 ± 4.0	0.20 ± 0.04	32.7 ± 1.5
d7, 40 °C	173 ± 4.5	0.17 ± 0.01	27.2 ± 1.8
d14, 25 °C	179 ± 3.1	0.19 ± 0.03	34.8 ± 0.3
d14, 40 °C	171 ± 0.4	0.21 ± 0.01	24.0 ± 2.4
d28, 25 °C	178 ± 2.3	0.19 ± 0.02	32.8 ± 0.2
d28, 40 °C	164 ± 1.6	0.21 ± 0.01	26.8 ± 0.4
m3, 25 °C	164 ± 1.7	0.07 ± 0.03	34.4 ± 0.4
m3, 40 °C	171 ± 2.6	0.06 ± 0.02	12.4 ± 0.5

CNE 1 and 3 showed appropriate DSs, PDIs, and ZPs after storage of 12 months for CNE 1 and three months for CNE 3 at 25 °C. Storage at 40 °C had disadvantageous effects on ZP, which significantly decreased to <30 mV. On the contrary to these

CNEs, the DS of CNE 2 increased, but is still <300 nm, the PDI is constant and the ZP only slightly decreased from 50.1 mV to 38.3 mV after storage of nine months at 25 °C. The fact that phase separation was observed for CNE 2 is a

disadvantage in terms of usability for further studies. On the other hand, the ZPs of CNE 1 and 3 are significantly decreasing but still <30 mV, which is also a drawback. It can be pointed out that the CNEs showed stable DS, PDI and ZPs after storage at 25 °C, except for CNE 2 with increasing DS. Here, it can be stated that using PSHCl for the outer aqueous phase has no beneficial effects on particle properties compared to PS used in the inner oil

3.2 Gel Retardation Assay of Cationic Nanoemulsion-pDNA Complexes

Our supposition that CNE 3 is not suitable for complexation pDNA was right, and a CNE3-pDNA complex was not obtained probably due to the ZP. According to the CNEs-pDNA complexation results, the complex of 1 µl plasmid and 5 µl CNE 1 (Figure 5a) and 1 µl plasmid and 0.5 µl

phase. If intended to use a freshly prepared formulation, CNE 2 seemed to be more appropriate due to the highest ZP of the CNEs. However, this was revised after the stability studies due to decreased ZP and increased DS results.

Further studies about complexation with pDNA, SDS release and cytotoxicity will help to find out the best possible formulation for delivering pDNA.

CNE 2 (Figure 5b), respectively, (1:10 diluted) were appropriate for further studies. For CNE 3 it was not possible to form a suitable complex with pDNA, so this CNE was rated as not appropriate for our purposes to form an appropriate complex with pDNA.

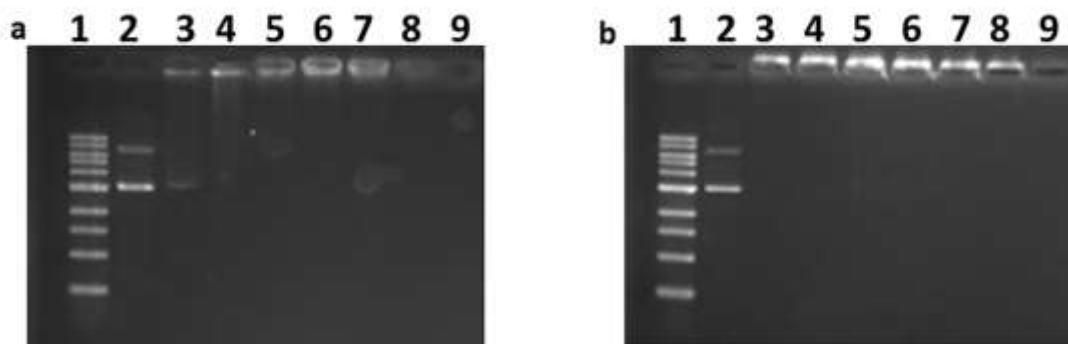


Figure 5: Gel electrophoresis image of the complexation assay between the constant amount of pEGFP-C1 with the increasing amount of CNE 1 (a) or CNE 2 (b). (1:1Kb plus DNA ladder, 2: Naked DNA as positive control, 3,4,5,6,7,8: pDNA:CNE complexes for the ratio of 1:0.5, 1:1, 1:2, 1:3, 1:4, 1:5 (v/v), respectively, and 9:CNE; CNEs were used as 1:10, diluted).

3.3 Particle Characterization of Cationic Nanoemulsion-pDNA Complex Formulations

For CNE 1, the DS only slightly decreased from 192 nm to 181 nm after complexation with pDNA, the PDI slightly decreased from 0.13 to 0.15, but the ZP decreased from +46.6 mV to +29.5 mV, still around the required value of 30 mV for stable nanoparticles (Figure 6). The formation of a CNE 2-pDNA complex resulted in a significant increase of the DS from 144 nm to 288 nm, an increase of the PDI from 0.14 to 0.21, and a significant decrease of the ZP from +47.9 mV to +5.1 mV. Comparing both CNE-pDNA complex formulations revealed that the DS of CNE 1-pDNA

is smaller (181 nm) than of CNE 2-pDNA (288 nm), the size distribution of CNE 1-pDNA is more narrow (PDI of 0.15) compared to CNE 2-pDNA (PDI of 0.21) and the ZPs of approximately +30 mV (CNE 1-pDNA) vs +5.1 mV (CNE 2-pDNA). These results can be explained with the different CNE:pDNA ratios. The ratio CNE 1:pDNA was 5:1, while for CNE 2:pDNA (0.5:1) the amount of CNE was lower, resulting in a significant increase of DS and decrease of ZP. Based on these particle characterization results, it could be stated that both CNEs are appropriate for the formation of a complex with pDNA. However, the cytotoxicity study results using HEK293 cells will give more insights.

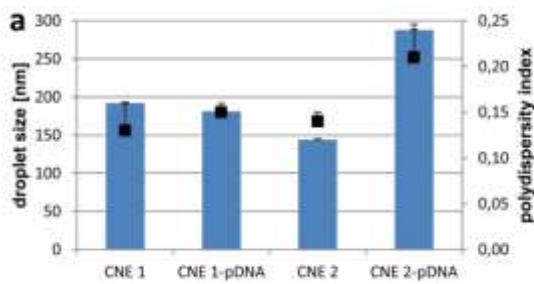


Figure 6: The droplet size, polydispersity index, and zeta potential results of the cationic nanoemulsions 1 and 2 before and after complexation with pDNA.

3.4 SDS Release Studies of pDNA from Cationic Nanoemulsion-pDNA Complexes

To investigate the SDS induced pDNA release studies from CNE-pDNA complexes, these were prepared in six different CNE:pDNA ratios from 0.5:1 to 5:1 (v/v). It could be shown that 1% SDS was appropriate for the release of pDNA, independent from the CNE-pDNA ratio (Figure 7).

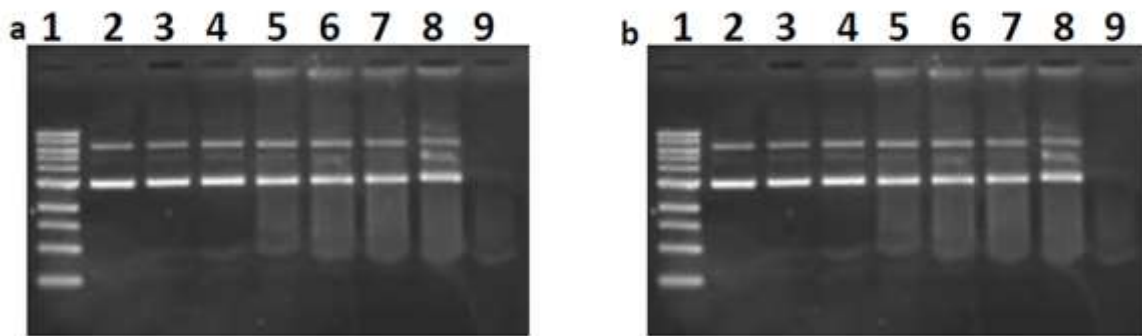


Figure 7: SDS release of pDNA from CNE 1-pDNA (a) and CNE 2-pDNA (b) complexes at six different ratios; lane 1: MW; lane 2: pDNA as control; 3-8: CNE-pDNA ratios from 0.5:1 - 5:1; lane 9: blank CNE.

3.5 Cytotoxicity

The cytotoxicity study results of the CNEs, CNE-pDNA complexes, OD-NE, PS, PSHCl and DOXO using HEK 293 revealed that with increasing the applied dose from 0.25 $\mu\text{g/ml}$ to 25 $\mu\text{g/ml}$, the viability of the HEK 293 cells decreased from 78% to 14% for CNE 1, from 73% to 12% for CNE 2, from 71% to 16% for CNE 3 (Figure 8a). This

decreasing effect of the viability of CNE 1 and CNE 2 is not desired on non-cancerous cells. For the CNE-pDNA complexes, the viability decreased from 99% to 77% for CNE 1-pDNA and from 96% to 79% for CNE 2-pDNA (Figure 8a). There are no significant differences in the viabilities between the CNE-pDNA complexes. Thus, complexation with pDNA resulted in increased viability.

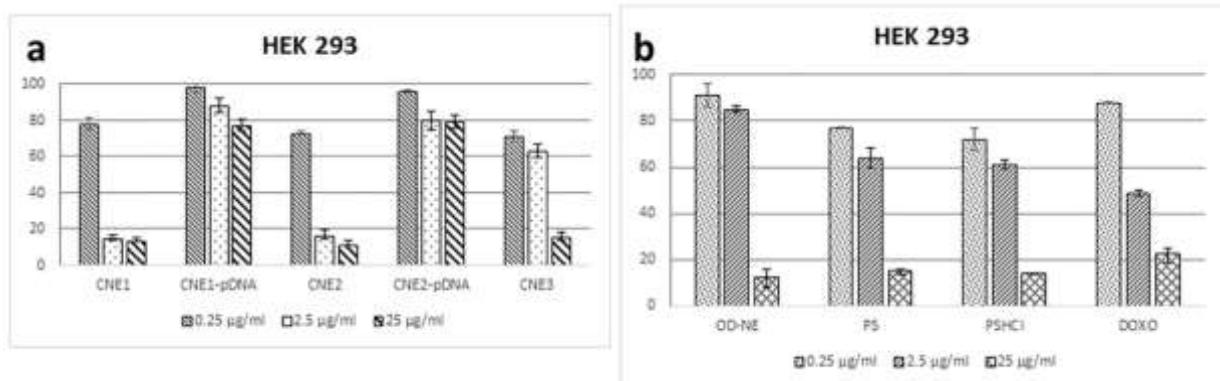


Figure 8: Cytotoxicity study results of CNEs, CNE-pDNA complexes, OD-NE, PS, PSHCL and DOXO on HEK 293 cells.

The viability of OD-NE decreased from 81% to 14% with increasing applied doses (Figure 8b). Thus, a distinctive effect of OD as the oil component on the viability of HEK 293 cells was observed.

Another factor influencing the cytotoxicity of the CNEs is the ZP. Applying a concentration of 2.5 µg/mL resulted in viabilities of 15% for CNE 1, 17% for CNE 2 and 63% for CNE 3, respectively. Comparing the ZPs of the CNEs showed results of 46.6 mV for CNE 1, 47.9 mV for CNE 2 and 34.1 mV for CNE 3. Thus, the higher the ZP, the more decreased viabilities were observed. A compromise of a ZP of approximately about 30 mV is indicated as appropriate for delivering nucleic acids like pDNA.

The viabilities decreased from 77% to 15% for PS, from 72% to 14% for PSHCl and from 88% to 22% for DOXO as positive control (Figure 8b). The viability results can be summarized in three groups: The first group with similar viabilities of CNE 1, CNE 2 and OD-NE. The second group with CNE 3, PS and PSHCl. And the third group with the CNE-pDNA complexes.

Regarding the cytotoxicity study results on HEK 293 it can be stated that all three CNE-pDNA complexes showed suitable viabilities. However, from the CNEs, CNE 3 seems to be more appropriate than CNE 1 and 2.

The cytotoxicity study results of the CNEs, CNE-pDNA complexes, OD-NE, PS, PSHCl and DOXO using MDA-MB-231 cells showed that with increasing the applied dose from 0.25 µg/ml to 25 µg/mL, the viability of the MDA-MB-231 cells decreased from 97% to 25% for CNE 1, from 95% to 10% for CNE 2, from 102% to 40% for CNE 3 (Figure 9a). The highest decrease in the viability to 10% was observed for CNE 2, containing PSHCl in the outer aqueous phase. The difference between CNE 1 and CNE 2 is the use of the cationic agents PS in the inner oil phase and PSHCl in the outer aqueous phase. Complexation of the CNEs with pDNA resulted in increased viabilities for all CNE-pDNA complexes, as expected (Figure 9a). The viability decreased from 98% to 26% for OD-EA. For PS, the viability decreased from 95% to 13%, from 103% to 12% for PSHCl and from 98% to 30% for DOXO as positive control (Figure 9b).

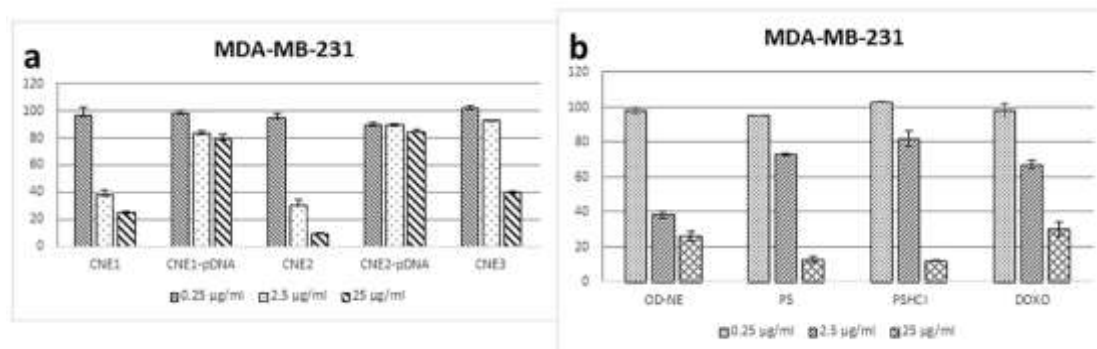


Figure 9: Cytotoxicity study results of CNEs, CNE-pDNA complexes, OD-NE, PS, PSHCl and DOXO on MDA-MB-231 cells.

Interestingly, the decrease of the viabilities on breast cancer cells is more distinctive for PS (13%) and PSHCl (12%), compared to DOXO (30%). Comparing CNE 1 and CNE 3 revealed that the concentration of the oil compound has a distinctive effect on cytotoxicity. The higher the oil concentration, the higher decrease in the viability was observed.

Regarding these results showed that CNE 2, showing the highest decrease in viability, is superior to CNE 1 and 3. These results can be explained with the DS and ZP results of the CNEs. The smallest DS and highest ZP were obtained for CNE 2 (144 nm and 47.9 mV). Thus, CNE 2 seems to be more appropriate.

With increasing the applied dose of CNEs, CNE-pDNA complexes, OD-NE, PS, PSHCl and DOXO from 0.25 µg/ml to 25 µg/mL, the viability of the MCF-7 cells decreased from 77% to 48% for CNE 1, from 85% to 13% for CNE 2 and from 107% to 54% for CNE 3 (Figure 10a). The highest decrease in the viability to 13% was observed for CNE 2, containing PSHCl in the outer aqueous phase with the highest ZP of 47.9 mV. Complexation of the CNE 1 and 2 with pDNA resulted in increased viability of 76% for CNE 1-pDNA and 86% for CNE 2-pDNA, compared to CNE 1 and 2 with viabilities of 48% and 13%, respectively, with an applied concentration of 25 µg/mL. For the OD-NE, the viability decreased from 92% to 50% (Figure 10b).

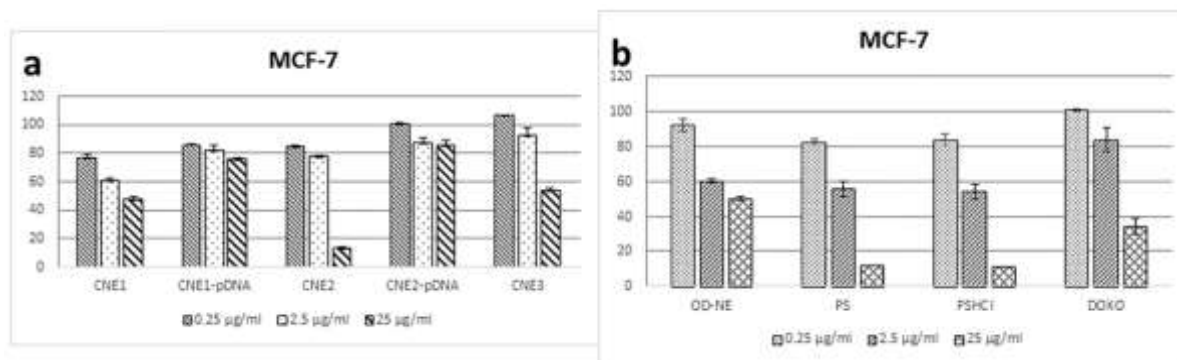


Figure 10: Cytotoxicity study results of CNEs, CNE-pDNA complexes, OD-NE, PS, PSHCL and DOXO on MCF-7 cells

The viability of MCF-7 cells decreased from 83 % to 12 % for PS, from 84 % to 11 % for PSHCL and from 101 % to 34 % for DOXO as positive control (Figure 10b). Again, the decrease of the viability is more distinctive for PS and PHCL, compared to DOXO, with viabilities of 12 % (PS), 11 % (PSHCL) vs. 34% (DOXO). Interestingly, incorporation of PSHCL into the CNE 2 has no effect on the viability, reflected as viability of 11 % for PSHCL compared to CNE 2 with a viability of 13 %. In addition, there is not a significant difference in the viabilities of CNE 1 (48 %) and CNE 3 (54 %) and OD-NE (50 %). Thus, the cytotoxic effect of CNE 1 and 3 is probably not based on PS, but on the CNE itself.

Evaluation of zeta potential in gene delivery systems is crucial in terms of electrostatic interaction with genetic materials and interaction with the negatively charged cell membrane, but also in terms of cytotoxicity. The substance that provides the cationic charge in these systems is also the main source of the cytotoxicity [30,31]. Therefore, the evaluation of zeta potential also reflects the evaluation of the cationic content in the formulation as a whole.

Based on these results it can be stated that CNE 2 seems to be superior compared to CNE 1 and 3.

4. Conclusion

Three CNEs were prepared by microfluidization and characterized in terms of DS, PDI, ZP, long-term stability after storage at 25 and 40 °C, complexation with pDNA, SDS induced release and particle characterization of CNE-pDNA complexes and cytotoxicity on breast cancer cells MDA-MB-231 and MCF-7. The prepared CNEs showed appropriate properties like a small DS of <200 nm, a narrow size distribution, expressed as PDI <0.3, and a high zeta potential of >+30 mV. Long-term stability studies after storage at 25 and 40 °C have shown that after storage of six months at 40 °C phase separation was observed for CNE 2. Thus, CNE 2 seems to be not appropriate in terms of stability. Unfortunately, only CNE 1 and 2 were able to form complexes with pDNA. CNE 1-

pDNA had the smallest DS, a PDI of 0.15 and a ZP of still 29.5 mV, and released pDNA. On the other hand, the DS of CNE 2 increased twofold, the PDI increased significantly and the ZP decreased significantly. The highest decrease in the viabilities of MDA-MB-231 and MCF-7 cells to 10 % and 13 %, respectively, was observed for CNE 2.

Although the CNEs are not ideal and each showed some disadvantages, CNE 1 seems to be more appropriate than CNE 2 and CNE 3.

Acknowledgement

This paper is dedicated to the memory of Selen Isar, a graduate student, who lost her fight against stroke after 135 days. She was an outstanding student and loved by her family and colleagues.

Special thanks to Prof. Dr. Özgen Özer from the Department of Pharmaceutical Technology, Faculty of Pharmacy, EGE UNIVERSITY for her support during the particle characterization by Zetasizer Nano ZS.

Author's Contributions

Selen Isar: Drafted and performed some of the experiments like preparation, droplet size and zeta potential measurements.

Yiğit Şahin: Performed the cytotoxicity studies.

Hasan Akbaba: Drafted and performed some of the experiments like complexation studies, SDS release studies and performed the statistical analysis.

Ayşe Nalbantsoy: Drafted and supervised the cytotoxicity studies and analyzed their results.

Gülşah Erel Akbaba: Drafted some of the experiments, wrote and revised the manuscript,

Yücel Başpınar: Drafted and wrote the manuscript, performed some of the experiments and analyzed all results.

Ethics

There are no ethical issues after the publication of this manuscript.

References

- [1]. Rolland, A, Sullivan, SM. Mechanisms for Cationic Lipids in Gene Transfer. Pharm Gene Del Sys, Eastern Hemisphere Distribution, New York 2003.
- [2]. Taira, K, Kataoka, TN (Eds.). Non-Viral Gene Therapy. Gene Design and Delivery. Springer-Verlag, Tokyo 2005.
- [3]. Clement, J, Kiefer, K, Kimpfler, A, Garidel, P, Peschka-Suss, R. 2005. Large-scale production of lipoplexes with long shelf-life. *European Journal of Pharmaceutics and Biopharmaceutics*; 59: 35–43.
- [4]. Kawakami, S, Higuchi, Y, Hashida, M. 2008. Nonviral approaches for targeted delivery of plasmid DNA and oligonucleotide. *Journal of Pharmaceutical Sciences*; 97: 726–745.
- [5]. Schuh, R, Baldo, G, Teixeira, H. 2016. Nanotechnology applied to treatment of mucopolysaccharidoses. *Expert Opinion on Drug Delivery*; 13: 1709–1718.
- [6]. Verissimo, LM, Lima, LFA, Egito, LCM, de Oliveira, AG, do Egito, EST. 2010. Pharmaceutical emulsions: a new approach for gene therapy. *Journal of Drug Targeting*; 18: 333–342.
- [7]. Wasungu, L, Hoekstra, D. 2006. Cationic lipids, lipoplexes and intracellular delivery of genes. *Journal of Controlled Release*; 116: 255–264.
- [8]. Hara, T, Liu, F, Liu, D, Huang, L. 1997. Emulsion formulations as a vector for gene delivery in vitro and in vivo. *Advanced Drug Delivery Reviews*; 24:265–271.
- [9]. Liu, F, Yang, J, Huang, L, Liu, D. 1996. Effect of non-ionic surfactants on the formation of DNA/emulsion complexes and emulsion-mediated gene transfer. *Pharmaceutical Research*; 13: 1642–1646.
- [10]. Teixeira, H, Dubernet, C, Puisieux, F, Benita, S, Couvreur, P. 1999. Submicron cationic emulsions as a new delivery system for oligonucleotides. *Pharmaceutical Research*; 16: 30–36.
- [11]. Zhang, S, Xu, Y, Wang, B, Qiao, W, Liu, D, Li, Z. 2004. Cationic compounds used in lipoplexes and polyplexes for gene delivery. *Journal of Controlled Release*; 100: 165–180.
- [12]. Pavicic, T, Wollenweber, U, Farwick, M, Korting, H.C. 2007. Anti-microbial and -inflammatory activity and efficacy of phytosphingosine: an in vitro and in vivo study addressing acne vulgaris. *International Journal of Cosmetic Science*; 29: 181–190.
- [13]. Castro, A, Lemos, C, Falcao, A, Glass, NL, Videira, A. 2008. Increased Resistance of Complex I Mutants to Phytosphingosine-induced Programmed Cell Death. *The Journal of Biological Chemistry*; 283 (28), 19314–19321.
- [14]. Simbulan, CM, Tamiya-Koizumi, K, Suzuki, M, Shoji, M, Taki, T. 1994. Yoshida S. Sphingosine inhibits the synthesis of RNA primers by primase in vitro. *Biochemistry*; 33: 9007–12.
- [15]. Hung, WC, Chang, HC, Chuang, LY. 1999. Activation of caspase-3-like proteases in apoptosis induced by sphingosine and other long-chain bases in Hep3B hepatoma cells. *Biochemical Journal*; 338: 161–6.
- [16]. Gottlob, K, Majewski, N, Kennedy, S, Kandel, E, Robey, RB, Hay, N. 2001. Inhibition of early apoptotic events by Akt/PKB is dependent on the first committed step of glycolysis and mitochondrial hexokinase. *Genes & Development*; 15: 1406–18.
- [17]. Nagahara, Y, Shinomiya, T, Kuroda, S, Kaneko, N, Nishio, R, Ikekit, M. 2005. Phytosphingosine induced mitochondria-involved apoptosis. *Cancer Science*; 96: 83–92.
- [18]. Park, MT, Choi, JA, Kim, MJ, Um, HD, Bae, S, Kang, CM, Cho, CK, Kang, S, Chung, SY, Lee, YS, Lee, SJ. 2003a. Suppression of Extracellular Signal-related Kinase and Activation of p38 MAPK Are Two Critical Events Leading to Caspase-8- and Mitochondria-mediated Cell Death in Phytosphingosine-treated Human Cancer Cells. *Journal of Biological Chemistry*; 278: 50624–50634.
- [19]. Park MT, Kang JA, Choi JA, Kang CM, Kim TH, Bae S, Kang S, Kim S, Choi WI, Cho CK, Chung HY, Lee YS, Lee SJ. 2003b. Phytosphingosine Induces Apoptotic Cell Death via Caspase 8 Activation and Bax Translocation in Human Cancer Cells. *Clinical Cancer Research*; 9: 878–885.
- [20]. Baspınar, Y., Keck, C. Borchert, HH. 2010. Development of a positively charged prednicarbate nanoemulsion. *International Journal of Pharmaceutics*; 383 (1-2) 201–208.
- [21]. Baspınar, Y, Borchert HH. 2012. Penetration and release studies of positively and negatively charged nanoemulsions—Is there a benefit of the positive charge? *International Journal of Pharmaceutics*; 430:247–252.
- [22]. Başpınar, Y, Gündoğdu, E, Köksal, C, Karasulu, E. 2015. Pitavastatin-containing nanoemulsions: Preparation, characterization and in vitro cytotoxicity. *Journal of Drug Delivery Science and Technology*; 29, 117–124.
- [23]. Isar, S, Akbaba, H, Erel-Akbaba, H, Başpınar, Y. 2020. Development and characterization of cationic nanoemulsions as non-viral vectors for plasmid DNA delivery. *Journal of Research in Pharmacy*, 24(6), 952–960.
- [24]. Başpınar, Y, Gündoğdu, E, Karasulu, E, Borchert, HH. 2013. The preparation of prednicarbate nanoemulsions - a comparison of three homogenizers. *Nano-Bulletin*; 2: 130102.
- [25]. Muller, RH. Zetapotential und Partikeladung in der Laborpraxis, Wissenschaftliche Verlagsgesellschaft mbH, Stuttgart, 1996.
- [26]. Akbaba, H, Erel Akbaba, G, Kantarcı, AG. 2018. Development and evaluation of antisense shRNA-encoding plasmid loaded solid lipid nanoparticles against 5- α reductase activity. *Journal of Drug Delivery, Science and Technology*; 44: 270–277.
- [27]. Mosmann, T. 1983. Rapid colorimetric assay for cellular growth and survival: Application to proliferation and cytotoxicity assays. *Journal of Immunological Methods*; 65; 55–63.
- [28]. Nalbantsoy, A, Hempel, BF, Petras, D, Heiss, P, Göçmen, B, İğci, N, Yildiz, MZ, Süßmuth, RD. 2017. Combined venom profiling and cytotoxicity screening of the Radde's mountain viper (*Montivipera raddei*) and Mount Bulgar Viper (*Montivipera bulgardaghica*) with potent cytotoxicity against human A549 lung carcinoma cells. *Toxicol*; 135; 71–83.
- [29]. Baspınar, Y. 2009. Nano- and microemulsions for topical application of poorly soluble immunosuppressives
- [30] Shao, XR, Wei, XQ, Song X, Hao LY, Cai X X, Zhang, ZR, Peng Q, Lin YF. 2015. Independent effect of polymeric nanoparticle zeta potential/surface charge, on their cytotoxicity and affinity to cells. *Cell proliferation*, 48(4), 465–474. <https://doi.org/10.1111/cpr.12192>
- [31] Lam HT, Le-Vinh B, Phan T, Bernkop-Schnürch A. 2019. Self-emulsifying drug delivery systems and cationic surfactants: do they potentiate each other in cytotoxicity?. *The Journal of pharmacy and pharmacology*, 71(2), 156–166. <https://doi.org/10.1111/jph.13021>